8-2018

Wetting of Bio-Inspired Complexly-Shaped Fibers and Channels

Chengqi Zhang
Clemson University, chengqz@g.clemson.edu

WETTING OF BIO-INSPIRED COMPLEXLY-SHAPED FIBERS AND CHANNELS

A Dissertation
Presented to
the Graduate School of
Clemson University

In Partial Fulfillment
of the Requirements for the Degree
Doctor of Philosophy
Materials Science and Engineering

---

by
Chengqi Zhang
August 2018

Accepted by:
Dr. Konstantin G. Kornev, Committee Chair
Dr. Igor Luzinov
Dr. Olga Kuksenok
Dr. Ulf D. Schiller

ABSTRACT

This Dissertation is centered on studying the wetting of complexly-shaped fibers and channels which is inspired by the Lepidopteran proboscis. From materials science and engineering standpoint, the Lepidopteran proboscis is a multifunctional microfluidic device. The unique materials organization, morphology, structure, and surface properties of the proboscis allows the Lepidopterans to feed on various food sources from highly viscous to very thin liquids while keeping its surface clean. Thus, the study on the proboscis wetting phenomena has drawn great interests of materials scientists and engineers. The shape of the Lepidopteran proboscis has a very special design combining complexly-shaped fibers and channels. However, it remains unknown how this unique shape benefits the multiple functions of the proboscis. In this Dissertation, we investigate the effect of shape on the wetting properties of proboscis by separately studying the wetting of complexly-shaped fibers and channels, and then, applying the gained knowledge to explain various wetting phenomena observed on the Lepidopteran proboscis.

In Chapter I, the definition of wetting is introduced and the fundamental studies on wetting of fibers and channels are reviewed. Then the structure and function of Lepidopteran proboscis is introduced, and the motivation for conducting the research in this Dissertation is explained.

In Chapter II, several wetting phenomena on the ribbon-like fiber, e.g. the morphological transitions of droplet configurations, stability of coating films, capillary rise

of menisci on ribbon-like fiber, and wetting of the ribbon rail are studied experimentally and theoretically. This study sets up the foundation for investigating the wetting phenomena of other complexly-shaped fibers and channels. The developed experimental and theoretical methods are actively used throughout this Dissertation.

In Chapter III, the instability of a thin coating film on the internal and external walls of a straight hollow elliptical fiber is studied, and the mechanisms of drop formation from the coating films and the droplet morphology is briefly discussed. Then the study is expanded to the ring made of a curved elliptical tube to cover a broad range of wetting phenomena associated with such complexly-shaped fibers by discussing the effect of ring radius of curvature and the cross-sectional ellipticity.

In Chapter IV, a new method for studying the wetting of complexly-shaped channels is developed based on the Princen theory, and examined with the V-shaped channel. Then, the wetting/dewetting of C-shaped channel is systematically studied both experimentally and theoretically.

In Chapter V, several wetting phenomena associated with the Lepidopteran proboscises, e.g. the food uptake from a pool of liquid or from a limited volume of liquid, the stability of liquid films deposited on proboscis after dipping it into a nectar source, and self-assembly of proboscis after the insect emerges from the pupa, are discussed based on the study of wetting of complexly-shaped fibers and channels.

All the results are summarized in Chapter VI.

DEDICATION

This Dissertation is dedicated to my family for their support and encouragement throughout my PhD study.

ACKNOWLEDGMENTS

First of all, I would like to thank my advisor, Dr. Konstantin Kornev, for his guidance, patience and encouragement during my PhD study at Clemson University. His passion about science, broad knowledge in multiple disciplines, ingenious insights on research, and hard work certainly inspired and helped me grow as a scientist. I would also like to express my gratitude to my committee members, Dr. Igor Luzinov, Dr. Olga Kuksenok, and Dr. Ulf Schiller for their valuable comments, suggestions and time.

I want to thank all the past and current group members, in particular, Dr. Vladislav Vekselman, Pavel Aprelev, Golnaz Tomaraei, Salahuddin Kabir, Luke Sande, Dr. Arthur Salamatin, Tatiana Stepanova, Vaibhav Palkar, Yueming Sun, Bochuan Sun for their help and support during this journey. I also very thankful to Mykhailo Savchak for the help on silanization, and Dr. Peter Adler and his group members, Dr. Charles Beard and Ms. Suellen Pometto for their help with research on butterflies and moths. I would also like to thank Dr. Gary Lickfield, Kimberly Ivey, James Lowe, Stanley Justice, Diane Swope and all other faculty and staff members of MS&E department for their continuous support.

I would like to thank all my close friends especially Liying Wei and her husband Yuqi Zeng, Ying Yang, Yawei Wei, Zhaoxi Chen, Yuzhe Hong for making my life enjoyable and memorable at Clemson.

Last but certainly not least, I would like to thank my parents. No words can ever describe my gratefulness for your unwavering support and encouragements. You are the greatest parents in the World.

TABLE OF CONTENTS

Page

LIST OF TABLES

Table Page

LIST OF FIGURES

Figure Page

CHAPTER I

INTRODUCTION

1.1 Definition of wetting

Formal definition of wetting of a solid material requires an introduction of a thermodynamic process by which an interface separating a solid from a gas is replaced by an interface separating the same solid from a liquid. Whether the liquid spreading over a given surface or not depends on the values of the surface tensions at liquid/solid, σ_{SL}, solid/vapor, σ_{SV}, and liquid/vapor, σ_{LV}, interfaces. The Young's equation representing the balance of forces acting at the contact line in the plane parallel to the solid surface, sets a relation between the surface properties of dry and wet substrate:

$$\sigma_{SV} - \sigma_{SL} = \sigma_{LV} \cos\theta, \tag{1.1}$$

where θ is the contact angle, a physicochemical characteristic of the three dissimilar solid/liquid/vapor phases meeting at a contact line. The contact angle is introduced as an angle at which the fluid/fluid interface meets a solid surface.

Good wetting assumes that the contact angle formed by a droplet is acute. The material is considered poorly wettable if the drop beads up on the surface forming the contact angle greater than 90^0 , Fig. 1.1.

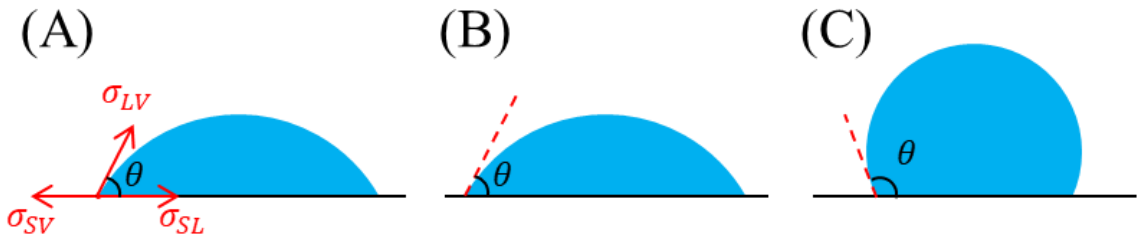

Figure 1.1. Drop shapes for different wetting scenarios: (A) Forces acting at the contact line. (B) Good wetting, (C) Poor wetting.

1.2 Wetting of fibers

With the development of modern textile industry, the field of wetting of fibers drew a lot of interest especially in context of coating, drying, cleaning, etc [1, 2]. The early scientific work on wetting was driven by the needs to control liquid penetration into fabrics and other porous solids [3]. More recently, with the rapid development of novel fibers, the study of wetting of fibers has become more and more important.

The early studies of wetting of fibers typically dealt with a cylindrical fiber as a model [4-12]. Wetting of cylindrical fibers has been studied extensively, including capillary rise of meniscus, film coating, and its instability resulting in formation of unduloidal waves and droplets of different morphology. These studies built a solid fundament and led the directions for the latter studies of wetting of complexly-shaped fibers.

Capillary rise of liquid/air interface induced by vertically dipping cylindrical tubes into a liquid reservoir was first documented by James Jurin [4]. Since then, this method becomes popular and it continues to generate new applications [5, 6]. The contact line of meniscus on the vertically placed fiber is always a circle. However, the meniscus height is

influenced by the fiber diameter and contact angle. The shape and height of meniscus on a vertically placed fiber was first calculated in [7]. The model was based on the pressure change in the vertical direction including hydrostatic pressure due to gravity. Unfortunately, the problem could not be fully solved due to the mathematical complexity. Instead, an approximate solution was proposed, which led to a noticeable discrepancy from the accurate meniscus profile. With the development of the method of matched asymptotic expansions, the calculation of meniscus profile was further improved [8, 9].

The study of coating film is very important for the dip coating process of fibers and textiles. Drawing a cylindrical fiber out of a bath of liquid at a constant velocity, one forms a uniform thin film of liquid deposited on the fiber surface. The thickness of this film is firstly identified by Goucher & Ward [13] to be affected by a key factor, the so-called capillary number: $\mathrm{Ca} = \eta V/\sigma$, where η and σ are the liquid viscosity and surface tension, and V is the drawing velocity. The accurate relation between the film thickness h and the capillary number Ca is determined by the theory developed by Landau, Levich, and Derjaguin (LLD theory) [14, 15]. And for the cylindrical fiber, the LLD law is written as: $h=1.34r\mathrm{Ca}^{2/3}$ [16], where r is the radius of the fiber. This relation is derived for small capillary numbers (it is also assumed that $h<<r$). As Ca increases, the relation is corrected as $h=1.34r\mathrm{Ca}^{2/3}/(1-1.34\mathrm{Ca}^{2/3})$ [17].

The pressure inside a uniform liquid thin film deposited on the cylindrical fiber surface should also be uniform according to Laplace law of capillarity. Therefore, no flow will be created inside the liquid film. However, if a small disturbance is introduced to the system, the liquid film would lose its stability and break into a series of droplets. This

phenomenon can be explained by the Plateau-Rayleigh instability [18, 19]. According to this theory, a liquid filament of the length longer than its circumference cannot be maintained cylindrical: any wave-like perturbations would break its uniformity. To avoid this instability in the industrial processes, the finish on the fiber is formulated in such a way that the deposited film gets dried faster than any instability develops.

The Plateau-Rayleigh instability [18, 19] also predicts that the liquid drop placed on a cylindrical fiber will not fully spread to form a uniform liquid film even if the liquid fully wets a flat substrate made of the same material [20]. The drop shape is governed by the Laplace equation of capillary:

$$\Delta \mathrm{P} = \sigma(\frac{1}{R_1} + \frac{1}{R_2}), \tag{1.2}$$

where R_1 and R_2 are the two principal radii of curvature of the liquid/vapor interface. Depending on the droplet volume and the contact angle between the liquid and fiber surface, the droplet can form two types of configurations: axisymmetric barrel and non-axisymmetric clam-shell [10, 11]. The criterion for the clam-shell – barrel transition was discussed by Carroll [12]. He related the length, surface area, volume, contact angle and Laplace excess pressure of a barrel drop adhering to a cylindrical fiber and showed that it was possible to define the critical drop volume for the clam-shell – barrel transition for a given fiber radius and liquid-fiber pair. The phase diagram describing these morphological transitions of droplets was calculated in [10].

The complexly-shaped fibers refer to the fibers with non-circular cross-sections. The cotton fiber has a bean-shaped cross-section as a result of the collapse of the dehydrated lumen; a silk fiber has a triangular shape [21]. However, wetting of complexly

shaped fibers was not systematically studied so far. With the development of fiber industry, hollow round, hollow triangle, hollow trilobal and hollow square fibers, rectangular, or arrow shaped fibers have been manufactured and widely used in different fields [22-33]. Therefore, an analysis of wetting phenomenon is long overdue.

The effect of the complex cross-sectional geometry of fibers on the capillary rise and meniscus shape was first discussed by Herb et al [34]. Recently, the capillary rise and meniscus shape on elliptical fiber was theoretically studied by Alimov and Kornev with the method of matched asymptotic expansions [35], where they found it very different from that on the circular cylinder. They also discovered singularities when the curvature of some points on the contour goes to infinity. This phenomenon was proved by their study of capillary rise of meniscus on the V-shaped edge [36]. The bundles of different complexly-shaped fibers show distinguishable wettability, such as the maximum liquid height of capillary rise, flux of saturated bundle, and the wicking velocity [37]. Another study shows that the yarn of Y- and H- shaped fibers exhibit a much stronger wicking ability than that of the bundle of cylindrical fibers [38].

These studies suggest that, in order to change the fiber wettability keeping the surface properties unaltered, one can change the fiber shape thus offering a new method to achieve the same purpose. In addition, the complexly-shaped fibers may provide directional and controlled moisture transport or drug flow.

1.3 Wetting of channels

Using channels with different size and shape for guiding of liquid flow has a very long history. Recently, with the development of microfluidic devices, different

microchannels have been manufactured and applied to transport minute amount of liquids[39-49]. Within this scale, the gravity can be neglected and the wetting/dewetting of the channel is mainly controlled by the capillary and wetting forces.

The wetting/dewetting phenomena and the morphological transitions of the drop configurations are inherently related [50-52]. The channel is considered wettable by the liquid when the liquid forms a columnar configuration in a channel of constant cross-sectional shape. This columnar shape would not be affected by adding more liquid. The channel is considered non-wettable by the liquid when the liquid forms a single or a series of clam-shell droplets in the channel.

Research shows that the specific morphology of liquid body formed in the channel is not only controlled by the contact angle, but also by the shape of the channels. The wetting/dewetting transition of liquid in the planar striped channel is found to solely depend on the contact angle, but not the width of the stripe [51]. But the transition in the V-shaped and rectangular channels is found to be affected by both [50].

The study of the wetting/dewetting transition in shaped channels is mainly done by calculating the minimum surface energy [53, 54]. This method, in principle, allows one to study all wetting scenarios. However, due to the mathematical complexity for calculating a complicated 3D geometry of the liquid body, the analysis of the wetting/dewetting transitions has been mostly done using 2D models of the droplets or menisci. The 2D model only considers the cross-sectional shape of a liquid column, but neglects the end effects where the contact lines meet the channel bottom. Thus, it neglects important force acting in the axial direction of the channel and forcing the drop to spread/contract. In this

Dissertation, we argue that this wetting force must be taken into account and illustrate this statement with a series of practically important examples.

Using this type of a 2D model, in a series of papers, Princen [55-57] studied stability of the columnar menisci formed between two and a bundle of parallel cylindrical fibers. He used the energy and force balance approaches to illustrate the method. In particular, the force balance analysis takes into account the cross-sectional shape of the column through the capillary pressure contribution and the effect of the fiber spacing through the tension on contact lines. Therefore, it can be extended to other fiber geometry to study the wetting/dewetting transitions of droplets.

While synthetic complexly shaped fibers and channels were invented long ago and went to the market, their applications are limited mostly because of lack of understanding of their wetting and transport features. The problem complexity can be inferred from an example of the butterfly proboscis.

1.4 Lepidopteran proboscis as a microfluidic device consisting of complexly-shaped fibers and channels

Butterflies and moths (Lepidoptera) have more than 180,000 species in 126 families, which takes approximately 10% of the total number of described species of living organisms and 28% of all fluid-feeding insects [58, 59]. The adult butterflies and moths are opportunistic feeders: they can feed on a wide range of fluids, from thick, highly viscous liquids, such as honey, to thin, almost inviscid mineral water, from various food sources such as soil, floral and extrafloral nectar, fruit, sap, plant surfaces, sugary exudates of plant-feeding insects, animal blood, carrion, dung, sweat, tears and urine [60-62]. The

feeding organ that they rely on to acquire liquid is called “proboscis”. Proboscis has been honed by natural selection for over millions of years into a multifunctional microfluidic device. This unique feeding device has drawn a lot of attentions of biologists, physicists, engineers, etc [60, 63-70].

The length and mean diameter of the Lepidopteran proboscises vary among species [70-72], but the proboscis structure is similar among species. The proboscis typically consists of a pair of C-shaped fibers, called galeae. Each galea carries muscles and trachea and is filled with blood called hemolymph [60], Fig. 1.2. These two galeae are joined by the dorsal and ventral linkage (legulae) forming a tubular food canal to transport the acquired liquid to the sucking pump in the head. The external contour of the proboscis, however, is not necessarily circular and typically non-uniform along the entire proboscis length [73].

The Lepidopteran proboscis is highly flexible and capable of a wide range of actions, from coiling to splaying for acquiring liquids and pollen [60]. These movements can, for instance, alter the spacing of the interlegular gaps to regulate fluid entry into the food canal, enlarge the food canal of the narrowed apex to reduce the suction pressure required to bring fluids to the mouth, and package the proboscis in a tight coil when not in use [60].

Since the Lepidopterans feed on fluidic food, the wetting property of the proboscis is extremely important for the success of feeding. The chemical composition of the proboscis includes hydrophobic chitin in its cuticle, coupled with surface lipids and waxes [74-77]. The roughness of the proboscis surface significantly changes the surface energy,

decreasing it in the case of waxed hydrophobic patches and increasing it in the case of protein-rich hydrophilic patches [78-82].

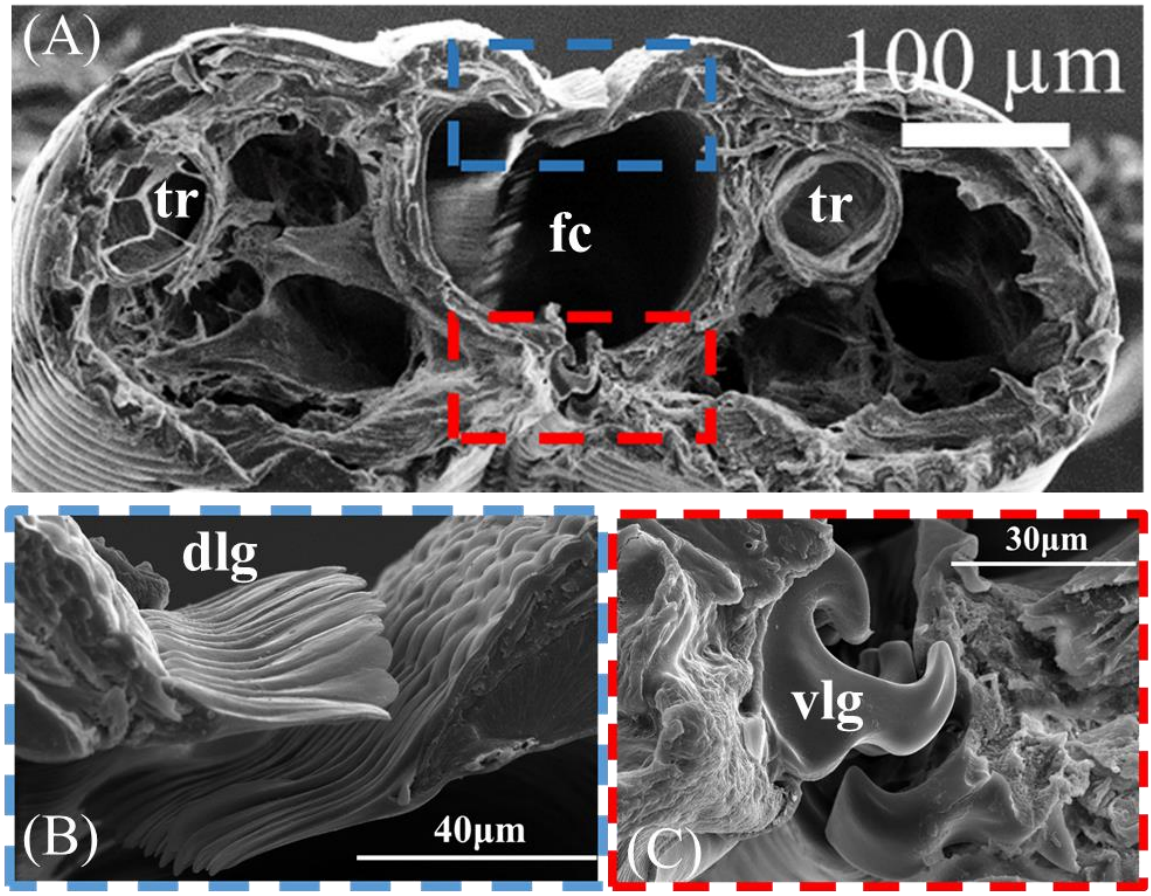

Figure 1.2. (A) Cross-section of proboscis of hawkmoth *Manduca sexta*; each galea contains a trachea (tr), muscles, and blood enclosed by a cuticular wall. When the galeae are united, at the dorsal legulae (dlg) and ventral legulae (vlg), their C-shaped walls form the food canal (fc). Magnification of the boxed area reveals the linkage mechanism formed by the legulae at the (B) dorsal and (C) ventral side of the proboscis.

A sharp boundary was found separating a hydrophilic drinking region and a hydrophobic non-drinking region [66]. The drinking region is located at the tip of the proboscis and the non-drinking region covers the rest. The ratio of the drinking region length to non-drinking region length varies among species [66]. Moreover, it is found that

the legular bands (dorsal and ventral) are always hydrophilic no matter whether one tests it in the drinking or non-drinking regions. This unique property is related to the feeding behavior.

For a long time, the proboscis has been compared functionally to a pipe or a drinking straw [71, 83-86], implying that the insect relies on a suction pump located in the insect's head to acquire liquid [65, 85-87]. This simple model can be qualitatively applied to explain the feeding from a pool of fluidic food source where the Lepidopterans can simply dip their proboscis into. However, this scenario was recently brought into question because the drinking straw model does not adequately represent proboscis function when the insects drink from porous substrates, such as wet soil or rotting fruit [64]. It has been shown that the legular bands, even in the non-drinking region, are not sealed, but have a large number of nanopores created by overlapping legulae at the interlegular spaces proximal to the drinking region [63]. These nanopores, together with the food canal, form a two-level pore hierarchy which enables the insect to acquire fluid along the entire length of the proboscis. Since the legular bands are hydrophilic and the rest of the proboscis surface is hydrophobic [66], the liquid tends to move toward these bands and leave the rest of the external surface dry and clean. Due to the capillary effect created by the nanopores and the function of the sucking pump, the liquid can sink into the food canal, form a series of liquid bridges, and get sucked [64].

The materials organization, morphology, structure, and surface properties of the proboscis are far from simple. In this Dissertation, we investigate the shape effect on wetting phenomena. From this aspect, the Lepidopteran proboscis can be seen as a

combination of complexly shaped fibers and channels: looking from outside, the proboscis is close to but more complex than elliptical fiber, and the ellipticity of the cross-section varies from head to tip [73]; looking from inside, the food canal remains circular but changes to elliptical when coiled, and it can be separated into semi-circular channels when breaking the linkage of the dorsal and ventral legulae. Therefore, the study of wetting of Lepidopteran proboscis can benefit a lot from the study of wetting of complexly-shaped fibers and channels.

1.5 Motivation

Understanding wetting phenomena associated with complexly-shaped fibers and channels important for many engineering applications, such as the design of microfluidics, textiles with controlled wettability and transport properties, and processing of fiber-based composites. The wetting phenomena appear to be in the core of engineering biology of insects, bringing new twist in the development of the materials science of surfaces and interfaces. However, the success of the currently limited applications of complexly shaped fibers and channels has mostly been achieved by the trials and errors approaches. The lack of understanding of the fundamental principles driving the wetting phenomena associated with the complexly-shaped substrates hinders progress in the development of fiber-based fluidic devices and textiles with controlled wettability and transport properties.

In most cases, the wetting of fibers and the wetting of channels are different. Therefore, we are going to separately study the wetting of complexly-shaped fibers and channels. We will discuss the wetting of the most common but important complexly-shaped fibers: ribbon-like fiber and elliptical fiber, in Chapter II and III, and the wetting of

V-shaped and C-shaped channels in Chapter IV. In Chapter V, we will apply the gained knowledge from the study of wetting of shaped fibers and channels to discuss the shape effect on wetting of Lepidopteran proboscis. Through this research, we hope to provide a solid fundament and bring new understanding to the study of wetting of complexly shaped fibers and channels.

1.6 References

[1] Danielli, J.F. 1958 Surface Phenomena in Chemistry and Biology. Pergamon Press.
[2] Adam, N.K. 1941 The Physics and Chemistry of Surfaces. Oxford University Press, H. Milford.
[3] Washburn, E.W. 1921 The dynamics of capillary flow. Physical Review 17, 273-283. (doi:10.1103/PhysRev.17.273).
[4] Jurin, J. 1717 An account of some experiments shown before the royal society; with an enquiry into the cause of the ascent and suspension of water in capillary tubes. By James Jurin, M. D. and R. Soc. S. Philosophical Transactions of the Royal Society of London 30, 739-747. (doi:10.1098/rstl.1717.0026).
[5] Lingstrom, R., Wagberg, L. & Larsson, P.T. 2006 Formation of polyelectrolyte multilayers on fibres: influence on wettability and fibre/fibre interaction. J Colloid Interface Sci 296, 396-408. (doi: 10.1016/j.jcis.2005.09.017).
[6] Pujado, P.R., Huh, C. & Scriven, L.E. 1972 On the attribution of an equation of capillarity to Young and Laplace. Journal of Colloid and Interface Science 38, 662-663. (doi: 10.1016/0021-9797(72)90410-9).
[7] White, D.A. & Tallmadge, J.A. 1965 Static menisci on the outside of cylinders. Journal of Fluid Mechanics 23, 325. (doi:10.1017/s0022112065001398).
[8] Lo, L.L. 1983 The meniscus on a needle – a lesson in matching. Journal of Fluid Mechanics 132, 65. (doi:10.1017/s0022112083001470).
[9] James, D.F. 1974 The meniscus on the outside of a small circular cylinder. Journal of Fluid Mechanics 63, 657. (doi:10.1017/s0022112074002126).
[10] McHale, G. & Newton, M.I. 2002 Global geometry and the equilibrium shapes of liquid drops on fibers. Colloids and Surfaces A: Physicochemical and Engineering Aspects 206, 79-86. (doi:10.1016/s0927-7757(02)00081-x).
[11] Carroll, B.J. 1986 Equilibrium conformations of liquid drops on thin cylinders under forces of capillarity. A theory for the roll-up process. Langmuir 2, 248-250. (doi:10.1021/la00068a024).
[12] Carroll, B.J. 1976 The accurate measurement of contact angle, phase contact areas, drop volume, and Laplace excess pressure in drop-on-fiber systems. Journal of Colloid and Interface Science 57, 488-495. (doi:10.1016/0021-9797(76)90227-7).
[13] Goucher FS & H., W. 1922 The thickness of liquid films formed on solid surfaces under dynamic condition. Philosophical Magazine 44, 1002–1014.

[14] Landau, L. & Levich, B. 1988 Dragging of a Liquid by a Moving Plate. Dynamics of Curved Fronts. 141-153. (doi:10.1016/b978-0-08-092523-3.50016-2).
[15] Derjaguin, B.V. 1943 Thickness of the liquid film adhering to a moving thread. Doklady Akademii Nauk Sssr.
[16] Derjaguin, B.V. & Levi, S.M. 1964 Film Coating Theory. London, The Focal Press.
[17] White, D.A. & Tallmadge, J.A. 1966 A theory of withdrawal of cylinders from liquid baths. AIChE Journal 12, 333-339. (doi:10.1002/aic.690120223).
[18] Plateau, J. 1873 Experimental and Theoretical Statics of Liquids Subject to Molecular Forces Only. Paris: Gauthier-Villars.
[19] Rayleigh, L. 1878 On the Instability of Jets. Proceedings of the London Mathematical Society s1-10, 4-13. (doi:10.1112/plms/s1-10.1.4).
[20] Minor, F.W., Schwartz, A. M., Wulkow, E. A., Buckles, L. C. 1959 The migration of liquids in textile assemblies: Part II: the wicking of liquids in yams. Textile Research Journal 29, 931–939.
[21] Chawla, K.K. 1998 Fibrous Materials. Cambridge, Cambridge University Press.
[22] Nakajima, P.T., Kajiwara, K. & McIntyre, J. 1994 Advanced Fiber Spinning Technology. Woodhead.
[23] De Rovere, A., Grady, B.P. & Shambaugh, R.L. 2002 The influence of processing parameters on the properties of melt-spun polypropylene hollow fibers. Journal of Applied Polymer Science 83, 1759-1772. (doi:10.1002/app.10128).
[24] Karaca, E. & Ozcelik, F. 2007 Influence of the cross-sectional shape on the structure and properties of polyester fibers. Journal of Applied Polymer Science 103, 2615-2621. (doi:10.1002/app.25350).
[25] Nijdam, W., Dejong, J., Vanrijn, C., Visser, T., Versteeg, L., Kapantaidakis, G., Koops, G. & Wessling, M. 2005 High performance micro-engineered hollow fiber membranes by smart spinneret design. Journal of Membrane Science. (doi: 10.1016/j.memsci.2005.02.022).
[26] Huang, Q., Seibig, B. & Paul, D. 1999 Polycarbonate hollow fiber membranes by melt extrusion. Journal of Membrane Science 161, 287-291. (doi:10.1016/s0376-7388(99)00122-2).
[27] Jung, I., Sang Yong, K. & Tae Hwan, O. 2009 Effects of spinning conditions on shape changes of trilobal-shaped fibers. Textile Research Journal 80, 12-18. (doi:10.1177/0040517509105279).
[28] Lee, M.S., Oh, T.H., Kim, S.Y. & Shim, H.J. 1999 Deformation kinetics of polypropylene hollow fibers in a continuous drawing process. Journal of Applied Polymer Science 74, 1836-1845. (doi:10.1002/(sici)1097-4628(19991114)74:7<1836::aid-app28>3.0.co;2-h).
[29] Petrulis, D. 2004 Fundamental study of the effect of the fiber wall thickness and inner diameter on the structure of polyamide and polypropylene hollow fibers. Journal of Applied Polymer Science 92, 2017-2022. (doi:10.1002/app.13722).
[30] Han, C.D. & Park, J.Y. 1973 A study of shaped fiber formation. Journal of Applied Polymer Science 17, 187-200. (doi:10.1002/app.1973.070170115).
[31] Rwei, S.-P. 2001 Formation of hollow fibers in the melt-spinning process. Journal of Applied Polymer Science 82, 2896-2902. (doi:10.1002/app.2145).

[32] Oh, T. 2006 Studies on melt spinning process of hollow polyethylene terephthalate fibers. Polymer Engineering & Science 46, 609-616. (doi:10.1002/pen.20499).
[33] Takarada, W., Ito, H., Kikutani, T. & Okui, N. 2001 Studies on high-speed melt spinning of noncircular cross- section fibers. I. Structural analysis of as-spun fibers. Journal of Applied Polymer Science 80, 1575-1581. (doi:10.1002/app.1250).
[34] Herb, C.A., Buckner, J.L. & Overton, J.R. 1983 The effect of cross-sectional geometry on the accuracy of the fiber-wetting balance. Journal of Colloid and Interface Science 94, 14-24. (doi:10.1016/0021-9797(83)90229-1).
[35] Alimov, M.M. & Kornev, K.G. 2014 Meniscus on a shaped fibre: singularities and hodograph formulation. Proceedings of the Royal Society A 470, 20140113. (doi:10.1098/rspa.2014.0113).
[36] Alimov, M.M. & Kornev, K.G. 2016 Piercing the water surface with a blade: Singularities of the contact line. Physics of Fluids 28, 012102. (doi:10.1063/1.4938171).
[37] Zhang, Y., Wang, H.P. & Chen, Y.H. 2006 Capillary effect of hydrophobic polyester fiber bundles with noncircular cross section. Journal of Applied Polymer Science 102, 1405-1412. (doi:10.1002/app.24261).
[38] Fuller, L. 2009 Production and Characterization of Novel Shaped Fibers for Fluid Sorption and Transport (Doctoral Dissertation). Clemson University.
[39] Chin, C.D., Linder, V. & Sia, S.K. 2012 Commercialization of microfluidic point-of-care diagnostic devices. Lab on a Chip 12, 2118-2134. (doi:10.1039/c2lc21204h).
[40] Li, D. 2004 Electrokinetics in Microfluidisc. Amsterdam, Elsevier Academic Press.
[41] Verma, M.K., Majumder, A. & Ghatak, A. 2006 Embedded template-assisted fabrication of complex microchannels in PDMS and design of a microfluidic adhesive. Langmuir 22, 10291-10295. (doi:10.1021/la062516n).
[42] Wilson, M.E., Kota, N., Kim, Y., Wang, Y., Stolz, D.B., LeDuc, P.R. & Ozdoganlar, O.B. 2011 Fabrication of circular microfluidic channels by combining mechanical micromilling and soft lithography. Lab on a Chip 11, 1550-1555. (doi:10.1039/c0lc00561d).
[43] Love, J.C., Anderson, J.R. & Whitesides, G.M. 2001 Fabrication of three-dimensional microfluidic systems by soft lithography. MRS Bulletin 26, 523-528. (doi: 10.1557/mrs2001.124).
[44] Waits, C.M., Modafe, A. & Ghodssi, R. 2003 Investigation of gray-scale technology for large area 3D silicon MEMS structures. Journal of Micromechanics and Microengineering 13, 170-177. (doi: 10.1088/0960-1317/13/2/302).
[45] Lee, P.J., Hung, P.J., Shaw, R., Jan, L. & Lee, L.P. 2005 Microfluidic application-specific integrated device for monitoring direct cell-cell communication via gap junctions between individual cell pairs. Applied Physics Letters 86, 223902. (doi:10.1063/1.1938253).
[46] Dong, L., Popov, S. & Friberg, A.T. 2011 One-step fabrication of polymer components for microphotonics by gray scale electron beam lithography. Journal of The European Optical Society - Rapid Publications 6, 51. (doi: 10.2971/jeos.2011.11010).
[47] Jia, Y.F., Jiang, J.H., Ma, X.D., Li, Y., Huang, H.M., Cai, K.B., Cai, S.X. & Wu, Y.P. 2008 PDMS microchannel fabrication technique based on microwire-molding. Chinese Science Bulletin 53, 3928-3936. (doi:10.1007/s11434-008-0528-6).

[48] Wu, H., Odom, T.W. & Whitesides, G.M. 2002 Reduction photolithography using microlens arrays: applications in gray scale photolithography. Analytical Chemistry 74, 3267-3273. (doi:10.1021/ac020151f).
[49] De Ville, M., Coquet, P., Brunet, P. & Boukherroub, R. 2011 Simple and low-cost fabrication of PDMS microfluidic round channels by surface-wetting parameters optimization. Microfluidics and Nanofluidics 12, 953-961. (doi:10.1007/s10404-011-0929-8).
[50] Khare, K., Herminghaus, S., Baret, J.C., Law, B.M., Brinkmann, M. & Seemann, R. 2007 Switching liquid morphologies on linear grooves. Langmuir 23, 12997-13006. (doi:10.1021/la701899u).
[51] Seemann, R., Brinkmann, M., Kramer, E.J., Lange, F.F. & Lipowsky, R. 2005 Wetting morphologies at microstructured surfaces. Proceedings of the National Academy of Sciences of the United States of America 102, 1848-1852. (doi:10.1073/pnas.0407721102).
[52] Bormashenko, E. 2010 Wetting transitions on biomimetic surfaces. Philosophical Transactions of The Royal Society A 368, 4695-4711. (doi:10.1098/rsta.2010.0121).
[53] Roy, R.V. & Schwartz, L.W. 1999 On the stability of liquid ridges. Journal of Fluid Mechanics 391, 293-318. (doi:10.1017/s0022112099005352).
[54] Brauner, N., Rovinsky, J. & Moalem Maron, D. 1996 Determination of the interface curvature in stratified two-phase systems by energy considerations. International Journal of Multiphase Flow 22, 1167-1185. (doi:10.1016/0301-9322(96)00046-8).
[55] Princen, H.M. 1969 Capillary phenomena in assemblies of parallel cylinders: I. Capillary rise between two cylinders. Journal of Colloid and Interface Science 30, 69-75. (doi:10.1016/0021-9797(69)90379-8).
[56] Princen, H.M. 1969 Capillary phenomena in assemblies of parallel cylinders: II. Capillary rise in systems with more than two cylinders. Journal of Colloid and Interface Science 30, 359-371. (doi:10.1016/0021-9797(69)90403-2).
[57] Princen, H.M. 1970 Capillary phenomena in assemblies of parallel cylinders: III. Liquid Columns between Horizontal Parallel Cylinders. Journal of Colloid and Interface Science 34, 171-184. (doi:10.1016/0021-9797(70)90167-0).
[58] Capinera, J.L. 2008 Butterflies and moths. In *Encyclopedia of Entomology* (pp. 626–672. Springer.
[59] Robert G. Foottit & Adler, P.H. 2009 Insect Biodiversity: Science and Society. England, Wiley-Blackwell Publishing.
[60] Krenn, H.W. 2010 Feeding mechanisms of adult Lepidoptera: structure, function, and evolution of the mouthparts. Annual Review of Entomology 55, 307-327. (doi:10.1146/annurev-ento-112408-085338).
[61] Adler, P.H. & Pearson, D.L. 1982 Why do male butterflies visit mud puddles Canadian Journal of Zoology 60, 322-325. (doi:10.1139/z82-043).
[62] Smedley, S.R. & Eisner, T. 1995 Sodium uptake by puddling in a moth. Science 270, 1816.
[63] Monaenkova, D., Lehnert, M.S., Andrukh, T., Beard, C.E., Rubin, B., Tokarev, A., Lee, W.K., Adler, P.H. & Kornev, K.G. 2012 Butterfly proboscis: combining a drinking straw with a nanosponge facilitated diversification of feeding habits. Journal of Royal Society Interface 9, 720-726. (doi:10.1098/rsif.2011.0392).

[64] Kwauk, K.J., Hasegawa, D.K., Lehnert, M.S., Beard, C.E., Gerard, P.D., Kornev, K.G. & Adler, P.H. 2014 Drinking with an unsealed tube: fluid uptake along the butterfly proboscis. Annals of the Entomological Society of America 107, 886-892. (doi:10.1603/An14027).
[65] Knopp, M.C.N. & Krenn, H.W. 2003 Efficiency of fruit juice feeding in Morpho peleides (Nymphalidae, Lepidoptera). Journal of Insect Behavior 16, 67-77. (doi:Doi 10.1023/A:1022849312195).
[66] Lehnert, M.S., Monaenkova, D., Andrukh, T., Beard, C.E., Adler, P.H. & Kornev, K.G. 2013 Hydrophobic-hydrophilic dichotomy of the butterfly proboscis. Journal of Royal Society Interface 10, 20130336. (doi:10.1098/rsif.2013.0336).
[67] Tsai, C.C., Mikes, P., Andrukh, T., White, E., Monaenkova, D., Burtovyy, O., Burtovyy, R., Rubin, B., Lukas, D., Luzinov, I., et al. 2011 Nanoporous artificial proboscis for probing minute amount of liquids. Nanoscale 3, 4685-4695. (doi:10.1039/c1nr10773a).
[68] Tsai, C.C., Monaenkova, D., Beard, C.E., Adler, P.H. & Kornev, K.G. 2014 Paradox of the drinking-straw model of the butterfly proboscis. Journal of Experimental Biology 217, 2130-2138. (doi:10.1242/jeb.097998).
[69] Kornev, K.G., Salamatin, A.A., Adler, P.H. & Beard, C.E. 2017 Structural and physical determinants of the proboscis-sucking pump complex in the evolution of fluid-feeding insects. Scientific Report 7, 6582. (doi:10.1038/s41598-017-06391-w).
[70] Lehnert, M.S., Beard, C.E., Gerard, P.D., Kornev, K.G. & Adler, P.H. 2016 Structure of the Lepidopteran proboscis in relation to feeding guild. Journal of Morphology 277, 167-182. (doi:10.1002/jmor.20487).
[71] Krenn, H.W., Zulka, K.P. & Gatschnegg, T. 2001 Proboscis morphology and food preferences in nymphalid butterflies (Lepidoptera: *Nymphalidae*). Journal of Zoology 254, 17-26. (doi: 10.1017/S0952836901000528).
[72] Kunte, K. 2007 Allometry and functional constraints on proboscis lengths in butterflies. Functional Ecology 21, 982-987. (doi:10.1111/j.1365-2435.2007.01299.x).
[73] Bauder, J.A., Lieskonig, N.R. & Krenn, H.W. 2011 The extremely long-tongued neotropical butterfly *Eurybia lycisca* (Riodinidae): proboscis morphology and flower handling. Arthropod Structure & Development 40, 122-127. (doi: 10.1016/j.asd.2010.11.002).
[74] Holdgate, M.W. 1955 The Wetting of Insect Cuticles by Water. Journal of Experimental Biology 32, 591-617.
[75] Beament, J.W. 1961 The water relations of insect cuticle. Biological Review Cambridge Philosophical Society 36, 281-320. (doi:10.1111/j.1469-185X.1961.tb01291.x).
[76] Vincent, J.F. & Wegst, U.G. 2004 Design and mechanical properties of insect cuticle. Arthropod Structure & Development 33, 187-199. (doi: 10.1016/j.asd.2004.05.006).
[77] Vincent, J.F.V. 2009 If it's Tanned it Must be Dry: A Critique. The Journal of Adhesion 85, 755-769. (doi:10.1080/00218460903291296).
[78] Cassie, A.B.D. 1948 Contact angles. Discussion of the Faraday Society 3, 11-16.
[79] Cassie, A.B.D. & Baxter, S. 1944 Wettability of porous surfaces. Transactions of the Faraday Society 40, 0546-0550. (doi: 10.1039/tf9444000546).

[80] Quere, D. 2008 Wetting and roughness. Annual Review of Materials Research 38, 71-99. (doi: 10.1146/annurev.matsci.38.060407.132434).
[81] Liu, K., Yao, X. & Jiang, L. 2010 Recent developments in bio-inspired special wettability. Chemical Society Review 39, 3240-3255. (doi:10.1039/b917112f).
[82] Bhushan, B. & Jung, Y.C. 2011 Natural and biomimetic artificial surfaces for superhydrophobicity, self-cleaning, low adhesion, and drag reduction. Progress in Materials Science 56, 1-108. (doi: 10.1016/j.pmatsci.2010.04.003).
[83] Eastham, L.E.S. & Eassa, Y.E.E. 1955 The feeding mechanism of the butterfly *Pieris-Brassicae* L. Philosophical Transactions of The Royal Society B 239, 1-43. (doi:10.1098/rstb.1955.0005).
[84] Krenn, H.W. 1990 Functional morphology and movements of the proboscis of Lepidoptera (Insecta). Zoomorphology 110, 105-114. (doi:10.1007/bf01632816).
[85] Krenn, H.W. & Kristensen, N.P. 2000 Early evolution of the proboscis of Lepidoptera (Insecta): external morphology of the galea in basal glossatan moths lineages, with remarks on the origin of the pilifers. Zoologischer Anzeiger 239, 179-196.
[86] Buttiker, W., Krenn, H.W. & Putterill, J.F. 1996 The proboscis of eye-frequenting and piercing Lepidoptera (Insecta). Zoomorphology 116, 77-83. (doi: 10.1007/s004350050010).
[87] Westneat, M.W., Socha, J.J. & Lee, W.K. 2008 Advances in biological structure, function, and physiology using synchrotron X-ray imaging*. Annual Review of Physiology 70, 119-142. (doi: 10.1146/annurev.physiol.70.113006.100434).

CHAPTER II

WETTING OF RIBBON-LIKE FIBERS

2.1 Introduction

A ribbon with the width W much greater than its thickness h, can be considered as a complexly shaped fiber with the simplest geometry, provided that the width is less than millimeter so that the fiber can be used in the textile constructs. Having two almost flat surfaces and two very sharp edges, this shaped fiber is expected to demonstrate wetting behavior drastically different from that of the cylindrical fiber. Another characteristic scale important for the ribbon-like fibers is the capillary length $l_c = \sqrt{\sigma/\rho g}$, where σ is surface tension of the liquid, ρ is density of the liquid, and g is the acceleration due to gravity. To distinguish wetting phenomena associated with fibers from those associated with macroscopic plates, the fiber width W should be much smaller than the capillary length, $W \ll l_c$ [1].

When a liquid of low surface energy is dropped on a flat surface of high surface energy, it spreads out to form a thin film and cover a large area of the surface. However, when a liquid film is deposited on a sharp edge, it would be quickly displaced from the edge by the high capillary pressure built up spontaneously inside the liquid. With the combination of these unique geometric features, the ribbon-like fibers have been widely

used in the wetting related applications both in Nature and in Engineering to achieve some extraordinary functions. Many plants, such as iris, have leaves which are ribbon-like. It was found that these ribbon-like leaves prevent the water droplets deposited on the top surface to roll over to the bottom surface where the pores for gas exchange are located [2]. This helps the plant to protect these pores from blocking by the water. Ribbon-like fibers are used in athletic fabrics and geotextiles [3] and seriously considered for filtration applications [4]. For the latter, it is critical to know what kind of morphological shape the deposited aerosol or emulsion droplets are taking on and how easy one can shake them off the ribbon. However, because of the lack of systematic study, the understanding of wetting of ribbon-like fiber and its application in the related field remain empirical.

In this chapter, we will systematically study several wetting phenomena specific for the ribbon-like fiber, including the morphological transitions of droplet configurations, stability of coating films, capillary rise of menisci on ribbon-like fiber, and wetting of the ribbon rail. This study will set up the foundation for investigating the wetting phenomena in other complex-shaped fibers and channels, and the developed experimental and theoretical methods will be actively used throughout this Dissertation.

2.2 Morphological transitions of droplet configurations on the ribbon-like fibers

As discussed in the introduction chapter, Section 1.2, the liquid droplets on a cylindrical fiber will not spread to form a film even if it makes zero contact angle with a fiber, but can form two distinct configurations: an axisymmetric barrel-like configuration or a clam-shell-like configuration depending on the contact angle and droplet volume [5-

8]. However, the droplet configurations on the ribbon-like fiber and the transition criteria remain unknown. To study this, we will control the same parameters, the contact angle and the volume of the droplet deposited on the ribbon. We limit ourselves to the case when the droplet volume V is large enough to cover the ribbon width W, i.e. when the inequality $\sqrt[3]{V} \gg W$ holds true.

2.2.1 Experiments

2.2.1.1 Characterization of liquids and ribbons

The tantalum ribbons with the width of $W = 1.3$ mm and thickness of $h = 0.03$ mm were used in these experiments. DI water and the aqueous solutions of Sodium Dodecyl Sulfate (SDS) with three different concentrations, 0.5 g/L, 1 g/L, 3 g/L, were used as the wetting liquids; glycerin droplets were also tested. Their surface tensions were measured with the Kruss Drop Shape Analyzer (DSA 10) through the pendant drop method. The results are summarized in Table 2.1. The contact angles of different solutions with the ribbons were also measured by the same instrument.

To measure the contact angles, the droplets of different solutions with the volume less than $V = 0.5$ μL were placed on the ribbons to make sure that the droplets were sitting on the ribbon side without contacting the ribbon edges. The advancing contact angle was measured from these placed droplets. The receding contact angle was measured by gradually sucking out the liquid from these droplets with a micro needle until their contact line has started to move. The needle was pulled out from the droplet and the receding contact angle was measured from the remained sessile droplet. The advancing and receding contact angles were measured by fitting the data with the 'Tangent method 1' in the Kruss

DSA software. The obtained results are shown in Table 2.1. Each result is averaged by five measurements and the error bar represents the standard deviation of these measurements.

Table 2.1. The advancing and receding contact angles between the ribbon and studied liquids

	DI water	0.5 g/L SDS	1 g/L SDS	3 g/L SDS	Glycerin
Surface tension (mN/m)	71±2	59±3	52±2	35±1	63±2
Advancing contact angle	70±1°	64±2°	57±2°	31±3°	69±3°
Receding contact angle	43±3°	33±2°	31±2°	25±3°	39±1°

2.2.1.2 Clam-shells and columns

The 3 μL droplets of different solutions were placed on the ribbons and their shape was imaged after 30 seconds when the droplets have taken on their equilibrium shapes. The droplet volume was chosen to satisfy the inequality $\sqrt[3]{V} \gg W$ to ensure that the droplet will spread out to the ribbon edges and be pinned by the edges. For imaging the droplet profile from the side, the camera was placed in front of the ribbon edge so that the objective was making 90° with the ribbon long axis. Fig. 2.1 illustrates a series of the equilibrium droplet shapes. When the contact angle is large, the droplet sits on the ribbon as a clam-shell, as shown in Figs. 2.1(A)-(C). At the highest SDS concentration in this series providing the 31° contact angle, the droplet suddenly spreads into a column having a zero curvature at the column central part as shown in Fig. 2.1(D).

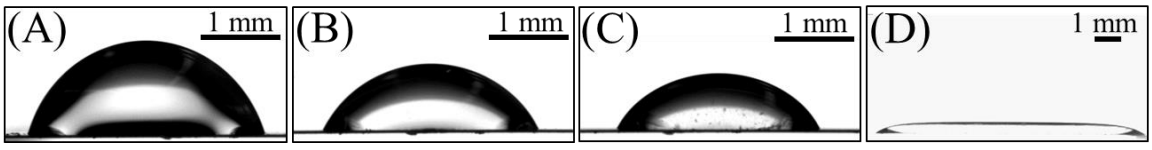

Figure 2.1. Droplet configurations on the ribbons, the contact angles are (A) 70°, (B) 64°, (C) 57°, (D) 31°.

In another series of experiments, we varied the droplet size keeping the same contact angle. The original column made of 3 g/L of SDS solution remained in the columnar shape even after adding more liquid. This column spreads over the ribbon increasing its length but not changing its height.

The situation changes when one applies the droplets of DI water, 0.5 g/L and 1 g/L of SDS solutions to the ribbon. The 3 μL droplets were placed on the ribbon positioned horizontally as shown in the left column images of Figs. 2.2(A), (B), and (C), respectively. All droplets formed a clam-shell configuration. When the droplet volume was increased with 1 μL steps, the droplet became larger and larger, but it did not form a column, see the middle 3 images. Reaching a critical volume, the droplet falls down from the ribbon as shown in the right column images. Typically, the two small residue droplets on each side of the ribbon remained, but the droplet never formed the barrel. Glycerin droplets behaves the same way, Fig. 2.2(D), suggesting that the mechanism of droplet breakup is not caused by surfactants.

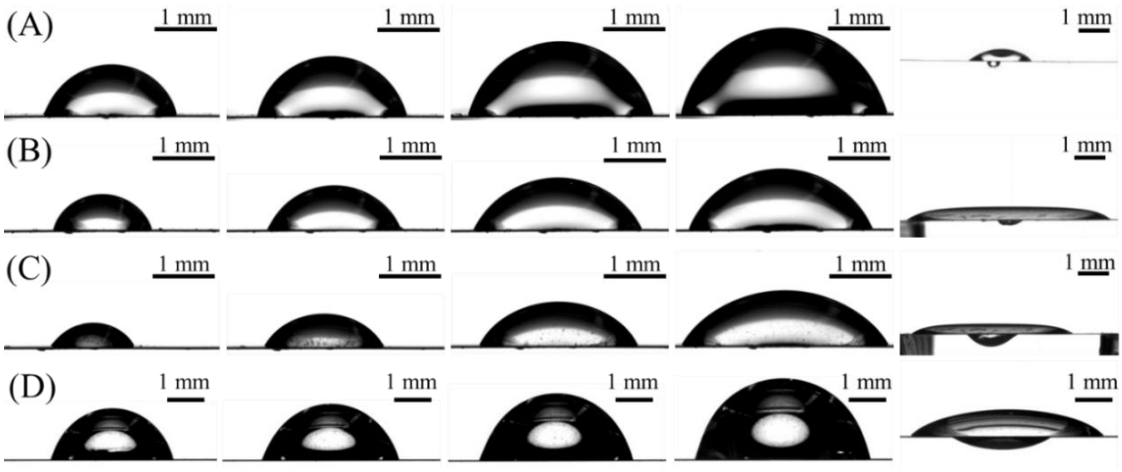

Figure 2.2. Droplet configurations on ribbons with increasing droplet volume from left to right; the contact angles are (A) 70° (DI water), (B) 64° (0.5 g/L SDS), (C) 57° (1 g/L SDS), (D) 67° (Glycerin).

Looking at the remaining droplets on the ribbon in the right column images in Figs. 2.2(A), (B), and (C), we observed that their configurations are different. At the larger contact angle, Fig. 2.2(A), the remaining liquid still forms the clam-shell configuration, similar to the mother droplet. But at smaller contact angles, Figs. 2.2(B) and (C), the remaining liquid forms the column configuration, which is very different from the mother droplet. In order to find out the reason of this difference, we further investigated the process of formation of the mother droplet and the remaining droplet.

To slow down the flow dynamics, glycerin of a high viscosity ($\eta = 0.63\ Pa \cdot s$, measured with Brookfield Digital DV-III Ultra Programmable Rheometer) was studied in detail. A 3 μL droplet of glycerin was placed on the ribbon positioned horizontally, the top view of it is shown in Fig. 2.3(A). Then the volume of the droplet was gradually increased as shown in Figs. 2.3(B)-(D). As the volume increases, the visible contact lines move along the long ribbon axis. The sides of the droplet sitting outside the ribbon area are sagged down, but the droplet remains pinned to the ribbon edges: the continuation of the visible contact line coincides with the ribbon edges as will be discussed later, Figs. 2.5(C) and (D).

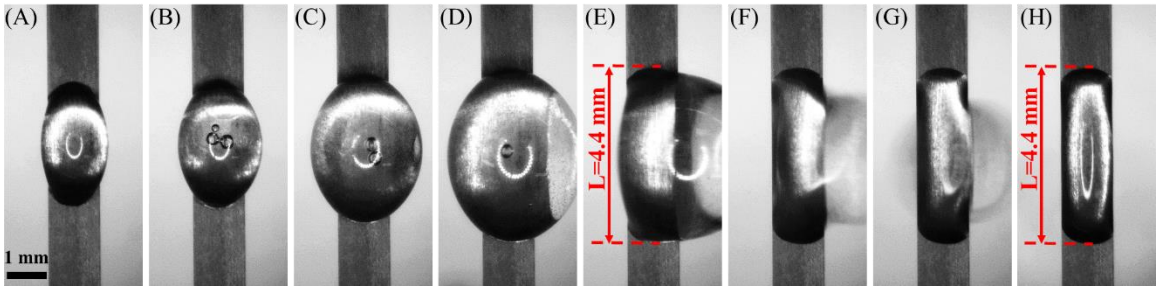

Figure 2.3. Illustration of the phenomenon of droplet roll over. Top view. The droplet volume is gradually increased from (A) to (E). At the moment (E), the droplet starts to roll over. Images (E)-(H) show the characteristic steps of the droplet roll over and fall. Image (H) demonstrates the final configuration of the relaxed droplet. The droplet base length L = 4.4 mm is shown by the arrows. The final droplet (H) has the same length L as that of droplet (E) starting to roll over.

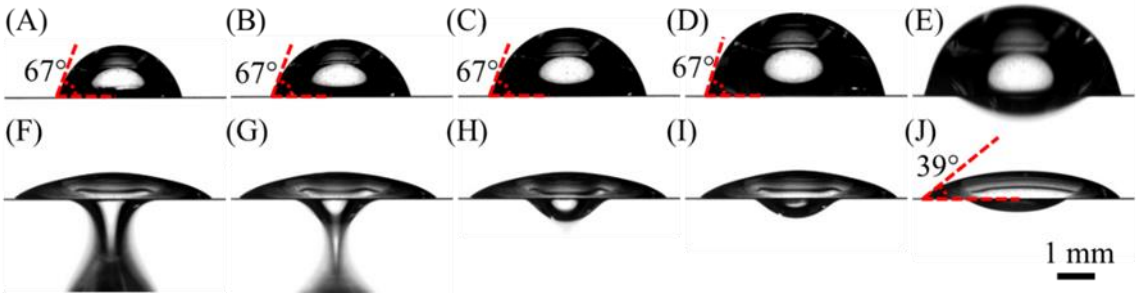

Figure 2.4. Illustration of the phenomenon of droplet roll over. Side view. (A)-(D) The droplet volume is gradually increased. In response, the droplet spreads over the ribbon increasing the base length L. This sequence of equilibrium configurations shows that the contact angle remains the same. (E)-(G) The details of the droplet roll over (E) and fall (F)-(G). Starting from the moment (D), a slight increase of the droplet volume results in the droplet roll over which is followed by the formation of the liquid bridge (F)-(G). After the bridge breakup, a residual droplet is formed at the lower side of the ribbon. The shapes of remaining droplets relax (H)-(I) to their equilibrium shape (J). The final droplet acquires the receding contact angle.

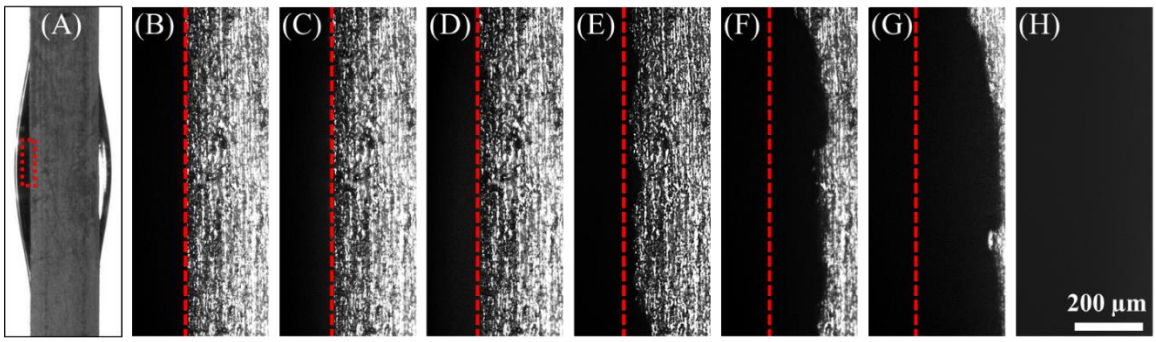

Figure 2.5. Illustration of the phenomenon of droplet roll over. Bottom view. (A) Schematic showing the region of observation. (B) No liquid was placed on the ribbon. (C)-(D) The droplet shown in (A) is formed and then the droplet volume is gradually increased, but the contact line remains pinned by the edge of the ribbon shown by the dashed line. (E)-(H) The details of the droplet roll over. The film (which is darker) gradually spreads from left to right to wet the bottom surface of the ribbon. The dashed line marks the ribbon edge. The film spreading is fast: after the contact line de-pins from the ribbon edge at (E) at time moment t = 0 s, the contact line in (F) travels for t=0.06 s, the contact line in the (G) travels for t=0.08 s, and the film covers the boxed area shown in (A) during (H) t = 0.09 s.

When the droplet volume has reached some critical value, the droplet falls down from the ribbon as shown in Fig. 2.3(E). Since it was practically impossible to place a perfectly symmetrical droplet on the ribbon, the roll over and fall of the droplet always happened from one side. The droplet in Figs. 2.3(E)-(G) started rolling over from the right

side. After the fall, some liquid remained on the lower surface of the ribbon, Fig. 2.3(H). Comparing Figs. 2.3(E) and (H), we observed that the droplet base length *L* remained the same, i.e. the contact lines remained pinned and did not move during the droplet flow and droplet breakup.

To investigate the evolution of the droplet profile during the droplet roll over and breakup, the droplet was imaged from the side using the same experiment, Fig. 2.4. Figs. 2.4(A)-(D) illustrate the droplet behavior upon increase of its volume: the droplet accommodates an additional liquid by mostly increasing its base length shifting the contact lines along the ribbon long axis. However, during this displacement of the contact lines, the contact angle remained almost the same. In Fig. 2.4(E), the droplet has started to fall down from the top side of the ribbon.

The fall of the upper droplet is interesting as it does involve the process of sidewise flow of a liquid film resulting in the de-pinning of the contact line from the ribbon edges. This de-pinning occurs through formation of a thin liquid film spreading over the lower dry surface of the ribbon, Fig. 2.5. Finally, when the lower surface gets completely wet and covered with a film, the droplet falls down.

The falling droplet forms a liquid bridge connecting the droplet remaining on the lower surface of the ribbon and the fallen one. The bridge gradually thins down and finally breaks. The process is illustrated in Figs. 2.4(F)-(G). After the liquid bridge breakup and relaxation of the shapes of remaining droplets as illustrated in Figs. 2.4(H)-(I), the two equilibrium droplets remained on both sides of the ribbon, Fig. 2.4(H).

We examined whether these two remaining droplets are connected by a liquid film. To answer this question, a tube was inserted into the upper droplet to suck up some volume with an expectation that, if connected, the lower droplet would react on this imposed flow by changing its volume and shape. Multiple observations revealed that the volume and shape of the lower droplet remained the same, Fig. 2.6. These experiments confirmed that the two droplets do not communicate and hence are completely separated from each other.

As shown in Figs. 2.2 and 2.4, the configurations and contact angles of the remaining droplets are different from the original ones. Comparison of the droplet shapes in Fig. 2.4(H) and Fig. 2.4(D) revealed that the contact angle significantly decreased from 67° to 39°. This jump from the larger to smaller contact angles has been observed for all studied droplets in Fig. 2.2. We hypothesized that this might be a manifestation of the phenomenon of contact angle hysteresis [9]. To confirm this hypothesis, the receding contact angles were measured, see Table 2.1, and the hypothesis was supported: indeed, the contact angle formed by the droplet remaining on the upper ribbon surface after the fall of the mother droplet does correspond to the receding contact angle. Thus, when the mother droplet falls down, the total volume of the droplet remaining on the ribbon dramatically decreases. But the base length of the droplet remains the same, Figs. 2.3(D) and (H). This droplet wants to contract and has to switch its contact angle from the advancing to receding.

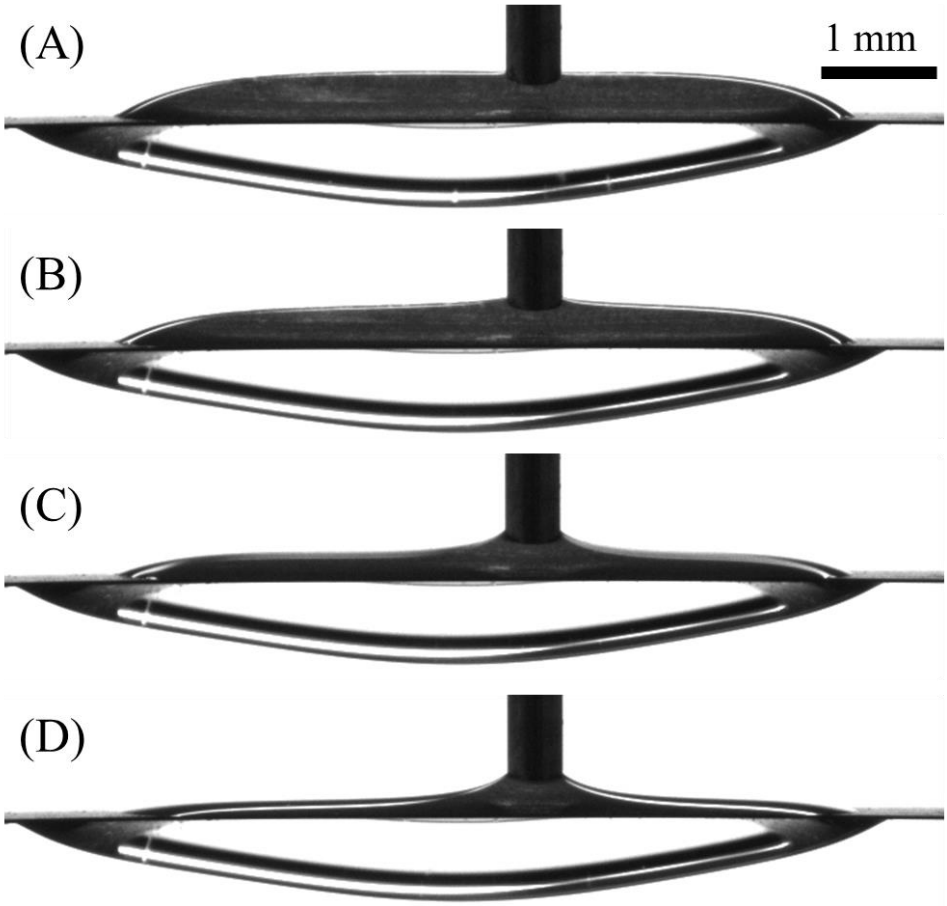

Figure 2.6. The proof that the two droplets are separated from one another. A needle was inserted into the upper droplet and some liquid was sucked out from the droplet. The lower droplet does not change the shape and its volume remained the same.

2.2.2 Criteria for the clam-shell – column transition. The force balance analysis

All possible configurations of droplets are described by the Laplace equation of capillarity which can be written in the form $\sigma\nabla\cdot\boldsymbol{n}=P$ [10], where vector $\boldsymbol{n}$ is the outward unit normal vector to the air/liquid interface, the dot product is the mean curvature of the air/liquid interface, σ is the surface tension, and P is the pressure in the droplet measured relative to the atmospheric pressure. To make the analysis more illustrative, the clam-shell – column transition is explained by the analysis of forces causing the droplet to spread. We

will use the first integral of the Laplace equation representing the force balance and, in parallel, directly use the free body diagram. The ribbons and droplets are macroscopic and hence the effect of line tension can be neglected in the force balance equation [11].

Following Princen theory [12] and building up a free body diagram for a droplet, we make an imaginary cut at the droplet center perpendicularly to the ribbon as show in Fig. 2.7. One part of the droplet is then replaced with an equivalent system of forces acting in the Z-direction parallel to the ribbon long axis. First, it is instructive to analyze the conditions for the column existence.

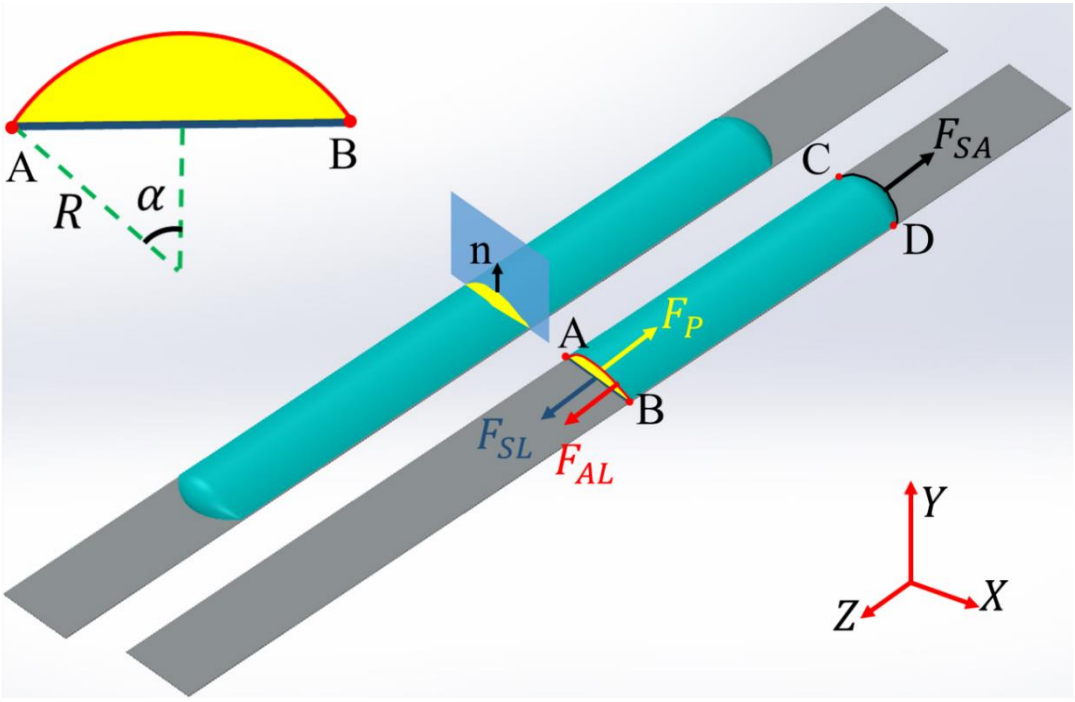

Figure 2.7. Schematic for the free body diagram analysis. The droplet is mirror symmetric with respect to plane Z=0 of a Cartesian system of coordinates (X, Y, Z) with the Z-axis parallel to the ribbon axis. A droplet is pined to the ribbon edges. Vector ***n*** is the outward unit normal vector to the air/liquid interface. Making an imaginary cut at the droplet center perpendicularly to the ribbon axis, one can replace one part of the droplet with an equivalent system of forces acting on the droplet cross-section at the cut. The force F_{AL} acting along the arc AB is associated with the surface tension at the air/liquid interface, the force acting along the line AB, F_{SL}, is associated with the surface tension at the solid/liquid interface, and the force F_p acting perpendicularly to the cut is associated with the pressure P. This system of forces is balanced by the force F_{SA} acting along the contact line CD; this external force is associated with the surface tension at the solid/air interface.

At the central part of the liquid column, the Z-component of vector $\boldsymbol{n}$ is zero, $n_z = 0$. This implies that the dot product in the Laplace equation is rewritten as $\nabla \cdot \boldsymbol{n} = \partial \mathrm{n}_Z / \partial \mathrm{X} + \partial \mathrm{n}_Y / \partial \mathrm{Y}$. Since the pressure in the droplet must be constant, the term $\partial \mathrm{n}_Z / \partial \mathrm{X} + \partial \mathrm{n}_Y / \partial \mathrm{Y}$ representing the curvature of curve AB in Fig. 2.7 must be constant. Thus, the curve AB is a circular arc. We denote the radius of arc AB by R and the subtending angle by 2α, where the angle vertex is the center of the circle AB. Therefore, the pressure in the liquid column is equal to $P = \sigma/R$.

According to the free body diagram in Fig. 2.7, the force balance in the z-direction is written as:

$$F_{AL} + F_{SL} - F_{SA} - F_P = 0, \tag{2.1}$$

where $F_{AL} = \sigma \cdot \widehat{AB} = 2\sigma R\alpha$ is the force due to surface tension at the air/liquid interface; $F_{SL} = \sigma_{SL} \cdot \overline{AB} = 2\sigma_{SL} R \sin\alpha$ is the force due to surface tension σ_{SL} at the solid/liquid interface; $F_{SA} = \sigma_{SA} \cdot \overline{AB} = 2\sigma_{SA} R \sin\alpha$ is the force due to surface tension σ_{SA} of the solid/air interface (where $\overline{AB} = 2R \sin\alpha$ is the exact X-projection of contact line $\widehat{CD}$); $F_P = P \cdot A$ is the pressure resultant acting perpendicularly to the cross-section of area $A = \alpha R^2 - R^2 \sin\alpha \cos\alpha$ embraced by $\widehat{AB}$ and $\overline{AB}$. Employing the Young-Laplace equation, $\sigma_{SA} - \sigma_{SL} = \sigma \cos\theta$, where θ is the contact angle formed by the liquid column with the flat side of the ribbon, eq. (2.1) is rewritten as:

$$\sigma\left(\widehat{AB} - \overline{AB} \cos\theta\right) - PA = 0, \tag{2.2}$$

This equation can be also obtained by integrating the Laplace equation of capillarity. In the Cartesian system of coordinates (X, Y, Z), the meniscus profile $Z = h(X,Y)$ describes the liquid elevation above the reference plane (X, Y), which coincides with the

cut shown in Fig. 2.7. It is convenient to rewrite the mean curvature through the surface elevation as $\mathbf{n} = \left(1+|\nabla h|^2\right)^{-1/2}\left(-\partial h/\partial X, -\partial h/\partial Y, 1\right)$ [13]. Thus, the Laplace equation is written as [1, 14] $\sigma\nabla\cdot\left[\left(1+|\nabla h|^2\right)^{-1/2}\nabla h\right]-P=0$, where the divergence operator is taken in its 2D form and the boundary conditions are written as $\left(1+|\nabla h|^2\right)^{-1/2}\partial h/\partial R = 1,$ at $X^2+Y^2=R^2; \left(1+|\nabla h|^2\right)^{-1/2}\partial h/\partial Y = -\cos\theta$ at $Y=0$. The first boundary condition follows from the singularity analysis as $\partial h/\partial R \to \infty$. Therefore, integrating the Laplace equation through cross-section A and using the divergence theorem, we obtain:

$$\int \sigma\nabla\cdot\boldsymbol{n}dA - PA = \sigma\int((1+\left(\frac{\partial h}{\partial R}\right)^2)^{-1/2})\frac{\partial h}{\partial R}\, d\widehat{AB} +$$

$$\sigma\int(1+\left(\frac{\partial h}{\partial X}\right)^2+\left(\frac{\partial h}{\partial Y}\right)^2)^{-1/2}\frac{\partial h}{\partial Y}d\overline{AB} - PA = \sigma\left(\widehat{AB}-\overline{AB}cos\theta\right)-PA = 0. \tag{2.3}$$

This derivation confirms the validity of the force balance eq. (2.2). After simplification, eq. (2.2) takes on the form

$$\cos\theta = \frac{1}{2}\left(\frac{\alpha}{\sin\alpha}+\cos\alpha\right), \tag{2.4}$$

where the angle α is allowed to change from 0 to π, describing a family of the column configurations ranging from a flat film to a circular cylinder, respectively.

Fig. 2.8 summarizes the numerical analysis of eq. (2.4). For the cases I, II, and III, the droplets always spread to form the columns with $0 < \alpha < \frac{\pi}{2}$. The column curvature

changes from infinity at $\alpha = 0$, to $1/R = 2/\overline{AB}$ at $\alpha = \frac{\pi}{2}$. Thus, the liquids satisfying the complete wetting condition, $\theta = 0$, will always form a flat film.

However, not all wetting liquids would form columns: the force balance, eq. (2.4), does not have solutions for α when the contact angle is greater than the critical angle $\theta_{cr} = \arccos\frac{\pi}{4} = 38.24°$. Thus, only those liquids which form the contact angles with the ribbon in the range $\theta < \arccos\frac{\pi}{4}$ are able to spread into the columns. This magic angle was first theoretically discovered by Brinkmann and Lipowsky [15] using the variation of surface energy constrained by the constancy of droplet volume of droplet on stripped domain on a flat surface. The force analysis explains the physics behind this transition: the tension on the contact line and pressure in the droplet pull the droplet to form a column. However, as the air/liquid and the liquid/solid surface tensions grow stronger, these two forces would contract the column back to the clam-shell state.

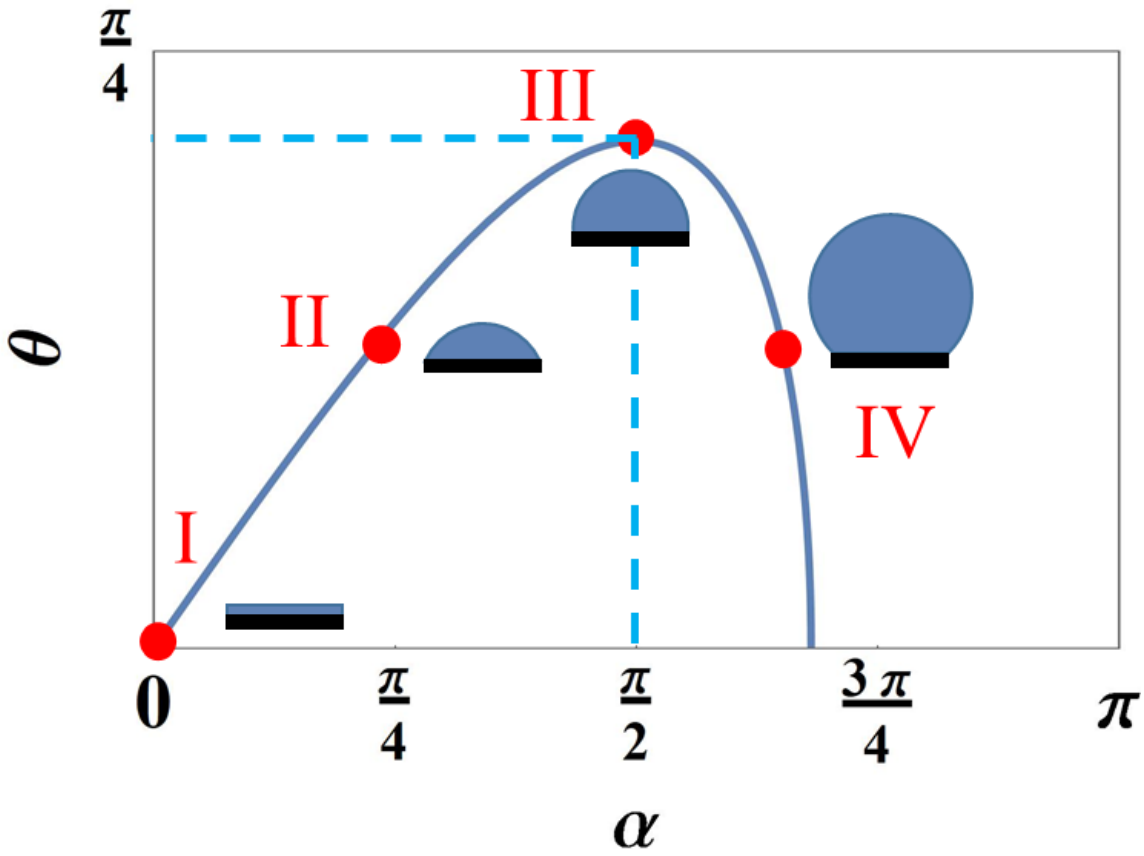

Figure 2.8. The theoretical bifurcation diagram for the liquid columns on the ribbon-like fibers. The vertical line $\alpha = \frac{\pi}{2}$ separates the left stable columns from the right unstable ones. The dashed line corresponds to the critical contact angle $\theta_{cr} = \arccos\frac{\pi}{4} = 38.24°$.

As discussed by Brinkmann and Lipowsky [15], there should be another unstable column bulging up, $\alpha > \pi/2$, see illustrative case IV in Fig. 2.8. These column solutions satisfy eq. (2.4) and bifurcate from the stable solution at $\theta \to 0$, $\alpha \to 0$. Such column with $\alpha > \pi/2$ is proved always unstable to wave-like perturbation [16]. Based on our experimental results with the droplets making the contact angle smaller than the critical angle 38.24°, we confirm that these columns are unstable and cannot be formed on the ribbons. These unstable configurations, however, are important to mention as they help to understand the mechanism of this morphological transition. The unstable bulged columns

can be used to construct an analytical perturbation procedure which could help to shed light on the mechanics of shape transition and reveal the cause of energy minimum for the clam-shells.

In the clam-shells, the Z-component of vector $\boldsymbol{n}$ is not zero, $n_z \neq 0$ at the droplet central part. Therefore, the curve AB is not a circular arc. The force balance eq. (2.1) is still applied, but the pressure P and cross-sectional area of the cut, A, cannot be related to the circular arc equation. Thus, the clam-shell shapes have to be determined by solving numerically the Laplace equation constrained by the given droplet volume. Brinkmann and Lipowsky [15] discussed this problem in details.

Although the constructed model would not allow us to fully describe geometry of the clam-shell configuration, it allows us to determine the criteria for the clam-shell – column transition. The analysis above suggests that if the contact angle between the droplet and the ribbon surface is greater than the critical angle $38.24°$, the droplet will form column configuration; if the contact angle is greater than $38.24°$, the droplet will form column. Volume of the droplet does not contribute to this clam-shell – column transition.

2.2.3 Comparison of experimental and theoretical results

This theoretical analysis of the column stability allows us to interpret the phenomena observed in the experiments Section 2.2.1. Following from the contact angle data in Table 2.1, all droplets making the contact angle greater than $38.24°$ should take on the clam-shell configuration. To confirm this statement, the comparison of experimental and theoretical results is concluded in Table 2.2. The droplets with the advancing contact angle greater than $38.24°$ always form clam-shells. However, when some critical volume

is added and the mother droplet falls off, the remaining droplet is prone to recede. If its receding angle is greater than 38.24°, the droplet should remain as a clam-shell, DI water. Otherwise, it will form a column. The droplets made of 0.5 g/L SDS and 1 g/L SDS having the receding contact angle smaller than 38.24° fall into this category and form columns.

Table 2.2. Comparison between the experimental and theoretical results proving the critical contact angle of 38.24° for the clam-shell – column transition on ribbon-like fibers

Figure	Liquid	Advancing or receding	Contact angle	Droplet configuration
Figure 2.1(A)	DI water	Advancing	70±1°	Clam-shell
Figure 2.1(B)	0.5 g/L SDS	Advancing	64±2°	Clam-shell
Figure 2.1(C)	1 g/L SDS	Advancing	57±2°	Clam-shell
Figure 2.1(D)	3 g/L SDS	Advancing	31±3°	Column
Top residue droplet Figure 2.2(A)	DI water	Receding	43±3°	Clam-shell
Top residue droplet Figure 2.2(B)	0.5 g/L SDS	Receding	33±2°	Column
Top residue droplet Figure 2.2(C)	1 g/L SDS	Receding	31±2°	Column
Figure 2.2(D)	Glycerin	Advancing	69±3°	Clam-shell
Figures 2.4(A)-(D)	Glycerin	Advancing	69±3°	Clam-shell
Figures 2.4(J)	Glycerin	Receding	39±1°	Clam-shell

2.2.4 Instability of the coating film and droplet formation

The difference between the stripped planar substrates and the ribbons is that the ribbons, in principle, should allow the drop to roll over the ribbon and make both its sides covered by a barrel-like drop. However, our experiments demonstrate that the drop deposition from one side of the ribbon has never led to the barrel formation. This

observation brings about a question of whether the drop could ever be collected on a ribbon as a barrel.

We therefore dip-coated the ribbons with the same liquids and observed how the coating films behave. The same tantalum ribbon was horizontally withdrawn from a capillary tube (inner diameter of 1.6 mm) filled with the liquid in question. When the ribbon is pulled out from the tube, a thin liquid film formed on its entire surface. The film quickly loses its stability and breaks into two drops at each side of the ribbon, Fig. 2.9. The two drops are separated by the ribbon edge, so that they are actually not connected and hence are able to take on different configurations. Also, since the drops were formed by dewetting the ribbon surface, the resulting receding contact angles appear smaller than the advancing one given in Fig. 2.1. Consequently, the drops in Fig. 2.9 (A) and (B) look as clam-shells but the drops in Figs. 2.9 (C) and (D) are transformed into columns.

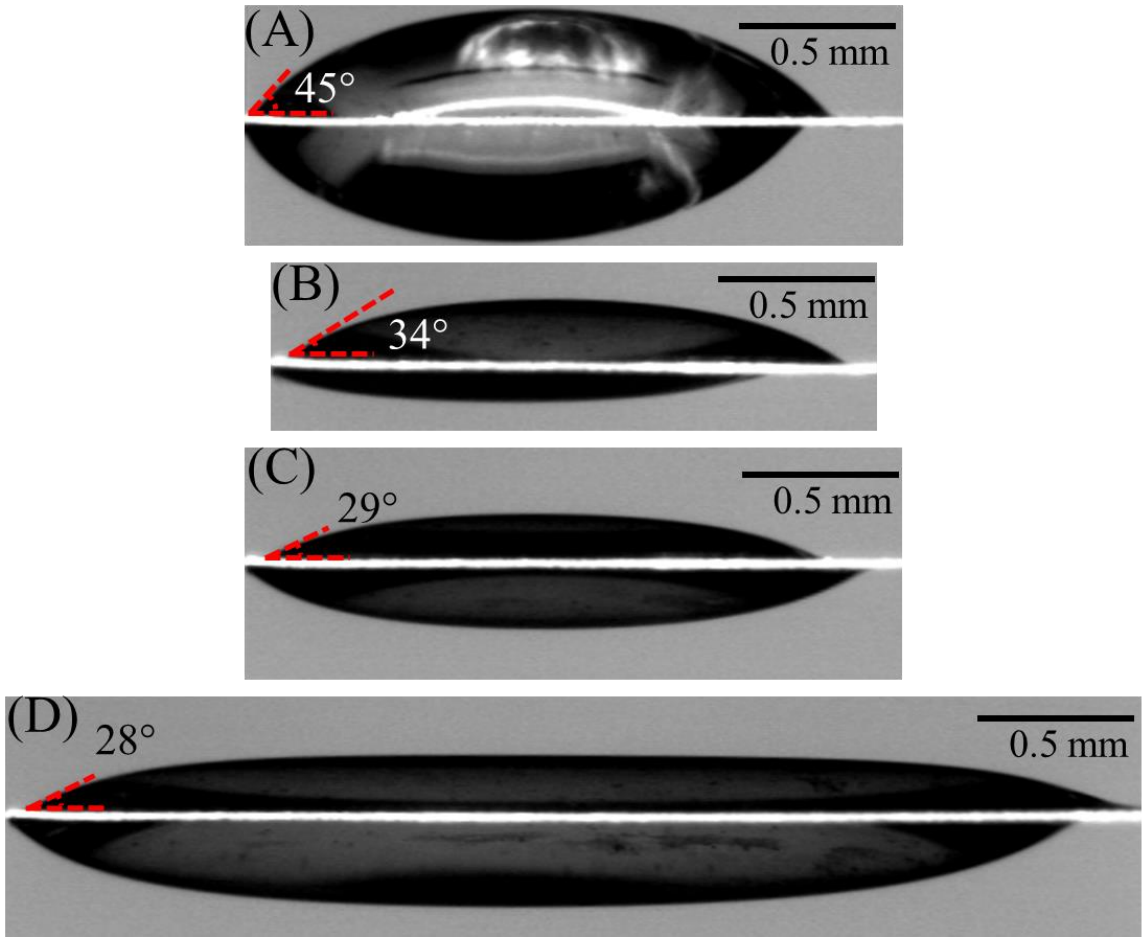

Figure 2.9. Final configurations of drops formed on the ribbons after coating, the receding contact angles are (A) 45°, (B) 34°, (C) 29°, (D) 28°.

We hypothesized that high curvature of the coating film at the sharp edge of the ribbon pushed the liquid toward the ribbon sides forcing the drops to move away from the edge. To support this hypothesis, an additional series of experiments have been conducted. The ribbon was withdrawn horizontally at the speed of 5 mm/s from a capillary tube full of glycerin. Fig. 2.10 illustrates this series of experiments showing the deposition process at a larger scale. The tube with Glycerin moves to the right leaving behind a thin film. A liquid meniscus labeled by ***m*** is formed at the tube end; it connects the tube with the ribbon

and when the tube moves to the right, this meniscus deposits a film covering the ribbon completely.

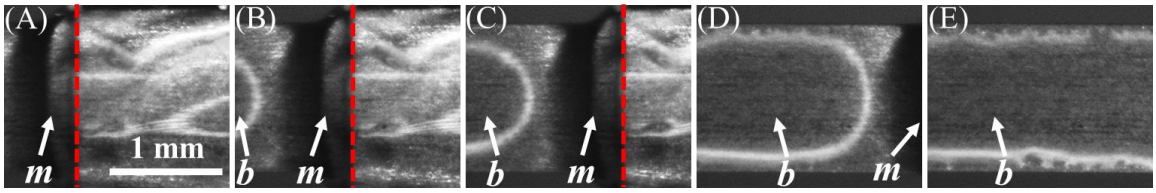

Figure 2.10. Evolution of a thin film on the ribbon surface, top view. The images are taken at the time moments (A) t=0 s, (B) t =0.05 s, (C) t = 0.1 s, and (D) t = 0.6 s. The red dashed line marks the end of the capillary tube which is on the right. The bulky meniscus connecting the tube edge with the ribbon is marked by ***m***; the bump on the liquid film is marked by ***b***. D) Observe the two wiggly contact lines shifted from the ribbon edges.

A bright light reflection in the form of horseshoe in Figs. 2.10 (B), (C) and (D) indicates that the film is not uniform but is bumped on the ribbon surface. The bump on the liquid film is marked by ***b***. When the tube end moves far away from the bump, the latter transfers into a drop shown in Fig. 2.10 (E).

We studied the process of formation of these contact lines at the higher magnification under the upright microscope (Olympus BX51) and imaged the film at the ribbon edge. Again, the tube with the immersed ribbon is withdrawn horizontally to eliminate any influence of gravity. The ribbon edge was magnified and the objective was focused on the dry surface prior to the ribbon coating. In Fig. 2.11, the tube with Glycerin is shown moving upward leaving behind a thin film. The shiny area sits in the focal plane of the objective and hence corresponds to the dry surface of the ribbon. Any blurriness is associated with the liquid film which surface is elevated above the dry surface of the ribbon.

The blurry regions in Figs. 2.11 (B)-(G) at the top correspond to the transition region from this meniscus to the film. As the film covering the edge thins down owing to

a high capillary pressure pushing the liquid to the flat sides of the ribbon, a wiggly contact line starts to appear, see the boxed area in Fig. 2.11(D). The expansion of the contact line, Figs. 2.11(D)-(G), is further observed indicating that the film de-wets a greater area of the ribbon edge. In this experiment, the wiggly contact line was only observed only on one side because the drops formed on two sides of the ribbon are not symmetric, as shown in Fig. 2.9.

As the tube with meniscus moves away from the region of interest, the liquid from the existing film flows to the bumps to form droplets at the flat sides of the ribbon. Finally, the entire edge is dried up, Fig. 2.11(H). The contact line was de-pinned from the ribbon edge, as shown in Fig. 2.10(E), therefore, could not be observed in the focal plane of Fig. 2.11(H).

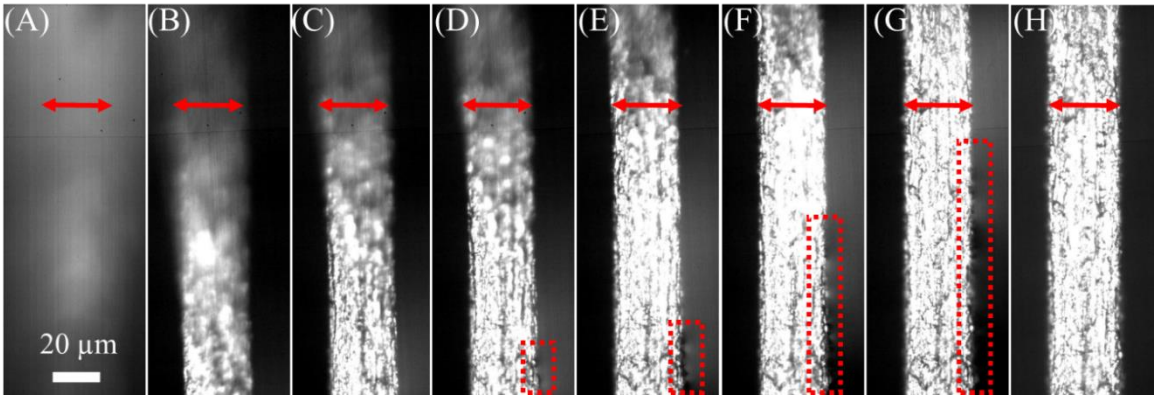

Figure 2.11. Evolution of liquid film coating the ribbon. The sharp edge of the ribbon was imaged from the side. The arrowed bar shows the thickness h=30µm of metal ribbon without film. (A) At the moment t=0 s, the ribbon is inside the tube full of Glycerin. (B) t = 0.01 s, (C) t = 0.02 s, (D) t = 0.03 s, (E) t = 0.04 s, (F) t = 0.05 s, (G) t = 0.06 s, and (H) t= 1s. In images (B) and (C), the ribbon is already outside of the tube but no contact line was observed indicating that the film covers it completely. In image (D), one observes the first signs of the ribbon edge dewetting when a wiggly contact line forms in the boxed region. This contact line further develops in images (E)-(G). In image (H), the edge is dry but the two droplets sitting on the opposite sides of the ribbon have been completely formed.

This experimental analysis supports the first observations and theory [17, 18] suggesting that the contact line on the ribbon should jump along the ribbon edges from the points where the meniscus first meets the edges to the points where the two pieces of the contact line belonging to the different ribbon sides actually emanate from. The wetting phase diagram for the ribbon case revealed that the meniscus surface is not able to approach the ribbon edges as a locally planar surface [17]. The edge always assumes a singular behavior of meniscus: in the discussed case, for example, it results in the drop separation and the contact line splitting.

2.2.5 Section conclusion

Different configurations of the droplets on thin ribbons are observed using the two methods of droplet formation. In the first method, the droplet is placed on one side of the ribbon and its volume is gradually increased by adding more liquid to it. In the second method, the ribbon was coated by withdrawing it from the tube filled with the liquid in question. Aqueous solutions of Sodium Dodecyl Sulfate and Glycerin were used for testing. When the volume of the deposited droplet is greater than the ribbon width, $\sqrt[3]{V} \gg W$, one can classify the configurations of droplets as the clam-shells and columns. Surprisingly, for these large droplets, the transition from the liquid column to the clam-shell droplet does not depend on the droplet volume. This transition is completely controlled by the contact angle. We propose a simple explanation of this phenomenon based on the analysis of forces acting on the droplet. Our theoretical results confirm the original Brinkmann – Lipowsky theory of wetting of substrates with chemically different surface stripes [15]. While the theory of wetting of the striped flat substrates is somewhat applicable to the ribbons,

experiments show that the scenarios of wetting of the ribbon-like fibers are different from those of the flat substrates and completely different from the scenarios of wetting of cylindrical fibers. In the reported series of experiments, the ribbons were not able to accommodate the barrel-like droplets. The sharp edges of ribbons generated very high capillary pressure which pushed the liquid from the edges breaking the barrel-like droplet onto a series of clam-shells.

2.3 Capillary rise of menisci on ribbon-like fibers

After discussing the wetting of the horizontal placed ribbon-like fiber by small droplets and thin films where the gravity is mostly not important, we would like to discuss another wetting scenario where gravity plays a very important role. Capillary rise of menisci on ribbon-like fibers is such an example. The capillary rise of the liquid surface on cylindrical fiber and elliptical fiber have been discussed in the introduction chapter, Section 1.2. As we emphasized, the theoretical calculation of the capillary rise on elliptical fiber predicts the occurrence of singularities if the ellipticity of the fiber cross-section is large enough to create sharp edges [1, 17, 18]. A ribbon-like fiber has two sharp edges, and therefore, is suitable to test this prediction.

2.3.1 Experiments

2.3.1.1 Fabrication of model ribbons

The glass bars of rectangular cross-section were cut from the VWR® NO.1 square micro cover glass with a diamond cutter. The resulting specimens had the length of about 20 mm, the width in the range of 1~2 mm, and the thickness in the range of 0.15±0.02 mm. The dimensions are shown in Fig. 2.12(A). Fig. 2.12(B) shows a collection of obtained glass bars. The length and width of each bar varies owing to the uncertainties caused by

the cutting method. In all cases, however, the ratio of width/length is smaller than 0.1. The accurate width of the bar at the contact line in each particular trial is measured directly from the image.

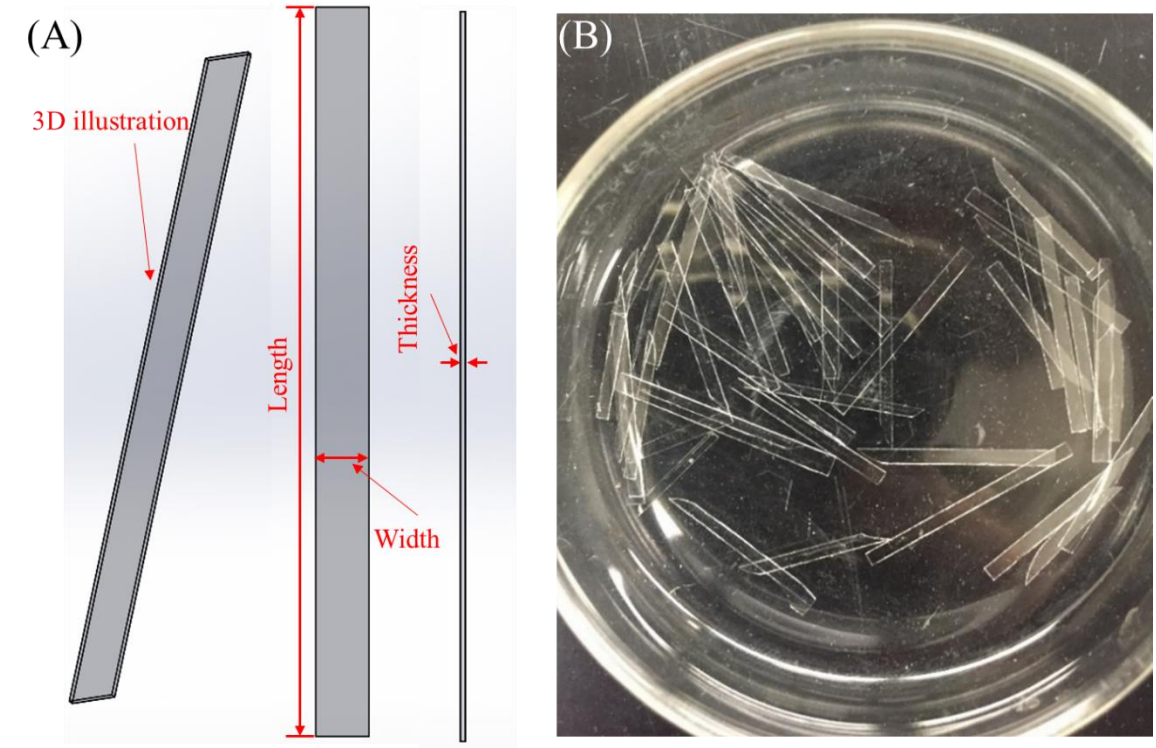

Figure 2.12. Glass bars cut from the VWR® NO.1 square micro cover glass. (A) A 3D schematic showing the dimensions of the bars. (B) A collection of all glass bars used in experiments.

2.3.1.2 Surface modification with silanes

The deionized water was used as the wetting liquid. To examine the contact angle effect on the capillary rise of the water menisci, we alter the surface energy of the glass bars by modifying their surfaces with different silanes. The glass ribbons were divided into five groups with eight pieces in each. A single piece of the non-cut VWR® NO.1 square micro cover glass was added to each group and treated together with the glass bars for the convenience of surface wettability characterization. One group was cleaned with methanol and kept without any further treatment as a reference. The other four groups were placed

inside the plasma treatment instrument (PLASMA CLEANER/STERILIZER, Harrick Scientific Corp, PDC-32G, Input power 100 W, Highest settings: 720V DC, 25 mA DC, Applied to 18 W) for fifteen minutes to activate their surfaces. After plasma treatment, one group from these four was used to conduct experiment immediately (within 15 mins), which provide a group of experiment with the contact angle close to zero. The other three groups were separately put into three 50 ml VWR® Polypropylene Centrifuge Tubes with different silanes present, and then left for overnight to vapor deposit and graft silanes to the glass surface. The silanes we used are (3-Aminopropyl)triethoxysilane, 2-[Methoxy(polyethyleneoxy)6-9proply]trimethoxysilane, Trimethylethoxysilane.

After surface silanization, the resulting contact angle was measured on the whole pieces of the non-cut micro cover glass treated together with the glass bars. We applied the KRUSS® Drop Shape Analyzer (DSA 25) to conduct these measurements. A 5 μL drop of deionized water is first placed on the glass substrate to measure the advancing contact angle. Then the water was sucked out from the drop by a syringe until the contact line of water had contracted. The receding contact angle was measured by analyzing the shape of remaining drop. The results are collected in Table 2.3. Each result is averaged by five measurements and the error bar represents the standard deviation of these measurements. The column '3-A' represents the bars modified with (3-Aminopropyl)triethoxysilane, the column '2-Me' represents the bars modified with 2-[Methoxy(polyethyleneoxy)6-9proply]trimethoxysilane, the column 'Trime' represents the bars modified with Trimethylethoxysilane, the column 'Origin' represents the bars that was cleaned with

methanol and kept without any further treatment, and the column ‘Plasma’ represents the bars which were used immediately after plasma treatment.

Table 2.3. Advancing and receding contact angles that the droplets of deionized water made with each group of glass bars.

Fiber group	3-A	2-Me	Trime	Origin	Plasma
Advancing contact angle (◦)	75±2	48±3	60±2	41±3	10±4
Receding contact angle (◦)	61±2	37±3	43±2	28±4	9±4

2.3.1.3 Experimental setup and protocol

The capillary rise of meniscus of the deionized water on the treated glass bars was studied with the setup shown in Fig. 2.13. A textile yarn was taped to the bottom of rotation plate and a glass bar was attached to the free end of the hanging yarn. To increase the bar weight, a paper clip of weight 1.2 g was attached to the lower end of the vertically hanging bar. This weight was sufficient to vertically align the bar in water. Then a 3D linear stage (Mitutoyo® Newport 460) and the rotation plate were adjusted to make sure that the wider part of the bar was perpendicular to the camera axis.

After these adjustments, a rectangular container with the deionized water was lifted up to almost completely immerse the bar into water. Then the direction of the stage movement has been reversed and we imaged receding menisci by moving the stage downward with small steps. The receding contact were used for charactering these shapes. Taking advantage of the mirror symmetry of the side menisci, only one side was imaged including the horizontal free water/air interface far away from the ribbon, as shown in Figs. 2.14 and 2.15. This allowed us to calibrate the meniscus features against the reference horizontal water surface.

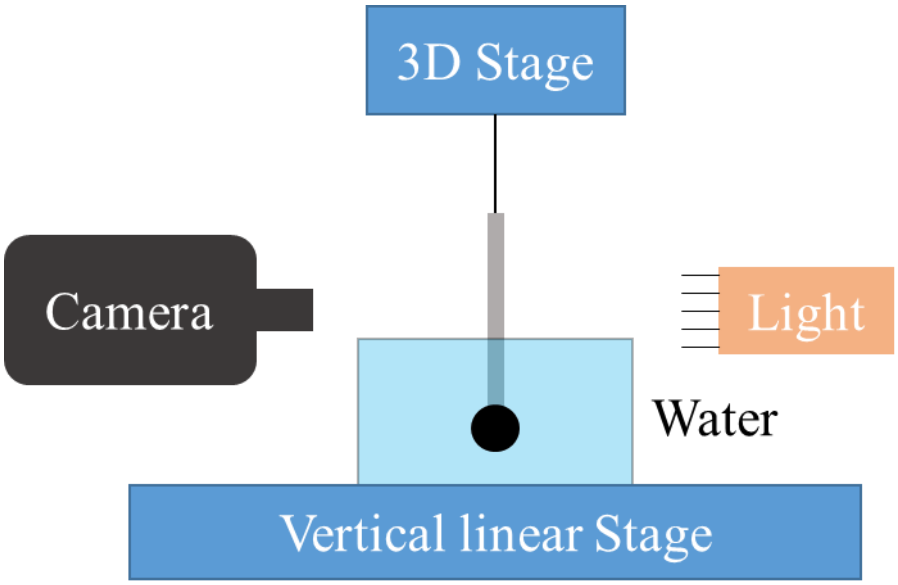

Figure 2.13. Imaging system for observation of the capillary rise of water surface on the glass bars.

2.3.2 Results

An example of the water meniscus formed on the glass bar is shown in Fig. 2.14. A wire with the known diameter was placed parallel to the glass bar in the same focal plane. It served as a scale to measure the meniscus height in the region of interest.

In contrast to the capillary rise of meniscus on a plate where the plate width W is much greater than the capillary length l_c, the contact line on the bar is curved, not straight [19]. The profile of the contact line is also distinct from that formed on the circular cylindrical fiber where the contact line describes the circles perpendicular to the fiber axis [20]. Moreover, the contact lines on the glass bars are not continuous but jumping at the bar edges from the lowest point A where the water/air interface first touches the bar edge to the upper point B where the contact line sitting on the bar side emanates from, Fig. 2.14. The pieces AB of the meniscus contact line are straight vertical lines running along the bar

edges. We call the length AB of this discontinuity the jump height, Fig. 2.14. The maximum height of the meniscus CD is defined as the distance from the highest point C of the curved contact line to the horizontal free liquid/air interface D, Fig. 2.14.

This meniscus singularity was predicted theoretically in [1, 17, 18]. The sharp edges of the bar create very high capillary pressure, which squeezes the liquid out from the edges either to the bar sides or to the free meniscus.

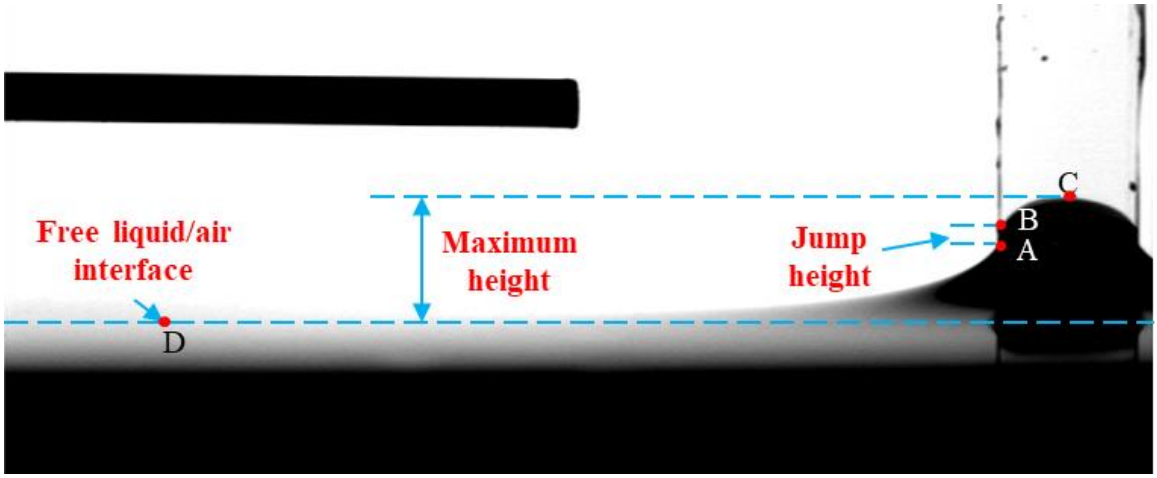

Figure 2.14. Profile of meniscus formed on the glass ribbon. The wire is set as a reference, its diameter is 0.5 mm. The dashed horizontal line marks the free liquid/air interface far away from the bar, D.

A gallery of images of menisci making different contact angles with bars are shown in Fig. 2.15. It is clear that the shape of menisci and its maximum height significantly depends on the contact angle. To quantify the effect of contact angle, the jump height and maximum height of menisci were measured from the images and plotted as a function of contact angle, Fig. 2.16. When the contact angle increases, the jump height and maximum height of menisci both decrease.

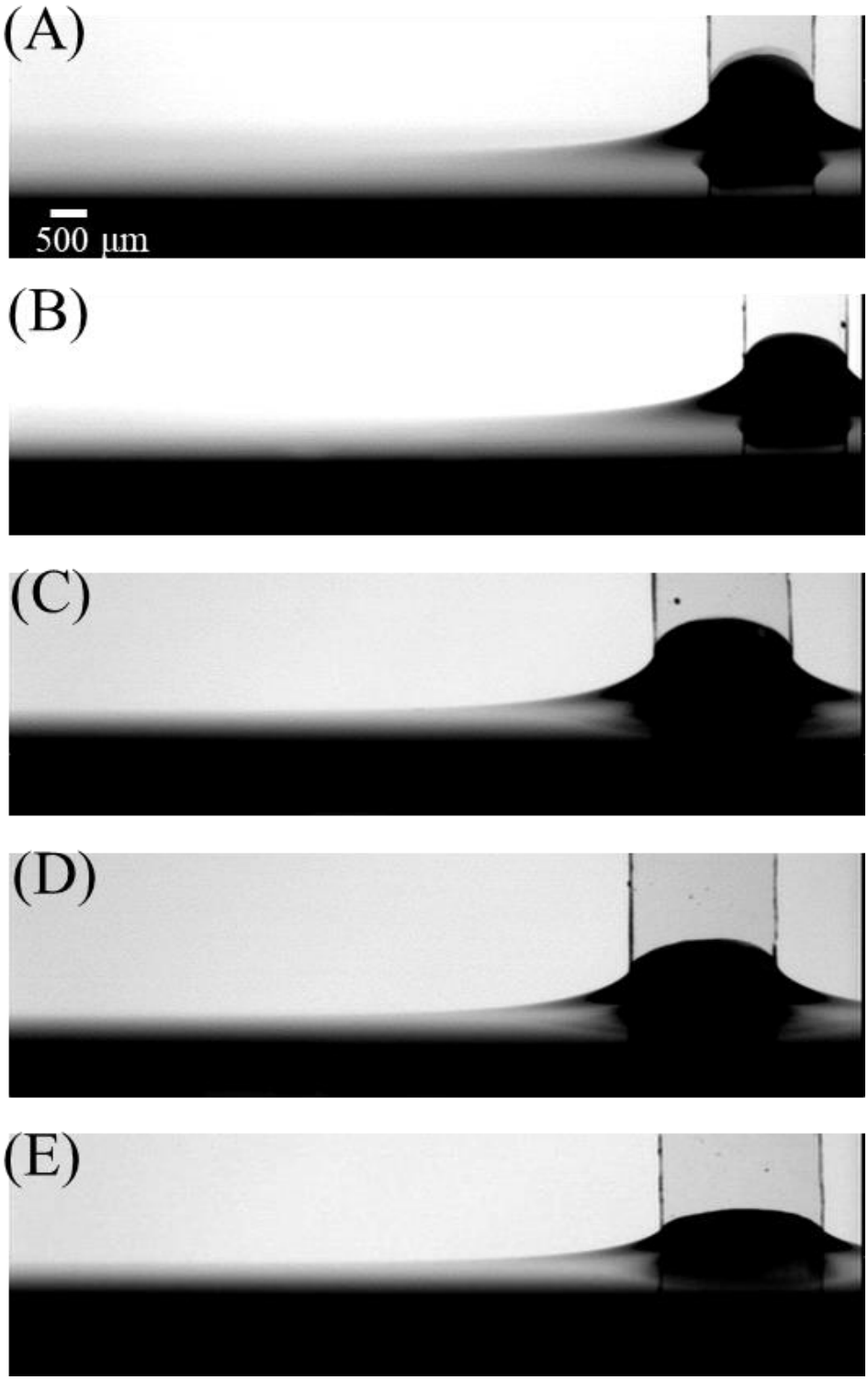

Figure 2.15. Water menisci on glass bars of different contact angles. The bar (corresponding to the group in Table 2.3) and the contact angle are: (A) Plasma, 9°; (B) Origin, 28°; (C) 2-Me, 37°; (D) Trime, 43°; (E) 3-A, 61°.

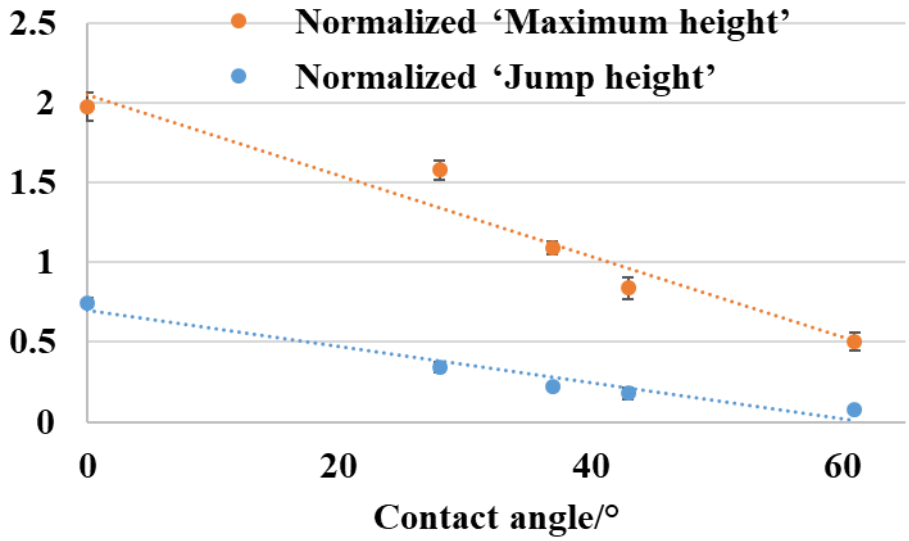

Figure 2.16. Dependence of the 'Jump height' and 'Maximum height' on the contact angle. The 'Jump height' and 'Maximum height' are normalized by the half width of the bar.

2.3.3 Section conclusion

The capillary rise of liquid surfaces on the rectangular glass bars modeling ribbon-like fibers is experimentally studied in this section. The singularity of contact line is observed at the bar edges. Its relation with the contact angle is quantified by two features of the contact line, the jump height and maximum height. These two characteristic heights of menisci are found to decrease with the increasing contact angle.

2.4 Wetting of the ribbon rail

In Sections 2.2 and 2.3, we discussed the wetting phenomena associated with a single ribbon-like fiber. Wetting phenomena associated with the textile constructs consisting of multiple ribbon-like fibers are poorly understood. We therefore turn to an analysis of these phenomena. As we already learned, the wetting liquid cannot cover the ribbon edges, so that it can only stay between two neighbor fibers. Since the liquid slug

between each pair of fibers is separated by the ribbon edge, it is sufficient to study the liquid behavior trapped between the ribbon rail and then periodically continue this picture to discuss an array of ribbons.

Similar to the wetting of a rail consisting of two cylindrical fibers [12], the liquid between the ribbon rail is expected to form a long liquid column filling the gap. Following Princen's analysis [12], we construct the model of a droplet trapped between the ribbon rail, Fig. 2.17. A column-like drop is sitting between two parallel identical ribbon-like fibers of width W, length L, and separation distance $2d$. The inequalities $L >> W$, $L >> d$ hold true. In setting up the model, we note that the separation distance, $2d$, is typically much smaller than the capillary length $2d \ll l_c$. Therefore, the gravitational effects can be neglected. Thus, menisci are mostly shaped by capillary forces. The contact angle between liquid and the ribbon surface is θ.

In the Cartesian system of coordinates (X, Y, Z), where the ribbon axis is parallel to the Z-axis, the meniscus profile $Y = h(X)$ describes the liquid elevation above the reference plane $Y = 0$ (Fig. 2.17). The two menisci forming the liquid bridge are assumed to be mirror-symmetric with respect to the X and Y axes.

The force balance in the Z-direction is obtained by constructing a free-body diagram and making an imaginary cut perpendicular to the Z-axis and replacing one part of the bridge with an equivalent system of forces (Fig. 2.17). At this cut, the Z-component of the force consists of five contributions: the two surface forces F_{AL} acting along the air/liquid interface, the two surface forces F_{SL} acting along the solid/liquid interface, and the force F_P caused by the pressure in the liquid; this force, F_P, acts over the cross-sectional

area cut. These five forces are counter-balanced by the force acting at the contact line at the end of the liquid bridge, F_{SA}, and is associated with the solid/air interface. The force balance is thus written as:

$$F_{AL} + F_{SL} - F_{SA} - F_P = 0. \tag{2.5}$$

To calculate these forces, one needs to distinguish the following two scenarios of the meniscus shaping: (1) the contact lines of the menisci of the columnar bridge are supported by the ribbon faces away from the ribbon edges (Fig. 2.17(B)), or (2) the contact lines are pinned at the ribbon edges (Figs. 2.17(C), (D)). The geometry of the cross-section of columnar liquid bridge for each scenario is illustrated in Fig. 2.18.

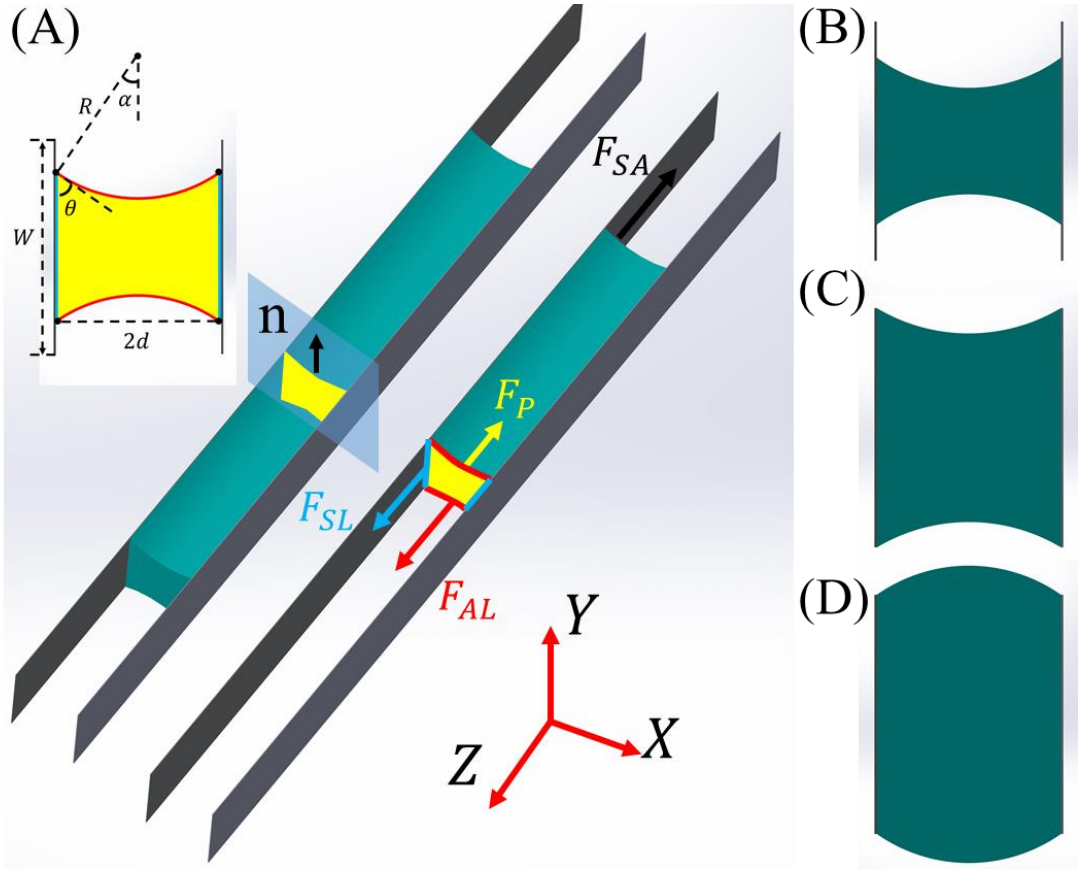

Figure 2.17. (A) A 3D schematic illustrating the shape of the columnar bridge of liquid formed between the ribbon rail. The cross-section is taken through a normal vector ***n*** vertical to X-Z plane.

(B) Bridge cross-section perpendicularly to the Z-axis assuming that the contact lines are sitting inside the food canal. (C) A case of a liquid bridge with concave menisci; the bridge cross-section shows contact lines pinned at the edges of ribbons. (D) A case of a liquid bridge with convex menisci; the bridge cross-section shows contact lines pinned at the edges of ribbons.

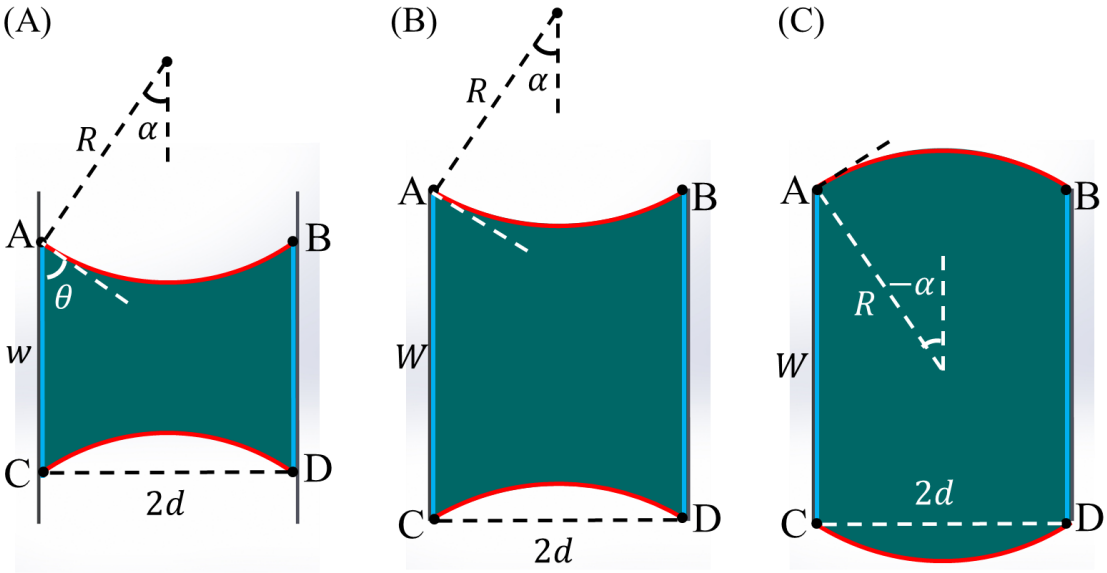

Figure 2.18. Schematic showing the cross-section of columnar liquid bridge between two ribbons with (A) contact lines staying away from the edges, (B) concave menisci with contact lines pinned by the edges, and (C) convex menisci with contact lines pinned by the edges.

2.4.1 The contact lines are sitting away from the ribbon edges

The columnar liquid bridge in the ribbon rail with the contact lines away from the edges meet the internal ribbon surfaces at the contact angle θ, Fig. 2.18 (A). Since we only consider the wetting case with contact angle $\theta \leq 90°$, the menisci AB and CD should always be concave arcs. Accordingly, the pressure in the liquid column measured relative to atmospheric pressure is negative, $P = -\sigma/R$. Employing the Young-Laplace equation, $\sigma_{SA} - \sigma_{SL} = \sigma \cos\theta$ [9], the force balance equation is reduced to the following equation:

$$(AB + CD) - (BD + AC)\cos\theta + A_{\mathrm{ACDB}}/R = 0. \quad (2.6)$$

Based on the geometry, we have the following relations:

$AC = BD = w$, $AB = CD = 2(\frac{\pi}{2} - \theta)R$, $R = d/\cos\theta$,

$$A_{\mathrm{ACDB}} = 2wd - R^2(\pi - 2\theta - \sin 2\theta), \tag{2.7}$$

where w is the width covered by the liquid, Fig. 2.18(A). Substituting all the above geometric relations in eq. (2.6), the following equation is obtained:

$$\frac{\pi - 2\theta + \sin 2\theta}{\cos^2\theta} \cdot d = 0\ . \tag{2.8}$$

When $0° \leq \theta \leq 90°$ the fraction $\frac{\pi - 2\theta + \sin 2\theta}{\cos^2\theta}$ cannot be zero and $d \neq 0$. Thus, eq. (2.8) cannot be satisfied suggesting that for the specified conditions no solutions describing a liquid bridge exist.

2.4.2 The contact lines are pinned at the ribbon edges

The case where the columnar liquid bridge is pinned to the ribbon edges is special: the contact angle at which the meniscus meets the sharp edge of any substrate is not defined and can take on any arbitrary value [17]. We, therefore, allow the circular arcs of the two menisci to approach the edges at any arbitrary angle. The liquid bridge can take on two configurations: one with concave menisci (Fig. 2.18(B)) and one with convex menisci (Fig. 2.18(C)).

2.4.2.1 Liquid bridge with concave menisci

For the concave menisci, eq. (2.6) is still applicable since $P = -\sigma/R$. At the reference cross-section, each liquid/air interface, AB or CD, is a part of a circular cylinder of radius R with the cylinder axes parallel to the Z-axis. The position of the contact lines where the meniscus meets the ribbons are specified by the angle α formed at the intersection of the y-axis and the continuation of the normal vector to the meniscus surface

at the edge (Fig. 2.19(A)). Thus, the central angle α completely defines the free surface of the liquid column. The geometric relation in this case is as follow:

$AC = BD = W$, $AB = CD = 2\alpha R$, $R = d/\sin\alpha$,

$$A_{\mathrm{ACDB}} = 2Wd - R^2(2\alpha - \sin 2\alpha), \tag{2.9}$$

Substituting all the above geometric relations in eq. (2.6), the following equation is obtained:

$$\frac{d}{W} = \sin\alpha\,(\cos\theta - \sin\alpha)/(\alpha + \sin\alpha\cos\alpha). \tag{2.10}$$

2.4.2.2 Liquid bridge with convex menisci

For the convex menisci, $P = \sigma/R$, which changes eq. (2.6) to:

$$(AB + CD) - (BD + AC)\cos\theta - A_{\mathrm{ACDB}}/R = 0. \tag{2.11}$$

To distinguish this case from the case of a concave columnar column, we define the angle α as the negative. Therefore, the geometric relation changes as well:

$AC = BD = W$, $AB = CD = -2\alpha R$, $R = d/\sin(-\alpha)$,

$$A_{\mathrm{ACDB}} = 2Wd - R^2(2\alpha - \sin 2\alpha), \tag{2.12}$$

Substituting all the above geometric relations in eq. (2.11), the following quadratic equation is obtained:

$$\frac{d}{W} = \sin\alpha\,(\cos\theta - \sin\alpha)/(\alpha + \sin\alpha\cos\alpha), \tag{2.13}$$

which is the same as eq. (2.10). Therefore, we can use the same equation to describe both cases with the angle $-180° \leq \alpha \leq 90°$.

2.4.3 Stable liquid bridges

The angle α can be plotted as a function of the dimensionless separation distance d/W, Fig. 2.19. It can be seen that for each parameter d/W one has two possible α in different regions (Region I and Region II), separated by the critical α_c. To obtain the value of α_c, d/W is taking the derivative with respect to α based on eq. (2.13) as:

$$\frac{\partial(d/W)}{\partial\alpha} = \frac{\cos\alpha(\cos\theta - 2\sin\alpha)}{\alpha + \sin\alpha\cos\alpha} - \frac{\sin\alpha(\cos\theta - \sin\alpha)(1+\cos^2\alpha - \sin^2\alpha)}{(\alpha+\sin\alpha\cos\alpha)^2}. \quad (2.14)$$

Eq. (2.14) shows that $\frac{\partial(d/W)}{\partial\alpha} = 0$ at $\alpha = -90°$ for all $\theta \in [0,90°]$, which implies that α_c is always equal to $-90°$, marked by the black dashed line in Fig. 2.19. The maximum separation distance $(d/W)_{max}$ below which the columnar liquid bridge can exist is reached at $\alpha = \alpha_c = -90°$. The critical ratio $(d/W)_{max} = 2(\cos\theta + 1)/\pi$ depends only on the contact angle.

The liquid column with $\alpha < -90°$ (Region II) is proved always unstable to wave-like perturbations[16], and therefore, is eliminated in further discussion. Only Region I where $-90° < \alpha < 90°$ will be considered in the following discussion.

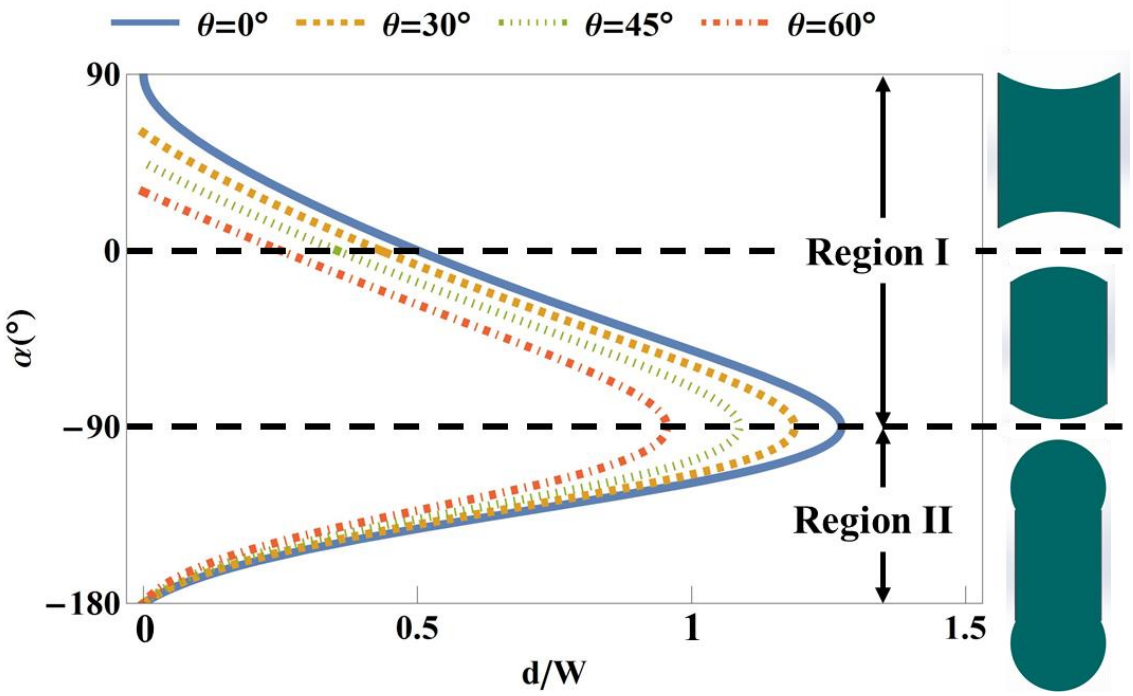

Figure 2.19. The angle α as a function of the dimensionless separation distance d/W at different contact angles θ=0°, 30°, 45°, 60°.

2.4.4 Capillary force acting on the ribbon

Considering the capillary force per unit length f (i.e., force density) caused by the liquid bridge, we can evaluate it using the free-body diagram (Fig. 2.20(A)). An imaginary cut is made along the columnar bridge, the dashed line. The obtained cross-section of this column along the rail axis is a curved rectangle: two sides of the rectangle are straight lines running parallel to the rail axis Z, the two sides that belongs to the two end menisci are curved. We remove the left side of the column and introduce an equivalent system of forces to support the remaining part of the column in equilibrium. When the column is much longer than the width of the ribbon, the contribution to the force balance of the two curved sides at the ends of this cut is negligibly small and we can neglect this contribution. Thus,

the capillary force exerted by the columnar bridge on unit length of the ribbon consists of the two components: the surface tension component and pressure component:

$$f = 2\sigma - P \cdot \overline{AB}, \tag{2.15}$$

where the first term on the right side, $2\sigma \cdot 1$, is the tension on the two surfaces along the unit length of the A and B sides of the curved rectangle; the second term is the product of the cross-sectional area $\overline{AB} \cdot 1$ and pressure $P = \mp\sigma/R$ in the liquid bridge for concave and convex columnar bridges, respectively.

Substituting into eq. (2.15) the relations $\overline{AB} = W \mp 2(R - R\cos\alpha)$, $d = \pm R\sin\alpha$, for concave and convex columnar bridges, respectively, we obtain:

$$f = 2\sigma \pm (\sigma/R)[W \mp 2(R - R\cos\alpha)] = \sigma(2\cos\alpha + \sin\alpha\,/(d/W)). \tag{2.16}$$

It is convenient to introduce a scale for the capillary force f as σ. We show the dependence of dimensionless force f/σ on the ratio d/W for different contact angles θ, Fig. 2.20(B). It shows the force f/σ decreases with the increasing separation distance d/W. After passing the zero-force distance which is marked by the solid dots on each curve, the force changes from positive attraction force to negative repulsion force.

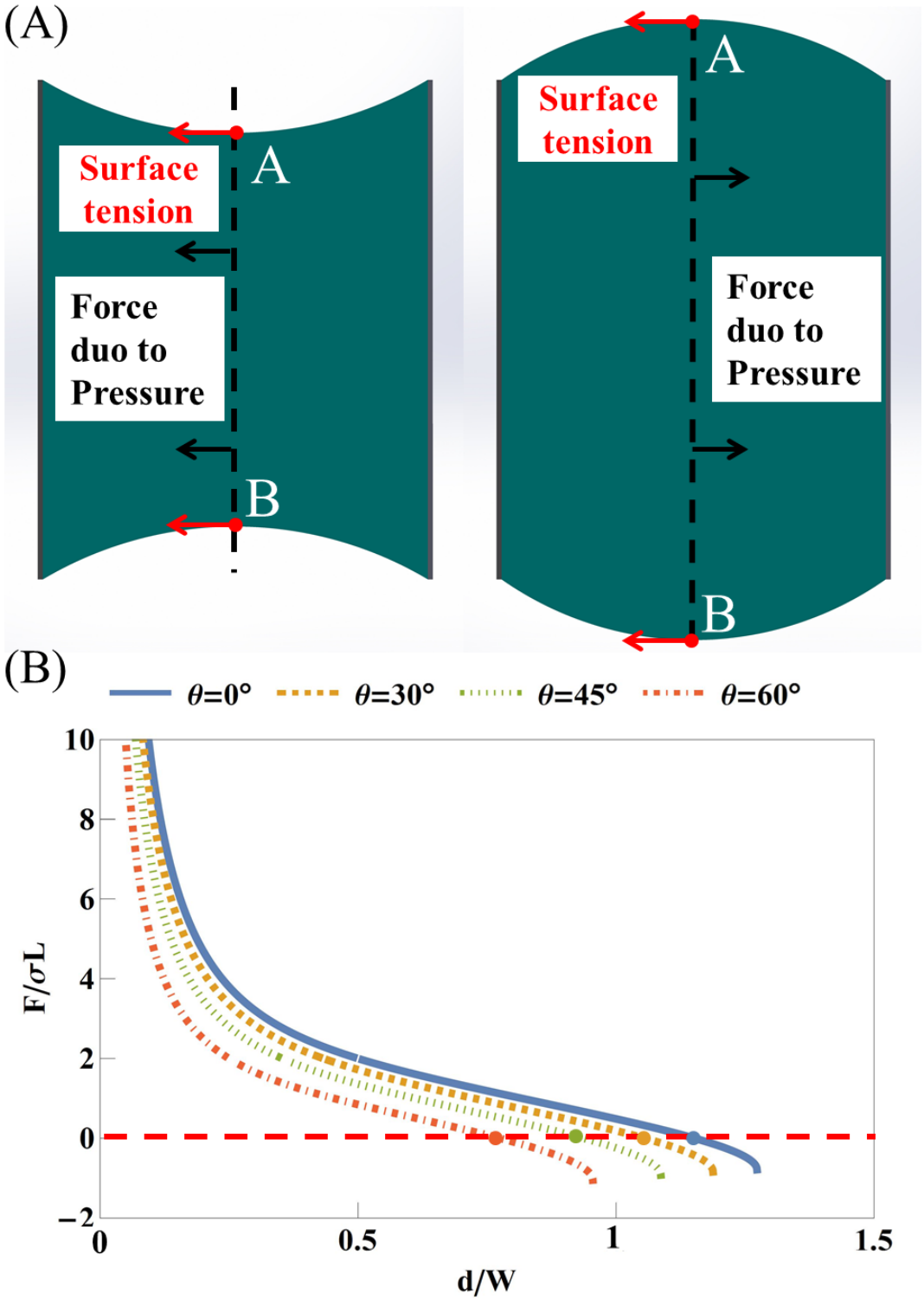

Figure 2.20. (A) Schematic illustrating the force analysis on concave and convex liquid bridges. (B) The normalized capillary force f/σ is plotted as a function of normalized separation distance d/W at different contact angles θ=0°, 30°, 45°, 60°.

2.4.5 Section conclusion

In this section, the liquid bridge trapped between the ribbon rail is studied theoretically. The morphology of the columnar bridge is calculated for different contact angles and separation distances. The maximum separation distance below which the columnar liquid bridges exist is affected only by the contact angle. The capillary force caused by the columnar liquid bridge is calculated. This study gives us a fundament to study the self-assembly of Lepidopteran proboscis in Chapter V.

2.5 References

[1] Alimov, M.M. & Kornev, K.G. 2014 Meniscus on a shaped fibre: singularities and hodograph formulation. Proceedings of The Royal Society A 470, 20140113. (doi:10.1098/rspa.2014.0113).

[2] Diah, S.Z.M., Karman, S.B. & Gebeshuber, I.C. 2014 Nanostructural colouration in malaysian plants: lessons for biomimetics and biomaterials. Journal of Nanomaterials, 1-15. (doi:10.1155/2014/878409).

[3] Hongu, T., Phillips, G.O. & Takigami, M. 2005 New Millenium Fibers. Cambridge, England, Woodhead Publishing Ltd.

[4] Brown, P. & Cox, C. 2017 Fibrous Filter Media, Woodhead Publishing.

[5] Adam, N.K. 1937 Detergent action and its relation to wetting and emulsification. Journal of the Society of Dyers and Colourists 53, 121-129. (doi:10.1111/j.1478-4408.1937.tb01955.x).

[6] Carroll, B.J. 1986 Equilibrium conformations of liquid drops on thin cylinders under forces of capillarity. A theory for the roll-up process. Langmuir 2, 248-250. (doi:10.1021/la00068a024).

[7] Brochard, F. 1986 Spreading of liquid drops on thin cylinders: The “manchon/droplet” transition. The Journal of Chemical Physics 84, 4664-4672.

[8] McHale, G. & Newton, M.I. 2002 Global geometry and the equilibrium shapes of liquid drops on fibers. Colloids and Surfaces A: Physicochemical and Engineering Aspects 206, 79-86. (doi:10.1016/s0927-7757(02)00081-x).

[9] Adamson, A.W. & Gast, A.P. 1997 Physical Chemistry of Surfaces. New York, Wiley.

[10] Langbein, D.W. 2002 Capillary Surfaces: Shape - Stability - Dynamics, in Particular Under Weightlessness. New York, Springer.

[11] Bonn, D. & Ross, D. 2001 Wetting transitions. Reports on Progress in Physics 64, 1085-1163. (doi:10.1088/0034-4885/64/9/202).

[12] Princen, H.M. 1970 Capillary phenomena in assemblies of parallel cylinders: III. Liquid Columns between Horizontal Parallel Cylinders. Journal of Colloid and Interface Science 34, 171-184. (doi:10.1016/0021-9797(70)90167-0).

[13] Oprea, J. 2007 Differential Geometry and its Applications. 2nd ed. Washington DC, The Mathematical Association of America.
[14] Keller, J.B. 1998 Surface tension force on a partly submerged body. Physics of Fluids 10, 3009-3010. (doi:10.1063/1.869820)
[15] Brinkmann, M. & Lipowsky, R. 2002 Wetting morphologies on substrates with striped surface domains. Journal of Applied Physics 92, 4296-4306. (doi:10.1063/1.1506003).
[16] Roy, R.V. & Schwartz, L.W. 1999 On the stability of liquid ridges. Journal of Fluid Mechanics 391, 293-318. (doi:10.1017/s0022112099005352).
[17] Alimov, M.M. & Kornev, K.G. 2014 Singularities of meniscus at the V-shaped edge. Mechanics Research Communications 62, 162-167. (doi:10.1016/j.mechrescom.2014.10.003).
[18] Alimov, M.M. & Kornev, K.G. 2016 Piercing the water surface with a blade: Singularities of the contact line. Physics of Fluids 28, 012102. (doi:10.1063/1.4938171).
[19] Laplace, P.S. 1805 Mechanique Celeste. Paris Encyclopaedia Britannica.
[20] White, D.A. & Tallmadge, J.A. 1965 Static menisci on the outside of cylinders. Journal of Fluid Mechanics 23, 325. (doi:10.1017/s0022112065001398).

CHAPTER III

WETTING OF ELLIPTICAL FIBERS

3.1 Introduction

Elliptical fiber is a more general complexly- shaped fiber which cross-section includes the ribbon and a circular fiber as the two limiting cases of the cross-sectional ellipse. The ellipticity of its cross-sectional ellipse is defined as $e = b/a$, where a and b are the ellipse semi-axes. It is expected to play an important role in the wetting phenomena because its inherent relation to the surface curvature. Indeed, as the two semi-axes become the same, $e = 1$, the fiber turns into a circular cylinder with all associated wetting features; as one of the ellipse axis increases, so that the fiber ellipticity goes either to infinity or zero, the fiber turns into a ribbon with all associated wetting features. Therefore, understanding of the wetting features of elliptical fiber is critical to reveal the effect of curvature on the stability of coating films, droplet formation and plethora of morphological transitions in liquid bodies adhered to the surface of these fibers.

In this chapter, we will first introduce a general mathematical description of an elliptical fiber looped in a circular ring as a basic element of a textile construct. This mathematical setup will be used to analyze different wetting phenomena. We will start by studying the wetting features of a straight elliptical fiber, for the sake of generality

including a hollow fiber. The stability of a coating film on internal and external walls of this fiber, the mechanisms of drop formation from the coating films, and the droplet morphology will be discussed. Then we will expand our study to the ring made of a curved elliptical tube, analyze the wetting of both internal and external walls of the tube, and discuss the effect of cross-sectional ellipticity and ring radius of curvature. This study will cover a broad range of wetting phenomena associated with such complexly-shaped fibers. It will set a groundwork for further discussion of the wetting phenomena associated with Lepidopteran proboscis in Chapter V.

3.2 Mathematical description of a thin film on an elliptical hollow fiber coiled in a circular ring

3.2.1 Model construction

Fig. 3.1(A) introduces the main geometrical parameters of a ring with radius r made of an elliptical hollow fiber. Hereafter, the left cross-section (Figs. 3.1(B), (C)) is used as the reference; hence, all angles and positions will be evaluated according to the left cross-section. When $r \to +\infty$, the model describes a straight fiber.

The position of any point M sitting on the ring surface is conveniently specified by a Cartesian system of coordinates (X, Y, Z), with the Z-axis taken perpendicular to the ring plane (X, Y). The center of this (X, Y, Z) coordinate system is placed in the ring center O. The ring surface is created by rotating an ellipse with semi-axes a and b around the Z-axis. It is convenient to introduce a local system of coordinates (x, Z) (Fig. 3.1(B)), with its center placed at the center of the ellipse O_1. Thus, the profile of this ellipse is defined by the following formula:

$$\frac{x^2}{a^2} + \frac{Z^2}{b^2} = 1. \tag{3.1}$$

One can introduce an alternative system of coordinates specifying the position of point M on the ring surface by latitude ϕ and longitude λ. The latitude ϕ is measured by the angle formed by the outward normal vector $\boldsymbol{n}$ at point M and the ring plane $Z = 0$. We introduce the plane Ω containing the vector $\boldsymbol{n}$ at point M and axis OZ. The longitude λ is defined as the angle formed by the plane Ω and reference plane, X=0.

All points on the ring surface with the same latitude ϕ form a closed curve called the parallel. All points on the ring surface with the same longitude λ form a closed curve called the meridian. Meridians and parallels constitute a parametric grid on the ring surface, with the ellipses as meridians and the circles as parallels. Point M, for example, belongs to the meridian formed by cutting the ring by the plane Ω (Figs. 3.1(A), (B)). Using the latitude and longitude, we can make an alternative parameterization specifying the position of point M as (ϕ, λ).

There is another convenient parameterization with an auxiliary angle $0 < \varphi < 2\pi$ such that $x = a\cos\varphi$, $Z = b\sin\varphi$. With this parametrization, the local coordinates of point M (x, Z) on this ellipse are expressed as M$(a\cos\varphi, b\sin\varphi)$. Alternatively, this point can be specified in the local polar system of coordinates M$(\rho(\theta), \theta)$, with angle θ formed by the line MO_1 with the ring plane Z=0; the radius $\rho(\theta)$ is defined from equation $\rho(\theta) = ab((bcos\theta)^2 + (asin\theta)^2)^{-1/2}$. In the polar system of coordinates, the vertexes of the ellipse are identified by angle θ: at point A, $\theta = -\frac{\pi}{2}$; at point B, $\theta = 0$; at point C, $\theta = \frac{\pi}{2}$; and at point D, $\theta = \pi$ (Fig. 3.1(B)).

The tangent plane at point M is associated with the normal vector $\boldsymbol{n}$ at point M (Figs. 3.1(B), (C)). The tangent plane is perpendicular to the line O_2O_3 and makes angle α with the ring plane $Z = 0$, Fig. 3.1(B). Thus, the angle α defining the slope of the ellipse at point M, $\tan\alpha$, can be found through derivative $\tan\alpha = \frac{dZ}{dx}$, and can be further expressed through angle φ by applying the chain rule of differentiation with $x = a\cos\varphi$, $Z = b\sin\varphi$ as

$$\tan\alpha = \frac{dZ}{dx} = \frac{dZ}{d\varphi}\cdot\frac{d\varphi}{dx} = -\frac{b}{a}\cot\varphi = -e\cot\varphi. \tag{3.2}$$

The angle θ of the polar system of coordinates and the auxiliary angle φ are connected through the following relationship:

$$\tan\theta = \frac{Z}{x} = \frac{b\sin\varphi}{a\cos\varphi} = e\tan\varphi, \tag{3.3}$$

In eqs. (3.2) - (3.3), the cross-sectional ellipticity e is introduced as $e = b/a$. The rings elongated along the Z-axis have ellipticity greater than 1, $e > 1$, and the rings elongated in the ring plane $Z = 0$ have $e < 1$.

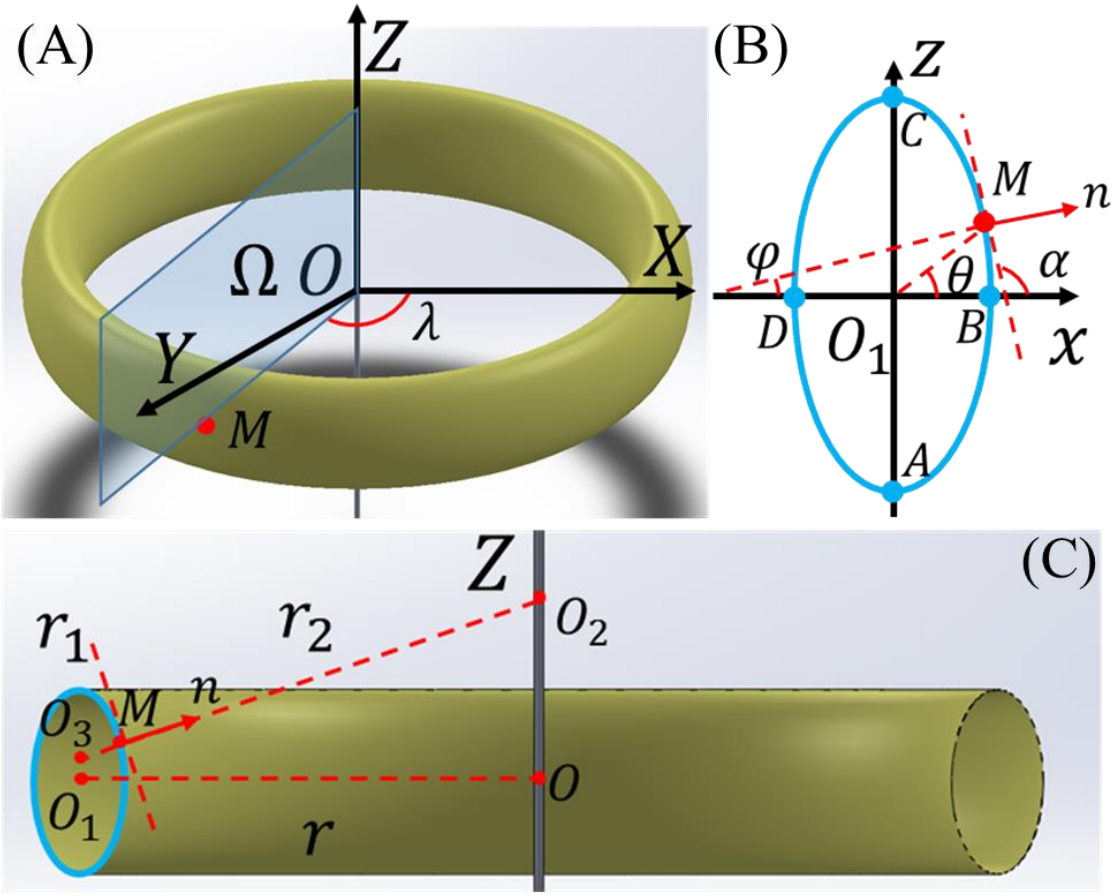

Figure 3.1. (A) The model of a ring of radius r with an elliptical cross-section. Longitude λ is defined as the angle formed by the plane Ω and the plane X=0. (B) Cross-section of the ring formed by cutting it with plane Ω. (C) Definitions of principal radii of curvature $r_1 = O_3M$ and $r_2 = MO_2$ of the ring surface at point M. The distance OO_1 is equal to the ring radius $OO_1 = r$. The fiber cross-section is assumed to be elliptical with semi-axes $O_1A = O_1C = b$ and $O_1B = O_1D = a$, where $O_1C \perp O_1O$ and $O_1D \parallel O_1O$.

3.2.2 Laplace law of capillarity applied to thin coating films

The thin film deposited on the internal and external walls is subject to the action of surface tension σ. The thickness of the liquid film h is small, $h << a, h << b, h << r$, so that it is safe to assume that gravity plays an insignificant role and only capillary force is important [1, 2]. The film non-uniformity can be also neglected, assuming that the air-liquid interface h (X, Y, Z) is positioned equidistant to the ring surface; in other words, at

any longitude λ, the film profile is specified by equation $\frac{x^2}{(a+h)^2}+\frac{Z^2}{(b+h)^2}=1$. Because the film is thin, $h << a, h << b$, one can estimate the pressure distribution over the air-liquid interface by applying the Laplace law of capillarity directly to the fiber surface, $\frac{x^2}{(a+h)^2}+\frac{Z^2}{(b+h)^2}\approx\frac{x^2}{a^2}+\frac{Z^2}{b^2}\approx 1$. The Laplace law of capillarity states that the pressure under the film surface P_l differs from atmospheric pressure P_a, and the pressure differential is determined by the surface tension σ and the mean curvature of the surface as

$$P_l - P_a = \sigma\left(1/r_1 + 1/r_2\right), \tag{3.4}$$

where r_1 and r_2 are the principal radii of curvature of the liquid-air interface, which, in a first approximation, coincides with the ring surface.

We distinguish the behavior of *internal films* coating which is deposited on the internal surface of the ring from that of *external films* coating which is deposited on the external surface. To understand the differences in pressure distributions for external and internal films, one has to bear in mind that the sign of curvature in the Laplace law is associated with the outward normal vector to the given point at the surface [3]. Because the directions of outward normal vectors for the internal and external films are different, the capillary pressures also differ.

According to differential geometry [3], the circle centers O_2 and O_3, defining the principal radii of curvature, are sitting on the line obtained by continuation of the outward normal vector $\boldsymbol{n}$ to the surface at point M. For any axisymmetric surface, one center of these circles must be sitting on the Z-axis. In Fig. 3.1(C), this center of curvature is O_2 . Another center can be located anywhere along the line MO_2. The two principal radii of

curvature for the ring surface are denoted as $MO_3 = r_1$ and $MO_2 = r_2$, respectively. We define the radii of curvature r_1 and r_2 as positive when the vectors $\overrightarrow{MO_2}$, $\overrightarrow{MO_3}$ are pointing toward the Z-axis.

For convenience of calculation and analysis, we normalize all geometric parameters by the distance a. Therefore, the dimensionless radius of the ring is

$$R = \frac{r}{a}, \tag{3.5}$$

and the principal radius of curvature of the meridians is $R_1 = MO_3/a = r_1/a$. The radius R_1 is calculated by using the definition of curvature of a plane curve from differential geometry [3]: $R_1 = r_1 / a = a^{-1}\left(1+\left(\frac{dZ}{dx}\right)^2\right)^{\frac{3}{2}} / \left|\frac{d^2Z}{dx^2}\right| = (a^4 - a^2x^2 + b^2x^2)^{3/2} / (a^5 b)$. Inputting $x = a\cos\varphi$, $Z = b\sin\varphi$, $e = b/a$, we finally obtain:

$$R_1 = \frac{r_1}{a} = \frac{\left(\sin^2\varphi + e^2\cos^2\varphi\right)^{\frac{3}{2}}}{e}. \tag{3.6}$$

When an observer moves along the meridian, the radius of curvature changes from one position to the other.

The second principal radius of curvature $r_2 = MO_2$ is calculated using the geometrical construction in Fig. 3.1(C). For the two intervals $\theta \in [-\frac{\pi}{2}, \frac{\pi}{2}]$ and $\theta \in [\frac{\pi}{2}, \frac{3\pi}{2}]$, the expressions of r_2 are different:

$$R_2 = \frac{r_2}{a} = \frac{\left(r - \left|a\cos\varphi\right|\right)}{a\sin\alpha} = \frac{\left(R - \left|\cos\varphi\right|\right)}{\sin\alpha}, \ \theta \in [-\tfrac{\pi}{2}, \tfrac{\pi}{2}], \tag{3.7}$$

$$R_2 = \frac{r_2}{a} = \frac{\left(r + |a\cos\varphi|\right)}{a\sin\left(\alpha - \pi\right)} = -\frac{\left(R + |\cos\varphi|\right)}{\sin\alpha},\ \theta \in [\tfrac{\pi}{2}, \tfrac{3\pi}{2}]. \tag{3.8}$$

Substituting these equations into the Laplace law of capillarity, eq. (3.4), we obtain two different representations of the dimensionless pressure difference, $P = a(P_l - P_a)/\sigma$, for a film coating the external and internal wall of the ring:

Film coating the external wall:

$$P = \frac{\left(P_l - P_a\right)a}{\sigma} = \frac{e}{\left(\sin^2\varphi + e^2\cos^2\varphi\right)^{\frac{3}{2}}} - \frac{\sin\alpha}{\left(R - \cos\varphi\right)}, \tag{3.9}$$

Film coating the internal wall:

$$P = \frac{\left(P_l - P_a\right)a}{\sigma} = -\left(\frac{e}{\left(\sin^2\varphi + e^2\cos^2\varphi\right)^{\frac{3}{2}}} - \frac{\sin\alpha}{\left(R - \cos\varphi\right)}\right). \tag{3.10}$$

These two formulas together with eqs. (3.2) and (3.3) describe the pressure distribution over the liquid-air interface of a film covering either the external and internal wall of the ring.

3.3 Behavior of liquid films on straight elliptical hollow fiber

3.3.1 Instability of coating thin film on straight elliptical hollow fiber

As the ring radius goes to infinity, $R \to +\infty$, eqs. (3.9) and (3.10) are simplified to

$$P = \frac{a\left(P_l - P_a\right)}{\sigma} = \frac{e}{\left(\sin^2\varphi + e^2\cos^2\varphi\right)^{\frac{3}{2}}}, \tag{3.11}$$

$$P = \frac{a\left(P_l - P_a\right)}{\sigma} = -\frac{e}{\left(\sin^2\varphi + e^2\cos^2\varphi\right)^{\frac{3}{2}}}\ , \tag{3.12}$$

respectively. These pressure distributions are plotted in Figs. 3.2 (A) and 3.2(B) for external and internal films, respectively. Figs. 3.2(E) and 3.2(F) are the schematics showing where the liquid should be collected based on the pressure distribution predictions in Figs. 3.2(C) and 3.2(D), respectively.

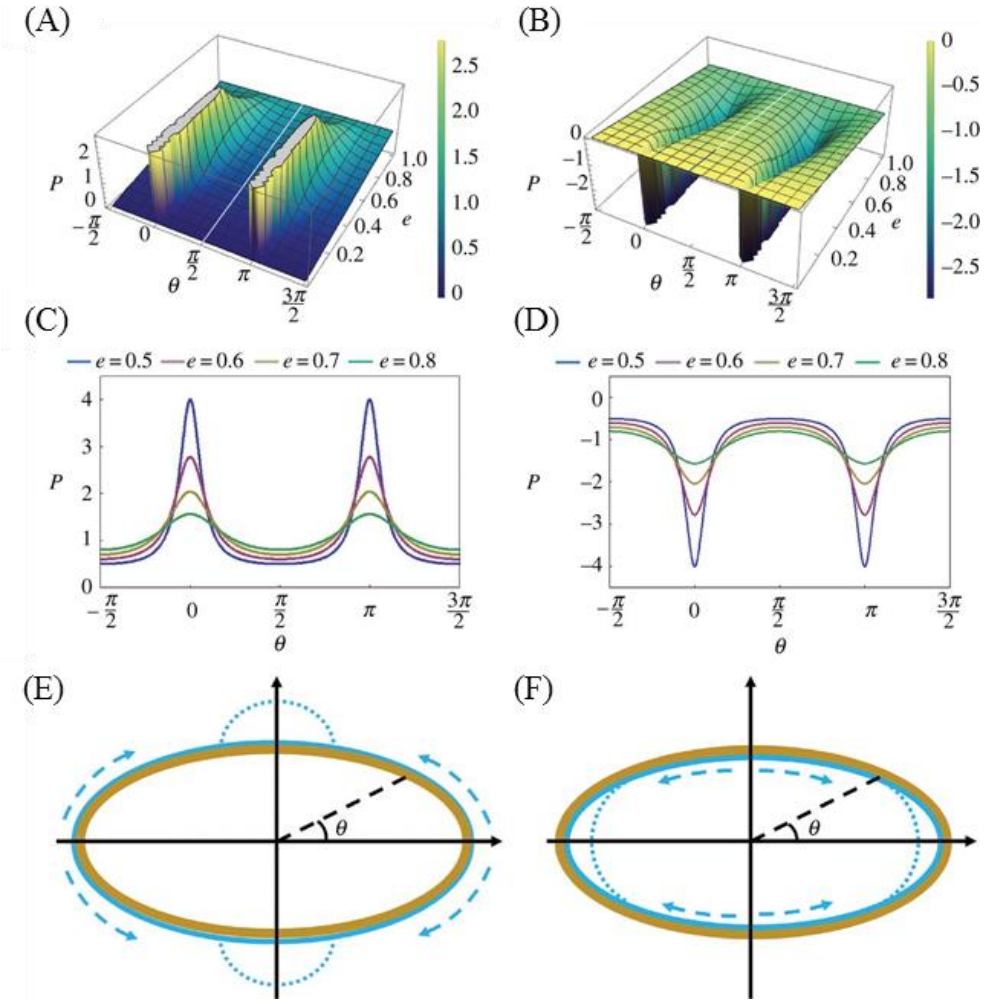

Figure 3.2. (A) Pressure distribution in the external film on an elliptical fiber. (B) Pressure distribution in the internal film on a straight elliptical tube. (C), (D) Pressure distribution showing positions where liquid is expected to flow and collect. (C) The external film is expected to collapse into two semi-cylindrical columns at the flattened sides ($\theta = -\pi/2$ and $\theta = \pi/2$). (D) The internal film is expected to flow toward the most curved sides ($\theta = 0$ and $\theta = \pi$) where it will form two liquid menisci. (E), (F) Schematics of surface activity, showing fluid flow and collection (E) externally at flatter regions, and (F) internally at more curved regions.

This model of films suggests that as soon as a liquid film is deposited on the external and internal walls of the elliptical hollow fiber and remain liquid state, it will lose its stability and the liquid in the film is prone to follow and collect at the low-pressure regions. To examine our hypothesis that liquid can be passively collected at the low-pressure regions, we coat a straight elliptical wire (SUS-304 stainless steel wire of elliptical cross-section (a =300 μm, b=200 μm)) with the setup shown in Fig. 3.3 and record the behavior of the coating film. The presence of the film and its thickness were evaluated using a dry elliptical wire (Fig. 3.4(A)) as a reference.

The elliptical wire is place with the more curved side facing the camera and then inserted into a capillary tube (inner diameter of 1.6 mm), filled with glycerin. It was then exposed by moving the tube at 1 mm/sec with linear positioning stages (VT-21, Micos) to the left while filming from the top using a high-speed camera (POINTGREY® FL3-U3-13S2C-CS) and microscopic lens (Meiji Techno® Short UNIMAC MacroZoom Lense MS-40); thus, we were able to magnify the wire and distinguish the flow features (Fig. 3.4(B) – (F)). Once the wire leaves the tube, its surface is covered with a film of glycerin. The film quickly loses its stability and breaks at the narrow side within 0.1 sec. The liquid at the narrow side flows to the wide sides of the wire, as shown by the observed contact line (white arrow in Fig. 3.4 (C) – (E)). The film finally broke into two parts sitting on each of the wide sides, forming clam-shell droplets (Fig. 3.4(F)).

This experiment partially proves our theoretical analysis in Fig. 3.2. The liquid thin film deposited on the straight elliptical fiber loses its stability and contracts into droplets at the flatter regions. However, the predicted liquid columns do not form, instead, we observe

the clam-shell droplets forming at the flatter regions. The film cannot move along meridians over the entire length of the wire at the same time. Instead, some liquid bands sitting at the most curved parts flowed faster. In Fig. 3.4, these bands are located at the right ends of the viewing regions. Once some islands on the wire surface were dewetted, a meniscus formed, which moved to the left, uncovering the rest of the surface.

This analysis leads to a question whether the columns shown in Figs. 3.2(E) and (F) could be realized.

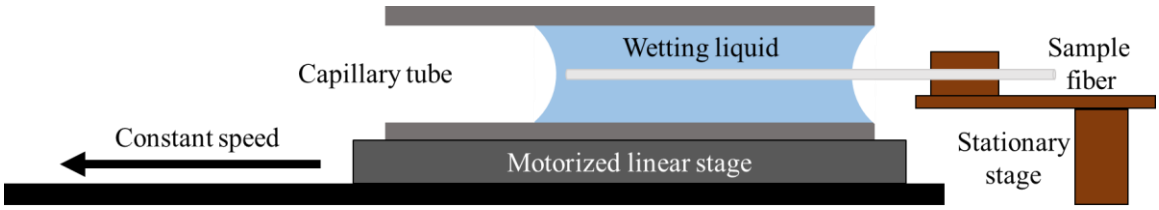

Figure 3.3. Experimental setup used in the wire-coating experiments. The tube with the wetting liquid is moved at a constant speed, 1 mm/s, and the meniscus leaves behind a film coating the fiber surface.

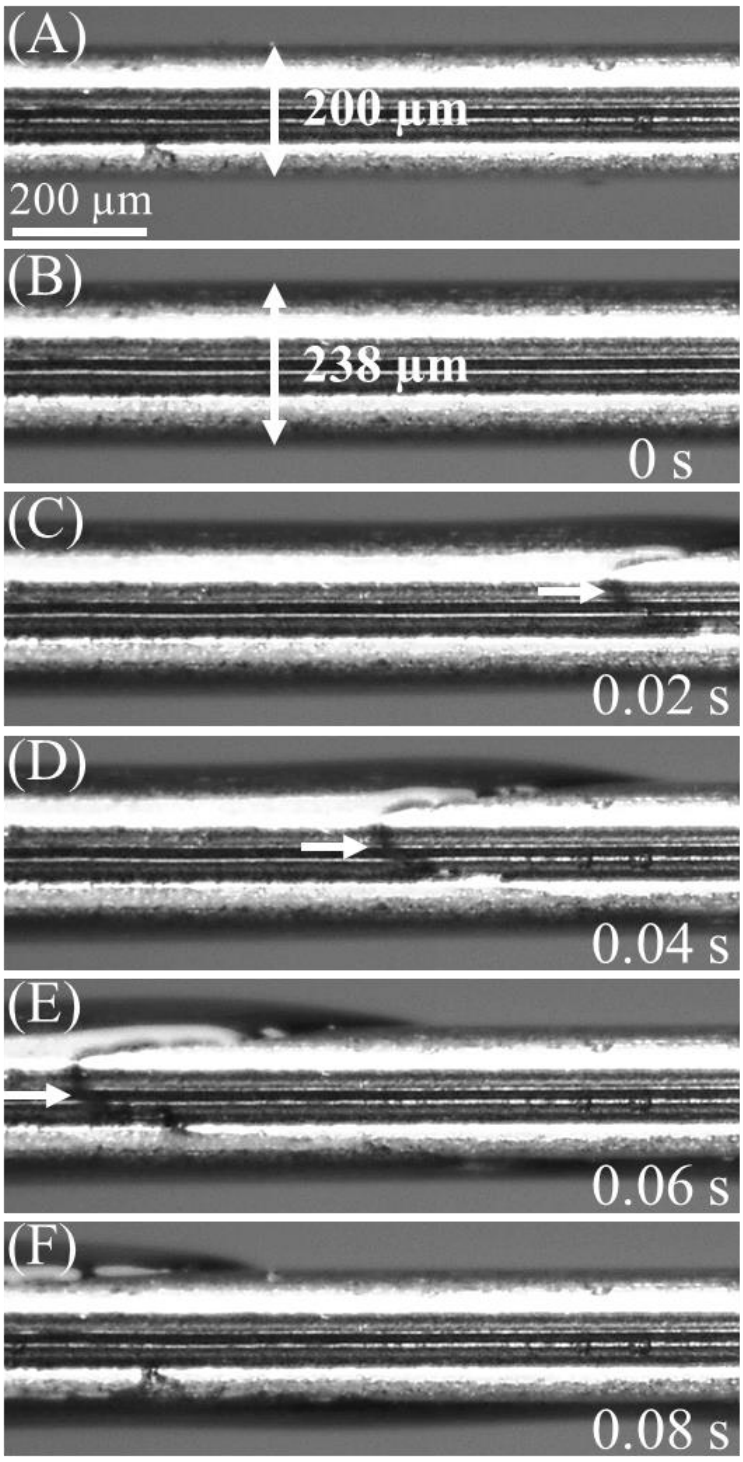

Figure 3.4. Instability of a glycerin film deposited on an elliptical wire. The narrow side is facing the camera. (A) Dry wire before film deposition. (B) Wire with a film after its deposition. (C) Formation of a contact line (shown by arrow). (D)-(F) The main features of the process of film breakup and separation into two clam-shell droplets sitting on the wider parts of the wire.

3.3.2 Stability analysis of liquid columns

3.3.2.1 Liquid column on the flatter region of the straight elliptical wire

A model of a liquid column formed on the flatter region of the straight elliptical wire is developed following the modified Princen method discussed in Section 2.2.2 for the ribbons, Fig. 3.5(A). Similarly, the force balance in the direction parallel to the fiber axis can be obtained as follow:

$$F_{AL} + F_{SL} - F_{SA} - F_P = 0 \tag{3.13}$$

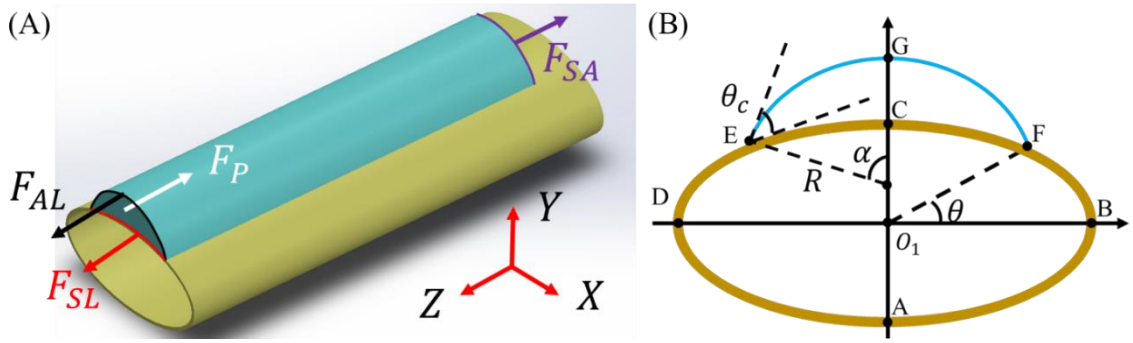

Figure 3.5. (A) Schematic showing the free body diagram of a liquid column on the flatter region of the straight elliptical wire. (B) Schematic showing the cross-section of the liquid column.

Fig. 3.5(B) shows the cross-section: the liquid column with the contact lines pinned at the fiber surface at points E($\cos(\pi - \varphi)$, $\sin\varphi$) and F($\cos\varphi$, $\sin\varphi$) where meniscus forms contact angle θ_c. As discussed before, φ is related with the polar angle θ through eq. (3.3). R is the radius of curvature of the liquid/air interface $\widehat{EGF}$ and α is the half of its subtending angle. Therefore, the forces in eq. (3.13) can be calculated as: $F_{AL} = \sigma \cdot \widehat{EGF}$ is the force due to surface tension at the air/liquid interface; $F_{SL} = \sigma_{SL} \cdot \widehat{ECF}$ is the force due to surface tension σ_{SL} at the solid/liquid interface; $F_{SA} = \sigma_{SA} \cdot \widehat{ECF}$ is the force due to surface tension σ_{SA} of the solid/air interface; $F_P = P \cdot A_{ECFGE}$ is the pressure resultant

acting perpendicularly to the cross-section of area A_{ECFGE}. The following geometric relations are used to calculate the component forces:

$$\widehat{EGF} = 2\alpha R$$

$$\frac{R}{a} = \frac{\cos(\theta_c - \alpha)}{\sin\alpha}\sqrt{\cos^2\varphi + \frac{e^2\cos^2\varphi}{\sin^2\varphi}}$$

$$\frac{\widehat{ECF}}{a} = \int_{\varphi}^{\pi-\varphi}\sqrt{\sin^2\varphi + e^2\cos^2\varphi}\,d\varphi$$

$$A_{ECFGE} = R^2(\alpha - \sin\alpha\cos\alpha) - \frac{ab}{2}(\pi - 2\varphi - \sin 2\varphi) \tag{3.14}$$

Employing the Laplace law of capillarity $P = \sigma/R$ and Young-Laplace equation, $\sigma_{SA} - \sigma_{SL} = \sigma\cos\theta_c$, and substituting eq. (3.14) into (3.13), the following equation is obtained.

$$(\alpha + \sin\alpha\cos\alpha)\left(\frac{\cos(\theta_c - \alpha)}{\sin\alpha}\sqrt{\cos^2\varphi + \frac{e^2\cos^2\varphi}{\sin^2\varphi}}\right)^2 -$$

$$\frac{\cos\theta_c\cos(\theta_c - \alpha)}{\sin\alpha}\sqrt{\cos^2\varphi + \frac{e^2\cos^2\varphi}{\sin^2\varphi}}\int_{\varphi}^{\pi-\varphi}\sqrt{\sin^2\varphi + e^2\cos^2\varphi}\,d\varphi + \frac{e}{2}(\pi - 2\varphi -$$

$$\sin 2\varphi) = 0. \tag{3.15}$$

Therefore, eq. (3.15) must be satisfied to have the equilibrium liquid column. If looking at the left part of eq. (3.15), it is a function of the contact angle θ_c, half of the center angle of the liquid/air interface α, the cross-section ellipticity e, and the polar angle θ since φ can be replaced with θ through eq. (3.3), which can be represented as $f(\theta_c, e, \alpha, \theta)$.

To determine the conditions of forming the equilibrium liquid column, we need to find when the function $f(\theta_c, e, \alpha, \theta)$ equals zero. For a specific liquid – fiber pair, the contact angle θ_c and the cross-section ellipticity e are constants. Therefore, we choose an

example with $\theta_c = \pi/6$ and $e = 1/2$ to illustrate typical results of numeric analysis of this problem. In Fig. 3.6, function $f\left(\frac{\pi}{6}, \frac{1}{2}, \alpha, \theta\right)$ is plotted as a function of α and θ.

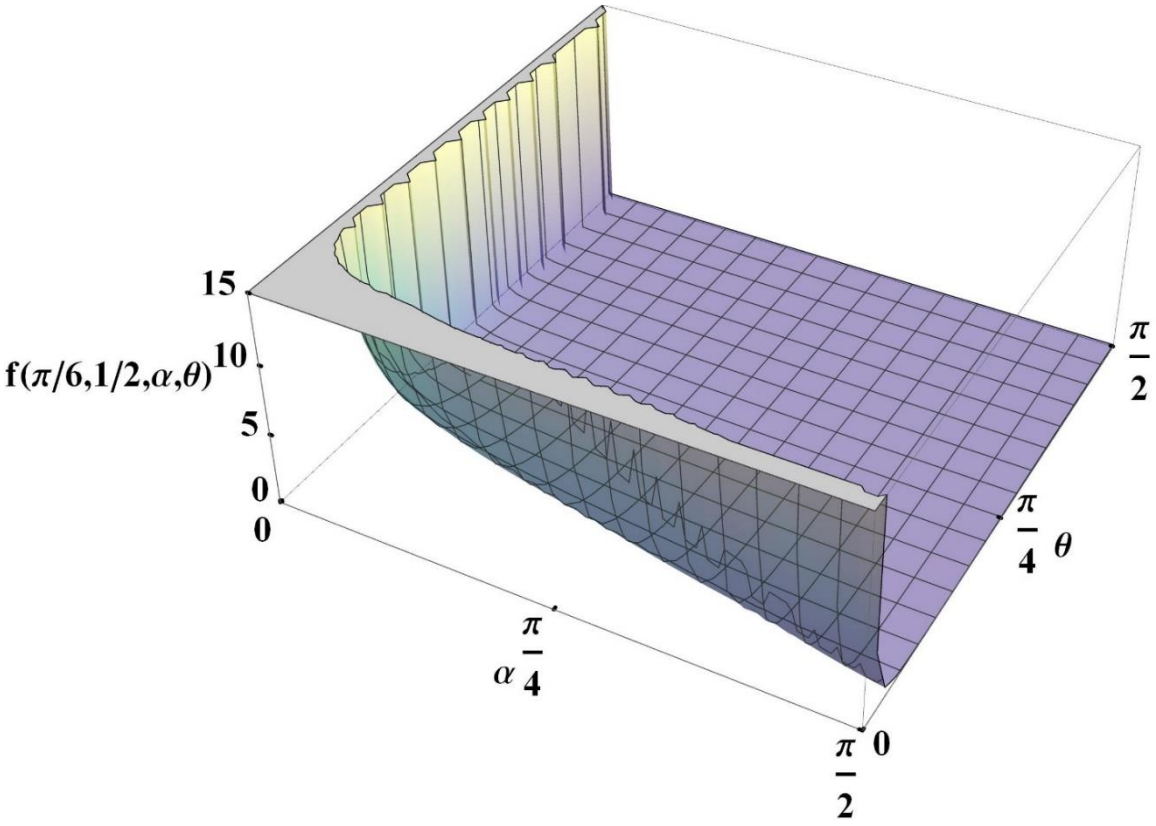

Figure 3.6. $f\left(\frac{\pi}{6}, \frac{1}{2}, \alpha, \theta\right)$ as a function of α and θ.

Fig. 3.6 shows that function $f\left(\frac{\pi}{6}, \frac{1}{2}, \alpha, \theta\right)$ is always greater than zero within the defined domain $\alpha \in [0, \frac{\pi}{2}]$, $\theta \in [0, \frac{\pi}{2}]$, suggesting no equilibrium liquid column sketched in Fig. 3.5 can be formed. The possible liquid droplet morphology which can be formed on straight elliptical fiber will be discussed in the following section.

3.3.2.2 Liquid column in the curved region of the straight elliptical tube

Following the same method, the force balance equation in this case is calculated as:

$$(\alpha + \sin\alpha\cos\alpha)\left(\frac{\cos(\theta_c+\alpha)}{\sin\alpha}\sqrt{e^2\sin^2\varphi+\frac{\sin^2\varphi}{\cos^2\varphi}}\right)^2 -$$

$$\frac{\cos\theta_c\cos(\theta_c+\alpha)}{\sin\alpha}\sqrt{e^2\sin^2\varphi+\frac{\sin^2\varphi}{\cos^2\varphi}}\int_{-\varphi}^{\varphi}\sqrt{\sin^2\varphi+e^2\cos^2\varphi}\,d\varphi+\frac{e}{2}(2\varphi-\sin 2\varphi)=0 \quad .$$

(3.16)

Eq. (3.16) must be satisfied to have the equilibrium liquid column in the elliptical tube. Similarly, the left part of eq. (3.16) is represented as $g(\theta_c, e, \alpha, \theta)$. And we choose an example with $\theta_c = \pi/6$ and $e = 1/2$ to represent the general case for this problem. In Fig. 3.7, $g\left(\frac{\pi}{6}, \frac{1}{2}, \alpha, \theta\right)$ is plotted as a function of α and θ.

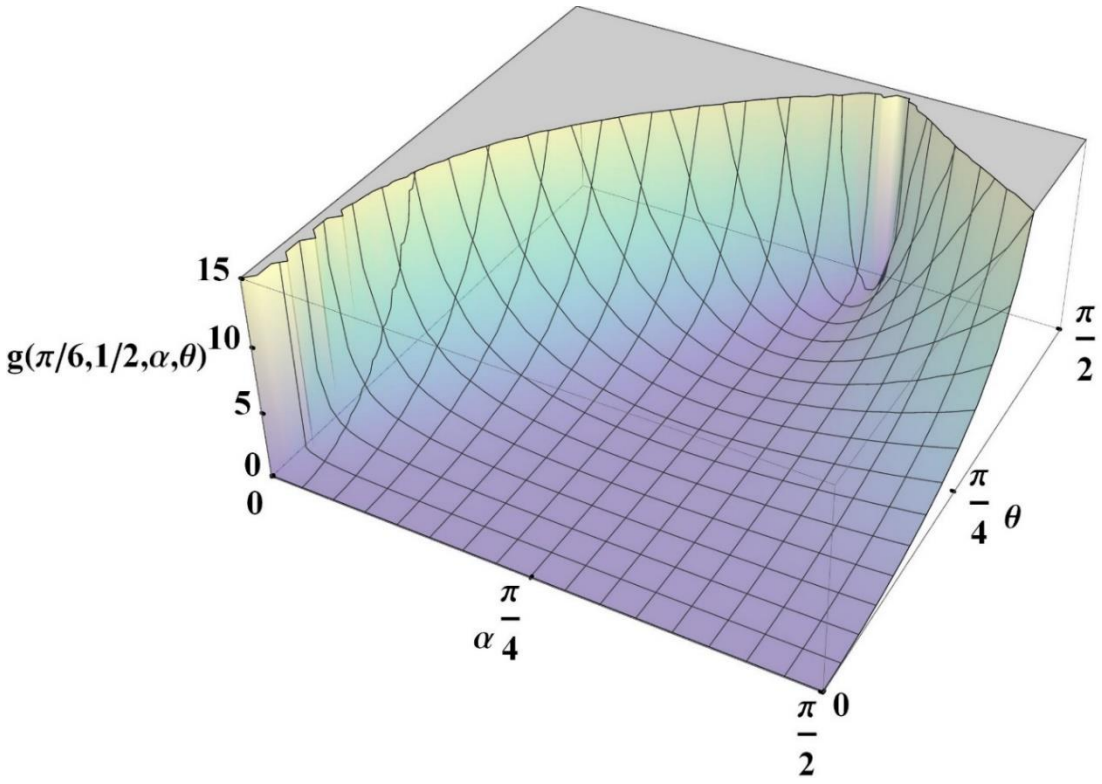

Figure 3.7. $g\left(\frac{\pi}{6}, \frac{1}{2}, \alpha, \theta\right)$ as a function of α and θ.

Figure 3.7 shows $g\left(\frac{\pi}{6},\frac{1}{2},\alpha,\theta\right)$ is always greater than zero, suggesting no equilibrium liquid column modeled in Fig. 3.5 can be formed.

The liquid columns formed in both scenarios are not stable, which means they should take on some other shapes. The liquid column in elliptical tube could form a system of liquid bridges. A possible liquid droplet morphology which can be formed on straight elliptical fiber will be discussed in the following section.

3.3.3 Droplet morphology on the straight elliptical fiber

To fully understand the behavior of the coating film on the straight elliptical fiber, the experiment in Fig. 3.4 is repeated at a withdrawal velocity 5 mm/s and imaged at lower magnification, Fig. 3.8. Within 0.1 second, the deposited film breaks into series of droplets with different shapes. Since the contact angle is the same, the difference in the final morphology of droplets should result from the difference in volume: the droplet with larger volume forms barrels (the dashed black box) and the droplets with smaller volume form clam-shells (the dashed red box). However, the difference in droplet volume is determined during the film breaking process, which cannot be simply controlled.

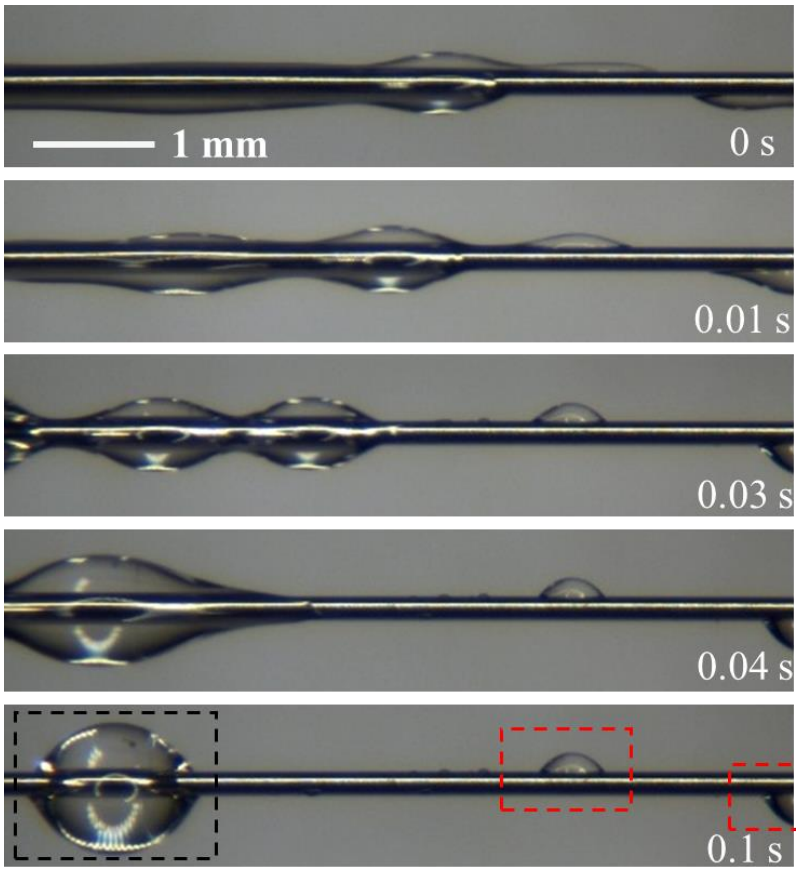

Figure 3.8. Evolution of the liquid film deposited on elliptical fiber. The film breaks within 0.1 s and forms the barrel droplets (the dashed black box) and a clam-shell droplet (the dashed red box).

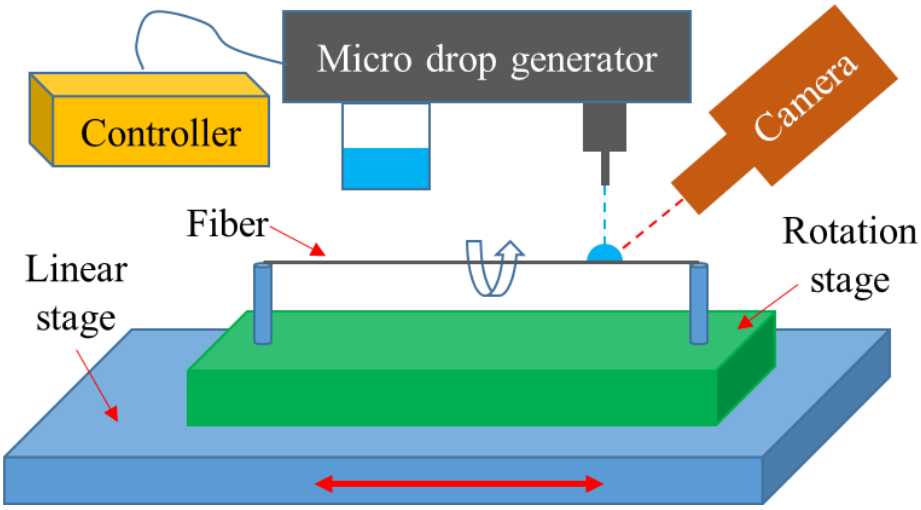

Figure 3.9. Schematic showing the experimental setup for drop generation and visualization of drop shape on elliptical fibers.

To systematically study the effect of droplet volume as well as the contact angle on the final droplet shape, another experimental setup was developed, Fig. 3.9. The micro drop generator (Microdrop Technologies®, MD-E-201H) was used to directly deposit a series of micro droplets of hexadecane on the fiber, one droplet at each 6000 μs. The volume of each micro drop was measured to be 4600 μm^3. The micro droplets were deposited on the fiber to the same location and formed one big droplet. The volume of this big droplet can be calculated knowing the volume of a single drop, 4600 μm^3, and the total time of deposition. Location of the deposition spot on the fiber and orientation of the fiber were both controlled by attaching a rotation stage to a linear positioning stage (VT-21, Micos). A high-speed camera (POINTGREY® FL3-U3-13S2C-CS) and microscopic lens (Meiji Techno® Short UNIMAC MacroZoom Lense MS-40) were used to image the droplet shape during the entire deposition process. To obtain different contact angles, the method of silanization described in Section 2.3.1.2 was used. The fibers were treated with the following silanes (3-Glycidyloxproply) thimethoxysilane, Trimethylethoxysilane, methacryloxypropyltrimethoxysilane, n-octyldimethylchlorosilane, 2-[Methoxy(polyethyleneoxy)6-9propyl]trimethoxysilane. The advancing and receding contact angles were measured with the force tensiometer (Kruss® K100), and the results are shown in Table 3.1. Each result is averaged by five measurements and the error bar represents the standard deviation of these measurements.

Table 3.1. The advancing and receding contact angles between hexadecane and the elliptical fibers modified through silanization.

	Advancing contact angle	Receding contact angle
(3-glycidyloxypropyl) trimethoxysilane	25.7±1.1°	24.6±1.2°
2-[Methoxy(polyethyleneoxy)6-9propyl]trimethoxysilane	27.4±0.7°	24.5±0.5°
Trimethylethoxysilane	26.2±0.3°	23.7±0.8°
n-octyldmethylchlorosilane	26.8±2°	24.7±3.2°
Methacryloxypropyltrimethoxy silane	22.8±1.6°	20.5±1.7°

Figs. 3.10(A), (B) show two sets of experiments with advancing/receding contact angle of 22.8°/20.5° and 27.4°/24.5°, respectively. The droplets spread over the fiber surface, therefore, the advancing contact angle will be used in the following discussion. The transition from clam-shell droplet to column droplet was observed by increasing the volume of the droplet. The critical volume for this transition is found to be influenced by the contact angle: with a contact angle of 22.8° (Fig. 3.10(A)), the critical volume is observed within 0.009 ~ 0.0098 μL; with a contact angle of 27.4° (Fig. 3.10(B)), the critical volume is observed within 0.017 ~ 0.024 μL. Further experimental and theoretical study is required to investigate the effect of the cross-section ellipticity and finalize the phase diagram of the clam-shell – barrel transition on elliptical fiber.

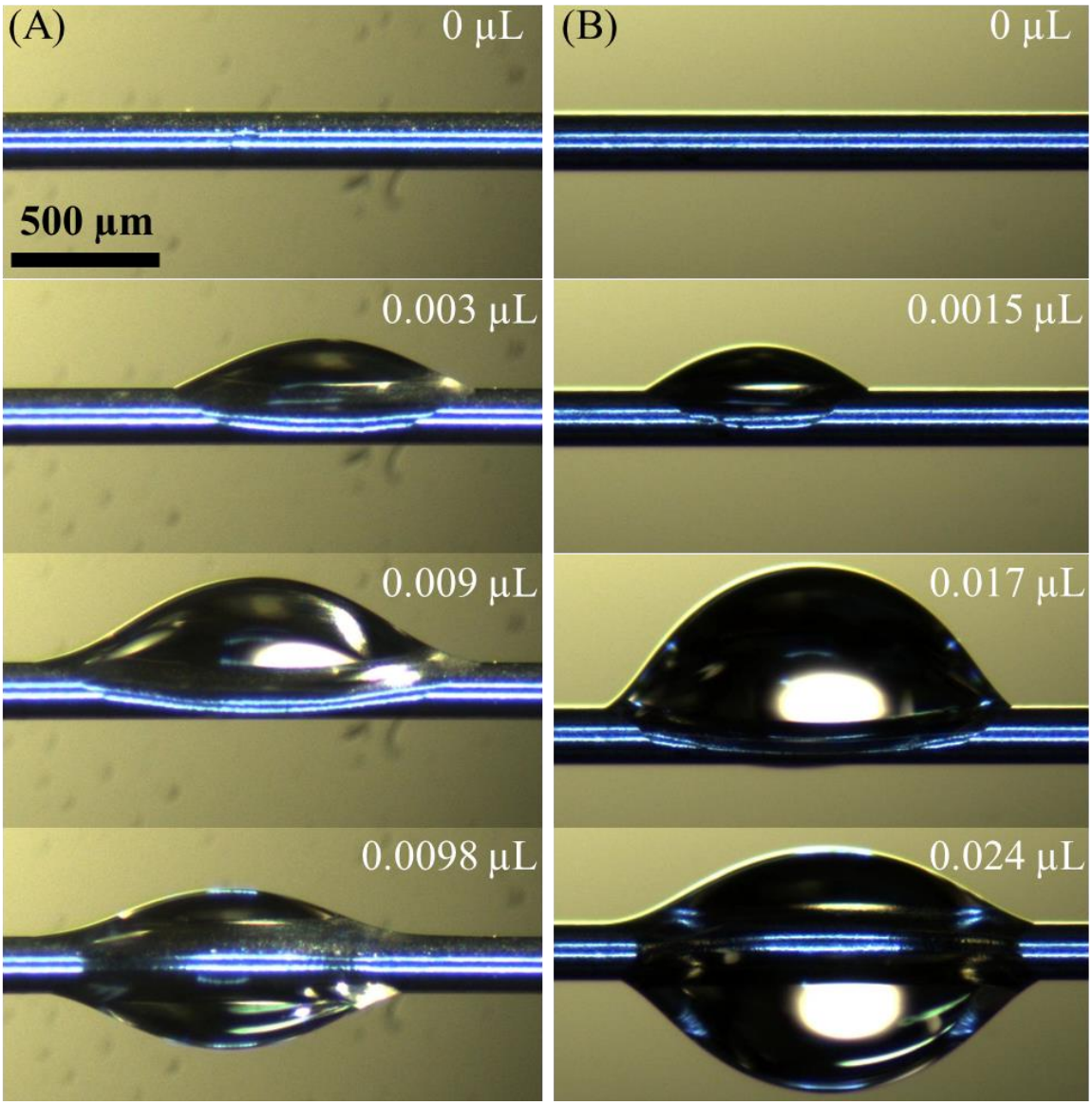

Figure 3.10. Morphological transition of hexadecane droplet on elliptical fibers of the contact angles (A) 22.8° and (B) 27.4°.

3.4 Behavior of liquid films on a ring coiled with elliptical hollow fiber

3.4.1 Special case with cylindrical fiber, $e = 1$

To start with, we would like to consider the liquid films deposited on the ring made of cylindrical hollow fiber. In contrast to the straight cylindrical fiber, for which the

pressure in the film is uniform along the circumference, the pressure becomes circumferentially non-uniform when the fiber is coiled. Taking into account eqs. (3.9) and (3.10), we obtain the following for the limit as $e = 1$:

Film coating the external surface:

$$P = \frac{\left(P_l - P_a\right)a}{\sigma} = 1 - \frac{\sin\alpha}{\left(R - \cos\varphi\right)}, \tag{3.17}$$

Film coating the internal surface:

$$P = \frac{\left(P_l - P_a\right)a}{\sigma} = -\left(1 - \frac{\sin\alpha}{\left(R - \cos\varphi\right)}\right). \tag{3.18}$$

Comparison of eqs. (3.17) – (3.18) and eqs. (3.9) – (3.10) reveals that the contribution of surface tension acting along the meridians to the capillary pressure is constant; for the external film, this contribution to the pressure difference is written in dimensional form as $\left(P_l - P_a\right)_{meridian} = \sigma / a$, and for the internal film it is $\left(P_l - P_a\right)_{meridian} = -\sigma / a$. This contribution is equal to the capillary pressure in a straight liquid cylinder (where pressure in the liquid is greater than the reference atmospheric pressure) or outside a cylindrical bubble (where pressure in the liquid is smaller than the reference atmospheric pressure in the bubble). Thus, the non-uniformity of the capillary pressure in eqs. (3.17) and (3.18) comes solely from the bending of the fiber. In Figs. 3.11(A), (B), we plot the distribution of capillary pressure that is spontaneously generated in the internal film and external film on the coiled fiber.

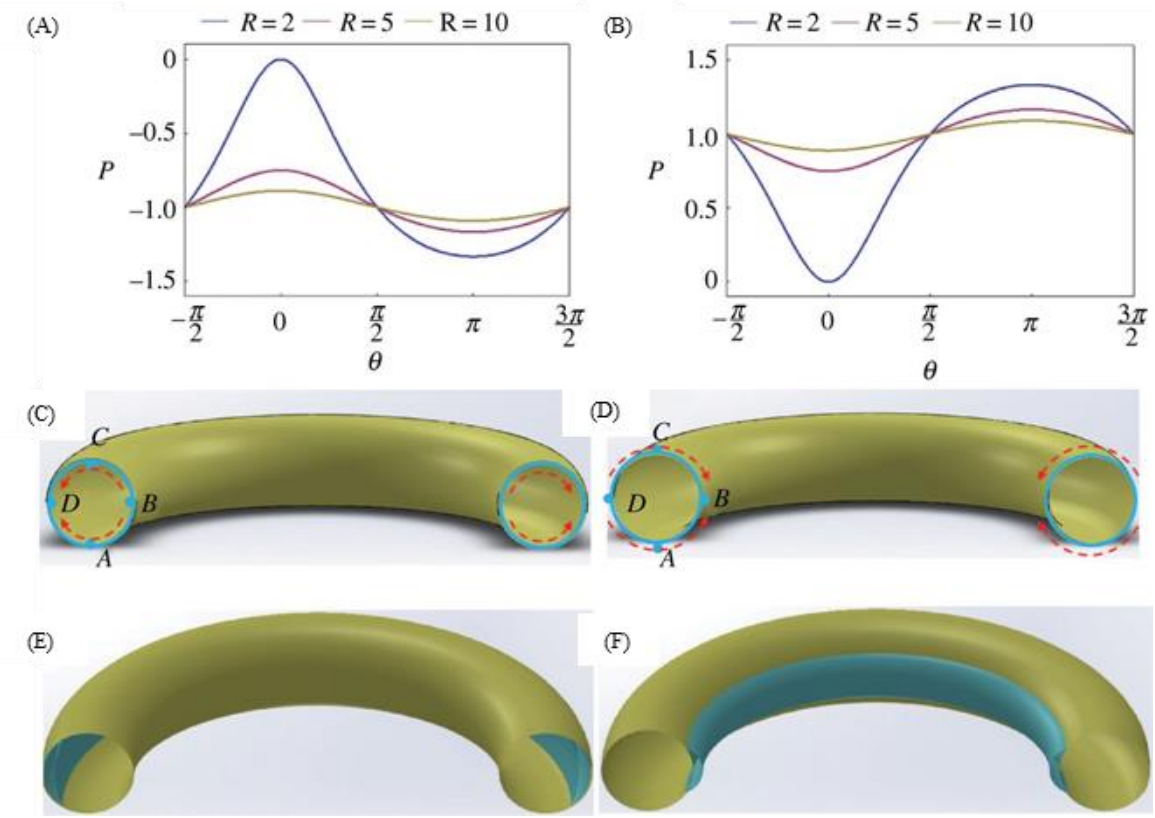

Figure 3.11. (A) Pressure distribution in the film coating the food canal; pressure for three different loop radii are shown. (B) Pressure distributions in the films coating the fiber exterior for three different loop radii. (C), (D) Schematics showing the flow directions for the internal (C) and external (D) films. (E), (F) Schematics showing the possible final configurations of the internal (E) and external (F) films. In theory, they should be shaped as unduloids[4].

According to Figs. 3.11(A), (B), the capillary pressure is minimal at the parallel $\theta = \pi$ for the internal film (point D in Fig. 3.11(C)) and at the parallel $\theta = 0$ for the external film (point B in Fig. 3.11(D)). These two parallels are identified as liquid attractors. Hence, the liquid will tend to flow spontaneously toward these attractor parallels as the most favorable locations for it to be collected, as shown in Figs. 3.11(E) and 3.11(F). These considerations help to understand the effect of concave-convex bends on the pressure distribution in the film.

As an illustration of these findings, we traced the evolution of thin glycerin films deposited on nylon fishing line (Berkley Trilene® Super Strong^{TM}, diameter 0.28 mm) looped for different radii of curvature (Fig. 3.12). Using the capillary rise experiment as discussed in [5], we obtained the contact angle of 31° for glycerin on these fibers. The loops were vertically withdrawn from a glycerin reservoir with the liquid completely covering the entire surface. The Bond numbers of drops formed, $Bo = \rho g V^{2/3}/\sigma$, where ρ is liquid density, g is acceleration due to gravity, and V is droplet volume, serve as a measure of importance of droplet weight with respect to the capillary forces. Estimating the volume of the drop from Fig. 3.12(A), we obtained its volume as ~ 2 μL. Inputting $\rho = 1.26 \times 10^3$ kg/m^3, $\sigma = 64 \times 10^{-3}$N/m, the resulting Bond number is estimated as Bo = 0.3. Thus, the effects of droplet weight and surface tension are comparable to each other, so that they both play important roles in the observed phenomenon shown in Fig. 3.12. When the radius of curvature of the loop is large (Fig. 3.12(A)), the capillary pressure differential is small (Fig. 3.12(B)), so that the effect of gravity dominates and the drops roll over to the bottom of the loop. In contrast to this case, when the radius of the loop decreases, the induced capillary pressure differential increases pushing the film to move toward the loop interior, as theory predicts. This capillary force is so strong that gravity can be defeated and the droplet forms on the internal side of the loop (Figs. 3.12(B), (C)).

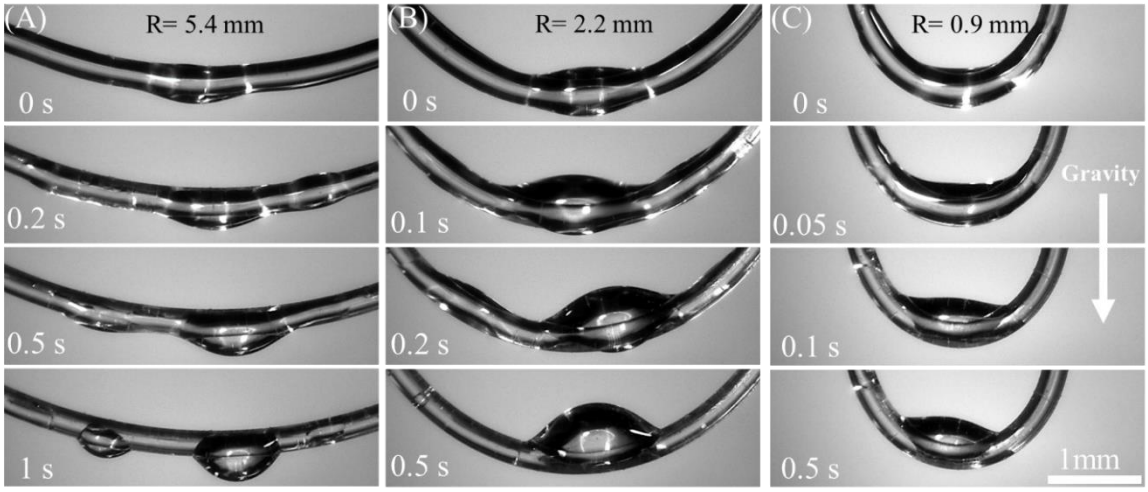

Figure 3.12. Evolution of a thin glycerin film deposited on a circular loop with different radii of curvatures. (A) 5.4 mm, (B) 2.2 mm, and (C) 0.9 mm. The film develops into a droplet collecting the film fluid on different regions of the loop.

3.4.2 General case with elliptical fiber

Based on Section 3.3, when changing the coiled fiber from cylindrical to elliptical, the direction of cross-sectional elongation of the fiber in the coiled state affects the attractor positions. Below, we evaluate the effect of coiling on liquid distribution for elliptical fibers. Two cases of orientation of fiber cross-section, with the ellipse elongation perpendicular to the coil plane (i.e., ellipticity $e > 1$), and with the ellipse elongation parallel to the coil plane ($e < 1$) are discussed separately. The internal and external films are both considered. Eqs. (3.2), (3.3), (3.9), (3.10) are applied for the following pressure distribution analysis.

3.4.2.1 External film

In Fig. 3.13(A), we plot the pressure distribution inside the external liquid film with different ellipticity e. The pressure profile changes drastically when the orientation of fiber elongation changes from the case $e < 1$ (Fig. 3.13(B)) to the case $e = 1$ (Fig. 3.13(C)) and to the case $e > 1$ (Fig. 3.13(D)). We select the pressure profile for $e = 1/2$, $e = 1$, and

$e = 2$ to represent each cases, respectively. The case of $e = 1$ has been discussed in Section 3.4.1, and therefore will not be discussed here.

For the case $e > 1$, the plot suggests that the pressure reaches the two local minimums at the parallels B and D, Fig. 3.13(D). Thus, the parallel B is no longer a single attractor for the liquid; the liquid collection can occur at the parallel D.

For the case $e < 1$, the plot suggests that the pressure reaches the two local minimums at the mirror symmetrical positions shifted from parallel B toward parallels A and C, Fig. 3.13(B). Thus, the parallel B is no longer a single attractor for the liquid; the liquid collection can occur at the two mirror-symmetrical parallels.

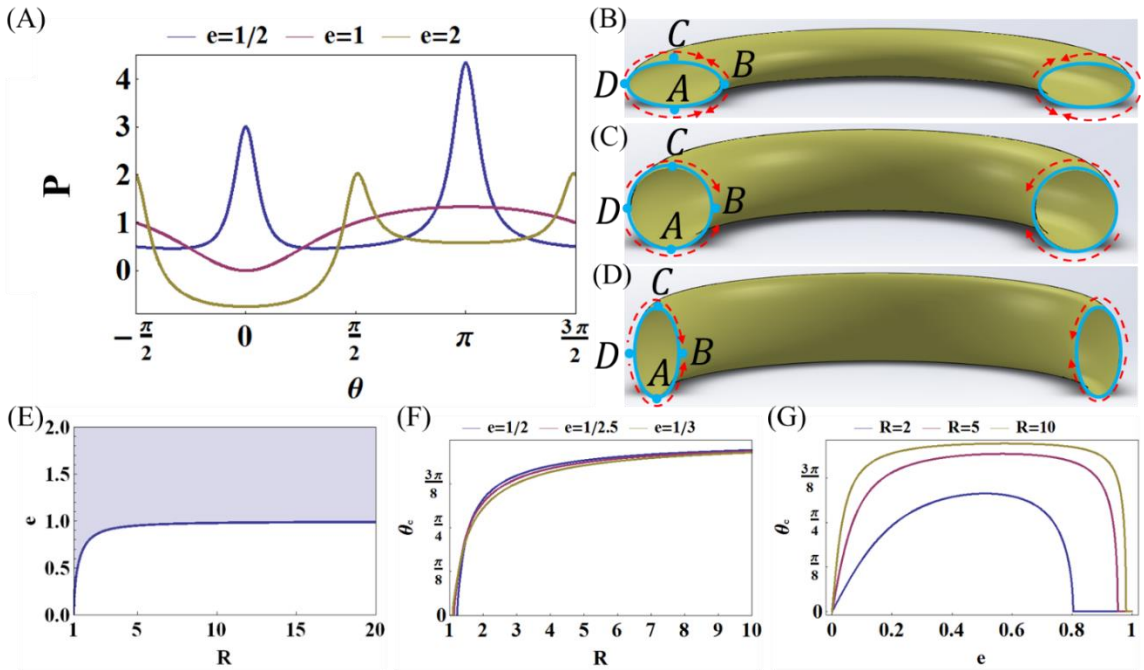

Figure 3.13. (A) Pressure distribution in films deposited on the external wall of a fiber with $e = 1/2$, 1, and 2 coiled in a ring of radius R = 2. (B)-(D) Schematic showing flow inside the external liquid film on three types of fibers with $e = \frac{1}{2}$, 1, and 2, illustrating the results of (A). (E) Diagram of transition from a single attractor at $\theta = 0$ (shaded region) to two attractors (white region). (F) Location of one of the mirror-symmetrical attractors specified by polar angle θ_c as a function of the dimensionless ring radius R for three different fiber ellipticities. (G) Location of one of the mirror-symmetrical attractors specified by polar angle θ_c as a function of fiber ellipticity for the three different ring radii R.

The transition from a single attractor of the case $e = 1$ to two attractors of the case $e < 1$ occurs because the pressure at the parallel $\theta = 0$ flips from a minimum to a maximum. Mathematically, this transition happens when the pressure profile passes an inflection point; that is, the second derivative of eq. (3.9) with respect to θ turns to zero at the parallels $\theta = 0$. This derivative gives us the following quadratic equation:

$$\frac{3\left(e^2-1\right)}{e^4}\left(R-1\right)^2+\frac{1}{e^2}\left(R-1\right)+1=0, \tag{3.19}$$

By solving this equation, we can plot the diagrams specifying a transition from a single attractor to the two attractors, Figs. 3.13(E).

These two parallels–attractors are specified by two angles $\pm\theta_c$, where $0 < \theta_c < \frac{\pi}{2}$. Different from the case $e > 1$, the position of these two attractors is influenced by the ellipticity e and the ring radius R as shown in Figs. 3.13(F), (G). At the given ellipticity e, the attractor position θ_c increases along with the coil radius R (Fig. 3.13(F)), approaching $\theta = \pi/2$ as the radius R goes to infinity and the fiber straightens out. At the given coil radius R, the attractor position θ_c changes non-monotonously with e, having a well pronounced maximum (Fig. 3.13(G)). This non-trivial result deserves special analysis.

When e is smaller than but close to 1 (i.e., the fiber is close to cylindrical), the attractors $\pm\theta_c$ should be positioned close to the parallel B, $\theta_c \to 0$. Once the attractor hits $\theta_c = 0$, further increase of fiber ellipticity e does not change the attractor position (Fig. 3.13(G)).

We must turn to the opposite limit as e goes to zero. In this case, the ring looks like a thin washer with nearly flat sides and sharp edges (Figs. 3.13(B), (E)). On the washer

sides, the capillary pressure goes to zero because the film is almost flat (Fig. 3.14). Therefore, we need to study pressure behavior near the edges B and D.

The behavior of pressure in the vicinity of parallel B can be studied asymptotically using eq. (3.9). In the vicinity of parallel B, one can asymptotically evaluate the α and φ parameters from eqs. (3.2) and (3.3) as $\alpha \approx \pi/2$, $\varphi \approx \theta/e$, provided that $\theta \to 0$. Substituting these parameters into eq. (3.9), we rewrite the Laplace equation in its asymptotic form as

$$\frac{\left(P_l - P_a\right)a}{\sigma} \approx \frac{e^4}{\left(\theta^2 + e^4\right)^{\frac{3}{2}}} - \frac{1}{\left(R-1\right)}, \quad \theta \to 0, e \to 0, R > 1. \tag{3.20}$$

When $\theta \approx \pm e^{\frac{4}{3}}(R-1)^{\frac{1}{3}}$, the solution of equation $\left(P_l - P_a\right)a/\sigma \approx 0$ can be matched to the zero pressure at the washer sides. As one moves further toward parallel B, decreasing the angular coordinate θ, the pressure increases because of the first term in eq. (3.20). In the vicinity of parallel B, the pressure becomes anomalously large, $\left(P_l - P_a\right)a/\sigma \approx 1/e^2$. At parallel D, similar arguments suggest that the pressure remains anomalously large with a similar asymptotic behavior $\left(P_l - P_a\right)a/\sigma \approx 1/e^2$. Equation (3.20) accurately describes the pressure distribution near the edge (Fig. 3.14). This analysis reveals that the attractors $\pm\theta_c$ must remain separated from the parallel $\theta = 0$ where the pressure is expected to be high and the liquid will be squeezed out immediately. The curvature associated with the coil radius R changes the scenario of a straight washer-like ring $e \to 0$, creating the two attractors in the vicinity of parallel B at $\theta = 0$.

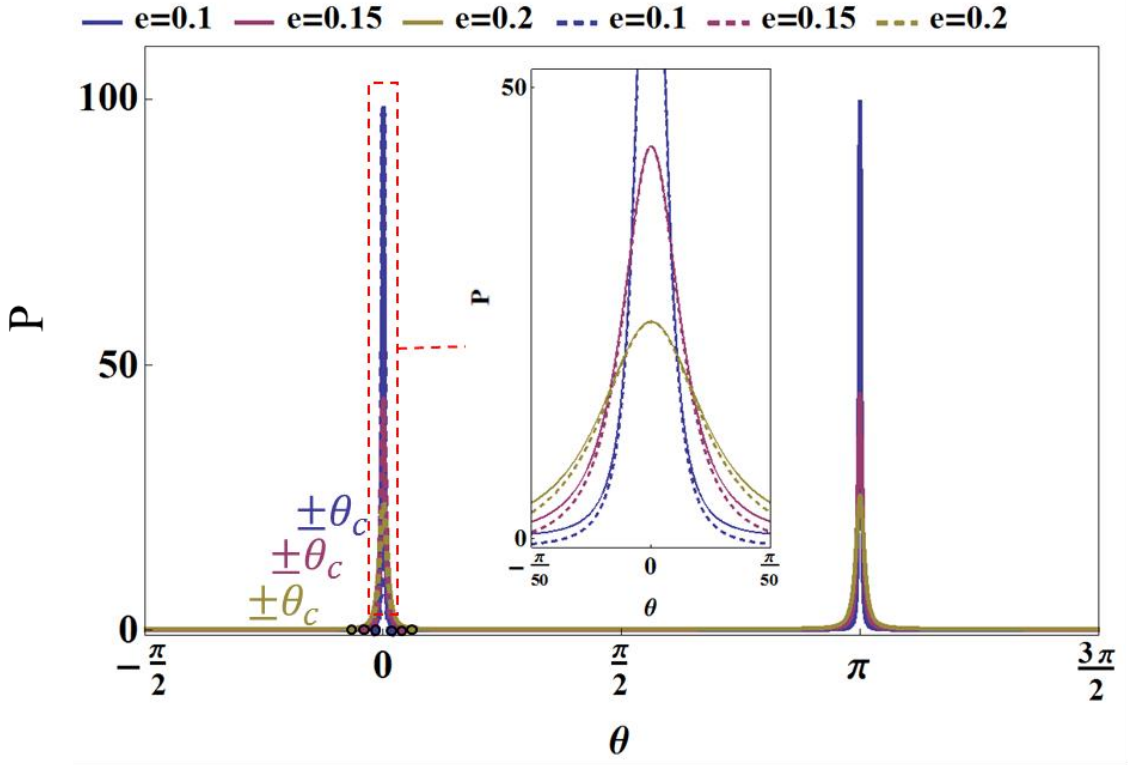

Figure 3.14. Pressure distribution in a film coating a washer-like ring with radius R = 2. The pressure is almost zero at the entire surface of this type of fiber and it spikes up at the edges. The dashed lines correspond to the asymptotic solution, eq. (3.15). The small circles on the horizontal axis near $\theta = 0$ show the attractor positions.

3.4.2.2 Internal film

In Fig. 3.15(A), we plot the pressure distribution inside the internal liquid film with different ellipticity e. We select the pressure profile for $e = 1/2$, $e = 1$, and $e = 2$ to represent the three cases $e < 1$ (Fig. 3.15(B)), $e = 1$ (Fig. 3.15(C)), and $e > 1$ (Fig. 3.15(D)), respectively. The case of $e = 1$ has been discussed in Section 3.4.1, and therefore will not be discussed here. Since eqs. (3.9) and (3.10) are only different in one negative sign, their results are very similar but with the maximums and minimums reversed.

For the case $e < 1$, the plot suggests that the pressure reaches the two local minimums at the parallels B and D, Fig. 3.15(B), making them as two attractors with fixed position.

For the case $e > 1$, the plot suggests that the pressure reaches the two local minimums at the mirror symmetrical positions shifted from parallel D toward parallels A and C, Fig. 3.15(D). Thus, the parallel D is no longer a single attractor for the liquid; the liquid collection can occur at the two mirror-symmetrical parallels.

The transition from a single attractor of the case $e = 1$ to two attractors of the case $e < 1$ occurs because the pressure at the parallel $\theta = \pi$ flips from a minimum to a maximum. Similarly, the second derivative of eq. (3.8) with respect to θ turns to zero at the parallels $\theta = \pi$, gives us the following quadratic equation:

$$\frac{3\left(e^2-1\right)}{e^4}\left(R+1\right)^2-\frac{1}{e^2}\left(R+1\right)+1=0\,, \tag{3.21}$$

By solving this equation, we can plot the diagrams specifying a transition from a single attractor to the two attractors, Figs. 3.15(E).

These two parallels–attractors can also be specified by two angles $\pm\theta_c$, but in this case $\frac{\pi}{2} < \theta_c < \pi$. The influence of the ellipticity e and the ring radius R on θ_c is shown in Figs. 3.15(F), (G). At given ellipticity e, angle θ_c decreases along with ring radius R (Fig. 3.15(F)), approaching $\theta = \pi/2$ as radius R goes to infinity and the fiber straightens out. At given radius R, angle θ_c decreases along with ellipticity e (Fig. 3.15(G)), approaching $\theta = \pi/2$ as ellipticity goes to infinity and the tube is transformed into a coiled slit-like channel. Thus, menisci are formed at the ends of this slit-like channel, as expected.

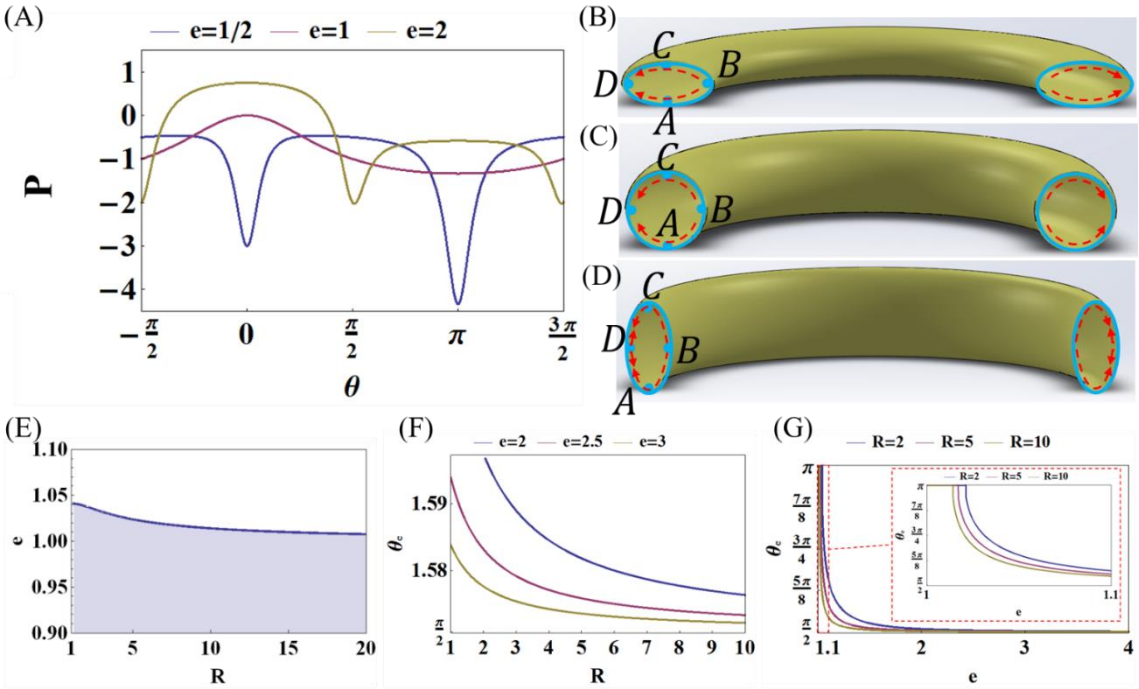

Figure 3.15. (A). Pressure distribution of a thin uniform liquid film deposited on the internal wall of a circular ring made of an elliptical tube with ring radius R = 2 at different cross-section ellipticities $e = \frac{1}{2}$, 1, and 2. (B). Flow inside the internal liquid film when $e = \frac{1}{2}$. (C). Flow inside the liquid film when $e = 1$. (D). Flow inside the liquid film when $e = 2$. (E) Diagram of transition from a single attractor at $\theta = \pi$ (shaded region) to two attractors (white region). (F). Influence of ring radius r on θ_c when the minimum pressure position is not at the critical positions $\theta = 0$ and $\theta = \pi$. (G). Influence of ring radius e on θ_c when the minimum pressure position is not at the critical positions $\theta = 0$ and $\theta = \pi$.

3.4.2.3 Engineering applications

Analysis of the stability of the external and internal liquid films is useful for engineering applications involving an elliptical fiber bent into a loop. One example would be mail armor, which is usually made of metal rings (Fig. 3.16(A)). The main enemy of mail armor is corrosion, caused by water films that might be left on the ring surface after a rain. To prevent corrosion, water should collect at those sides of the ring where it can easily evaporate or be shaken off, that is, at the ring sides. According to the analysis in Fig. 3.13, the most attractive candidates for mail armor should have ellipticity less than one, $e < 1$

(Fig. 3.16(B)). In this case, one would intuitively think of using washer-like rings with e close to 0. These rings, with a high curvature at $\theta = 0$, would force the liquid to flow toward the rings' flattened sides. However, the analysis summarized in Fig. 3.13(G) shows that the most attractive positions for water to flow are still near the ring edges where water can bridge two adjacent rings and might be trapped between them. The most distant position from the ring edges is determined by the maximum θ_c (Fig. 3.13(G)). In Fig. 3.16(E) these maximums are plotted as a function of ring radius R. In Fig. 3.16(F), we plot the critical ellipticity e_c taken from Fig. 3.13(G), corresponding to the given maximum θ_c; this is another version of Fig. 3.16(E), which is useful for ring design.

If the rings need to be coated with an anti-corrosion layer, our analysis suggests that elliptical rings would never have a uniform coating thickness (Fig. 3.13(A)). When a liquid film is deposited on a ring surface, the liquid will move toward the ring half closer to the axis of rotation. Therefore, the final coating layer will be thicker at the ring half closer to the axis of rotation (Fig. 3.16(C)). This effect is attractive for coating applications; it ensures that the thicker anti-corrosion coating will be deposited on its own at the ring contacts in the mail armor where water is likely to be trapped.

Another example is the design of knitted fabrics, in which the fibers or yarns are bent in loops forming the structure shown schematically in Fig. 3.16(B). In a first approximation, these loops can be modeled as parts of a circular loop. Because the fibers and yarns are typically round in cross section, the results summarized in Fig. 3.13(C) can be applied to the analysis of behavior of finishes or inks at the fiber or yarn level. By introducing a local system of coordinates placing its center at the center of each loop, one

can directly use the results of Section 3.4.1. As follows from that analysis, liquid is expected to move toward the parallel $\theta = 0$, as shown in Fig. 3.16(D). This effect can be used, for example, in making a fabric with a gradient of coloration at the loop scale: the outermost layers of the loop will be less colored than those sitting closer to the loop axis.

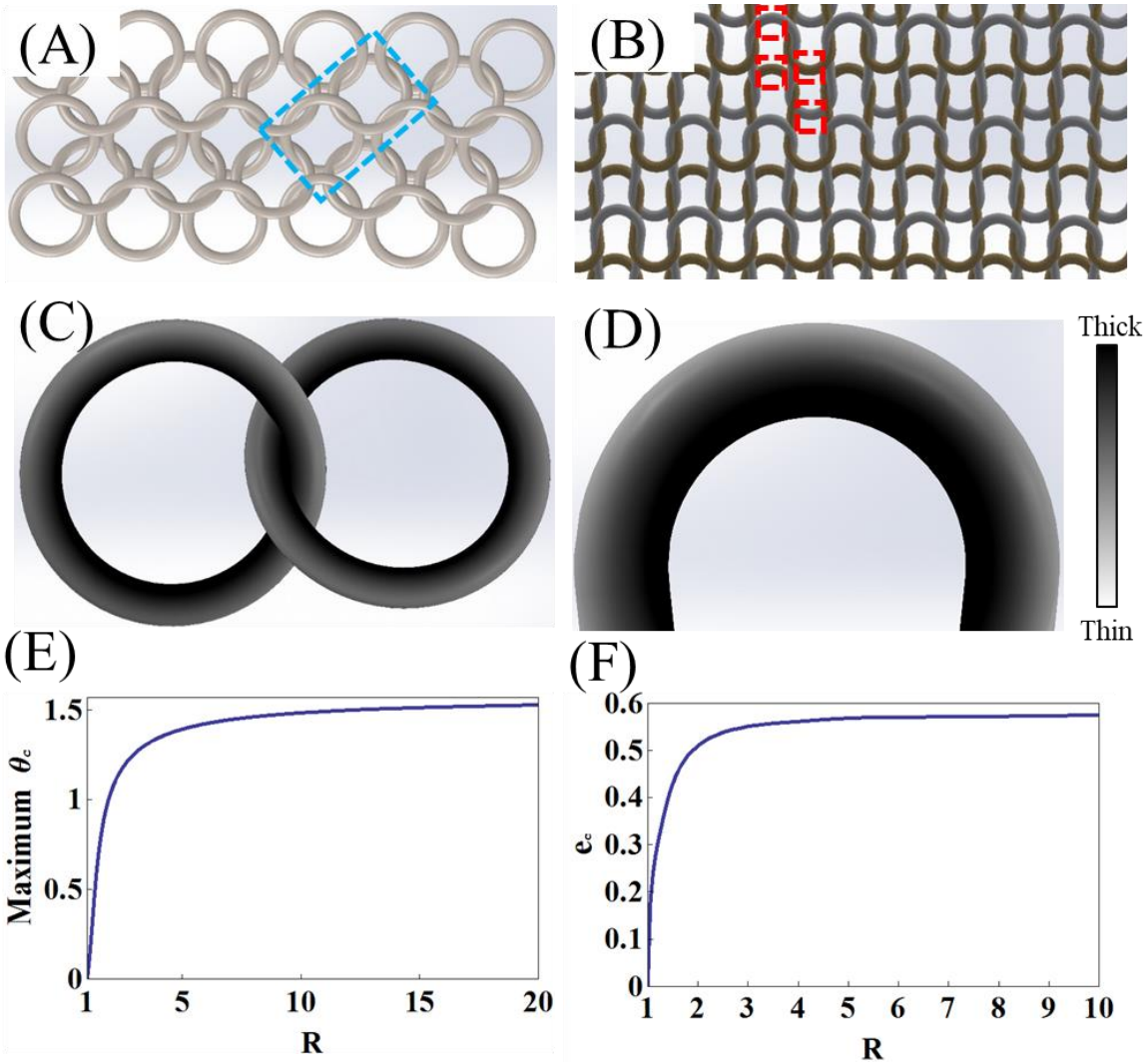

Figure 3.16. (A). Schematic of mail armor and (C) magnified picture of a ring couple with a non-uniform finish thickness. (B) Schematic of a knitted fabric. Some parts of the loop boxed by the dashed lines can be modeled in a first approximation by circular rings. (C) Illustration of the effect of non-uniform film thickness on mail armor rings: the darker, thicker films protect the rings against corrosion if water is trapped at the ring connections. (D). In the knitted fabric, the darker, thicker film is located at the loop interior while the brighter, thinner film is at the loop exterior. (E) Position of the finish collection as a function of radius R of a washer-like ring of ellipticity e_c specified in (F).

3.5 Conclusions

In this chapter, the wetting of elliptical fibers is studied by analyzing the stability of coating film. First, a general mathematical description of an elliptical fiber looped in a circular ring as a basic element is introduced in Section 3.2. By controlling the radius of the ring and the cross-sectional ellipticity, this mathematical setup can be used to analyze different scenarios from the straight to curved fibers with cross-sectional shapes from ribbon-like to elliptical then circular. The general equations describing the pressure distribution inside the external and internal films are calculated based on Laplace law of capillarity in eqs. (3.9) and (3.10). Together with eqs. (3.2) and (3.3), pressure inside the liquid film at every point on the fiber surface can be found, and thus the liquid flow inside the film can be predicted.

Based on the constructed model, the stability of coating films on a straight hollow elliptical fiber is firstly studied in Section 3.3. The external liquid film is predicted to be collected at the flatter regions and the internal film at the more curved regions, and form liquid columns, Fig. 3.2. Further analysis of the column stability based on the modified Princen theory shows that those columns are not stable and should break in a series of separated droplets, which is proved experimentally in Fig. 3.4. Then the droplet morphology formed on the external surface is experimentally studied. Depending on the contact angle and the droplet volume, two types of droplets, barrels and clam-shells, can be formed.

The study is expanded to the ring made of a curved elliptical tube in Section 3.4. First, the special case of a ring made of a curved cylindrical tube is discussed and compared

with the experimental results to show the applicability of the model. Then the effects of ring radius and cross-sectional ellipticity on the pressure distribution inside the external and internal films are discussed, Figs. 3.7 and 3.9 respectively. The positions of the liquid attractors are predicted based on the minimum pressure. And the transition between single-attractor scenario and two-attractors scenario is illustrated in the phase diagrams. Some engineering applications of the obtained results are proposed.

3.6 References

[1] Lehnert, M.S., Monaenkova, D., Andrukh, T., Beard, C.E., Adler, P.H. & Kornev, K.G. 2013 Hydrophobic-hydrophilic dichotomy of the butterfly proboscis. Journal of Royal Society Interface 10, 20130336. (doi:10.1098/rsif.2013.0336).
[2] Kornev, K.G., Monaenkova, D., Adler, P.H., Beard, C.E. & Lee, W.K. 2016 The butterfly proboscis as a fiber-based, self-cleaning, micro-fluidic system. In Bioinspiration, Biomimetics, and Bioreplication 2016 (eds. R.J. MartinPalma, A. Lakhtakia & M. Knez).
[3] Oprea, J. 2007 Differential geometry and its applications. 2nd ed. Washington DC, The Mathematical Association of America.
[4] Langbein, D.W. 2002 Capillary Surfaces: Shape - Stability - Dynamics, in Particular Under Weightlessness. New York, Springer.
[5] Tsai, C.C., Gu, Y. & Kornev, K.G. 2014 Wetting of nanofiber yarns. Colloid Surface A 459, 22-30. (doi:10.1016/j.colsurfa.2014.06.037).

CHAPTER IV

WETTING OF COMPLEXLY-SHAPED CHANNELS

4.1 Introduction

Our theory of morphological transitions of the shape of a droplet on a ribbon-like fiber, Section 2.2, is found to agree with the theory of morphological transitions of the shape of a droplet on a chemically inhomogeneous flat surface patterned with an array of stripes of distinct chemical composition [1]. The latter theory was based on the analysis of the surface energy landscape and is more general and hence more complex. Our method is based on the force balance analysis, which is a slight modification of the Princen theory [2]. It is quite straightforward and much easier and can be applied to study the wetting transitions of complexly-shaped channels, provided that only columnar configurations of the liquid bodies are of interest. Our studies show that the liquid column is a very common morphology of a liquid body formed inside the linear channels of different complex cross-sections. The columnar configuration of the liquid body is found to correspond to the wetting case. At the conditions when this columnar solution breaks down, the liquid body will assume other more complex shapes. The other morphologies typically correspond to the channel dewetting. To confirm this wetting/dewetting transition at the identified conditions, one needs to conduct experiments. Thus, due to its simplicity, the force balance

analysis for the existence of the columnar droplet is a good tool for studying the wetting/dewetting transition in complexly-shaped channels.

In this chapter, we will first examine the applicability of our method to study the shape of a liquid column in the V-shaped channel by comparing the experimental results of [3] with the theory. Then, we will systematically study the droplet morphology and the wetting/dewetting transition in the C-shaped channel.

4.2 Liquid column in the V-shaped channel

The experimental results of [3] show that in the V-shaped channel, the liquid droplet can take on different shapes. The shapes can be classified into columns implying wetting and clam-shells implying dewetting. In this section, we will modify the Princen theory to identify the conditions for forming the equilibrium columns. Then we will construct the phase diagram based on the results, and compare it with the established experimental results.

4.2.1 Model formulation

The V-shaped channel is assumed infinitely long and its cross-section is an isosceles triangle with the leg length l and vertex angle 2β, Fig. 4.1(A). The liquid column is supported by the internal wall of the channel, so the cross section of the solid/liquid interface coincides with the channel bottom. As discussed previously for the ribbon-like fiber, the liquid/air interface is a circular arc with the radius R and the center angle 2α, Fig. 4.1(B).

The free body diagram for the column is built up by making an imaginary cut at the center perpendicularly to the channel, as shows in Fig. 4.1(C). Half of the column is then

replaced with an equivalent system of forces acting in the z-direction parallel to the channel long axis. According to the free body diagram in Fig. 4.1(C), the force balance in the z-direction is written as:

$$F_{AL} + F_{SL} - F_{SA} - F_P = 0, \tag{4.1}$$

where F_{AL} is the force due to surface tension at the air/liquid interface; F_{SL} is the force due to surface tension σ_{SL} at the solid/liquid interface; F_{SA} is the force due to surface tension σ_{SA} of the solid/air interface; F_P is the pressure resultant acting perpendicularly to the cross-section.

The liquid columns in the V-shaped channels can be distinguished by the position of their contact lines: for one class of columns, the contact lines stay inside the channel, and for the other class of columns the contact lines are pinned at the channel edges. Fig. 4.1 illustrates the first case. Therefore, we need to discuss two different columns separately.

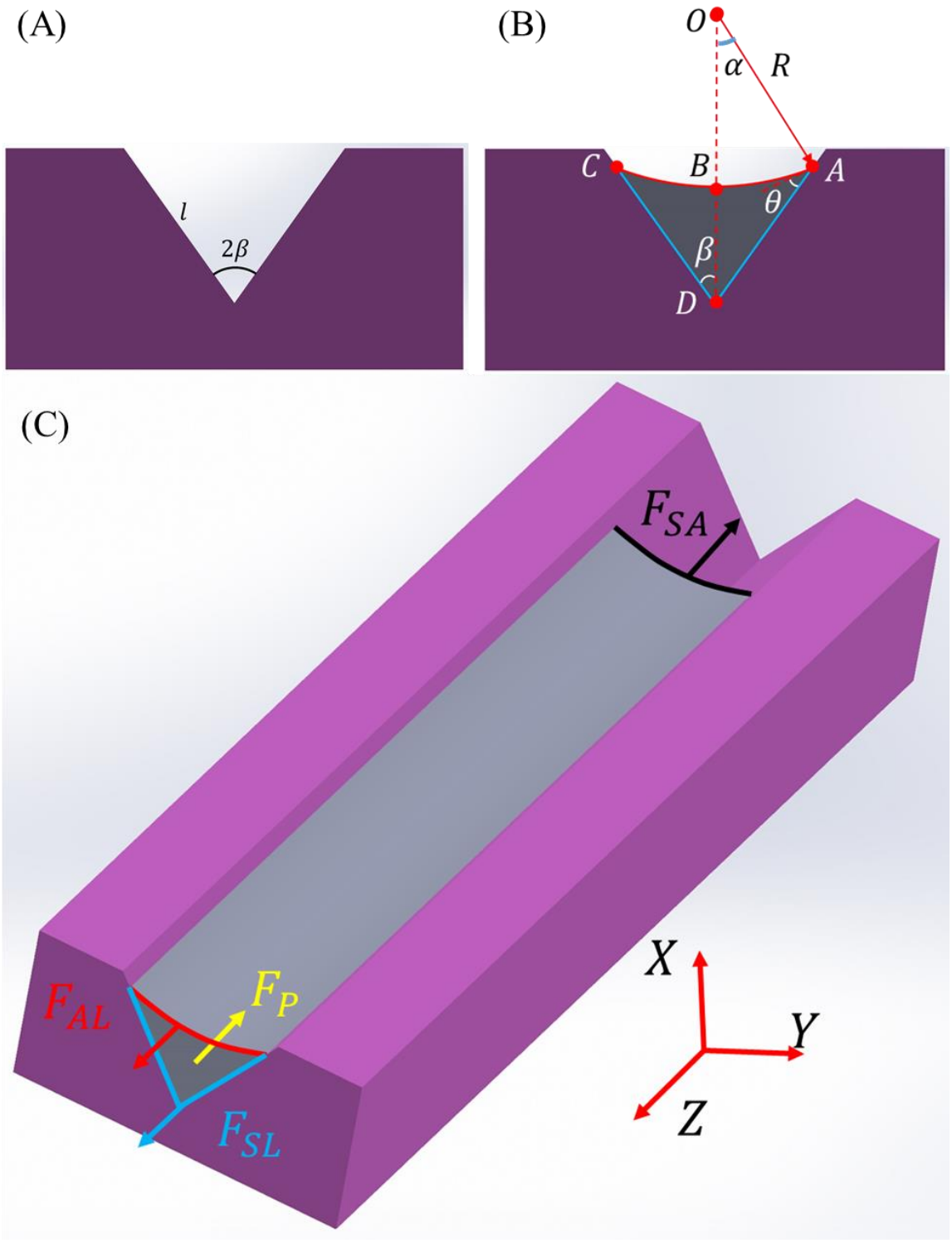

Figure 4.1. (A) Schematic showing the cross section of the V-shaped channel. (B) Schematic showing the cross section of the liquid column in the V-shaped channel. (C) Schematic helping to understand the free body diagram.

4.2.2 Liquid column with contact line inside the V-shaped channel

When the contact lines of the column are inside the channel, the angle that the meniscus makes with the channel is fixed by the contact angle θ. Depending on the vertex angle β and the contact angle θ, the meniscus can be either concave or convex, Fig. 4.2.

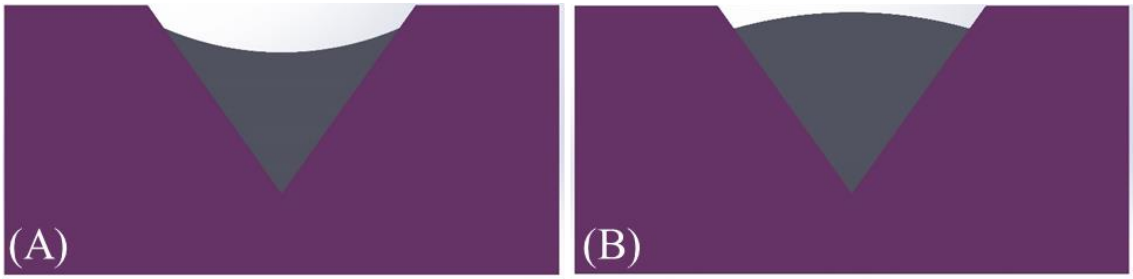

Figure 4.2. Cross-sections of different columns with the contact lines inside the V-shaped channel (A) Concave liquid/air interface and (B) Convex liquid/air interface.

Figs. 4.3(A)-(B) defines all necessary parameters needed for analysis of the concave case and convex case, respectively. To distinguish between these two cases, the angle α is defined as positive for the concave case, and negative for the convex one. The contact angle $\theta \in [0,90°]$, and the relation $\beta = 90° - (\theta + \alpha) \in (0°, 90°)$ always holds true.

Therefore the component forces in eq. (4.1) can be calculated for concave and convex cases respectively: $F_{AL} = \sigma \cdot \widehat{ABC} = \pm 2\alpha\sigma R$, where σ is the interfacial tension of the liquid/air pair; $F_{SL} = \sigma_{SL} \cdot (\overline{CD} + \overline{AC}) = \pm\sigma_{SL} \cdot 2R \sin\alpha \,/\, \sin\beta$, where σ_{SL} is the interfacial tension of the solid/liquid pair; $F_{SA} = \sigma_{SA} \cdot \widehat{ADC} = \pm\sigma_{SA} \cdot 2R \sin\alpha \,/\, \sin\beta$, where σ_{SA} is the interfacial tension acting over the solid/air interface; and $F_P = PA_{\mathrm{ABCD}}$, where $P = \mp\sigma/R$ is pressure in the liquid column with respect of pressure in the

atmosphere, and $A_{\mathrm{ABCD}} = \pm R^2(\sin^2\alpha\cos\beta\,/\sin\beta - \alpha + \sin\alpha\cos\alpha)$ is the cross sectional area of the liquid column.

Employing the Young-Laplace equation, $\sigma_{SA} - \sigma_{SL} = \sigma\cos\theta$, and substituting these expressions for the forces, eq. (4.1) can simplified to the same expression for the both cases as:

$$(\alpha + \sin\alpha\cos\alpha)\left(\frac{\cos(\theta+\alpha)}{\sin\alpha}\right)^2 - \frac{2\cos\theta\sin\alpha}{\cos(\theta+\alpha)} + \sin(\theta+\alpha)\cos(\theta+\alpha) = 0. \qquad (4.2)$$

Thus, eq. (4.2) describes the necessary conditions for equilibrium of a liquid column with the contact lines inside the V-shaped channel. To determine a dependence of the contact angle θ on the half of the center angle, α, we introduce the function $f(\alpha,\theta) = (\alpha + \sin\alpha\cos\alpha)\left(\frac{\sin\alpha}{\cos(\theta+\alpha)}\right)^2 - \frac{2\cos\theta\sin\alpha}{\cos(\theta+\alpha)} + \sin(\theta+\alpha)\cos(\theta+\alpha)$, which is the left hand side of eq. (4.2) and seek a set of parameters (α , θ) for which this function intersect with plane $f(\alpha,\theta) = 0$. Plotting this function in Fig. 4.3(C), we observe that $f(\alpha,\theta)$ never intersects the zero plane, suggesting that the liquid column with the contact lines inside the V-channel cannot be formed. This result is confirmed by [3], and the liquid column in this case will transform into a series of clam-shell droplets.

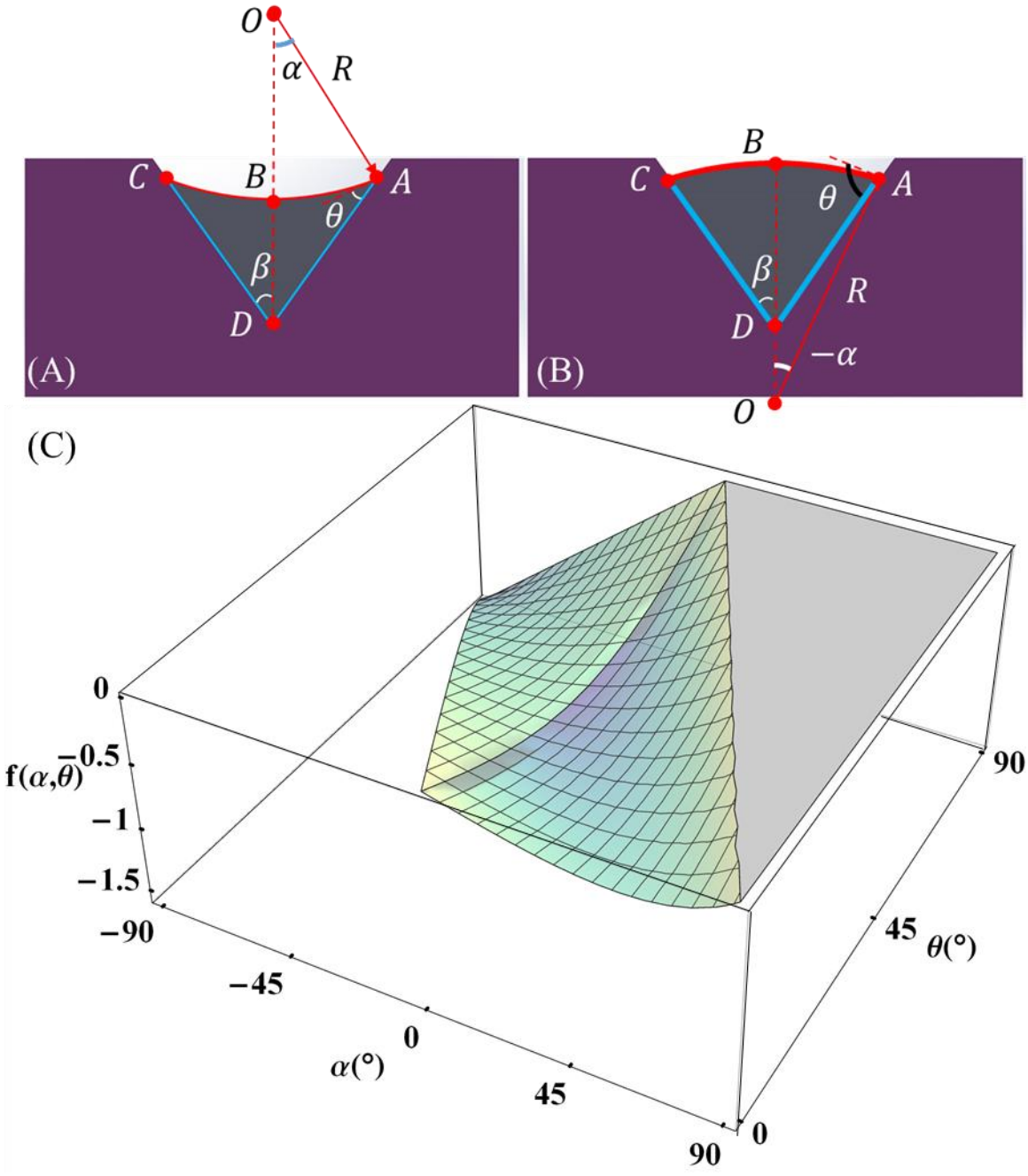

Figure 4.3. Schematic of a cross-section of the liquid column with (A) concave and (B) menisci formed in the V-shaped channel with the contact lines C and A inside it. (B) Plot of $f(\alpha, \theta)$ as a function of α and θ.

The physical interpretation of non-existence of a columnar meniscus supported by the contact lines inside the V-shaped channel is as follows. Consider first a concave

meniscus. A small deformation of its surface with a decrease of the radius of curvature will always lead to an increase of the capillary suction pressure. Thus, the column always tends to stretch into a thin liquid thread leaning toward the channel vertex. Thus, the final state will be either an infinitely thin liquid thread or a set of droplets, provided that the thread gets broken at some places.

For a convex columnar meniscus, any perturbations will lead to a decrease of the radius of curvature, resulting in a flow squeezing the liquid toward the channel edges. Thus, the final state will be either a liquid column pinned to the channel edges or a set of droplets.

4.2.3 Liquid column with contact line inside the V-shaped channel

As known from capillarity [4, 5], a liquid body can form any arbitrary contact angle with a sharp edge of any corner. Therefore, the contact angle at which the meniscus meets the sharp edge of any substrate is not defined and can take on any arbitrary value. We, therefore, allow the circular arcs of the meniscus to approach the edges at any arbitrary angle, Fig. 4.4(A) and (B). In these figures, the angle α is defined as positive for the concave meniscus and negative for the convex meniscus.

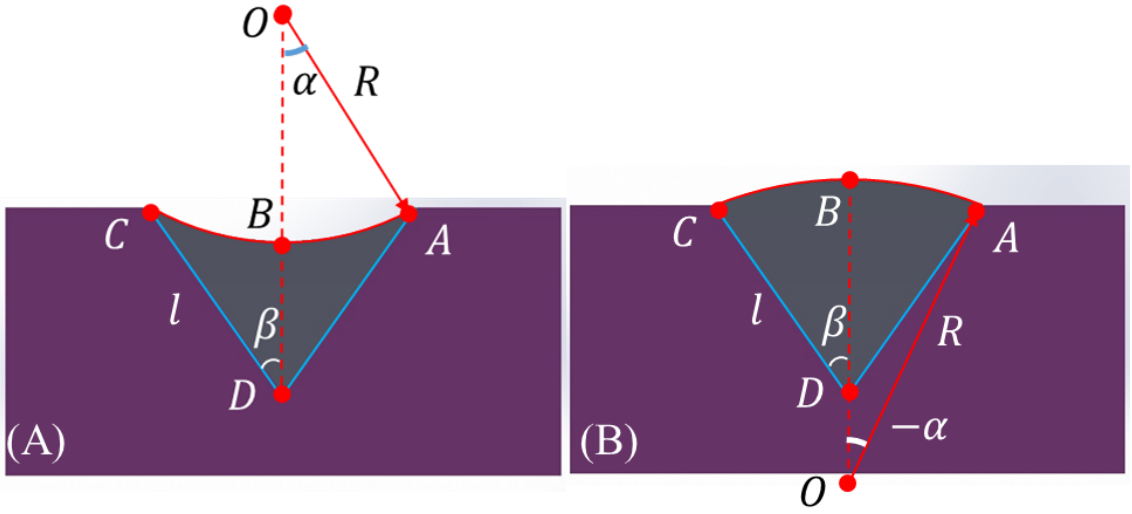

Figure 4.4 Schematic of meniscus cross-section when its contact lines C and A are pinned at the edges of the V-shaped channel; (A) the concave meniscus and (B) the convex meniscus.

Therefore, the component forces in eq. (4.1) can be calculated as: $F_{AL} = \sigma \cdot \widehat{ABC}$, $\widehat{ABC} = \pm 2\alpha R\sigma$ for concave and covex meniscus respectively; $F_{SL} = \sigma_{SL} \cdot (\overline{CD} + \overline{AC})$, $\overline{CD} = \overline{AC} = l$; $F_{SA} = \sigma_{SA} \cdot (\overline{CD} + \overline{AC}) = 2\sigma_{SA} l$; and $F_P = PA_{\mathrm{ABCD}}$, where the pressure in the liquid column with respect to the atmospheric pressure is $P = \mp\sigma/R$ for concave and covex meniscus, respectively, and $A_{\mathrm{ABCD}} = l^2 \sin\beta \cos\beta - R^2(\alpha - \sin\alpha \cos\alpha)$. According to sine law for the triangle ΔAOD, the relation $\frac{R}{l} = \pm \frac{\sin\beta}{\sin\alpha}$ hold true for concave and covex menisci, respectively.

Employing the Young-Laplace equation, $\sigma_{SA} - \sigma_{SL} = \sigma \cos\theta$ and substituting the calculated force components in the force balance equation eq. (4.1) and solving it for contact angle, we obtain the same solution for both concave and convex cases:

$$\theta = \arccos\left[\frac{\alpha \sin\beta}{2\sin\alpha} + \frac{\sin(\alpha+\beta)}{2}\right] \tag{4.3}$$

4.2.4 Liquid column with contact line inside the V-shaped channel

Eq. (4.3) is valid for any equilibrium liquid columns in the V-shaped channel. In Fig. 4.5(A), dependence of contact angle, θ on α and β is plotted. Contact angle θ ranges from 0° to 180°, half of the channel opening angle β ranges from 0° to 90°, and half of the center angle of the liquid/air interface α can possibly ranges from -180° to $90° - \beta$. Fixing, one can plot several cross sections parallel to the α - θ plane on this surface, some examples are shown in Fig. 4.5(B).

Within the defined domain, two values of α correspond to each value of θ, implying that two different column configurations with the same contact angle can be formed. The column with smaller $\alpha \in (-180°, -90°)$ is more convex than that with a larger $\alpha \in (-90°, 90° - \beta)$. The column with $\alpha \in (-180°, -90°)$ is proved unstable to perturbations, and thus, will consider no further [6]. Only the column with $\alpha \in (-90°, 90° - \beta)$ will be discussed in the following.

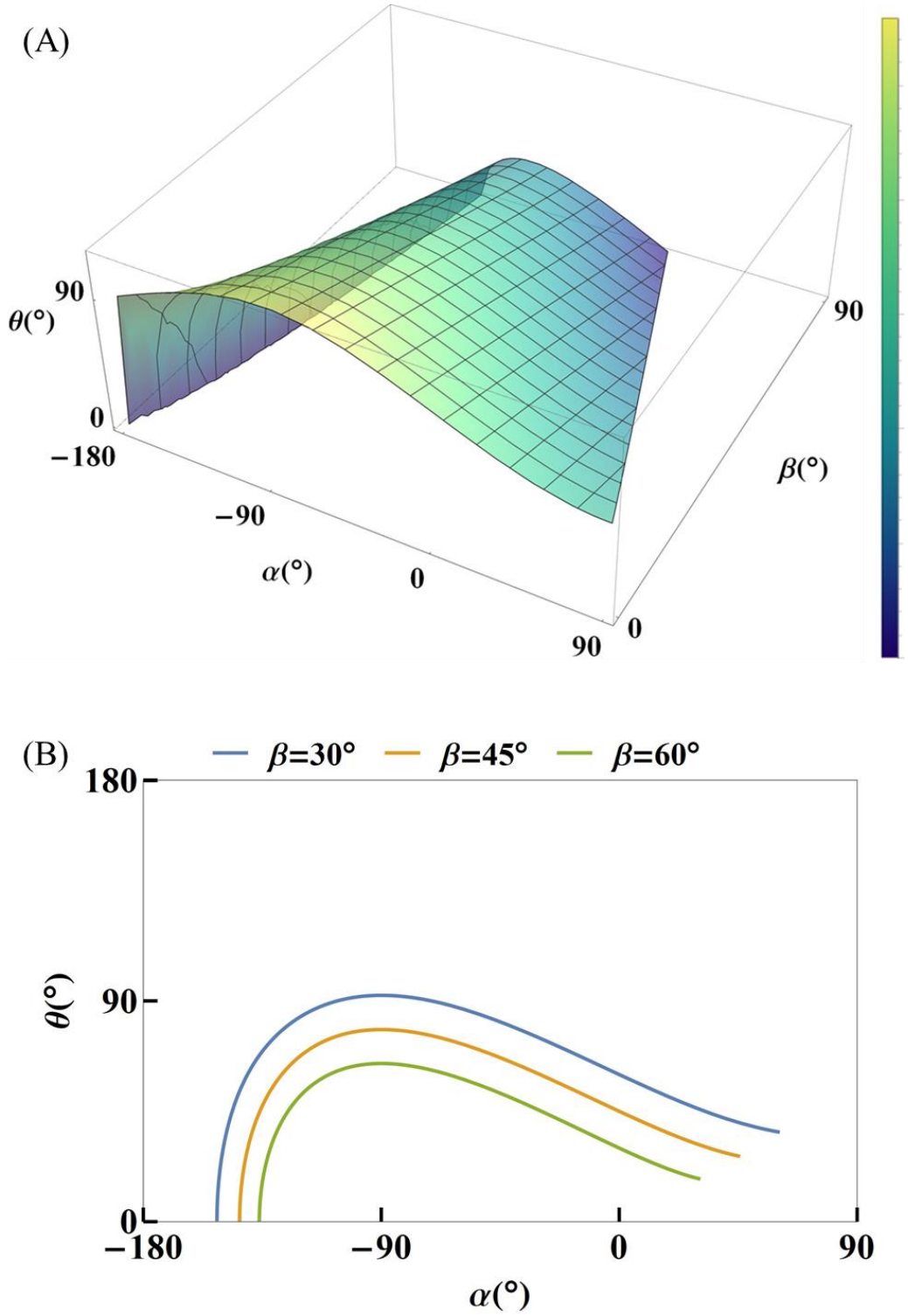

Figure 4.5. (A) 3D Plot of contact angle θ as a function of half of the center angle of the liquid/air interface α and half of the channel opening angle β. (B) Cross sections of the 3D plot in (A) for $\beta = 30°, 45°, 60°$.

The θ solution of eq. (4.3) exists within $\alpha \in (-90°, 90° - \beta)$. Substituting the lower limit, $\alpha = -90°$, and the upper limit $\alpha = 90° - \beta$ in eq. (4.3), we plot the two boundaries forming the dashed region in between where a liquid column could be formed, Fig. 4.6. Within this region, the concave and convex columns are separated when $\alpha = 0°$ in eq. (4.3), resulting in $\theta = \arccos(\sin\beta)$. Outside of this region, the liquid cannot form columns, but may form clam-shell droplets or thin liquid threads situated in a close vicinity of the channel vertex.

To support this statement, we use the experimental results of [3] where the configurations of liquid bodies where studied for the following pairs: $(\beta, \theta) = (54.7°, 31°)$, $(54.7°, 58°)$, and $(54.7°, 74°)$. The $(\beta, \theta) = (54.7°, 31°)$ pair provided concave columns, the pair $(\beta, \theta) = (54.7°, 58°)$ provided convex columns, and $(54.7°, 74°)$ provided clam-shells. Placing these data onto the phase diagram in Fig. 4.6, we see an excellent match. More experiments are needed to fully examine this phase diagram, especially in the region under the lower limit (the yellow curve).

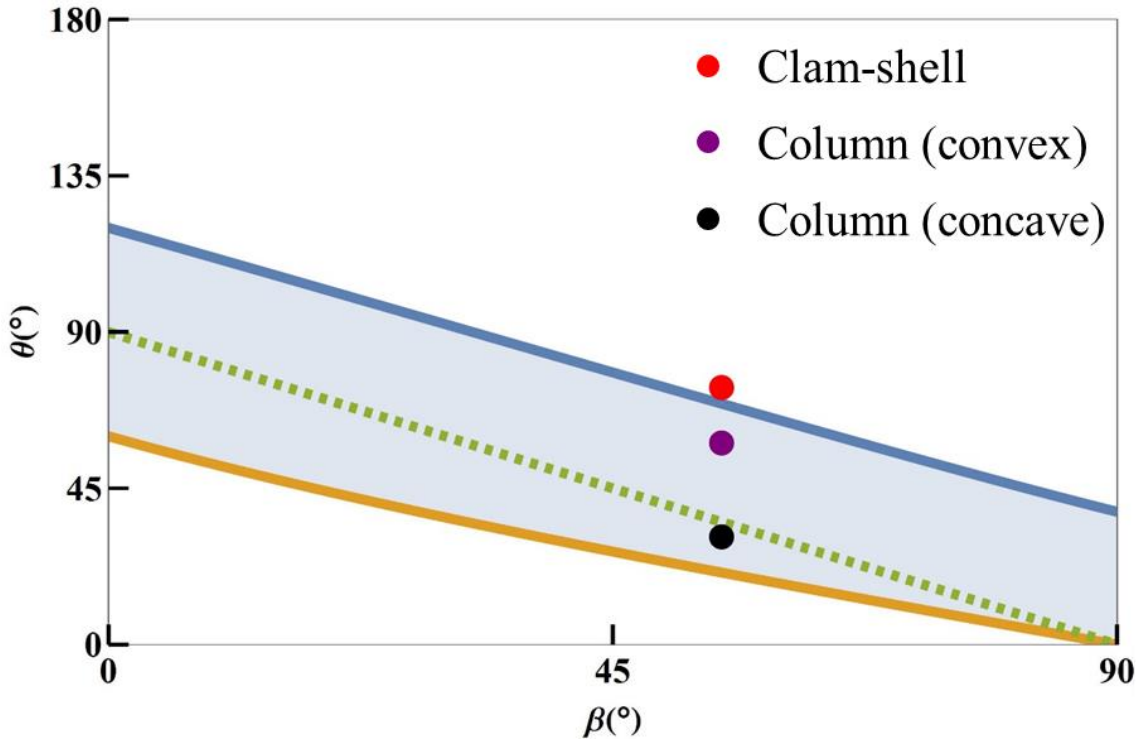

Figure 4.6. The wetting/dewetting phase diagram for the V-shaped channels in terms of contact angle θ and the channel opening angle β. The shaded region describes the wettable channels where the liquid will be form a column with the contact lines pinned at the channel edges, the dashed green line separates the regions of convex (above) and concave (below) columns; the white region describes the non-wettable channels where liquids will form a clam-shell like droplet and liquid threads situated in the vicinity of the channel vertex. The black solid dots are experimentally observed columns and the red solid dots are experimentally observed clam-shells.

4.3 Liquid droplet morphology in the C-shaped channel

The study of V-shaped channels favors the applicability of the Princen theory of the wetting/dewetting transition of liquids in these channels. In this section, we will continue applying Princen's method to study this transition for cylindrical channels, the C-shaped channels. The C-shaped channels are of great interest for many microfluidic applications inspired by biological systems [7-9]. Liquid flow in the C-shaped channels do not exhibit the flow stagnation phenomenon present in the corners of rectangular or triangular micro-channels [10]. With the development of polymer molding with

polydimethylsiloxane (PDMS), a simple and inexpensive reverse molding method is designed to fabricate the micro-scale C-shaped channels enabling studies of wetting phenomena experimentally.

4.3.1 Experimental section

4.3.1.1 PDMS C-shaped channel fabrication through reverse polymer molding

The C-shaped channels with different opening angles were fabricated through the reverse polymer molding with PDMS using the following the experimental protocol.

The reverse molds for fabricating the C-shaped channels were constructed by embedding the capillary tube into a wax substrate. A certain amount of paraffin wax (Carolina Biological Supply Company) was melt at 80 °C in glass Petri dish, and the capillary tube with a diameter of 1.7 mm was horizontally embedded into the liquid wax. The volume of the molten wax was controlled to make sure the capillary tube touches the bottom of the Petri dish, with a portion of capillary tube sticking out from the wax-air interface. By melting different amount of wax, different portion of the capillary will be exposed, offering a possibility to fabricate C-shaped channels with different opening angles. Then the wax/capillary mold was solidified at room temperature for 30 minutes, and then the solid wax menisci, which were formed by liquid wax wetting the wall of capillary tube, were carefully removed with a sculpture knife to form a flat surface near the capillary tube region. Fig. 4.7(A) shows the schematic of the final mold.

SYLGARD® 184 Silicone Elastomer Base was mixed with SYLGARD® 184 Silicone Elastomer Curing agent by mass ratio 10:1. After fully mixing and getting rid of bubbles in a plastic petri dish, the mixture was poured on the wax/capillary mold, and cured

at room temperature for 24 hours, Fig. 4.7(B). After curing, the solidified PDMS layer was carefully detached from the mold and the final C-shaped channel was obtained, Fig. 4.7(C).

Through this method, several types of C-shaped channels, with different opening angles ranging from 0° to 360°, were successfully fabricated. Figs. 4.7(D)-(G) show the cross sections of several examples.

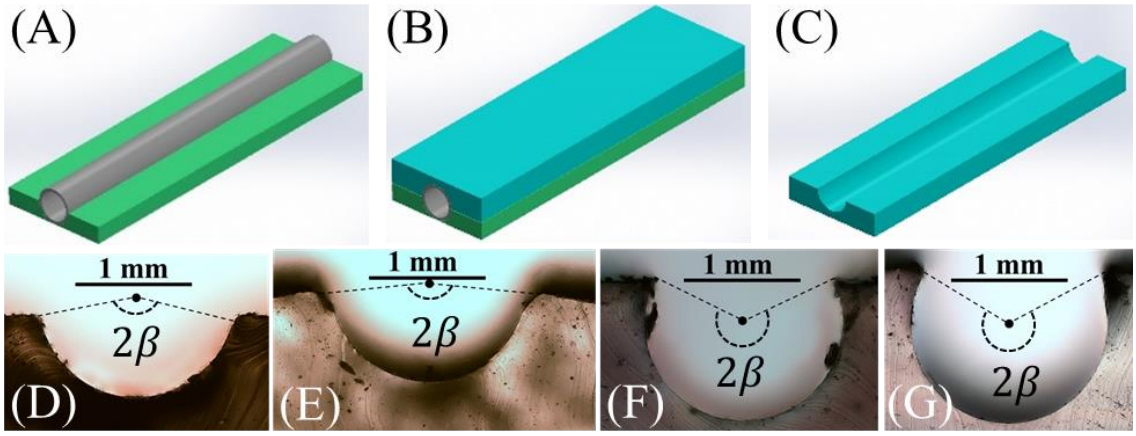

Figure 4.7. PDMS C-shaped channels fabrication through reverse polymer molding. (A)-(C) The 3-steps of the channel fabrication process, showing (A) the mold made of the wax mold (green) with embedded tube, (B) this mold was covered with a PDMS layer, and (C) the fabricated PDMS C-shaped channel after PDMS curing. (D)-(G) Cross sections of the fabricated PDMS C-shaped channels with different opening angle: (D) 2β = 158°, (E) 2β =170°, (F) 2β = 220°, (G) 2β = 240°.

4.3.1.2 Contact angle control through silanization

The PDMS surface has low surface energy, so that the normal wetting liquid cannot wet it. In order to permanently increase the surface energy of the channel surface, the method of chemical vapor deposition (CVD) of silanes on the substrate surface was chosen to conduct the surface modification.

Each type of the long channels fabricated above were cut into 4 pieces of short channels. The cutted channels were placed into the plasma instrument on the highest setting (PLASMA CLEANER/STERILIZER, Harrick Scientific Corp, PDC-32G, Input power

100 W, Highest settings: 720V DC, 25 mA DC, Applied to 18 W) for fifteen minutes to activate the surface. After the plasma treatment, they were put into three 50 ml VWR® Polypropylene Centrifuge Tubes with silanes present, and then left for CVD overnight in order to graft silanes to the surface of the PDMS pieces from the vapor phase. Four types of silanes were used to modify the four pieces of channels of each type to obtain different surface energies. The following silanes were applied: (3-glycidyloxypropyl)trimethoxysilane, 3-Methacryloxypropyltrimethoxysilane, Trimethylethoxysilane, n-octyldmethylchlorosilane and (heptadecafluoro-1 1 2 2-tetrahydrodecyl)trimethoxysilane.

After the surface modification, the contact angles between the channels and the wetting liquids, OMNIPAQUE^{TM} (iohexol) Injection and glycerin (surface tensions are 80 mN/m and 64 mN/m, respectively), were measured on the flat surface using Kruss Drop Shape Analyzer (DSA 10) with the 'Tangent method 1'. The results are shown in Table 4.1. Each result is averaged by five measurements and the error bar represents the standard deviation of these measurements.

Table 4.1. Contact angle between the wetting liquids and the C-shaped channels modified with different silanes. Iohexol droplets inside the C-shaped channels are marked as : “IG” for the (3-glycidyloxypropyl)trimethoxysilane coating; “IM” for the 3-Methacryloxypropyltrimethoxysilane coating; “IT” for the Trimethylethoxysilane coating; “IO” for the n-octyldmethylchlorosilane coating; “IH” for the (heptadecafluoro-1 1 2 2-tetrahydrodecyl)trimethoxysilane coating; Glycerin columns inside the C-shaped channels are marked as: “GG” for the (3-glycidyloxypropyl)trimethoxysilane coating;“GM” for the 3-Methacryloxypropyltrimethoxysilane coating; “GT” for the Trimethylethoxysilane coating; “GO” the n-octyldmethylchlorosilane coating; “GH” for the (heptadecafluoro-1 1 2 2-tetrahydrodecyl)trimethoxysilane coating;

	Iohexol		Glycerin	
	Advancing contact angle	Receding contact angle	Advancing contact angle	Receding contact angle
(3-glycidyloxypropyl) trimethoxysilane	23±5°(IG)	15±3°(IG)	45±3°(GG)	35±2°(GG)
3-Methacryloxypropyl trimethoxysilane	38±4°(IM)	26±2°(IM)	74±5°(GM)	52±3°(GM)
Trimethylethoxysilane	48±4°(IT)	38±3°(IT)	88±4°(GT)	64±3°(GT)
n-octyldmethyl chlorosilane	68±5°(IO)	55±3°(IO)	93±5°(GO)	74±3°(GO)
(heptadecafluoro-1 1 2 2-tetrahydrodecyl) trimethoxysilane	84±4°(IH)	63±3°(IH)	106±4°(GH)	80±4°(GH)

4.3.1.3 3D liquid morphology imaging through X-Ray Micro-CT

An analysis of the shapes of liquid bodies in the C-shaped channels were studied with the Bruker Skyscan 1176 X-Ray Micro-CT scanner with the 9 μm resolution. The liquid was injected into the channel with a syringe and after waiting for five minutes to let the liquid spread and acquire an equilibrium configuration, the channel with the liquid body was taped to a semi-cylindrical stage made of a plastic foam transparent to the X-ray. The stage was placed onto a semi-cylindrical holder inside the scanner so that the flat surface of the PDMS chip was oriented horizontally and ensuring that the C-shaped channel was sitting at the holder center. The filter, voltage and current were selected based on the

wetting liquid used. No filter, 90kV voltage, and 276 µA current were used for imaging the iohexol droplets (OMNIPAQUE^{TM} Injection). The 0.2 mm thick aluminum filter, 65 kV voltage, and 383 µA current were set for imaging glycerin droplets. NRecon reconstruction software were employed; the 3D droplet configurations were viewed with CTVox and the cross sections were acquired with DATAVIEWER. A series of the 3D images of liquid bodies and their 2D cross-sections are shown in Fig. 4.8. To distinguish the original gray image of the drop, the PDMS substrate is colored in pink. The dashed lines in Figs. 4.8 (B), (D) and (F) specify the channel edge. The increase and decrease of the cross-sectional area of liquid bodies in Fig. 4.8 (G) is almost mirror symmetric with respect to the area maximum indicating that the liquid bodies are mirror symmetric with respect to this cross-section. Moreover, the radius of cross-sectional meniscus for the columns remains almost constant except of the very ends where it gradually decreases.

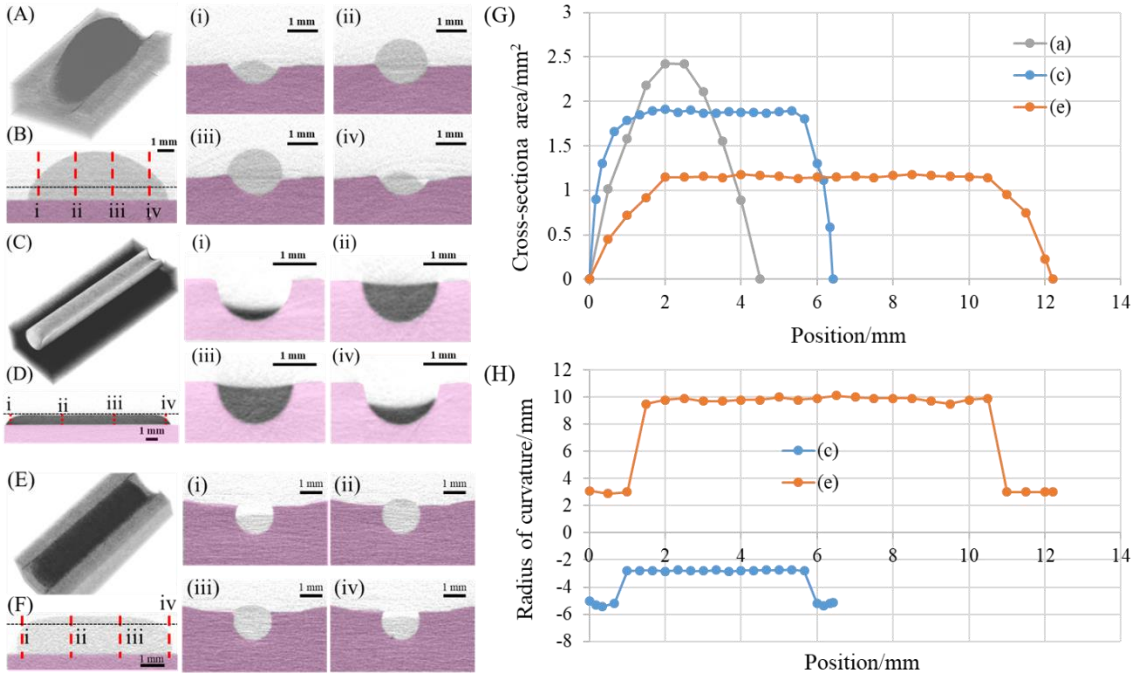

Figure 4.8 The 3D configurations of liquid bodies and their 2D cross-sections in the C-shaped channels. (A) A clamshell glycerin droplet in the C-shaped channel with opening angle $2\beta = 158°$ and contact angle $\theta = 88°$. (B) Side view of the clamshell. The cross-sections of the clam-shell at positions (i), (ii), (iii), and (iv) are shown in separate images (i), (ii), (iii), and (iv) on the right. (C) An iohexol column in the C-shaped channel with opening angle $2\beta = 170°$, and the contact angle $\theta = 38°$. (D) Side view of the liquid column. The cross-sections of the column at positions (i), (ii), (iii), and (iv) are shown in separate images (i), (ii), (iii), and (iv) on the right. (E) A glycerin column in the C-shaped channel with opening angle $2\beta = 220°$, and the contact angle $\theta = 93°$. (F) Side view of the liquid column. The cross-sections of the column at positions (i), (ii), (iii), and (iv) are shown in separate images (i), (ii),(iii), and (iv) on the right. (G) Dependence of the area of cross-sections of the clamshell in (A) and columns in (C) and (E) on position along the channel. (H) Dependence of the radius R of meniscus in cross-sections of columns in (C) and (E) on position along the channel. The radius is considered positive when menisci are concave as those in (D) (i)-(iv) and it is considered negative when menisci are convex as those in (F) (i)-(iv).

An analysis of configurations of liquid bodies of both liquids allows us to suggest that all equilibrium shapes of the observed liquid bodies can be categorized as clamshells (Fig. 4.8 (A)) and liquid columns (Figs. 4.8(C) and (E)). The columns are distinguished from the clamshells by the fact that one of the two principle curvatures goes to zero, i.e. $d^2R/dz^2 = 0$.

Fig. 4.8(A) shows one example of the clam-shell droplet, which was formed by glycerin in the PDMS channel with opening angle of 158°, and forming the 88° contact angle with the channel wall. Figs. 4.8(B) shows the side view of the liquid body. Several cross-sections of the droplet were made at different positions perpendicularly to the channel axis (Figs. 4.8(B) (i)-(iv)) along the column. The measured area of each cross-section as a function of position is shown in Fig. 4.8(G). Monotonous increase and then decrease of the cross-sectional area from one end of the droplet to another indicates a typical feature of a clamshell. The increase and decrease is almost mirror symmetric with respect to the drop maximum.

Fig. 4.8(C) shows one example of a columnar morphology. The column was formed by OMNIPAQUE^{TM} (iohexol) Injection in the PDMS channel had opening angle of 170°, and forming the 38° contact angle with the channel wall. Fig. 4.8(D) shows the side view of the liquid body. Similarly, several cross-sections at different positions along the column (Figs. 4.8(D) (i)-(iv)) were made, and the area of cross-sections (Fig. 4.8(G)) and radius of curvature of the liquid/air interface (Fig. 4.8(H)) were measured. At the two ends of the liquid column, the cross-sectional crescent menisci (i) and (iv) are supported by the contact lines sitting inside the channel. As one moves from the ends to the column center, the cross-sectional area gradually increases to a certain value and remains constant over the remaining length of the liquid column; within this region of constant cross-sectional area, the radius of curvature of the liquid/air interface remains almost the same.

Intuitively, when the drop makes a contact angle larger than 90° with the flat surface of the PDMS chip, the liquid in the C-shaped channels is expected to form a clam-shell. Surprisingly, with the contact angle 93° and the channel opening angle 220°, the drop of glycerin forms a column, as shown in Fig. 4.8(E). Figs. 4.8(F) shows the side view of the liquid body. The cross-section profiles at different positions along the column (Figs. 4.8(F) (i)-(iv)) and cross-sectional area and radius of curvature of the liquid/air interface are shown in Fig. 4.8(G) and (H). This liquid column is very similar to the one described in Fig. 4.8(E). However, at the two ends the contact angle is clearly larger than 90°.

After examining all column morphologies formed in the experiments, it was found that the channel walls were always fully covered by the liquid, meaning that the contact lines at the middle regions of the column were pinned by the channel edge instead of

locating inside the channel. Fig. 4.9 shows several examples of these observations deserving a special theoretically analysis in Section 4.3.2.

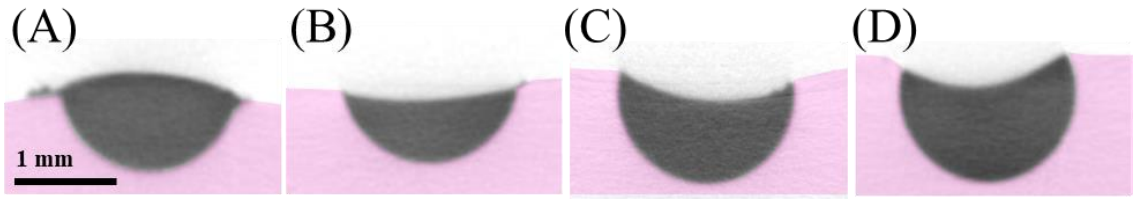

Figure 4.9. Cross sections at the middle region of the liquid columns formed with (A) contact angle 65° and channel opening angle 158°; (B) contact angle 38° and channel opening angle 158°; (C) contact angle 38° and channel opening angle 220°; (D) contact angle 48° and channel opening angle 240°.

The observed shapes of liquid bodies are summarized in Fig. 4.10. The phase diagram shows the data points for clam-shells and columns. To interpret this diagram theoretically, we need to find the criteria separating clam-shells from columns.

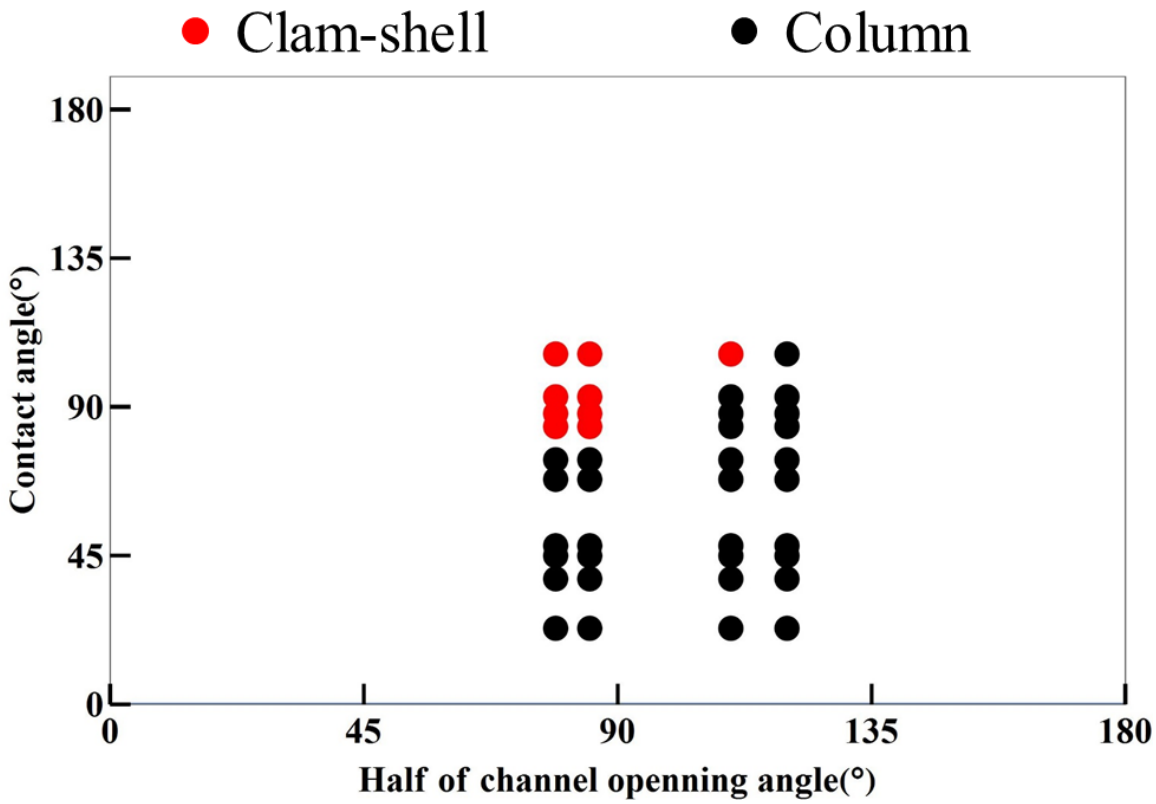

Figure 4.10. The experimental phase diagram for the clam-shells/columns.

4.3.2 Analysis of liquid column morphology in linear C-shaped channels: the modified Princen theory

To calculate the shape of a liquid body in the C-shaped channels, we proposed the following three-dimensional model based on the modified Princen theory in Fig. 4.11, which has been proved in the study of the V-shaped channels in Section 4.2. The C-shaped channel is infinitely long and its cross-section is an arc with radius r and center angle 2β, which is also the channel opening angle, Fig. 4.11(A). The liquid is supported by the internal wall of the channel, so the cross section of the liquid/solid (channel bottom) interface is also an arc with radius r. The clam-shell to column transition is explained by the analysis of forces causing the drop to spread. We will use the first integral of the Laplace equation representing the force balance and, in parallel, directly use the free body diagram on the column morphology.

The criterion for the clam-shell/column transition is associated with the condition of existence of the solution for the force balance equation written for the columns. The radius of the channel we used $r = 0.85$ mm is typically much smaller than the capillary length, $l_c = \sqrt{\sigma/\rho g}$, where ρ is the saliva density, g is the acceleration due to gravity, $l_c = 2.26$ mm for glycerin and $l_c = 2.31$ mm for OMNIPAQUE^{TM} (iohexol) Injection. Thus, the inequality $r/\,l_c < 1$ holds true hence the gravity can be neglected suggesting that the pressure inside the liquid columns should be constant.

In the Cartesian system of coordinates (X, Y, Z), where the channel is parallel to the Z-axis, Fig. 4.11(C), the profile $Z = h(X, Y)$ describes the entire liquid meniscus in the channel. The free body diagram for the column is built up by making an imaginary cut

perpendicularly to the channel axis Z in the middle of the column. One half of the column is then replaced with an equivalent system of forces acting in the Z-direction parallel to the channel long axis:

$$F_{AL} + F_{SL} - F_{SA} - F_P = 0, \tag{4.4}$$

where F_{AL} is the force due to surface tension at the air/liquid interface; F_{SL} is the force due to surface tension σ_{SL} at the solid/liquid interface; F_{SA} is the force due to surface tension σ_{SA} of the solid/air interface; F_P is the pressure resultant acting perpendicularly to the cross-section of area in the Z-direction. In this model, we do not restrict the contact lines to be pinned by the edge, but include the scenario that the contact lines can also locate inside the channel. Therefore, we need to discuss different scenarios separately.

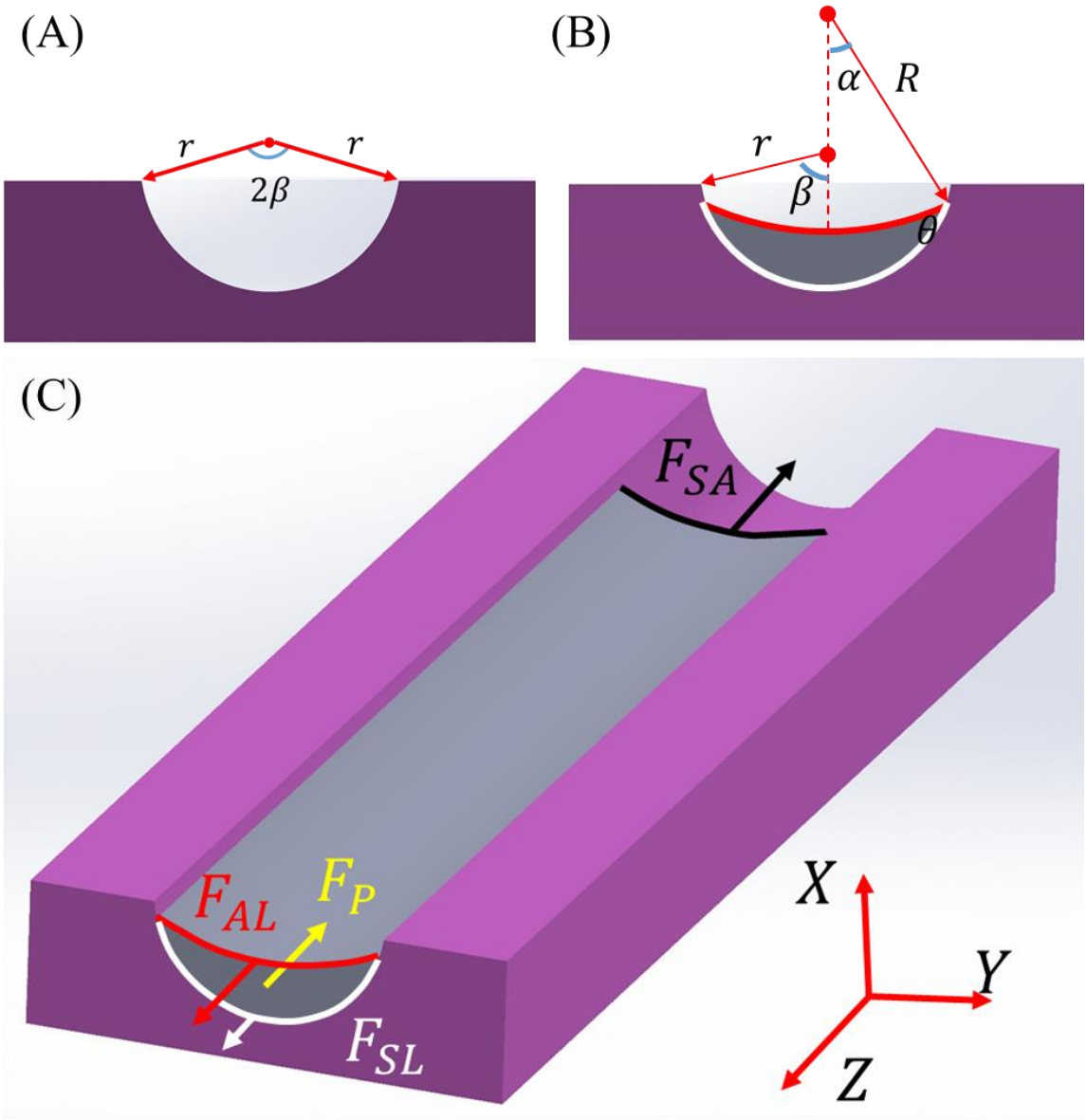

Figure 4.11. Model describing the column liquid morphology in a C-shaped channel. (A) Schematic showing the cross section of the C-shaped channel. (B) Schematic showing the cross section of the liquid column in the C-shaped channel. (C) Schematic showing the free body diagram.

4.3.2.1 Contact lines stay inside the channel

When the contact lines of the column are sitting inside the channel, the air/liquid interface should approach the C-wall at the contact angle θ. Depending on the position of the contact lines and the contact angle, the liquid may form concave or convex menisci as

shown in Fig. 4.12(A)-(D). All these cases need to be calculated separately. However, the study of the V-shaped channels suggests the stability analysis of these menisci can be made for either convex or concave case and the results can be applied for the other case as well. We consider a concave column ($\alpha \in [0,90°]$) formed in a C-shaped channel ($\beta \in (0,90°)$), Fig. 4.13. We have confirmed the results below for other cases as well.

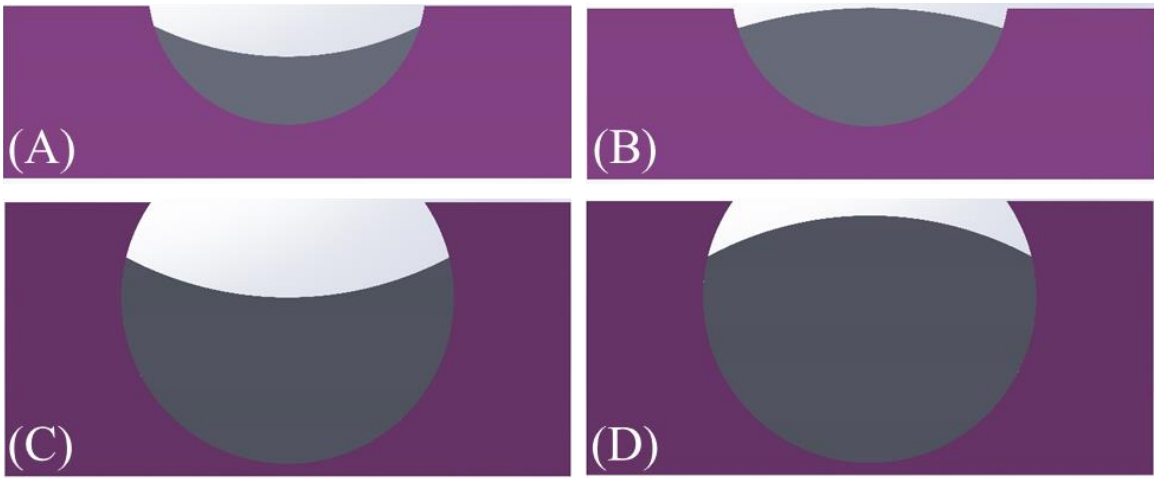

Figure 4.12. Cross-sections of different column morphologies with contact lines inside the C-shaped channel. (A) Concave, less than semi-circle; (B) Convex, less than semi-circle; (C) Concave, more than semi-circle; (D) Convex, more than semi-circle.

The schematic is shown in Fig. 4.13(A), where $\overline{AO_1} = R, \overline{AO_2} = r$. Therefore the forces $F_{AL} = \sigma \cdot \widehat{ABC} = 2\alpha\sigma R$, where σ is the interfacial tension of the liquid/air pair; $F_{SL} = \sigma_{SL} \cdot \widehat{ADC} = 2(\theta + \alpha)\sigma_{SL} r$, where σ_{SL} is the interfacial tension of the solid/liquid pair and θ is the contact angle between the liquid and the channel wall; $F_{SA} = \sigma_{SA} \cdot \widehat{ADC} = 2(\theta + \alpha)\sigma_{SA} r$, where σ_{SA} is the interfacial tension acting over the solid/air interface; and $F_P = PA_{\mathrm{ABCD}}$, where $P = -\sigma/R$ is pressure in the liquid column with respect of pressure in atmosphere and $A_{\mathrm{ABCD}} = (\theta + \alpha)r^2 - \alpha R^2 + Rr \sin\theta$ is the cross sectional area of the liquid column. R and r are related by the sine law in ΔAO_1O_2, $\frac{R}{r} = \frac{\sin(\theta+\alpha)}{\sin\alpha}$.

Employing the Young-Laplace equation, $\sigma_{SA} - \sigma_{SL} = \sigma \cos\theta$ and substituting the forces with these expressions, eq. (4.4) can be simplified to:

$$\alpha\left(\frac{\sin[(\theta+\alpha)]}{\sin\alpha}\right)^2 + (\sin\theta - 2(\theta+\alpha)\cos\theta)\left(\frac{\sin[(\theta+\alpha)]}{\sin\alpha}\right) + (\theta+\alpha) = 0. \quad (4.5)$$

Therefore, an equilibrium liquid column with the contact lines staying inside the C-shaped channel, must satisfy eq. (4.5). The left hand side of eq. (4.5), $f(\alpha, \theta)$, is a function of the contact angle θ and half of the center angle of the liquid/air interface α, and does not depend on the channel opening angle β. Plotting it as a function of α and θ, and finding where it intersects with the plane $f(\alpha, \theta) = 0$, one can determine equilibrium conditions of the column. So, we plot it within the range of physically meaningful α and θ, where $\alpha \in (0°, 90°)$ and $\theta \in (0°, 90°)$, in Fig. 4.13(B). Surprisingly we observe that $f(\alpha, \theta)$ never intersect the zero plane, suggesting that the liquid column cannot reach the equilibrium state in this scenario. The liquid column formed in this scenario will transform into the clam-shells.

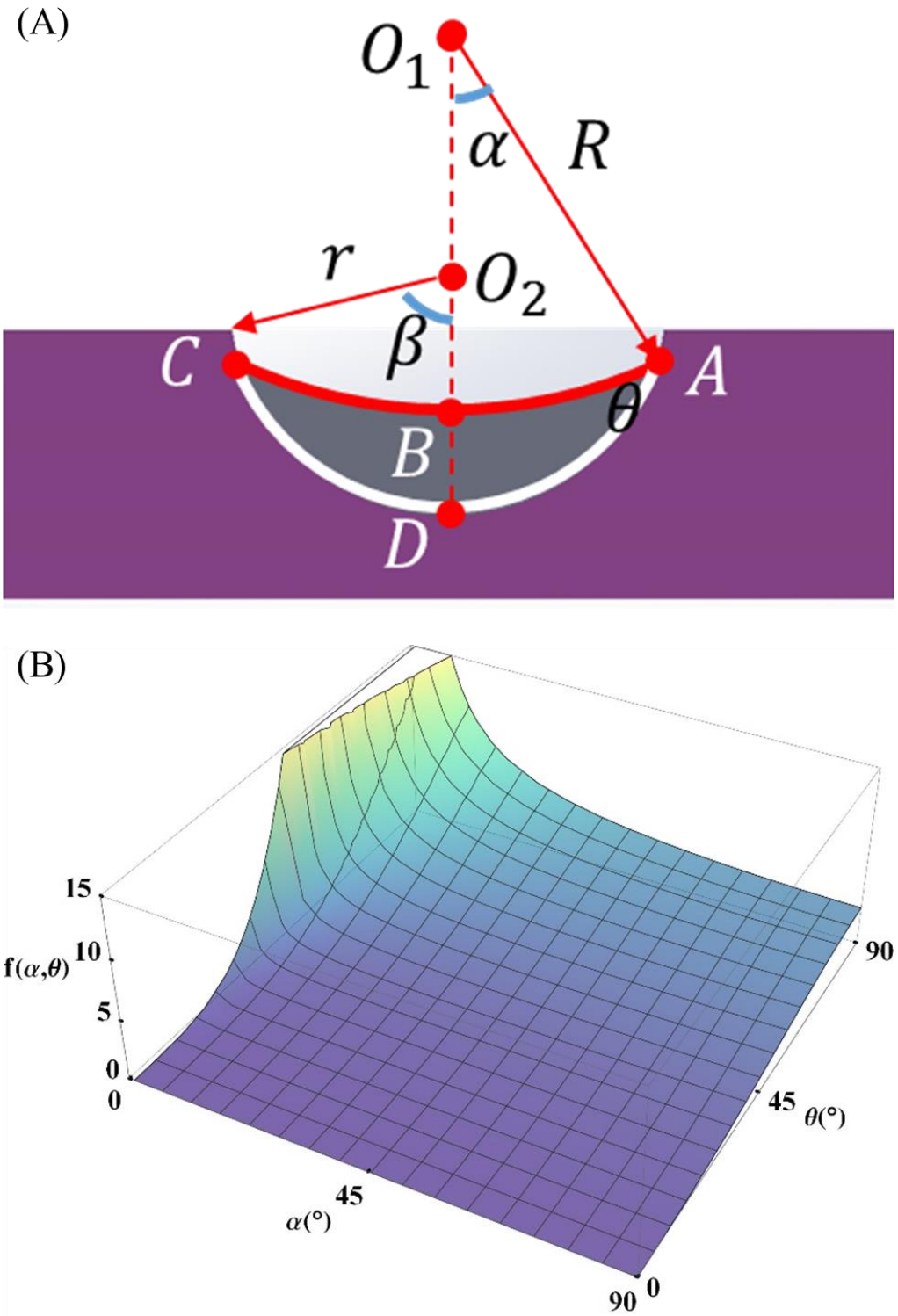

Figure 4.13. An example of liquid column formed in C-shaped channel with contact lines staying inside, $\alpha \in [0°, 90°]$, $\theta \in [0°, 90°]$ and $\beta \in (0°, 90°)$. (A) Schematic of column cross-section showing the geometry. (B) Plot of $f(\alpha, \theta)$ as a function of α and θ.

4.3.2.2 Contact lines are pinned at the channel edges

When the contact lines of the column at the middle region are pinned by the channel edges, the angle that the liquid contacts the channel are not defined, and therefore, can possibly range from 0° to 360° and form concave or convex column as shown in Fig. 4.14(A) and (B), respectively. To distinguish between the two cases, the angle α is defined as positive for the concave meniscus and negative for the convex meniscus.

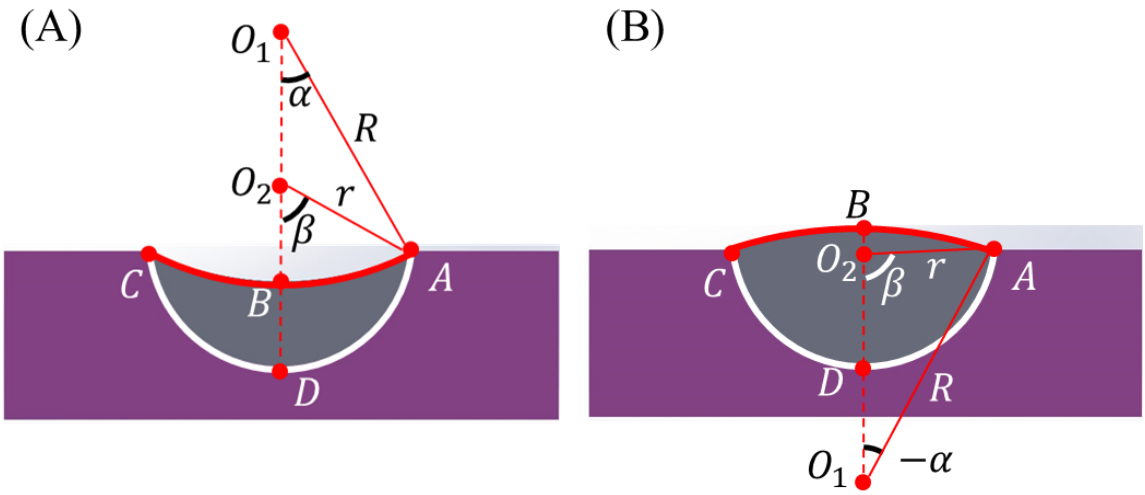

Figure 4.14. Schematic of meniscus cross-section when its contact line is pinned at the edges of the C-shaped channel and the air/liquid interface is (A) concave and (B) convex.

Therefore, the component forces in eq. (4.4) can be calculated as: $F_{AL} = \sigma \cdot \widehat{ABC}$, where σ is the interfacial tension of the liquid/air pair and $\widehat{ABC} = \pm 2\alpha R\sigma$ for concave and convex meniscus respectively; $F_{SL} = \sigma_{SL} \cdot \widehat{ADC}$, where σ_{SL} is the interfacial tension of the solid/liquid pair and $\widehat{ADC} = 2\beta\sigma_{SL}r$; $F_{SA} = \sigma_{SA} \cdot \widehat{ADC}$, where σ_{SA} is the interfacial tension acting over the solid/air interface; and $F_P = PA_{\mathrm{ABCD}}$, where P is pressure in the liquid column with respect of pressure in atmosphere and A_{ABCD} is the cross sectional area of the liquid column, where $P = \mp\sigma/R$ for concave and convex meniscus respectively and

$A_{\mathrm{ABCD}} = \beta r^2 - \alpha R^2 + Rr\sin(\beta - \alpha)$. The relation $\frac{R}{l} = \pm\frac{\sin\beta}{\sin\alpha}$ for concave and covex meniscus respectively hold true according to sine law in ΔAO_1O_2.

Employing the Young-Laplace equation, $\sigma_{SA} - \sigma_{SL} = \sigma\cos\theta$ and substituting the forces with these expressions, eq. (4.4) can be simplified to the same equation for both concave and convex cases:

$$\theta = \arccos\left[\frac{\alpha\left(\frac{\sin\beta}{\sin\alpha}\right)+\beta\left(\frac{\sin\alpha}{\sin\beta}\right)+\sin(\beta-\alpha)}{2\beta}\right]. \tag{4.6}$$

4.3.2.3 Phase diagram of liquid morphology in C-shaped channels

In order to have equilibrium liquid column morphology with contact lines pinned by the edges of the C-shaped channel, eq. (4.6) must be satisfied. Therefore, θ is plotted as a function of α and β in Fig. 4.15. Contact angle θ ranges from 0° to 180°, half of the channel opening angle β ranges from 0° to 180°, and half of the center angle of the liquid/air interface α ranges from -180° to β because α is always smaller than β.

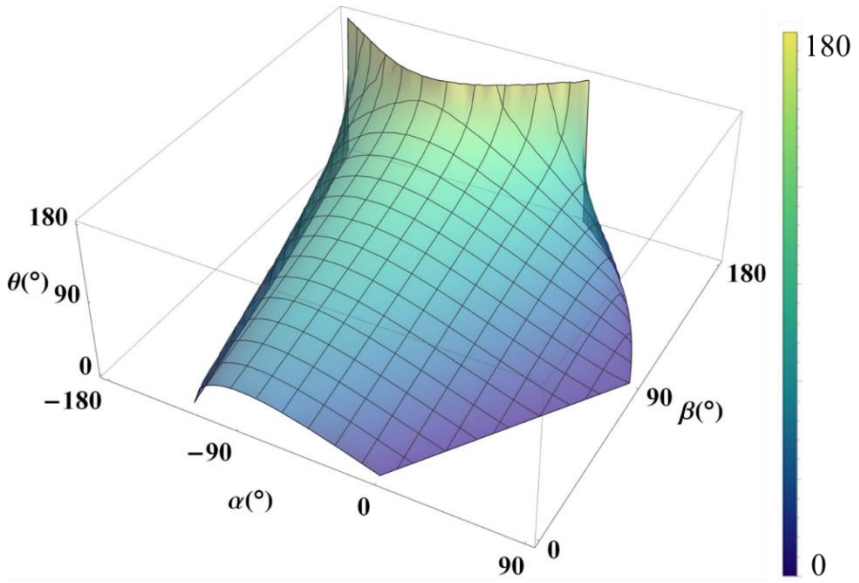

Figure 4.15. Plot of contact angle θ as a function of half of the center angle of the liquid/air interface α and half of the channel opening angle β.

As shown in Fig. 4.15, the equilibrium column with contact lines pinned by the channel edges can be formed inside the C-shaped channel. Furthermore, several cross sections parallel to the α - θ plane on this surface are taken by setting β equals to the respective constants. These cross sections are shown in Fig. 4.16.

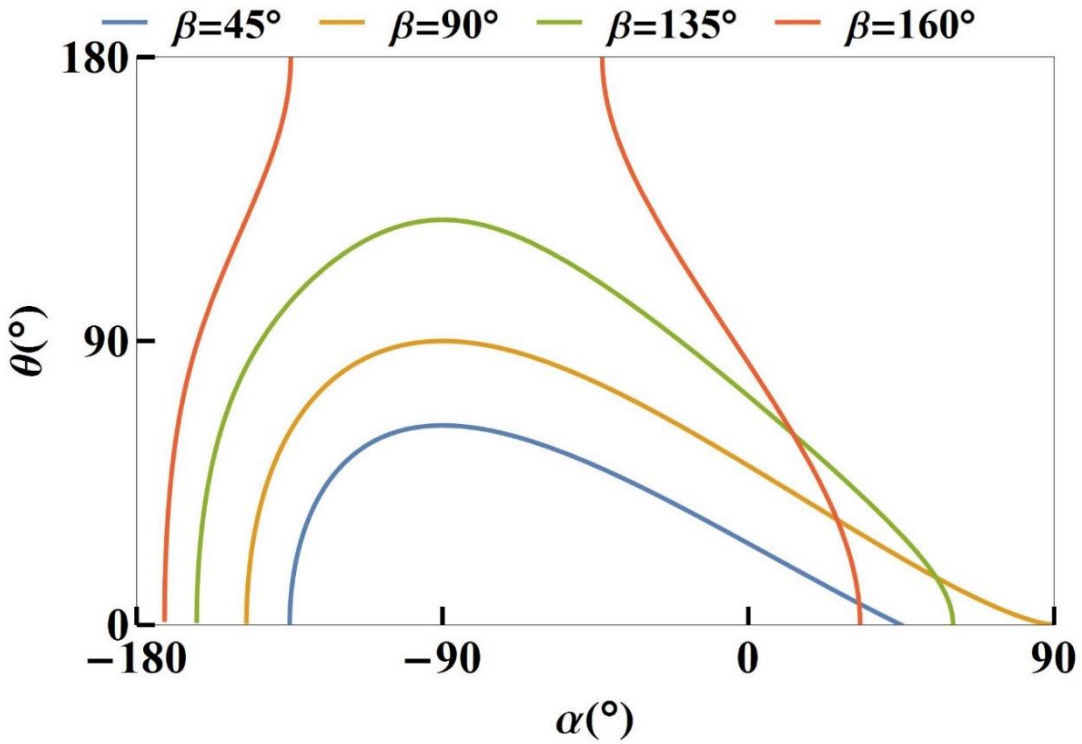

Figure 4.16. Cross sections of Fig. 4.15, which are parallel to the α - θ plane.

At $\beta = 45°, 90°, 135°$, the cross sections always form a maximum. Within this region, one value of θ corresponds to two values of α, which means that two different column morphologies with the same contact angle can be formed. The one with smaller value of $\alpha \in (-180°, -90°)$ are more convex than that with a larger $\alpha \in (-90°, 90°)$ value. The columns with $\alpha \in (-180°, -90°)$ is proved unstable to perturbations, and thus we will not consider it further [6]. Only columns with $\alpha \in (-90°, 90°)$ will be discussed.

The maximum value of θ is found to be the boundary separating the clam-shell and column regions. This maximum is different for different β. In order to find this maximum, the first derivative of θ was taken with respect to α based on eq. (4.6):

$$\frac{\partial\theta}{\partial\alpha} = -\frac{-\cos(\theta-\beta)+\beta\cos\alpha\csc\beta+\csc\alpha\sin\beta-\alpha\cot\alpha\csc\alpha\sin\beta}{2\beta\sqrt{1-\frac{(\beta\csc\beta\sin\alpha-\sin(\alpha-\beta)+\alpha\csc\alpha\sin\beta)^2}{4\beta^2}}}. \quad (4.7)$$

The critical α_c where θ reaches the maximum was calculated by setting $\frac{\partial\theta}{\partial\alpha} = 0$. And it is found that α_c always equals to -90°.

At $\beta = 160°$, the cross sections are no more a continuous curve but consists of two separated curves with θ ranging from 0° to 180°. The critical β_c separating these two cases, based on Fig. 4.16, can be obtained by setting $\theta = 180°$ and $\alpha = -90°$ and solving eq. (4.6), and it is $\beta_c = 149.6°$. In this case, all the values of θ ranging from 0° to 180° correspond to two α values. With the same argument discussed previously, the less convex columns with larger α value are more stable. This is a very interesting discovery which suggests that the liquid inside the C-shaped channels with opening angle larger than $2\beta_c$, 299.2°, will always form columns, no matter what the contact angle is.

With equilibrium columns, eq. (4.6) gives a relation among the angles α, β, and θ. Therefore, with two known parameters, this equation can be solved for the third. It can be used to predict the shape of a liquid drop formed in C-shaped channels with known opening angle 2β and contact angle θ, or more importantly characterizing the contact angle θ of C-shaped channels by imaging the drop morphology of the wetting liquid formed in the channels. The experimental protocol can be illustrated with an example in Fig. 4.17.

A drop of the wetting liquid is deposited in the C-shaped channel and spreads freely to reach the equilibrium column. Then, the entire sample is imaged with Micro CT to obtain the 3D profile of the liquid drop. Similar to what we did in Fig. 4.8, five cross sections at the middle region of the column are obtained through the image processing, Fig. 4.17(A)-(E). The radius of the channel r, the radius of curvature of the liquid/air interface R, and the length of the opening l_o, marked in Fig. 4.17(F) as an example, are measured based on these cross sections. The angles α, β can be calculated $\alpha = \arcsin\frac{l_o}{2R}$, $\beta = \arcsin\frac{l_o}{2r}$, and then are substituted into eq. (4.6) to calculate the contact angle θ.

We collect all these results categorizing them with respect to the silane type. The contact angle on the flat part of the PDMS chips functionalized with the same silane was measured with Kruss Drop Shape Analyzer (DSA 10) Table 5.1. As shown in Fig. 4.17 (G), the results obtained with these two methods are close to each other proving that the developed theory can be further applied to construct the wetting/dewetting phase diagram for these channels.

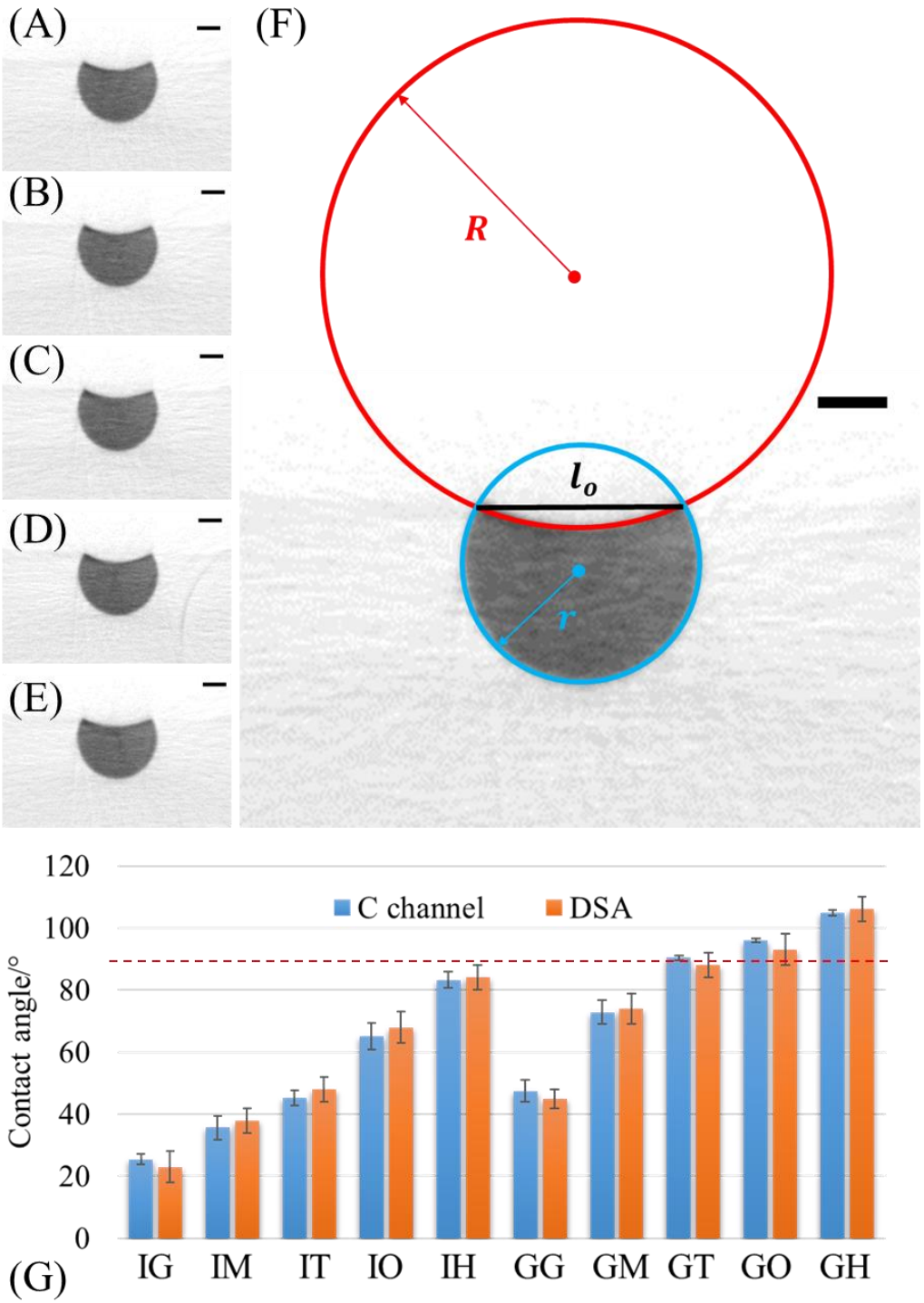

Figure 4.17. (A)-(E). Illustration of the method of measurements of the contact angle of liquid columns. Five cross sections taken at the middle of the liquid column allows one to extract the necessary parameters for the contact angle measurement as shown in (F). The scale bar is 0.5 mm. (G) Comparison of the indirect measurements of contact angle from X-ray images with those from Kruss DSA 10 in Table 4.1.

This method can be even simpler, if the shape of the channel is known. In this case, only the shape of the liquid/air interface is required to be imaged to measure its radius of curvature R, so that one can simply use the optical microscope instead of using Micro CT. This method would give us a new way to characterize the wettability of the micro C-shaped channels, and it allows us to conduct the measurement directly on the channel wall. Furthermore, we would expect this method can be applied to other shaped channels by slightly modifying the model based on the specific geometry.

However, the prerequisite of applying this method is forming the column in the channels. Therefore, it can only be applied to measure a range of contact angles as illustrated in Fig. 4.16.

The wetting/dewetting transition can be associated with the disappearance of columnar solutions satisfying eq. (4.6). Thus, the liquid columns cannot be formed in the C-shaped channels, i.e. the liquid will be gathered into the clamshell droplets. The criterion for disappearance of the columnar solutions is: $\alpha = -90°$. Substituting this α in the first eq. (4.6), we obtain:

$$\theta = \arccos\left[\left(\frac{\pi}{2}\cos\beta\sin\beta - \beta + \cos\beta\sin\beta\right)/(2\beta\sin\beta)\right]. \quad (4.8)$$

In the $\theta - \beta$ plane, eq. (4.8) separates the region of contact angles θ and the channel opening angles β where the liquid columns can exist from the region where only clam-shells can be found, Fig. 4.18. The experimental results from Fig. 4.10 were placed in Fig. 4.18 and compared with the theoretical predictions to illustrate good match. This suggests that the constructed phase diagram fully describes the behavior of liquids in the C-shaped channels.

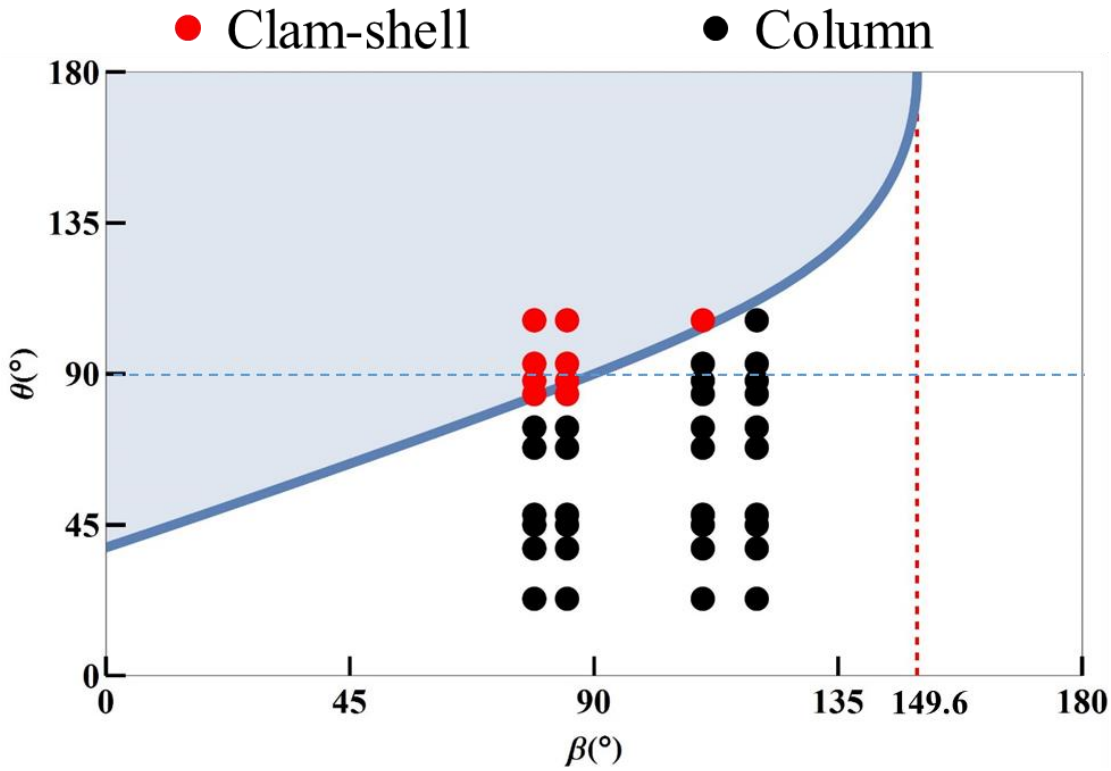

Figure 4.18. The wetting/dewetting phase diagram for the C-shaped channels in terms of contact angle θ and the channel opening angle β. The shaded region above the solid line describes the non-wettable channels where the liquid will be gathered in the clamshells; the region below the solid line describes the wettable channels where liquids will form self-contained columns. The black solid dots are experimentally observed columns and the red solid dots are experimentally observed clamshells.

4.4 Conclusions

In this chapter, the wetting and dewetting of complexly shaped channels is studied by studying the different liquid droplet morphologies formed in the channels. The column, which corresponds to the wetting scenarios, is studied based on the modified Princen theory to obtain the criteria for the wetting/dewetting transition.

First, the column in V-shaped channels is studied in Section 4.2. Different possible scenarios were discussed and the condition for forming the equilibrium column is obtained in eq. (4.3). The phase diagram describing the clam-shell (dewetting) – column (wetting)

transition is constructed in Fig. 4.6. The results are compared with the experimental results in [3] to prove the applicability of the modified Princen theory in studying the wetting and dewetting of complexly shaped channels.

Then the wetting and dewetting of C-shaped channels is systematically studied in Section 4.3. The C-shaped channels with different opening angles are fabricated through the reverse molding method with PDMS, and surface modified through the method of silanization to obtain different contact angle with the wetting liquids. The liquid morphology in the channels is imaged through Micro-CT, and two types of morphology, clam-shell and column, are observed. The clam-shell – column transition is theoretically calculated based on the modified Princen theory. The phase diagram describing this transition is constructed in Fig. 4.26, which shows good agreement with the experimental results.

4.5 References

[1] Seemann, R., Brinkmann, M., Kramer, E.J., Lange, F.F. & Lipowsky, R. 2005 Wetting morphologies at microstructured surfaces. Proceedings of the National Academy of Sciences of the United States of America 102, 1848-1852. (doi:10.1073/pnas.0407721102).
[2] Princen, H.M. 1970 Capillary phenomena in assemblies of parallel cylinders: III. Liquid Columns between Horizontal Parallel Cylinders. Journal of Colloid and Interface Science 34, 171-184. (doi:10.1016/0021-9797(70)90167-0).
[3] Khare, K., Herminghaus, S., Baret, J.C., Law, B.M., Brinkmann, M. & Seemann, R. 2007 Switching liquid morphologies on linear grooves. Langmuir 23, 12997-13006. (doi:10.1021/la701899u).
[4] Alimov, M.M. & Kornev, K.G. 2014 Singularities of meniscus at the V-shaped edge. Mechanics Research Communications 62, 162-167. (doi: 10.1016/j.mechrescom.2014.10.003).
[5] Langbein, D.W. 2002 Capillary Surfaces: Shape — Stability — Dynamics, in Particular Under Weightlessness. New York, Springer.
[6] Roy, R.V. & Schwartz, L.W. 1999 On the stability of liquid ridges. Journal of Fluid Mechanics 391, 293-318. (doi:10.1017/s0022112099005352).

[7] Guo, X. & Zhu, R. 2016 Controllable in-situ cell electroporation with cell positioning and impedance monitoring using micro electrode array. Scientific Report 6, 31392. (doi:10.1038/srep31392).
[8] Lee, P.J., Hung, P.J., Shaw, R., Jan, L. & Lee, L.P. 2005 Microfluidic application-specific integrated device for monitoring direct cell-cell communication via gap junctions between individual cell pairs. Applied Physics Letters 86, 223902. (doi:10.1063/1.1938253).
[9] Sabounchi, P., Ionescu-Zanetti, C., Chen, R., Karandikar, M., Seo, J. & Lee, L.P. 2006 Soft-state biomicrofluidic pulse generator for single cell analysis. Applied Physics Letters 88, 183901. (doi:10.1063/1.2195106).
[10] Li, D. 2004 Electrokinetics in Microfluidisc. Amsterdam, Elsevier Academic Press.

CHAPTER V

WETTING AND CAPILLARY EFFECTS ASSOCIATED WITH LEPIDOPTERAN PROBOSCIS

In this chapter, we will study wetting phenomena associated with complexly-shaped natural fibers, Lepidopteran proboscises. We will discuss the physical mechanisms of food uptake from a pool of liquid or from a limited volume of liquid, the capillary and wetting phenomena related to stability of liquid films deposited on proboscis after dipping into a nectar source, and the self-assembly of proboscis after the insect emerges from the pupa.

5.1 Feeding from a liquid pool: unusual behavior of menisci on proboscis

The internal structure of Lepidopteran proboscis has been illustrated with an example of hawkmoth *Manduca sexta* in Fig. 1.2. Macroscopically, the external contour of the proboscis cross-section can be approximated by an ellipse [1-3]. When the butterfly dips proboscis in a liquid pool, the liquid surface deforms to form a meniscus, the contact line of the meniscus on an elliptical cylinder has different heights, lower on the highly curved sides and higher on the flattened sides [4]. Moreover, proboscis has been shown to demonstrate the wetting dichotomy [5]. Namely, when the butterfly submerses just a tip of the proboscis, the meniscus forms an acute contact angle with the proboscis surface

indicating that the surface is wettable by water, i.e. hydrophilic. When the butterfly immerses proboscis deeper in water, at some depth, the meniscus starts to dimple inwardly into the water indicating that the surface becomes nonwettable by water, i.e. hydrophobic. This way, one can identify the *drinking region* where the meniscus forms an acute contact angle [5]. The border line separating the drinking region from the non-drinking region corresponds to the apparent contact angle $\theta_{ap}=90°$ [5].

Remarkably, the dorsal and ventral legular bands are found to be hydrophilic even in the non-drinking region. The surface of the food canal was shown to be hydrophilic as well. It is known that proboscises of the ancient Lepidopterans and of some currently existing moths are not united. Yet these insects are able to drink water. These observations suggested us to look into the mechanism of wetting of these complexly shaped fibers.

Two representative Lepidoptera species, Mornach (*Danaus plexippus*) butterfly and, hawkmoth (*Manduca sexta*) were chosen as the models for these studies. The head was cut off from the insect body with a blade right before the capillary rise experiments. The experimental setup developed in Fig. 2.13 for observing the capillary rise on the ribbon-like fiber was used in this experiment were the ribbon was replaced with the proboscis. The proboscis was immersed in water and its position was controlled by the 3D linear stage (Mitutoyo® Newport 460). The meniscus formed on proboscis was observed from different directions with respect to the dorsal and ventral ligulae by rotating proboscis with the rotation plate.

Fig. 5.1 shows an exemplary image of the meniscus formed on the united proboscis of the monarch butterfly. The horizontal water level shown in the picture was located 5

mm away from the tip. The proboscis length of monarch butterflies was measured to be 20 mm. This meniscus was imaged from the dorsal side of the proboscis. A 500 μm diameter metal wire was placed in the focal plane as a reference. The free horizontal surface of the liquid far away from the proboscis is marked by the black dashed line. The maximum height of meniscus was systematically measured with respect to the horizontal liquid level.

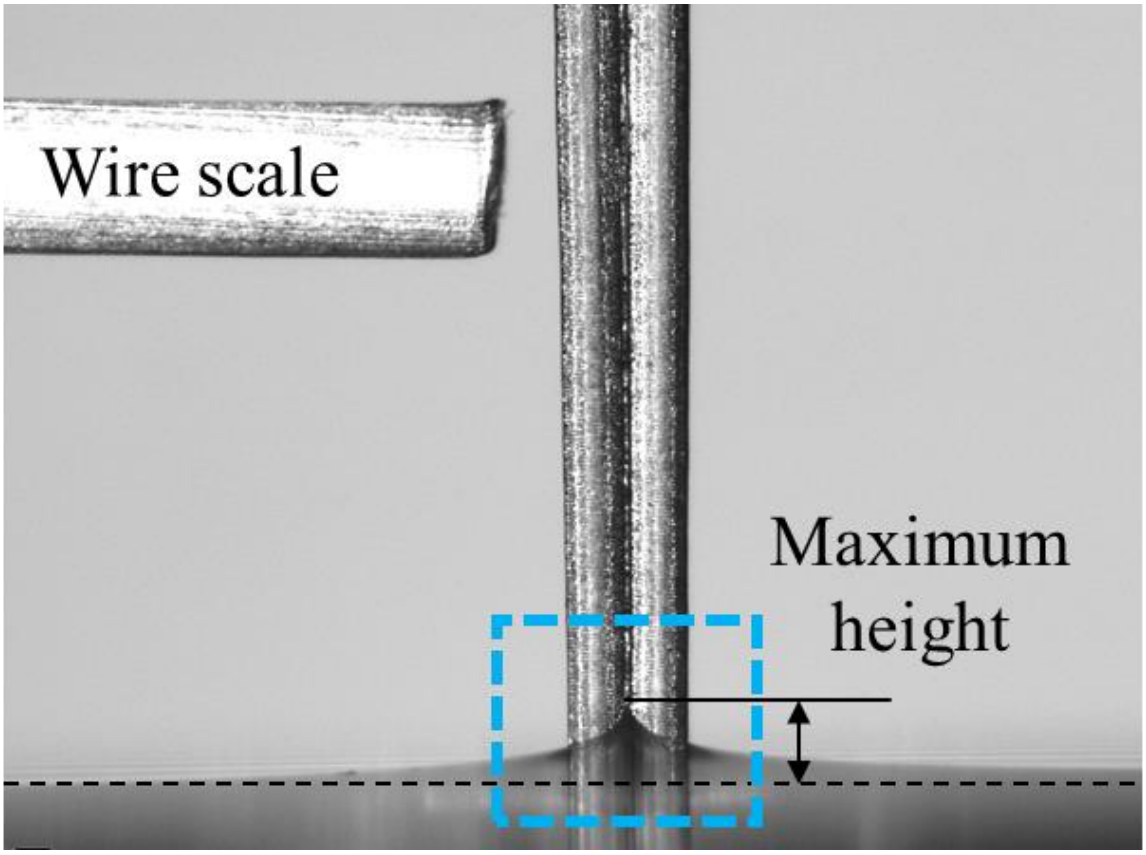

Figure 5.1. An example of water meniscus (boxed) formed on the dorsal side of monarch proboscis.

Fig. 5.2 shows different shapes of menisci obtained by the capillary rise of the water/air interface on the united proboscis monarch butterfly. These menisci were produced by submersing proboscis at different depth and imaging them from different

angles. Figs. 5.2(A), (B) and (C) are taken at positions of 5 mm, 12 mm, and 18 mm with respect to the head, respectively.

At the positions of 5 mm (Fig. 5.2(A)) and 12 mm (Fig. 5.2(B)) away from the tip, the menisci appear cusped at the dorsal and ventral legular bands. As the observer moves from the proboscis tip toward the head, the proboscis diameter increases, yet the menisci remained cusped at these two legular bands. The cusp of meniscus at the dorsal legulae is more developed, its height is greater than that of meniscus at the ventral side. The pictures taken from the side confirms this statement.

Formation of the cusped menisci is mainly caused by the hydrophobic-hydrophilic dichotomy of the proboscis surface. The proboscis surface, except of the dorsal and ventral legulae, are hydrophobic [6], so that it should result in dimpling of the water/air interface. However, because the dorsal and ventral legulae are super hydrophilic, these bands pull the water surface causing its capillary rise; as a result, this pull elevates the entire meniscus and form the cusp. The difference in capillary rise, i.e. the cusp height, suggests that there is a difference in hydrophilicity of the dorsal and ventral legulae. This can benefit the insect. The dorsal legular band is formed by overlapping legulae which form a large number of nanopores from which the liquid can enter the food canal [7]. Therefore, the main purpose of this apparent superhydrophilicity of legulae is to pull the water/air interface ensuring that the created meniscus and its cusp covers the largest possible area of available porous body. The more it covers, the more liquid could be available for the insect to uptake. The ventral legulae, however, are closely packed, so that a much fewer number of nanopores are available for liquid uptake. The capillary rise of the liquid/air interface at the ventral

legulae could also slightly increase the drinking rate, but it is putatively less effective because of the low permeability of the ventral legular band [7].

At the position close to the head (Fig. 5.2(C)), the capillary rise of the water/air interface and the cusp are almost invisible, suggesting that the dorsal and ventral legulae are much less hydrophilic. It is reasonable because in the wild, the insect would not use this region for feeding, but would need to keep it clean; hence making it less hydrophilic or even hydrophobic.

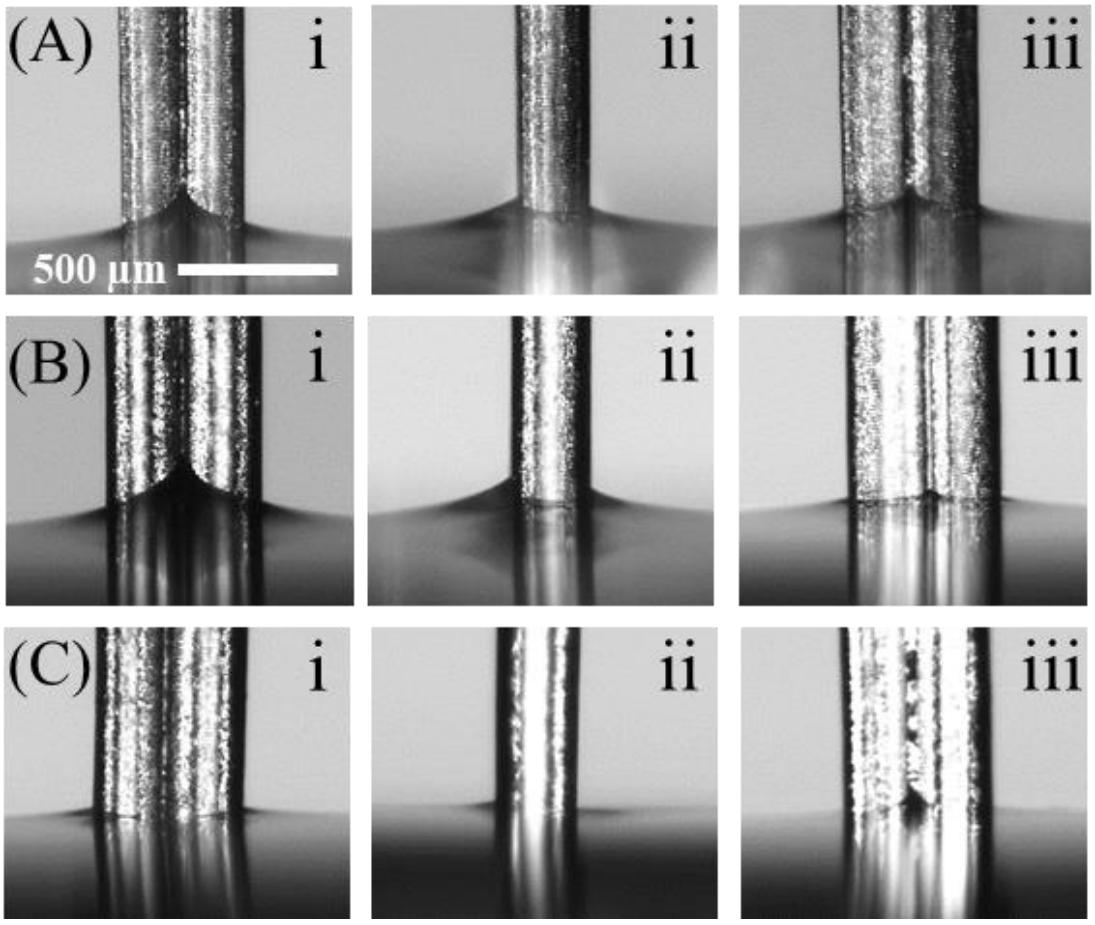

Figure 5.2. The capillary rise of the water/air interface and resulting menisci of on the united proboscis of the monarch butterfly at different positions along proboscis, (A) 5 mm, (B) 12 mm, and (C) 18 mm away from the tip (the entire proboscis is 20 mm) from different viewing angles. The images i, ii, iii in each column show the menisci on the dorsal legulae, side (the dorsal legulae at the left and ventral legulae at the right), and ventral legulae facing the camera, respectively.

The menisci on the united proboscis of hawkmoth look completely different. As shown in Fig. 5.3, the entire surface of hawkmoth proboscis is hydrophilic. Even the proboscis side surface excluding the legulae causes a significant capillary rise of the water/air interface. The dorsal and ventral legulae are proved even more hydrophilic. Vertically dipping the proboscis into water, one observes the water fingers rising up over the side surfaces of the proboscis and the fingers rising along the dorsal and ventral legular bands propagate even further beyond the area of camera focus. The dorsal legulae show a slightly higher hydrophilicity than the ventral legulae which is indicated by a small difference of the shape of menisci.

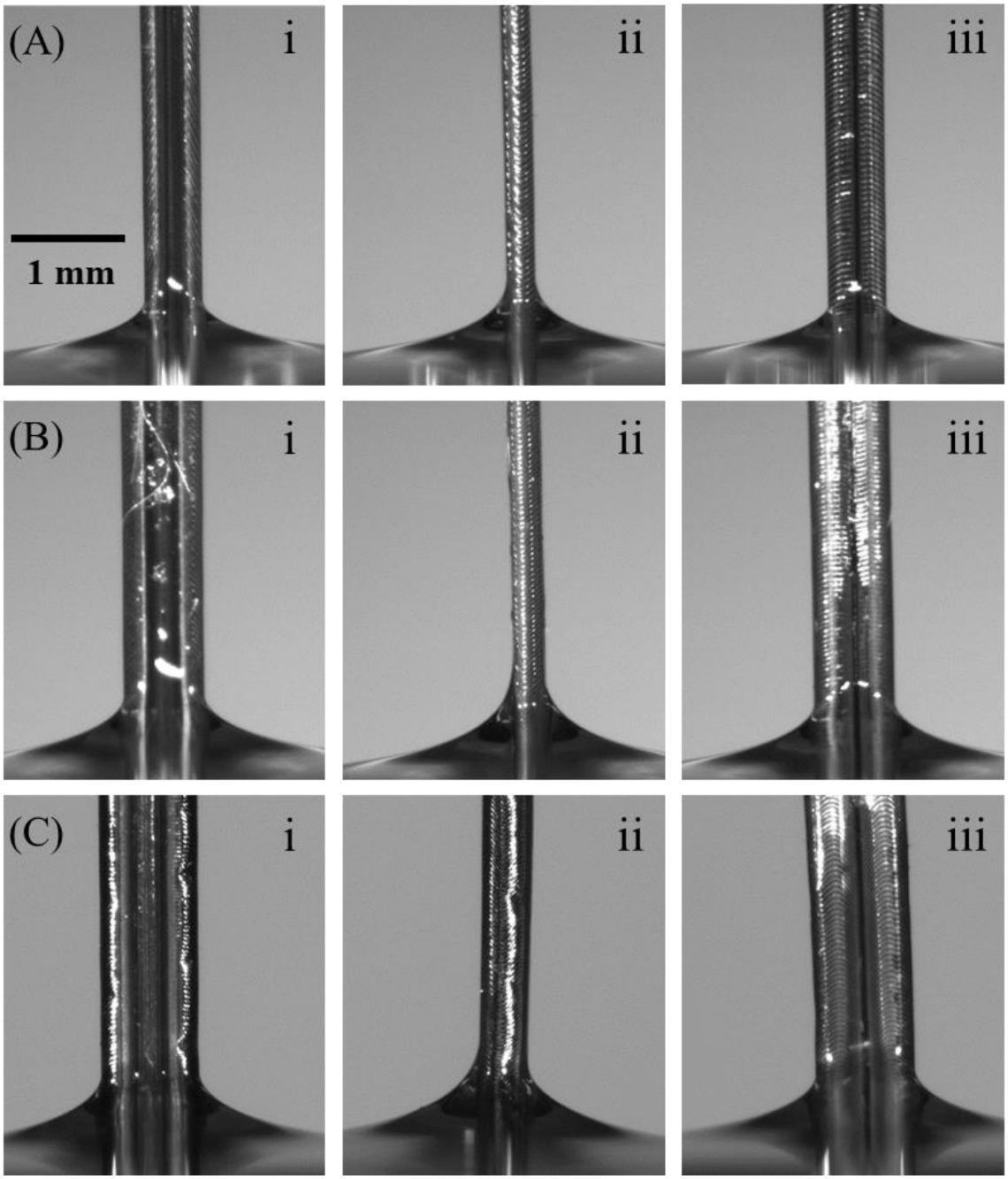

Figure 5.3. The capillary rise of the water/air interface and resulting menisci on the united proboscis of the hawk moth at different positions along proboscis, (A) 1 cm, (B) 4 cm, and (C) 7 cm away from the tip (the entire proboscis length is 8 cm) from different viewing angles. The images i, ii, iii in each column show the menisci with the dorsal legulae, the side (the dorsal legulae at the left and ventral legulae at the right), and the ventral legulae facing the camera, respectively.

These experiments show that not all Lepidopterans exhibit the hydrophobic-hydrophilic dichotomy. The specific design can be related to the feeding habits of butterflies and moths. The monarch butterfly is an opportunistic feeder and is able to spend a long time probing the food source by its feet and dipping the proboscis into the liquid or mopping the substrate to pick up the liquid [7-10]. By making the legulae hydrophilic and the rest of proboscis surface hydrophobic, it can increase the drinking rate by increasing the drinking area while keeping the rest of proboscis surface clean. Hawkmoth with its long proboscis (~ 8 cm), hovers over the flower dipping the entire proboscis into the corolla and quickly withdrawing it within one second [11]. By making the entire proboscis hydrophilic, the insect maximizes the nectar pickup which is deposited on the proboscis surface as the insect withdraws proboscis from the nectar pool. This process is similar to dip coating process widely used in engineering. The evolution of the film will be discussed in Section 5.2 to completely explain the feeding behavior of the hawkmoth.

5.2 Feeding from a deposited thin film: effect of curvature on wetting and dewetting of Lepidopteran proboscises

As mentioned above, it has been observed that after each dip of the proboscis into a flower or other food source, the hawkmoth (and some other species of Lepidoptera) can acquire a thin liquid film covering the entire proboscis, which is similar to the dip-coating process of fibers [11]. In this case, the problem of delivery the liquid in this film to the food canal is reduced to the analysis of the flow in this liquid film. Before formulating the fluid mechanics model for this process, an understanding of the driving forces causing the flow of thin films toward the food canal is required. Field observations suggest that the thickness

of the nectar layer is much smaller than all characteristic dimensions of the proboscis [12]. Therefore, we can apply our study in Section 3.2 on to explain this driving force through the capillary effect of a liquid film associated with a flexed or coiled proboscis, answer the question of how the proboscis geometry and coiling and bending the proboscis benefit the insect in this process.

5.2.1 Film on the external surface of the straightened proboscis: the effect of proboscis geometry

The proboscis of hawkmoth *Manduca sexta* was cut from the head when it is flexible, and fixed to straight by attaching the two ends to the double side tape. Then it is dried at room temperature for 48 hours. After drying, the proboscis can remain straighten even unattached from the tape, Fig. 5.4(A). To examine the behavior of the liquid film deposited on the external surface, we dip-coated the proboscis with the set up described in Fig. 3.3. We use this straightened proboscis as the sample fiber, and black ink (Radiant^{TM} Colors Turbo Black) as the wetting liquid which would enable us to see the clear contact line. The straightened proboscis is inserted into a capillary a capillary tube (inner diameter of 1.6 mm) filled with ink, and immediately (within 10 seconds) exposed by moving the tube at 1 mm/sec with linear positioning stages (VT-21, Micos) to the left while filming from the top using a high-speed camera (POINTGREY® FL3-U3-13S2C-CS) and microscopic lens (Meiji Techno® Short UNIMAC MacroZoom Lense MS-40). In this way, once the proboscis leaves the tube, its surface is covered with a film of ink (Fig. 5.4(B), (C)), but the liquid has not fully fill the food canal to leave space for the further wetting. After the dip-coating, the ink film behaves by itself without any influence from outside.

It has been observed that the film gradually flows from the sides with a smaller radius of curvature toward the dorsal legular band and forms liquid finger, leaving the proboscis sides dewetted (Fig. 5.4(D), (E)). The arrows in these figures mark the two contact lines receding toward the dorsal legular band. Fig. 5.4(F) schematically describes this process. Then since the dorsal legular band is proved to be permeable [7], the liquid is drawn into the food canal through the porous legular band and the liquid finger keeps shrinking with the two contact lines receding toward the legular band and more and more the structure on the sides of the proboscis reveals (Fig. 5.4(G), (H)). Fig. 5.4(I) schematically describes this process. With more and more liquid sinks into the food canal, the film on the external surface become thinner and thinner so that the structure on the legular band becomes visible through the ink (Fig. 5.4(J), (K)). Fig. 5.4(I) schematically describes this process.

The observed phenomena can be explained step by step with our knowledge gained from Chapter III and IV. After the ink film deposited on external surface of the straightened elliptical proboscis, high capillary pressure is created at the narrow sides (sides of the proboscis) and low capillary pressure is created at the wide sides (dorsal and ventral legular bands), Fig. 3.2(A), (C), (E). Due to this pressure differential, the liquid is squeezed away from the sides and collected at the dorsal legular band. Following the similar experimental observation on elliptical wire (Fig. 3.4) and our study in Section. 3.3.2, the liquid collected on the dorsal legular band should form a series of clam-shell droplets, but not a liquid finger (column) which is observed in Fig. 5.4. However, if looking at the cross-sectional shape of the proboscis, Fig. 5.4, one can see it is not a complete ellipse. At the dorsal legular band

region, the profile concaves in and form channel-like structure. This channel like structure, as learned in Chapter I, would allow the liquid inside it to form column morphology. Compared to a series of clam-shell droplets, the formed liquid column significant increases the area that the liquid contacts the legular band, and therefore, enhancing the rate proboscis absorbing the liquid food.

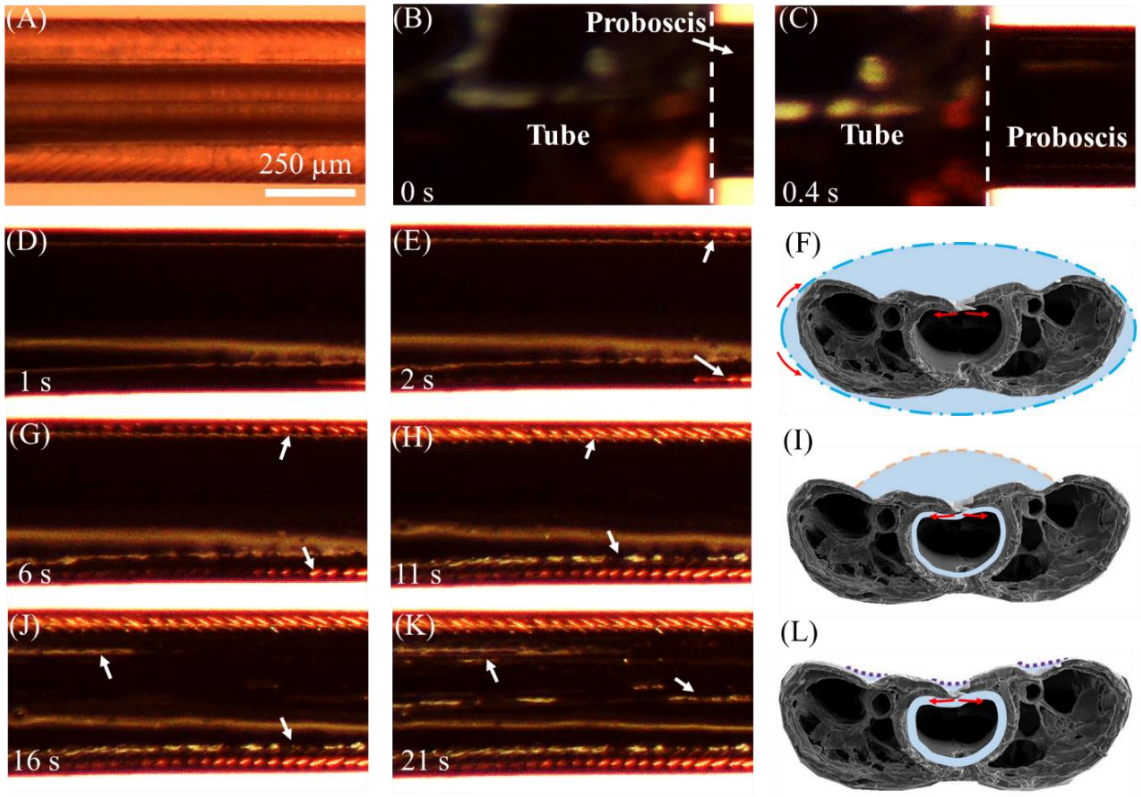

Figure 5.4. Dewetting of the proboscis of hawkmoth *Manduca sexta* by an ink film. (A) A dry, straightened proboscis before it is coated with ink. The dorsal legular band running along the proboscis appears darker compared to the rest of the proboscis. (B), (C) Film deposition process. The tube of ink (left of the dashed line) is moved to the left and a black film is deposited on the proboscis. (D), (E) After the film forms, it flows from the sides to the center (i.e., toward the legular band). (D) The proboscis is completely covered with the film. (E) Two contact lines (shown by arrows) form after dewetting of the proboscis sides. (F) Schematic illustration of the movement of the external film in images (D) and (E). (G), (H) The contact lines recede from the proboscis sides toward the legular band. (I) Schematic illustration of the movement of liquid in images (G) and (H). (J), (K) The legular bands dewet as the film moves into the food canal. The bright bands (shown by arrows) are the grooved features of this band shown in detail in Fig. 5.4. (L) Schematic illustration of the movement of liquid in images (J) and (K).

5.2.2 Effect of coiling on the thin films deposited on the external surface and the wall of food canal of the Lepidopteran proboscis.

A single loop of the coiled Lepidopteran proboscis can be model with a combination of the exterior shape Fig. 3.7(D) with cross-sectional ellipse elongated parallel to the coiling axis and the food canal shape Fig. 3.5(C) which is circular [1-3, 12]. Therefore, the analysis of these two parts in Chapter III requires special attention to discuss in detail for explaining the effect of coiling on the behavior of the deposited thin films.

5.2.2.1 Thin film deposited on the external surface of proboscis

Following the model describe in Section 3.2, the corresponding cross-section ellipticity for proboscis $e > 1$. Based on eqs. (3.2), (3.3), and (3.9), the effects of coil radius R and cross-sectional ellipticity e on the pressure distribution inside the film are illustrated in Fig. 5.5(A), (B), respectively. The dimensionless pressure difference P is plotted as a function of the polar angle θ. Similar to the straight proboscis, two maximum pressures are obtained at parallels A and C ($\theta = \pm\frac{\pi}{2}$), sides of the proboscis, and they are equal. However, the two minimum pressures, one absolute minimum at $\theta = 0$ (parallel B in Fig. 5.5(C), ventral legular band), and one local minimum at $\theta = \pi$ (parallel D in Fig. 5.5(C), dorsal legular band), are of different values, making two uneven attractors. This is very different from the straight proboscis. The attractor on the ventral legular band collects more liquid than the dorsal legular band. Although the location of the attractor parallels is not influenced by the value of parameters R and e (Fig. 5.5(A), (B)), their difference might be affected by these parameters. We, therefore, examined the dependence of this difference $\Delta P = \left(P_l^{local\ min} - P_l^{absolute\ min}\right)a/\sigma$ on these parameters:

$$\Delta P = \left(P_l^{local\ min} - P_l^{absolute\ min}\right) a/\sigma = \frac{1}{(R+1)} + \frac{1}{(R-1)}. \quad (5.1)$$

It is found that this dimensionless pressure difference does not depend on proboscis ellipticity, but on the coil radius, Fig. 5.5(D). It increases when the radius of the proboscis coil, R, decreases. The drinking region with enlarged interlegular pores is near the proboscis tip. Therefore, by coiling the proboscis (decreasing coil radius) the liquid moves more to the ventral legular band under a stronger pressure difference. This same coiling scenario supports the movement of liquid from distant regions of the proboscis toward the drinking region; the pressure at the ventral band (absolute minimum in Fig. 5.5(A)) decreases as the insect bends its proboscis. Therefore, the natural coiling behavior ensure that liquid will not be lost but will be collected at the ventral legular band of the outmost loop and then transferred to the more permeable dorsal legular band [7] of the neighboring loop.

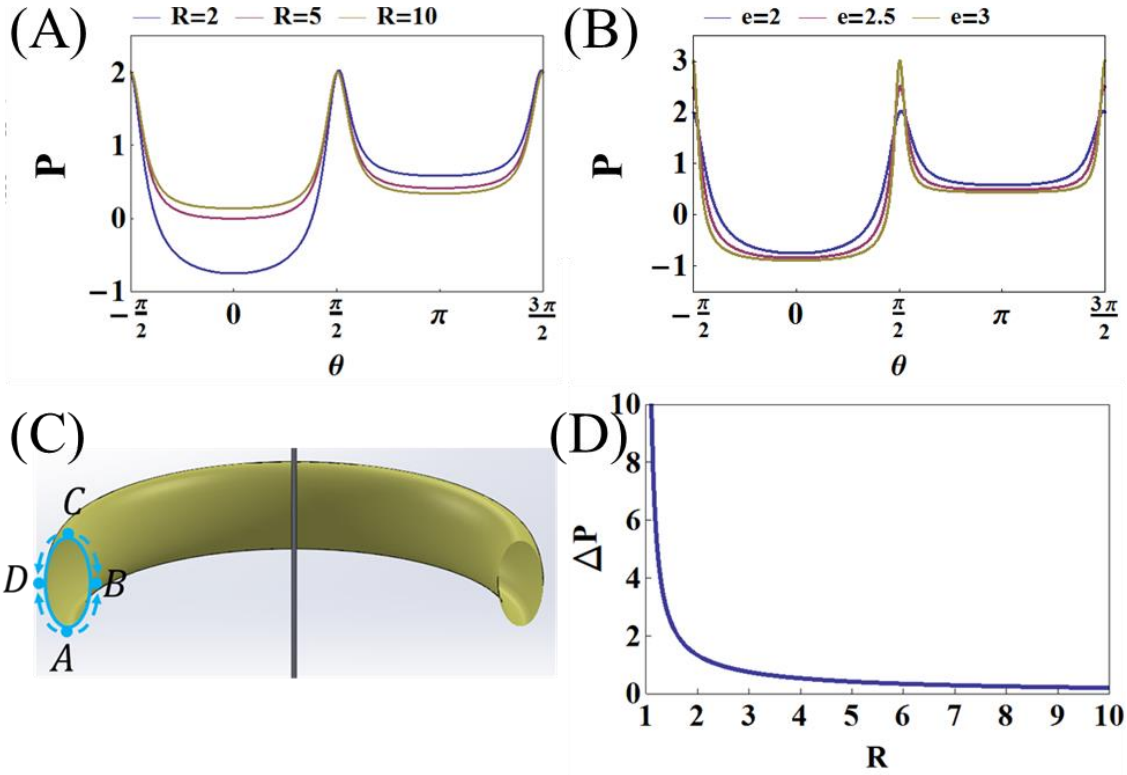

Figure 5.5. (A) Dimensionless pressure difference P versus angle θ for different dimensionless coil radii R at fixed ellipticity $e = 2$. (B) Dimensionless pressure difference P versus angle θ for different ellipticities at the fixed dimensionless coil radius R=2. (C) Schematic of liquid transport from the proboscis sides, parallels A and C, toward the ventral and dorsal legular bands, parallels B and D, respectively. (D) Dimensionless pressure differential of the absolute minimum and local minimum, $\Delta P = \left(P_l^{local\ min} - P_l^{absolute\ min}\right)a/\sigma$, as a function of the dimensionless coil radius of the proboscis model.

However, because of the parameter a, which is approximately the radius of food canal, the dimensional pressure difference between the two attractors are different even with the same coil radius R. To quantitatively estimate the pressure difference, we calculated capillary pressure for films on the proboscises of five species of butterflies, based on geometric parameters of their proboscises[13] (Table 5.1). The pressure difference between the dorsal and ventral legular bands is small; it requires about a 2% more pressure to force the liquid to move from the proboscis sides (parallels A and C) to the dorsal legular band (parallel D) than to the ventral legular band when the loop radii are

of the order of a millimeter. Thus, when these butterflies coil their proboscises, they trigger liquid collection by lateral movement of liquid films toward the drinking region.

Greater proboscis ellipticity is associated with butterflies that routinely feed from wetted surfaces rather than from floral corollas. This ellipticity confers adaptive value when drinking from films because the contact line of the meniscus rises higher on the proboscis, compared with a cylindrical proboscis, thereby covering more interlegular spaces with fluid [11]. We found that capillary pressure suggests a relationship with feeding habits. The greatest pressures are associated with surface-film feeders (e.g., *Limenitis arthemis astyanax*) and the lowest pressures with routine flower visitors (e.g., *Danaus plexippus* and *Papilio glaucus*) (Table 5.1). Thus, the extremes of this pressure range reflect two long-recognized feeding guilds of Lepidoptera: flower visitors (nectar feeders) and nonflower visitors (non-nectar feeders) [3].

Table 5.1. Capillary pressure in a thin liquid film coating the proboscis exterior. Atmospheric pressure is taken as the reference, $P_a = 0$. AM is the absolute minimum pressure at the ventral legular band (parallel B in Fig. 5.6); LM is the local minimum pressure at the dorsal legular band (parallel D in Fig. 5.6); DLA is the difference between AM and LM; Max is the maximum pressure at parallels A and C in Fig. 5.6; and DML is the difference between Max and LM. Proboscis cross-section is assumed to be elliptical with semi-axes $O_1D = a$ and $O_1C = b$ (Fig. 3.1).

Species	a(μm)	b(μm)	r(mm)	Pressure (Pa)				
				AM	LM	DLA	Max	DML
Danaus plexippus	56	135	1.5	173	270	97	3125	2874
Papilio glaucus	65	182	1.5	92	189	97	3128	2939
Vanessa cardui	36	105	1.5	187	284	97	5882	5598
Limenitis arthemis astyanax	32	252	1.5	-13	84	97	17866	17782
Polygonia interrogationis	48	149	1.5	107	204	97	4695	4491

5.2.2.2 Thin film deposited on wall of food canal

If a thin film deposits on the wall of the circular food canal of a straight proboscis, the pressure inside the liquid is uniform both along the circumference and along the axis-direction. Therefore, if without any disturbance, the film will stay stable, which is hard to absorb by the insects. Coiling the proboscis can introduce the distance by creating pressure differential inside the thin film, as shown in Fig. 3.5(A), (C), and (E). For the reader's convenience, we copy these figures here as Fig. 5.6(A), (B), and (C), respectively. Because of this disturbance, the liquid film is easier to form a sequence of liquid columns and absorb by the insects.

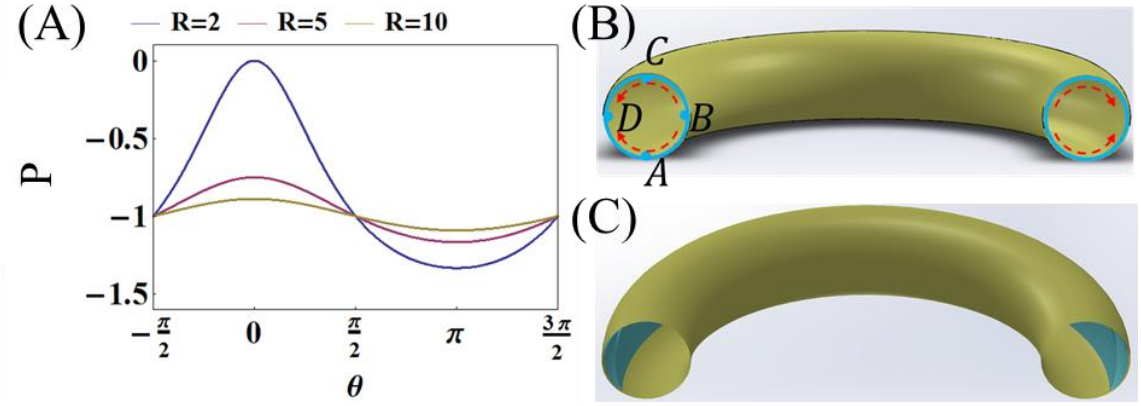

Figure 5.6. (A) Pressure distribution in the film coating the food canal; pressure for three different loop radii are shown. (B) Schematics showing the flow directions inside the film. (C) Schematics showing the possible final configuration of the film.

Fig. 5.6(A) shows the maximum pressure is obtained at the parallel B ($\theta = 0$), the ventral legular band, and the maximum pressure is obtained at the parallel D ($\theta = \pi$), the dorsal legular band. Therefore, the liquid will be collected at the only attractor locating at the dorsal legular band, Fig. 5.6(C). Liquid collection at the dorsal legular band from inside the food canal would also benefit Lepidopterans even when they are not feeding. An

important implication of this effect is related to the mechanism of holding the paired galeae together, especially at the dorsal legular band where the legulae do not have a lock-and-key mechanical linkage, in contrast to the ventral band for which this mechanism was identified long ago [13-16]. The dorsal legulae weakly overlap one another, forming slit-like pores of hundreds of nanometers [7]. In the slit pores formed by two adjacent legulae, the liquid collected at the dorsal legular band can sink into the slit and form liquid bridge connecting the two legulae. This liquid bridge could create a colossal capillary pressure, on the order of 10 Atmospheres (Fig. 5.7). Because the legulae are hydrophilic, this capillary pressure tends to bring the legulae together and hold them in place, yet allow them to slide over one another with little resistance [17-20].

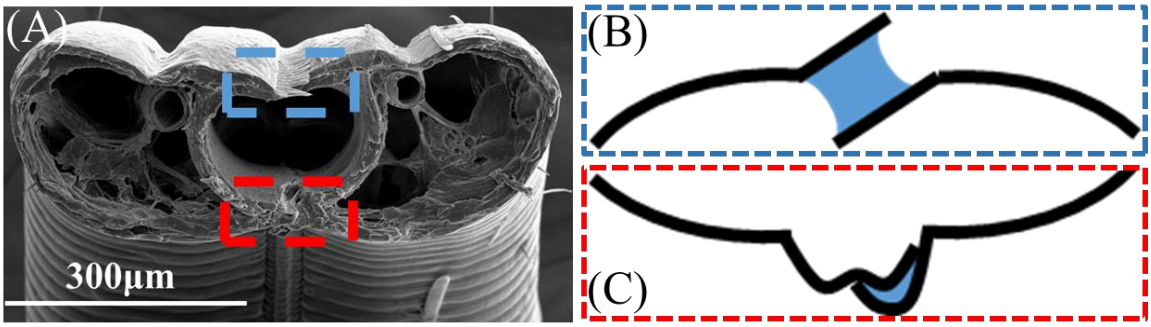

Figure 5.7. (A) SEM image of the proboscis of *Manduca sexta* in cross section, showing the position and structure of dorsal (red box) and ventral (blue box) legulae. Schematic showing capillary adhesion of (B) dorsal and (C) ventral legulae (black lines) by trapped fluid (blue).

5.2.3 Discussion

Liquid collection is a critical initial step in fluid feeding [21]. However, fluids available from floral corollas and other food sources are often limited. Fluid availability, therefore, can be a significant determinant of foraging behavior [22]. Maximizing fluid acquisition and minimizing evaporation, thus, become essential for efficient feeding and

water balance, and should be under strong selection pressure. Physical principles of the proboscis that enhance fluid collection would have been important in paleoenvironments with limited availability of suitable resources, and might have been critical in the evolution of the proboscis [7]. Our findings suggest that coiling and bending have adaptive value beyond the conventional benefits of packaging and protecting the proboscis; these movement provide an additional means of optimizing fluid intake.

When a butterfly inserts its proboscis into a flower or applies it to a liquid pool or surface, fluid gathers on the proboscis as a film, similar to industrial dip-coating. Liquid evenly distributed on a straight proboscis must then be transferred to the legulae where the interlegular gaps will allow fluid to enter the food canal. Thus, the second step in fluid feeding involves directional movement of the liquid. Bending or flexing of the proboscis causes dewetting—movement of fluid to the legular bands of permeability. On a straight proboscis, the ventral and dorsal legular bands are equivalent attractors of fluid. Once the proboscis bends, the attractors are no longer symmetrical, and liquid moves to the dorsal legulae. Bending brings into play gravitational forces; any increase in gravity will aid directional movement of fluid. The process would be facilitated during feeding as the proboscis undergoes flexion at the knee-bend (*sensu* Krenn [12]) or assumes a J shape, as well as between feeding bouts when the insect bends or coils the proboscis as it moves between flowers. Passive fluid collection would be aided not only by gravity, but also by acceleration from the sweeping and mopping movements of the proboscis, as described [23] for fruit- and sap-feeding Lepidoptera. An important material feature aiding fluid movement includes the chemical and physical composition of the proboscis surface. The

fine surface sculpture of the proboscis typically has micro-ridges and valleys that aid capillarity and direct fluid toward the hydrophilic legulae [6].

Water conservation could be enhanced not only during actual feeding but also by efficiently recycling body fluids. Many Lepidoptera produce saliva or exude water droplets from the anus to solubilize nutrients and make them available for uptake via the proboscis. Hesperiids, for example, direct the abdomen anteriorly to exude droplets of fluid onto dry surfaces and then reimbibe the liquid [24], particularly on dry days (unpublished observations) when conservation of fluids is most critical. Recycling essential fluids in saliva and exudates could be facilitated by proboscis bending and coiling.

The dorsal and ventral legular bands of the linking mechanisms at the C-edges of the galeae are hydrophilic [6, 25]. Thus, fluid readily spreads over the legular bands and sinks into the food canal through the interlegular gaps. The insect, therefore, is tasked to bring the liquid to the dorsal and ventral legular bands while drinking from floral corollas or other food sources. Our results corroborate our hypothesis that liquid is passively collected at the permeable dorsal and ventral legular bands due to proboscis ellipticity, as seen from the analysis of pressure distribution in a thin film covering an elliptical proboscis. An elliptical, rather than circular, proboscis brings the contact line of the meniscus higher on the drinking region, increasing the number of interlegular spaces covered with liquid [6].

This mechanism of nectar collection is important for Lepidoptera with long proboscises, such as *Xanthopan morganii praedicta* [26]. The moth inserts the proboscis into the flower and after about one second withdraws it. In so doing, the moth acquires a

liquid film, and as it removes the proboscis from the corolla, the film remains on the exterior surface of the proboscis. According to our results, this film is unstable and is prone to move toward the dorsal and ventral legulae.

Proboscis ellipticity is more noticeable in non-flower visiting butterflies and moths that probe sap flows and animal wastes (e.g., dung) with bacteria and sticky compounds [12, 27]. These insects move the liquid from the sides of the proboscis toward the central (legular) area, which is subject to rubbing during coiling and uncoiling of the proboscis such that the probability of removing debris is greater. Lepidoptera, thus, solve the problem of keeping their proboscises clean, while at the same time acquiring liquid food.

5.3 Self-assembly of Lepidopteran proboscis: the role of capillary forces

5.3.1 Introduction

The feeding device (proboscis) of butterflies and moths (Lepidoptera) consists of a pair of C-shaped fibers, the maxillary galeae [12, 14, 15]. The two galeae form separately during the pupal stage and typically are assembled by a defined sequence of repeated actions into the united proboscis when the insect emerges from the pupa [15, 28, 29] (Fig. 5.8). When the two galeae are united, the proboscis becomes a tube-like device, and the C-halves form a food canal through which liquid is delivered to the gut, aided by a suction pump in the head [7, 12, 18].

The galeae of the long-tongued moths and butterflies are joined by a series of cuticular projections called legulae; the galeal musculature of these Lepidopterans is fully developed to allow each galea to perform complex maneuvers [14, 29, 30]. The two galeae, united as the proboscis, function as a single organ during routine use by the insect.

We hypothesize that butterflies rely on natural physical phenomena acting independently and without muscle actuation to help unite the galeae into the proboscis. A theoretical investigation of biomechanical causes of galeal attraction becomes important for understanding assembly of the Lepidopteran proboscis.

An important clue in developing our hypothesis was previously suggested by biologists when they noticed that assembly of the proboscis is accompanied by the appearance of saliva [12, 14, 28, 29] (Fig. 5.9). Previous workers [14] have suggested that saliva acts as an adhesive gluing the galeae together. The gluing action of a liquid assumes its sliminess and stickiness. The saliva of butterflies has no mucin or other proteins imparting sliminess or viscoelasticity to the fluid, but instead follows purely Newtonian behavior and is nearly inviscid [31]. Therefore, while appreciating the important role of saliva during proboscis assembly, we hypothesize that Lepidoptera rely on capillary action of salivary bridges to pull and hold the galeae together while the insect mechanically couples the two strands. The most familiar example of this capillary effect is the coalescence of wet hair [32].

To evaluate our hypothesis of capillary-assisted gathering of the galeae, we provide an analysis of the action of a saliva column spreading along the length of the food canal including along the half of each separated galea. The distribution of saliva over the length of the separated galeae was specified using micro-computed tomography (micro-CT). With specified meniscus configurations, we set up a model for an intergaleal saliva column and theoretically find the critical conditions when this column can hold the galeae together. We then use our model to estimate the capillary forces acting on the galeae and test its

predictions on artificial plastic proboscises. We conclude that the forces are strong enough to hold the galeae in proximity to each other while the insect couples the with legulae.

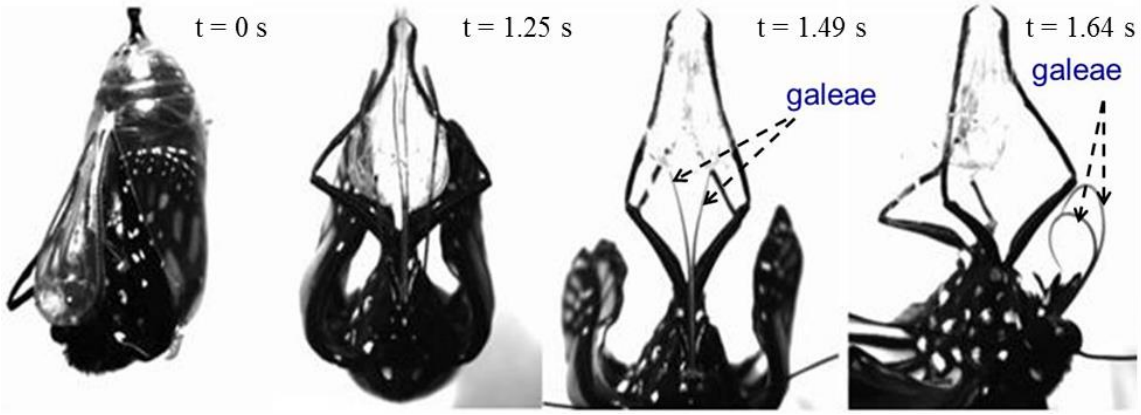

Figure 5.8. Adult of the monarch butterfly (*Danaus plexippus*) emerging from the pupa. The galeae of the proboscis are initially two separate strands. Emergence of the insect and proboscis assembly were tracked at 100 frames per second (fps), using a Sony Pro Camera DSLR A100.

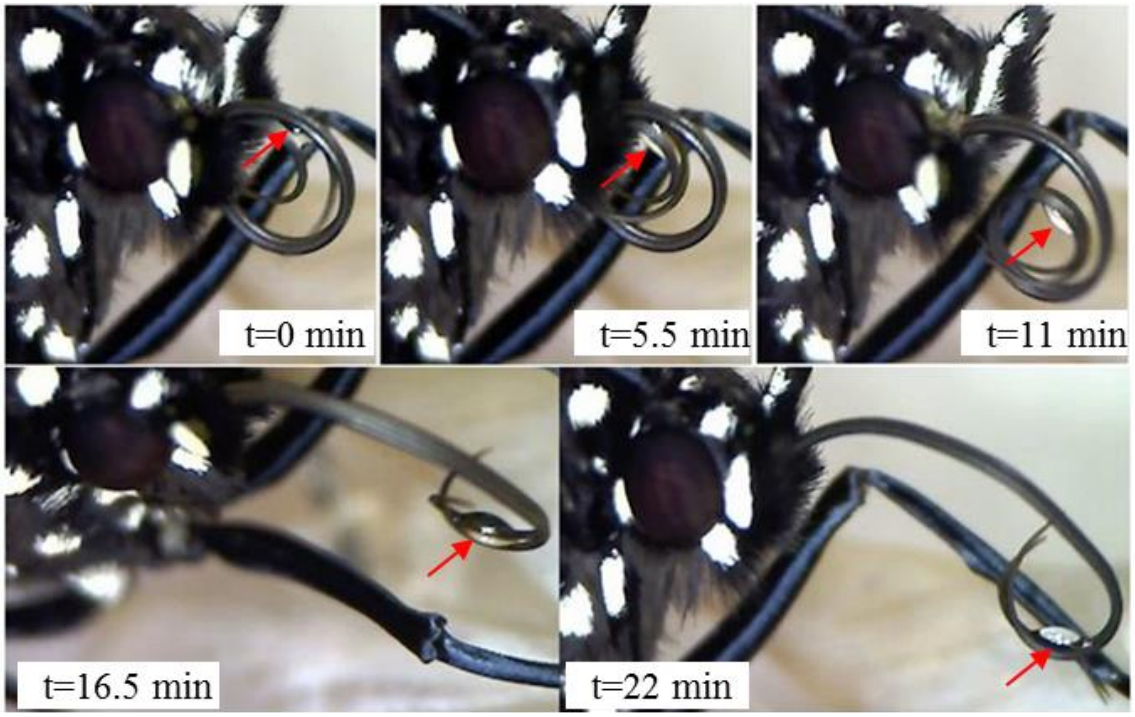

Figure 5.9. Saliva droplets are seen between two separated galeal strands of a just-emerged monarch butterfly (t = 0 min). When the proboscis is coiled, the drop is released near the head (t = 5.5 min). The drop of saliva then appears where the galeae are separated (t = 11 min). The proboscis is uncoiled (t = 16.5 and 22 min) and the galeae are brought together by capillary effect. Drop release was tracked at 30 fps, using a digital microscope (GSI® GWC60-1).

5.3.2 Behavioral features of proboscis assembly

5.3.2.1 Role of saliva in proboscis assembly

When the galeae are separated, we noticed that the butterfly produces saliva during the assembly (Fig. 5.9). However, saliva does not continuously wick into the gap separating the galeae. The release and retraction of saliva are controlled by a muscular pump in the butterfly's head, as inferred from our observations and those of Krenn [29]; saliva droplets periodically appear and disappear, suggesting that the insect produces saliva droplets as needed. Once released, saliva moves to the internal surface of the coil and collects at the point where the galeae are separated. This drop bridges the separated galeae. The butterfly pushes the drop back and forth and coils and uncoils the proboscis, adjusting the coil radius to ensure that the drop is placed in a position to hold the branching galeae together. We have previously discussed the physical mechanisms of drop formation on the inner margin of the coiled proboscis [33].

Proboscis assembly involves repetitive coiling and uncoiling and sliding of the galeae over one another in antiparallel movements, accompanied by discharge of saliva between the galeae. Coiling and uncoiling help align the separated galeae when they are sometimes slightly entangled with one another [29]. Antiparallel movements putatively contribute to galeal coupling of the ventral legulae [16]. Joining the galeae proceeds from the base to the apex of the proboscis and is facilitated by saliva [8]. Coiling and uncoiling the proboscis by the butterfly does not change the assembly scenario: the butterfly continues releasing saliva that bridges the galeae together until they are united [34].

During proboscis assembly, we observed saliva spreading over the medial surface of the galeae, forming a liquid column with menisci facing the air from the anterior and posterior ends of the proboscis (Figs. 5.9, 5.10). The surface tension of the air-saliva interface, together with capillary pressure under the menisci, would force the two galeae together. Our observations suggested that saliva can propagate along the entire length of the separated galeae while the butterfly is uniting them. However, optical imaging does not allow these observations to be validated, and the opportunity to capture proboscis self-assembly in the brief period (within ca. 1 hour) following emergence limits experimental investigation. We, therefore, used micro-CT on freshly killed insects to acquire the 3D configuration of liquid menisci by scanning with X-ray imaging based on the density contrast of materials.

5.3.2.2 Menisci in completely separated galeae

A Bruker SKYSCAN 1176 Micro CT instrument was used in our experiments. It allows features of the meniscus/substrate pair to be identified with an accuracy of 9 μm. Therefore, the larger the proboscis, the better the resolution of menisci. To increase the scale of the proboscis, we used the hawk moth *Manduca sexta*, with a proboscis length of about 7 cm and food canal diameter (at mid-length) of about 80 micrometers. Hawk moths (n = 5) within 24 hours after emergence from the pupa were frozen at -18 °C overnight, allowing us to exclude the influence of insect motion while retaining a flexible (and assembled) proboscis. The proboscis was uncoiled, and the galeae were separated from the tip toward the head at an angle of about 20°, while ensuring that a section of the proboscis near the head remained together. The separated tips of the proboscis were fixed to a plastic

foam stage with double-sided tape to maintain the shape of the separated proboscis. The head of the moth, with the holder, then was attached to a half-cylindrical polystyrene foam stage designed to fit the micro-CT channel.

About 1 µl of OMNIPAQUE^{TM} (iohexol) was injected at the vertex of the V-split galeae. It wetted the food canal and spread along the galeae. This liquid provides good contrast of menisci against other materials under the X-ray beam. Within five minutes after the contrast agent was fully spread and the menisci reached their equilibrium configurations, the sample was placed on the stage of the micro-CT instrument and scanned at 9-µm resolution. Five moths were used for the scan. Fig. 5.10(C) shows an example of the cross-sectional shapes of the liquid body taken at different positions along the united part of the proboscis and separated galeae.

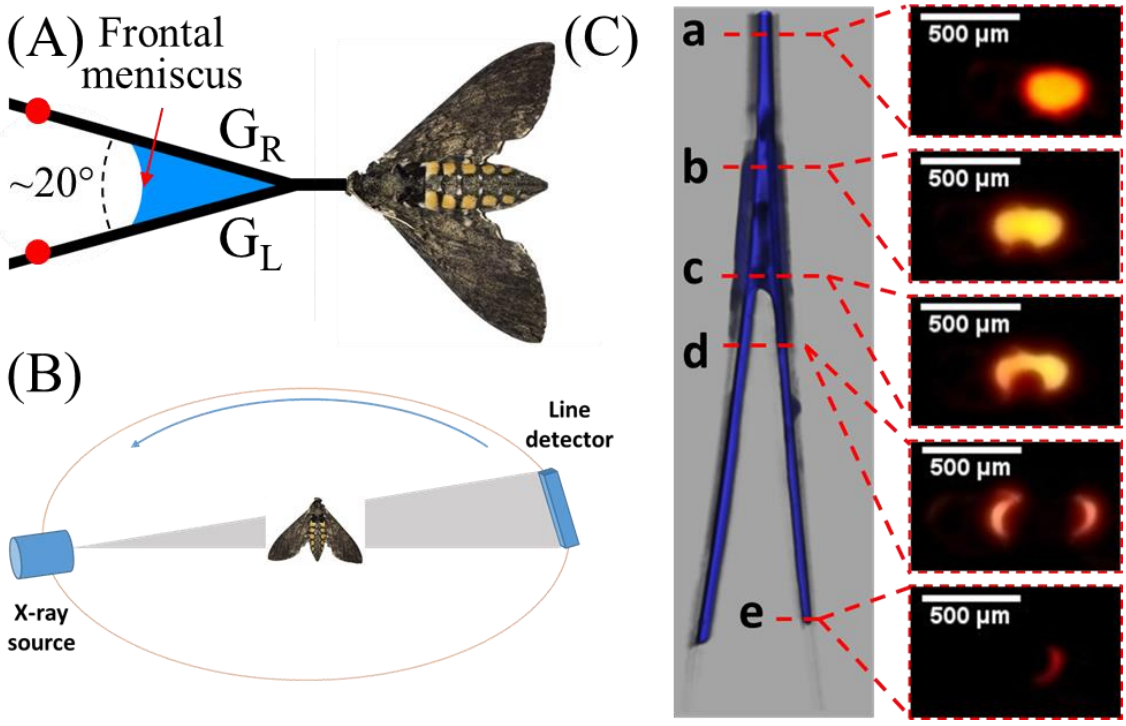

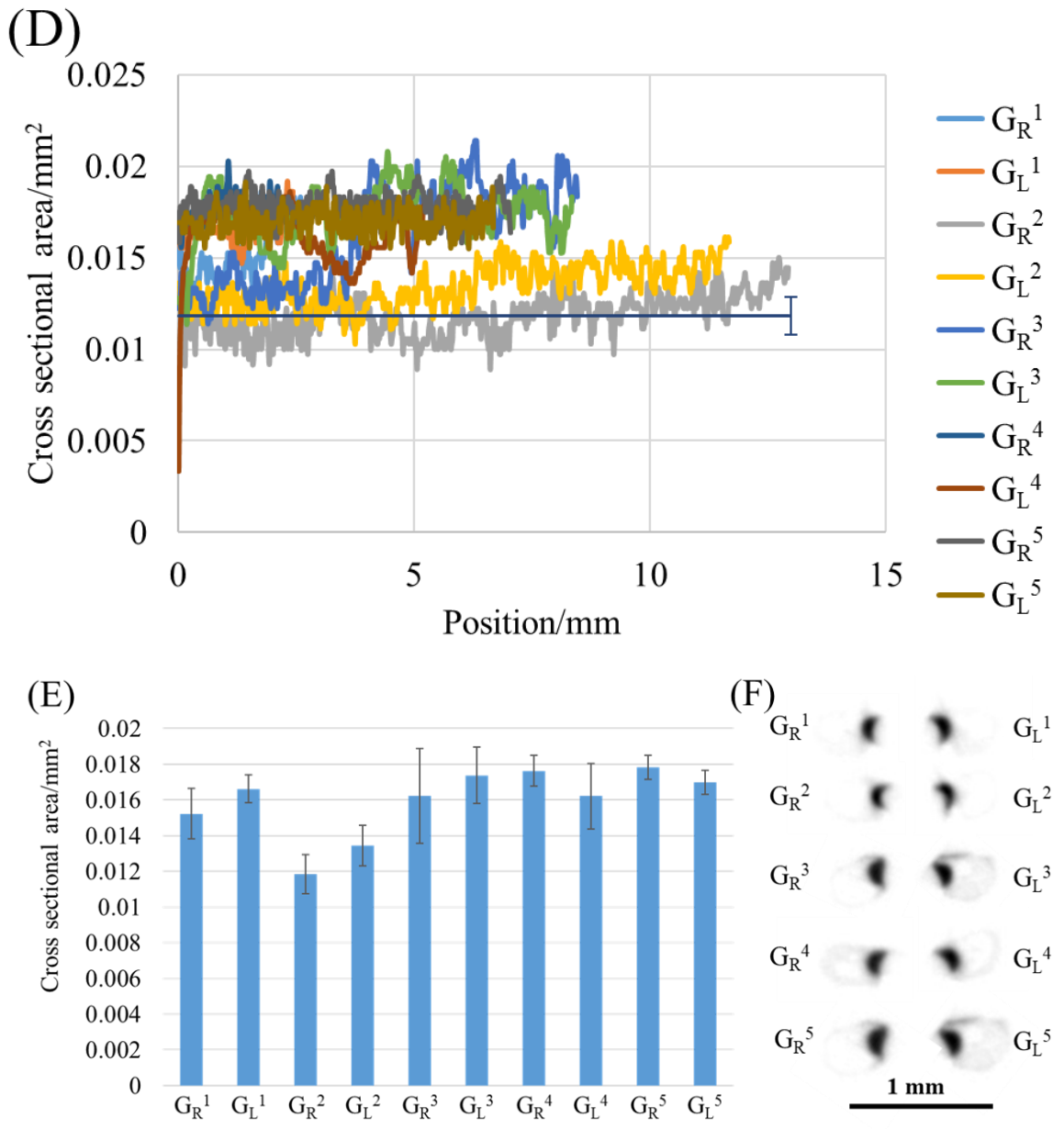

Figure 5.10. Modeling saliva action. (A) A hawk moth was pinned to the substrate, and the galeae were separated and straightened. Two pins (red dots) held the two galeae (subscripts "R" (G_R) and "L" (G_L) identify the right and left galae (G) as seen from the dorsal side of the proboscis) at the tips. A contrast agent, OMNIPAQUETM (iohexol), was injected at the vertex of the V-split galeae. A liquid bridge (blue curved triangle) was observed. (B) In the Bruker SKYSCAN 1176 instrument, the moth was stationary while the X-ray source and detector acquired images. (C) An illustrative example of the cross-sectional shapes of the liquid column taken at different positions along the proboscis from e) to a). The liquid finger with almost constant radius of curvature spreads over the 'd'–'e' span and ends at position 'e'. The frontal meniscus at 'c' has a complex saddle-like shape. The columnar liquid bridge spreads over the 'b' –'c' span. (D) Cross-sectional area of the liquid finger versus position along the separated galeae for different individuals; the zero point is taken at

the galeal tip. The gray data set for galea GL2 (i.e., the left galea of the second individual) is shown as a straight line (the mean) and its error bar (standard deviation). (E) Summary for the cross-sectional area of a liquid finger situated in each separated galea of five different individual moths; the solid blue bar represents the mean of all micro-CT measurements along each galea, and the error bar represents the standard deviation of these measurements. (F) Representative images for measurement of the cross-sectional area of the liquid finger for each individual.

Hereafter, we refer to the liquid body in the region 'b'–'c' as the columnar bridge or liquid column. The liquid body in the region 'c'–'d' of the separated galea is the liquid finger, and the air-liquid interface in each cross-section of the liquid body is the meniscus.

Three distinguishable configurations of meniscus profiles were observed. In the region where a segment of proboscis remained unseparated (position 'a' in Fig. 5.10(C)), the liquid formed a circular cylindrical column in the food canal of the united proboscis. Where the proboscis was separated at the vertex of the V (positions 'b' and 'c' in Fig. 5.10(C)), we observed a liquid bridge with two concave menisci indented toward the liquid interior; this liquid bridge connected the two separated galeae. We identified the shape of the liquid bridge as being formed by the two side arcs of the wall of the food canal and the two middle arcs as the interfaces of liquid and air.

In the region where the proboscis was fully separated (positions 'd' and 'e' in Fig. 5.10(C)), no liquid bridge was found; instead, we observed two separated liquid fingers running along the C-shaped walls of the galeae. The cross-sections at different positions in this region show that the fingers formed a crescent moon-shaped cross-section in each half of the food canal. The measured cross-sectional areas of fingers along each semi-circular half of the food canal remained almost the same (Fig. 5.10(D)), indicating each finger is a uniform liquid column. If modeling it as wetting of semi-circular channel, which has been

discussed in Chapter 4, we know the contact line of these columnar fingers are pinned by the leguleal edges. The average cross-sectional area of the liquid finger varies from one galea to the other, as a result of slight differences in the radius of the food canal and the wetting properties. The representative images for the measurements of the cross-sectional area of the liquid finger for each individual are in Fig. 5.10(F).

These observations suggest that the surface properties and geometrical shapes of the C faces of the galeae do not typically differ from one individual to another. The constancy of the finger cross-sectional areas over a long period of time (> 20 minutes) of micro-CT scanning suggests that the liquid fingers coexist in equilibrium with the liquid bridge. Accordingly, the formed fingers can be used for characterization of the wetting properties of the food canal.

Our experiment with the live hawk moth and our observations of live monarch butterflies and painted lady butterflies (*Vanessa cardui*) assembling their proboscises allow us to conclude that (1) saliva forms a cylindrical column in the unseparated food canal, (2) a liquid bridge forms at the conjunction of galeal separation. Experiments on freshly dead insects show that two liquid fingers form with crescent moon-shaped cross-sections in the semi-circular walls of the food canal of each galea. Therefore, the possible capillary force which helps the self-assembly of proboscis can only come from the liquid bridge. Based on this imaging, we build the model of a liquid bridge connecting the separated galeae.

5.3.3 Model formulation

According to our observations, the galeae come together only when their edges are aligned almost parallel to one another. Saliva is always present during proboscis self-

assembly and is pumped by the insect until the galeae unite. Therefore, the saliva column bridging the galeae together seems to facilitate galeal assembly.

Our observations on live butterflies and those of Krenn [29] revealed that in the vicinity of the splitting point where the galeae are separated, the radius of curvature of the proboscis coil is always much larger than the intergaleal distance. Therefore, when evaluating the capillary force acting on the galeae, as a first approximation we can consider the galeae as straight parallel beams [35-37] pulled together by a force f acting per unit length of each galea (Fig. 5.11).

This capillary force is expected to scale as $f = 2\sigma u(d/r)$, where σ is the surface tension of saliva measured in Newtons per meter, $2d$ is the spacing between the two opposite legular bands of the two galeae, and r is the radius of the food canal. The function $u(d/r)$, has to be identified by solving the Laplace problem of capillarity, which we do later.

A model of a liquid column bridging two parallel, round cylindrical fibers was first discussed and analyzed by Henry Princen [35, 38] and has since been widely used in different related applications [36, 39-43]. Princen showed [35, 38], that the mechanism of bridge breakup between the angled fibers can be revealed by analyzing the behavior of a bridge formed between two parallel fibers. We will follow this model of the two parallel galeae and assume that when the intergaleal gap reaches a certain critical value $d/r = (d/r)_{max}$, a continuous columnar bridge breaks up, forming two fingers running along the internal C-walls of the galeae (Fig. 5.10(C)). This model of two parallel galeae with a columnar bridge sitting between them allows us to estimate the capillary force exerted on

the galeae. We then check whether this force is sufficiently strong to hold the galeae together and help the insect unite the ventral legulae during proboscis assembly.

The Princen theory of bridge breakup has been designed to study the columnar bridges trapped between round cylindrical fibers, regardless of composition of the fibers [32, 35, 38, 40]. The galeae have a complex shape, preventing the immediate application of the Princen theory to this case. We, therefore, generalize the Princen theory and study the cross-sectional profile of the columnar bridge and its effect on proboscis self-assembly.

We model the galeae as two infinitely long semi-cylinders running parallel to one another. Only the capillary force caused by the saliva bridge is considered; any pressure contribution of flow during saliva pumping is put aside and will be discussed below. Thus, the columnar saliva bridge is assumed to coexist in equilibrium with the saliva fingers running along the walls of the separated galeae (Fig. 5.11(A)). We observed that the length L of the columnar saliva bridge is much greater than the diameter of the food canal and the intergaleal separation distance $2d$.

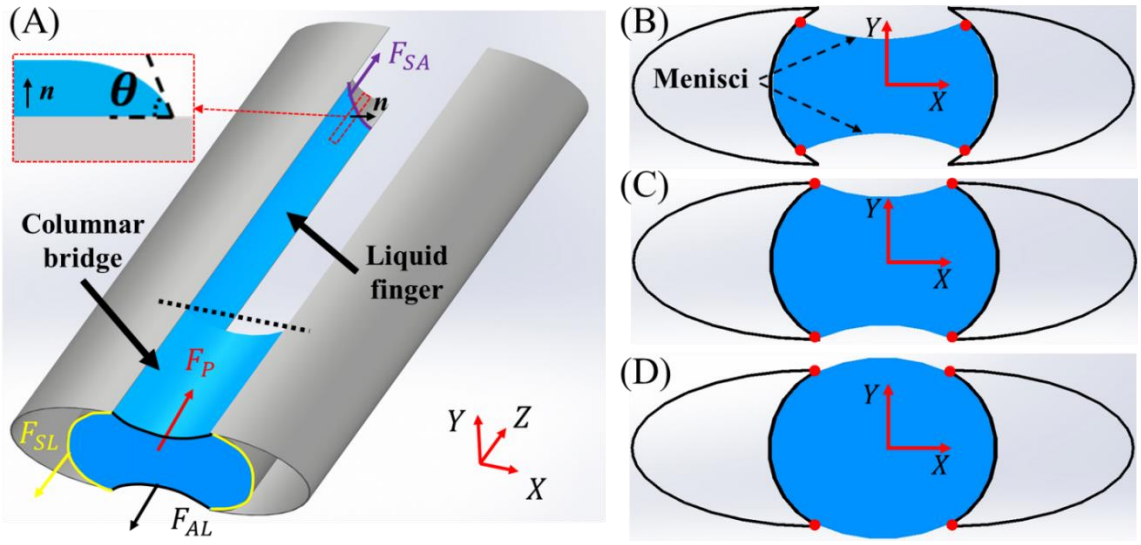

Figure 5.11. (A) A 3D schematic illustrating the shape of the columnar bridge of saliva formed between two separated galeae; the columnar bridge is in equilibrium with the liquid fingers, nucleated somewhere at the dashed line, running along the walls of each galeae. The dashed box shows a cross-section of the tip of the liquid finger defining the contact angle θ; the cross-section is taken through a normal vector n to the food canal surface parallel to the Z-axis along the food canal. (B) Bridge cross-section perpendicularly to the Z-axis assuming that the four contact lines (solid dots) are sitting inside the food canal. (C) A case of a liquid bridge with concave menisci; the bridge cross-section shows four contact lines (solid dots) pinned at the legular edges of the food canal. (D) A case of a liquid bridge with convex menisci; the bridge cross-section shows four contact lines (solid dots) pinned at the legular edges of the food canal.

The saliva bridge is supported by the C-face walls of the galeae, which are semi-circular arcs in cross-section (Fig. 5.11(A)). When the galeae are united, the food canal forms a cylindrical channel of radius r (Fig. 5.10(C)). The separation distance is denoted by $2d$ and corresponds to the distance between the two opposite legular edges of the two halves of the food canal. The inequalities $L >> 2r, L >> d$ hold true. In setting up the model, we note that the intergaleal gap, $2d$, is typically much smaller than the capillary length, based on our observations of the butterfly assembling its proboscis; thus, $l_c = \sqrt{\sigma/\rho g}$, where σ is the surface tension of saliva, ρ is the saliva density, and g is the acceleration due to gravity. For water, $l_c \sim 4$ mm. This inequality, $2d \ll l_c$, implies that gravitational effects can be neglected [44]. Thus, menisci are mostly shaped by capillary forces. The meniscus meets the walls of the food canal at the contact angle θ, which is a physical parameter of the saliva–cuticle pair.

In the Cartesian system of coordinates (X, Y, Z), where the galeae are parallel to the Z-axis, the meniscus profile $Y = h(X)$ describes the liquid elevation above the reference plane $Y = 0$ (Fig. 5.11). The two menisci forming the saliva bridge are assumed to be mirror-symmetric with respect to the X-axis. Since the columnar saliva bridge is

connected to the saliva fingers where the pressure is constant, the pressure in the saliva bridge also has to be constant. This condition of saliva equilibrium demands that the menisci must be shaped as circular arcs to satisfy the Laplace equation of capillarity, $P = -\sigma/R$, where R is the radius of the meniscus arc. Moreover, to satisfy the condition of mechanical equilibrium of the columnar bridge/two-fingers system, the Z-component of the force acting on the system must be zero.

The force balance in the Z-direction is obtained by constructing a free-body diagram and making an imaginary cut perpendicular to the Z-axis and replacing one part of the bridge with an equivalent system of forces (Fig. 5.11(A)). At this cut, the Z-component of the force consists of five contributions: the two surface forces F_{AL} acting along the air/liquid interface, the two surface forces F_{SL} acting along the solid/liquid interface, and the force F_P caused by the pressure in the saliva; this force, F_P, acts over the cross-sectional area cut. These five forces are counter-balanced by the force acting at the contact line at the end of the liquid finger, F_{SA}, and is associated with the solid/air interface. The force balance is thus written as:

$$F_{AL} + F_{SL} - F_{SA} - F_P = 0 \tag{5.2}$$

To calculate the component forces, one needs to distinguish the following two scenarios of the meniscus shaping: (1) the contact lines of the menisci of the columnar bridge are sitting inside the food canal (Fig. 5.11(B)), or (2) the contact lines are pinned at the legular edges of the food canal (Fig. 5.11(C), (D)).

5.3.4 Analysis of possible scenarios of the saliva bridge shaping and conditions for its existence

5.3.4.1 The contact lines are sitting inside the food canal

A saliva bridge connecting separated parallel galeae with the contact line inside the food canal can take on two configurations: one with a concave meniscus (Fig. 5.12(A)) and one with a convex meniscus (Fig. 5.12(B)). The mechanism to evaluate the force balance is the same; here we will take the concave case as an example. Its parameters are defined in Fig. 5.12(C).

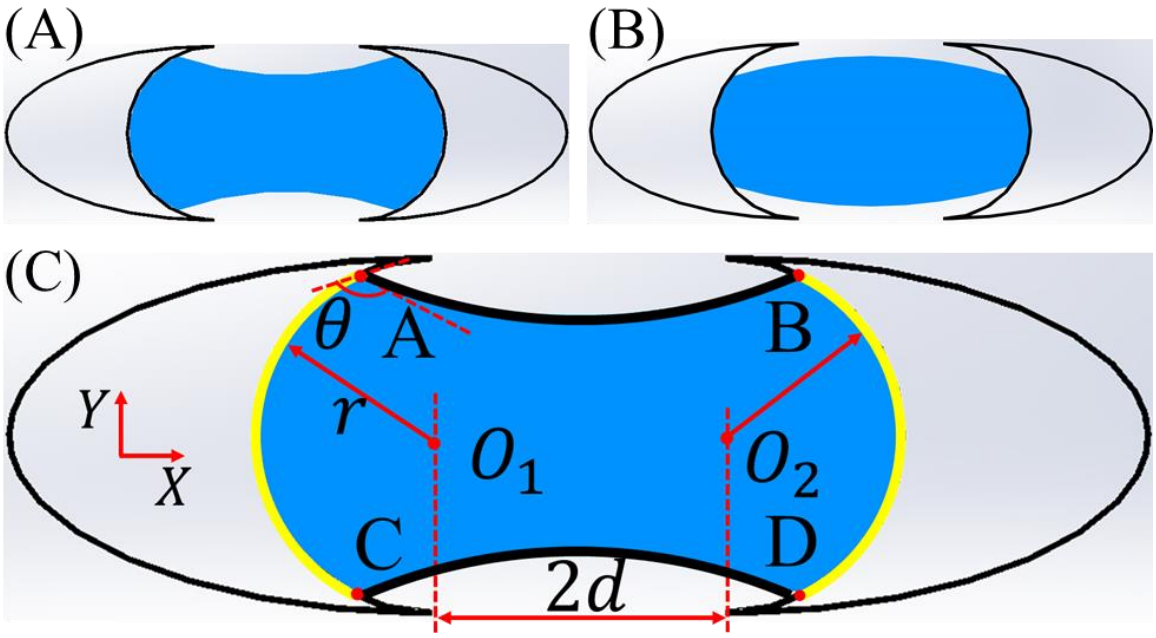

Figure 5.12. Schematic of the cross-sectional shape of a saliva bridge connecting separated parallel galeae with the contact line inside the food canal of (A) concave and (B) convex meniscuses. (C) The geometrical parameters of concave meniscus.

Following the assumption that the menisci AB and CD are the parts of circular cylinders, we obtain the pressure in the liquid column measured relative to atmospheric

pressure from the Laplace equation of capillarity as $P = -\sigma/R$. Therefore, the force balance equation is reduced to the following equation [38]:

$$(AB + CD) - (BD + AC)\cos\theta + A_{\mathrm{ACDB}}/R = 0 \tag{5.3}$$

Based on this geometry, we have the following relations:

$$AC = BD = 2r\alpha\ ,\ AB = CD = 2R\left(\frac{\pi}{2} - (\theta - \alpha)\right),\ R = (d + r\cos\alpha)/\cos(\theta - \alpha),$$

$$A_{\mathrm{ACDB}}/4r^2 = \left(\frac{d}{r} + \cos\alpha\right)\sin\alpha + \frac{1}{2}(\alpha - \sin\alpha\cos\alpha) - \left(\frac{\pi}{4} - \frac{\theta-\alpha}{2}\right)\left(\frac{d/r+\cos\alpha}{\cos(\theta-\alpha)}\right)^2 +$$

$$\frac{1}{2}\left(\frac{d/r+\cos\alpha}{\cos(\theta-\alpha)}\right)^2 \cos(\theta - \alpha)\sin(\theta - \alpha). \tag{5.4}$$

Substituting all the above geometric relations in eq. (4), the following quadratic equation is obtained:

$$a\left(\frac{R}{r}\right)^2 + b\left(\frac{R}{r}\right) + c = 0\ , \tag{5.5}$$

where

$$a = \frac{\pi}{4} - \left(\frac{\theta-\alpha}{2}\right) + \frac{\sin(2\theta-2\alpha)}{4}\ ,$$

$$b = \sin\alpha\cos(\theta - \alpha) - \alpha\cos\theta\ ,$$

$$c = \frac{\alpha}{2} - \frac{\sin 2\alpha}{4}\ .$$

Numerical analysis of the determinant $D = b^2 - 4ac$ of quadratic eq. (5.5) as a function of angle α at different contact angles θ shows that the determinant is always negative for the hydrophilic food canal ($0 \leq \theta \leq 90°$) (Fig. 5.13). This analysis suggests that for the specified conditions no solutions describing a saliva bridge exist.

The nonexistence of a saliva bridge can be physically explained as follows. Given that the contact lines are not pinned, the liquid is free to flow inside the food canal, wetting its walls. The force acting at the solid/air interface at the end of each liquid finger cannot be balanced and will stretch the meniscus, thinning the liquid bridge until the contact line is pinned by the legular edges. Otherwise, the liquid bridge will break into two separated fingers.

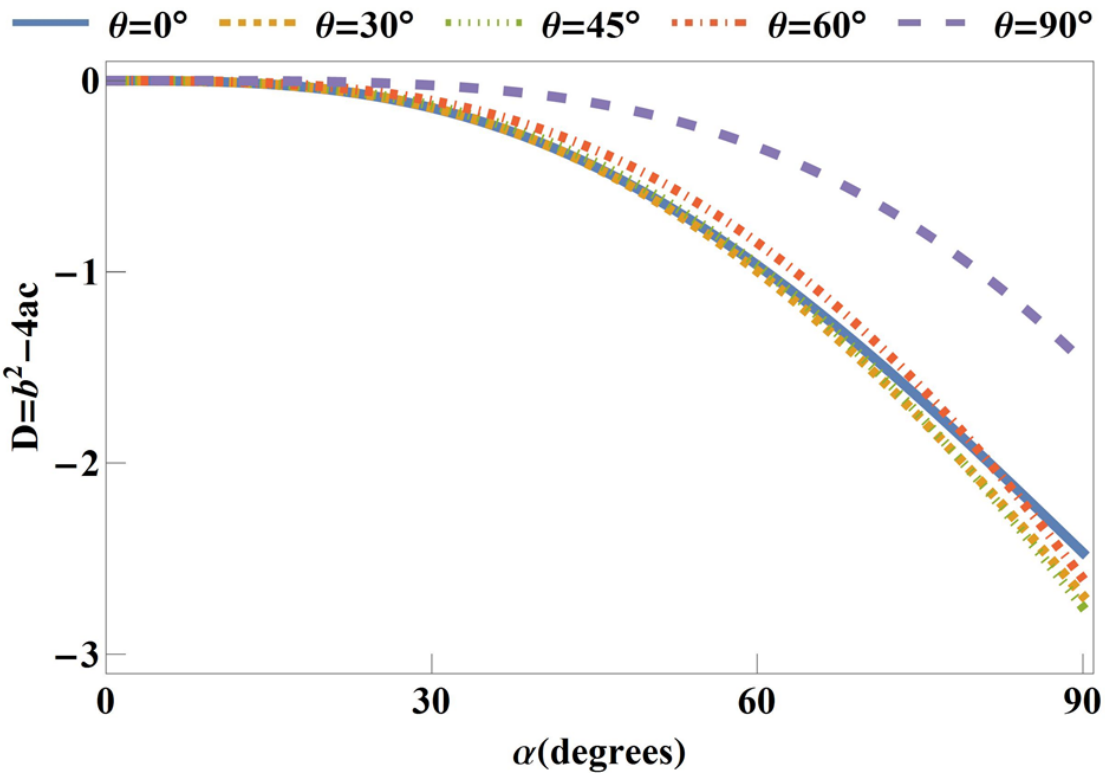

Figure 5.13. The determinant $D = b^2 - 4ac$ of eq. (5.5) as a function of α at different contact angles: $\theta = 0°, 30°, 45°, 60°, 90°$.

5.3.4.2 The contact lines are pinned at the edges of the food canal

The case where the liquid bridge is pinned to the edges of the food canal is special. As known from capillarity [45, 46], a liquid body can form any arbitrary contact angle with

a sharp edge of any corner. Therefore, the contact angle at which the meniscus meets the sharp edge is not defined and can take on any arbitrary value. We, therefore, allow the circular arcs of the two menisci to approach the edges at any arbitrary angle. The liquid bridge can take on two configurations with concave (Fig. 5.14(A)) and convex (Fig. 5.14(B)) menisci. At first, we would consider all possible scenarios solely based on the mathematical model, without taking the physical reality into account.

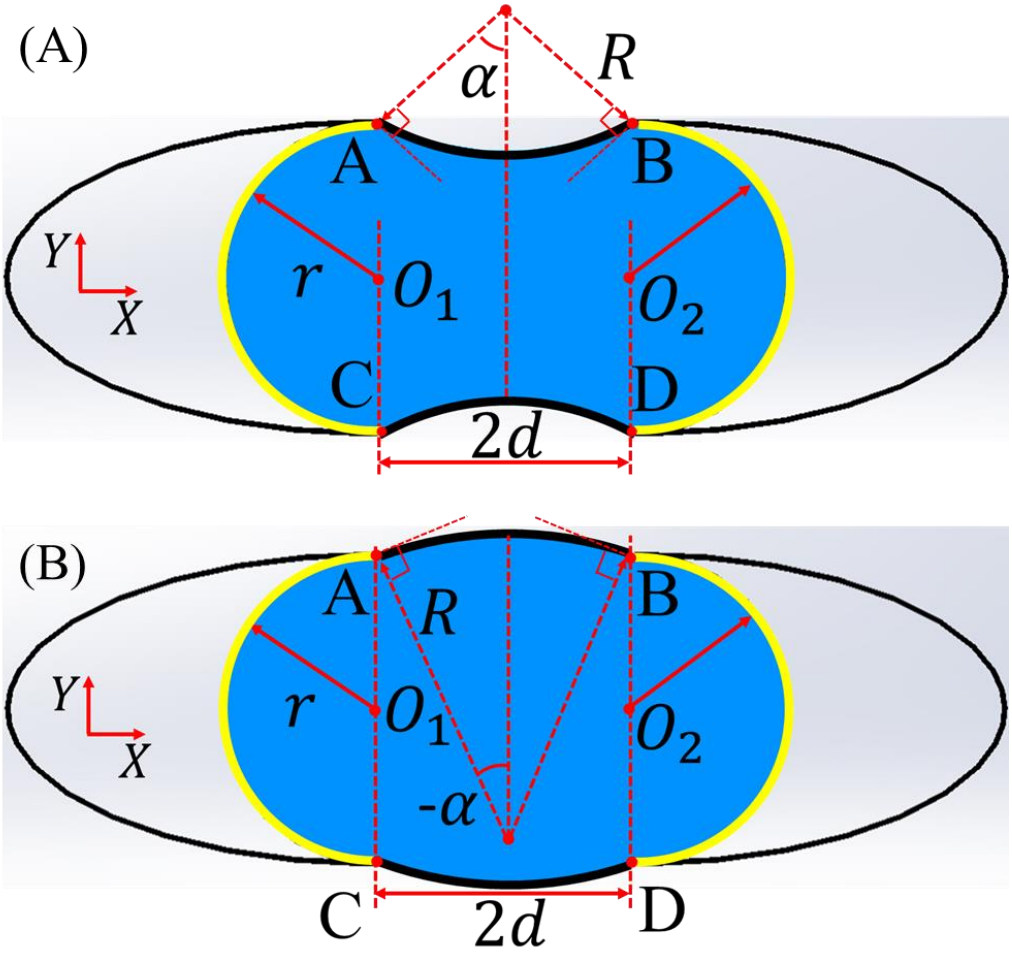

Figure 5.14. (A) Schematic of the cross-sectional shape of a saliva bridge with concave menisci connecting the two separated, parallel galeae with the contact lines pinned at the legular edges of the galeae. (B) Schematic of the cross-sectional shape of a saliva bridge with convex menisci. In (A) and (B), the angles formed by joining the thick solid curve and red dashed lines at points A and B are right angles, as indicated by the small red squares.

5.3.4.2.1 The contact lines are pinned at the edges of the food canal

The geometry has been defined in Fig. 5.14(A). The atmospheric pressure is obtained from the Laplace equation of capillarity as $P = -\sigma/R$, and the force balance equation (eq. (5.2)) is reduced to the same as eq. (5.3).

As defined in Fig. 5.14(A), the following relations between the geometrical parameters hold true:

$AC = BD = \pi r$, $AB = CD = 2\alpha R$, $d = R\sin\alpha$

$$A_{\mathrm{ACDB}}/r^2 = \pi + \frac{4R\sin\alpha}{r} - 2\alpha\left(\frac{R}{r}\right)^2 + \left(\frac{R}{r}\right)^2 \sin 2\alpha \qquad (5.6)$$

Substituting these relations in eq. (2), the following quadratic equation is obtained:

$$\left(\frac{R}{r}\right)^2 (2\alpha + \sin 2\alpha) + \frac{R}{r}(4\sin\alpha - 2\pi\cos\theta) + \pi = 0, \qquad (5.7)$$

Numerical analysis of the determinant $D = b^2 - 4ac$ of quadratic eq. (5.7) as a function of angle α at different contact angles θ for the hydrophilic food canal ($0 \leq \theta \leq 90°$) shows that a critical angle $\alpha = \alpha_0$ always exists, which makes D equal to zero (Fig. 5.15(A)). Therefore, the critical angle α_0 is calculated by setting $D = b^2 - 4ac = 0$.

$$\cos\theta = \frac{1}{\pi}\left[2\sin\alpha_0 + \sqrt{\pi(2\alpha_0 + \sin 2\alpha_0)}\right], \qquad (5.8)$$

The plot of $\alpha_0(\theta)$ is presented in Fig. 5.15(B). Only the concave meniscus with $0 \leq \alpha \leq \alpha_0$ can be formed.

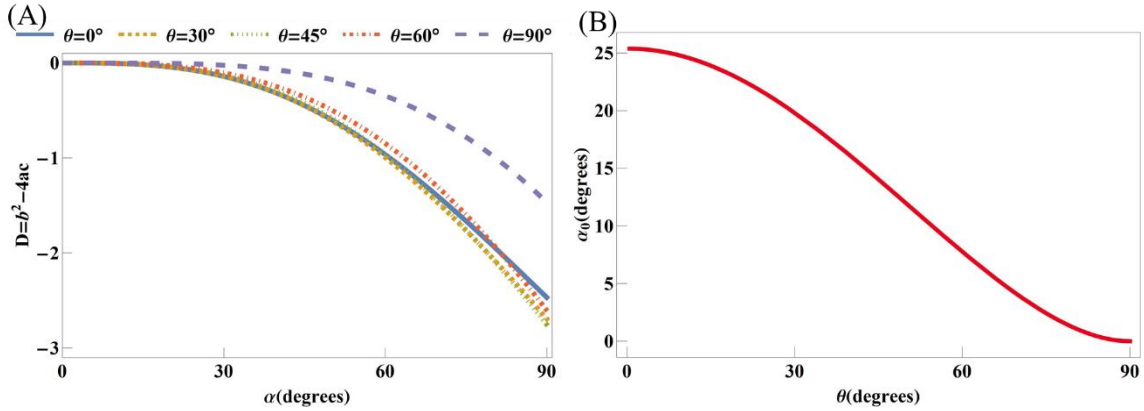

Figure 5.15. (A) The determinants $D = b^2 - 4ac$ of eq. (5.7) as a function of α at different contact angles: $\theta = 0°, 30°, 45°, 60°, 90°$. (B) The maximum angle α_0 as a function of contact angle θ.

5.3.4.2.2 The contact lines are pinned at the galeal edges

The geometry of this case is defined in Fig. 5.14(B). The atmospheric pressure is obtained from the Laplace equation of capillarity as $P = \sigma/R$, and the force balance equation is reduced to:

$$(AB + CD) - (BD + AC)\cos\theta - A_{\mathrm{ACDB}}/R = 0 \tag{5.9}$$

As defined in Fig. 5.14(B), the following relations between the geometrical parameters hold true:

$AC = BD = \pi r$, $AB = CD = -2\alpha R$ (α is negtive value), $d = R\sin(-\alpha)$

$$\frac{A_{\mathrm{ACDB}}}{r^2} = \pi - \frac{4R\sin\alpha}{r} - 2\alpha\left(\frac{R}{r}\right)^2 + \left(\frac{R}{r}\right)^2 \sin 2\alpha, \tag{5.10}$$

The resulting force balance is represented as the quadratic equation

$$-\left(\frac{R}{r}\right)^2 (2\alpha + \sin 2\alpha) + \frac{R}{r}(4\sin\alpha - 2\pi\cos\theta) - \pi = 0, \tag{5.11}$$

Numerical analysis of the determinant $D = b^2 - 4ac$ of quadratic eq. (5.11) as a function of angle α at different contact angles θ for the hydrophilic food canal ($0 \leq \theta \leq$ 90°) is shown in Fig. 5.16.

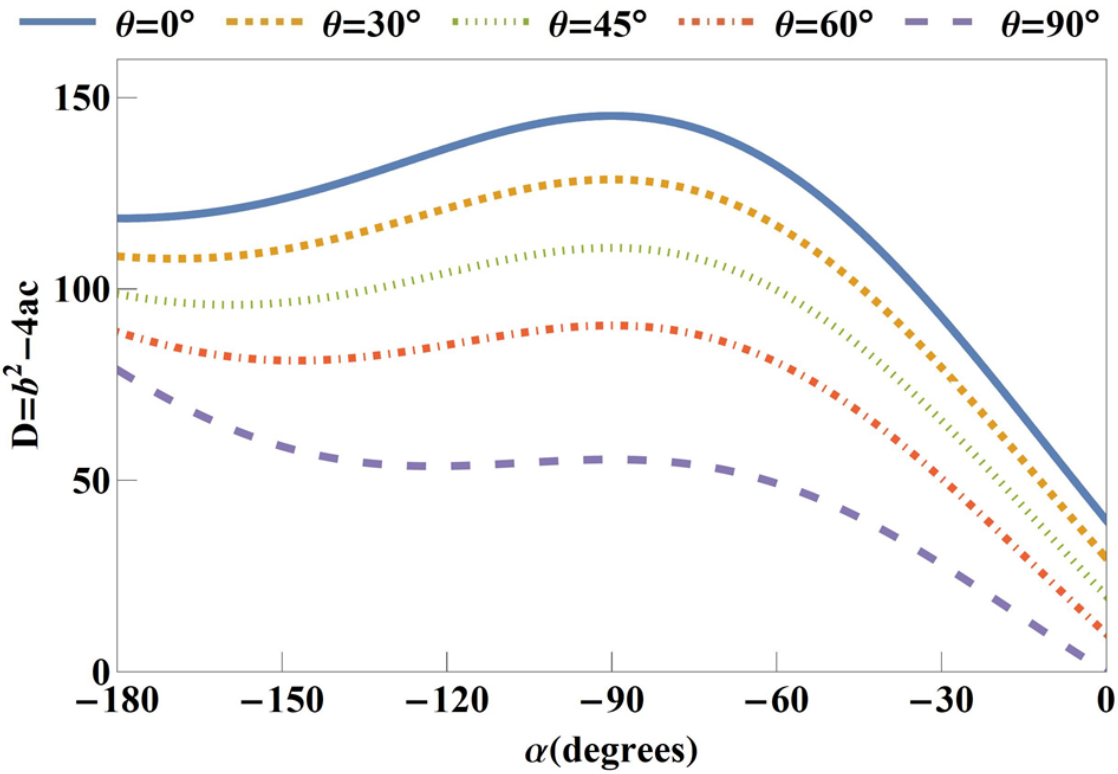

Figure 5.16. The determinant $D = b^2 - 4ac$ of eq. (5.11) as a function of α at different contact angles: $\theta = 0°, 30°, 45°, 60°, 90°$.

5.3.4.2.3 Combination of the scenarios with concave and convex meniscus

We plot the angle α as a function of the intergaleal distance d/r combining both concave and convex scenarios in Fig. 5.17, and show the meniscus profiles illustrating the main features of the solutions (contact angle $\theta = 30°$). Similar to Section 2 for the study of ribbon-like fiber rail, it can be divided into two regions (I and II) which is separated by the critical α_c. To obtain the value of α_c, the intergaleal distance $\frac{d}{r}$ is calculated as a function of α and θ using eq. (5.11) and $\frac{d}{r} = -\frac{R}{r}\sin\alpha$, and then taking the derivative with respect to α as:

$$\frac{\partial(d/r)}{\partial\alpha} = \frac{4\,(\cos\alpha)^2\sin\alpha(-\pi\cos\theta+2\sin\alpha-\sqrt{(\pi\cos\theta)^2-4\pi\cos\theta\sin\alpha+4(\sin\alpha)^2-2\pi(\alpha+\cos\alpha\sin\alpha)})}{(2\alpha+\sin 2\alpha)^2} -$$

$$\frac{4\sin\alpha\cos\alpha(1+\frac{\pi\cos\alpha+\pi\cos\theta-2\sin\alpha}{\sqrt{(\pi\cos\theta)^2-4\pi\cos\theta\sin\alpha+4(\sin\alpha)^2-2\pi(\alpha+\cos\alpha\sin\alpha)}})}{(2\alpha+\sin 2\alpha)^2} +$$

$$\frac{\cos\alpha(\pi\cos\theta-2\sin\alpha+\sqrt{(\pi\cos\theta)^2-4\pi\cos\theta\sin\alpha+4(\sin\alpha)^2-2\pi(\alpha+\cos\alpha\sin\alpha)})}{(2\alpha+\sin 2\alpha)^2}. \qquad (5.12)$$

The calculations show that $\frac{\partial(d/r)}{\partial\alpha} = 0$ at $\alpha = -90°$ for all $\theta \in [0,90°]$, which implies that α_c is always equal to $\alpha_c = -90°$. The maximum separation distance $(\frac{d}{r})_{max}$ is reached at $\alpha = \alpha_c = -90°$.

We distinguish region I where the pressure increases as the intergaleal distance increases; and region II where the pressure decreases as the intergaleal distance increases (Fig. 5.17(B)). The region II provide solution of columns with $\alpha < -90°$, which is proved to be unstable to perturbations [47]; hence we consider it no further. The solution in region I will be discussed in the following section.

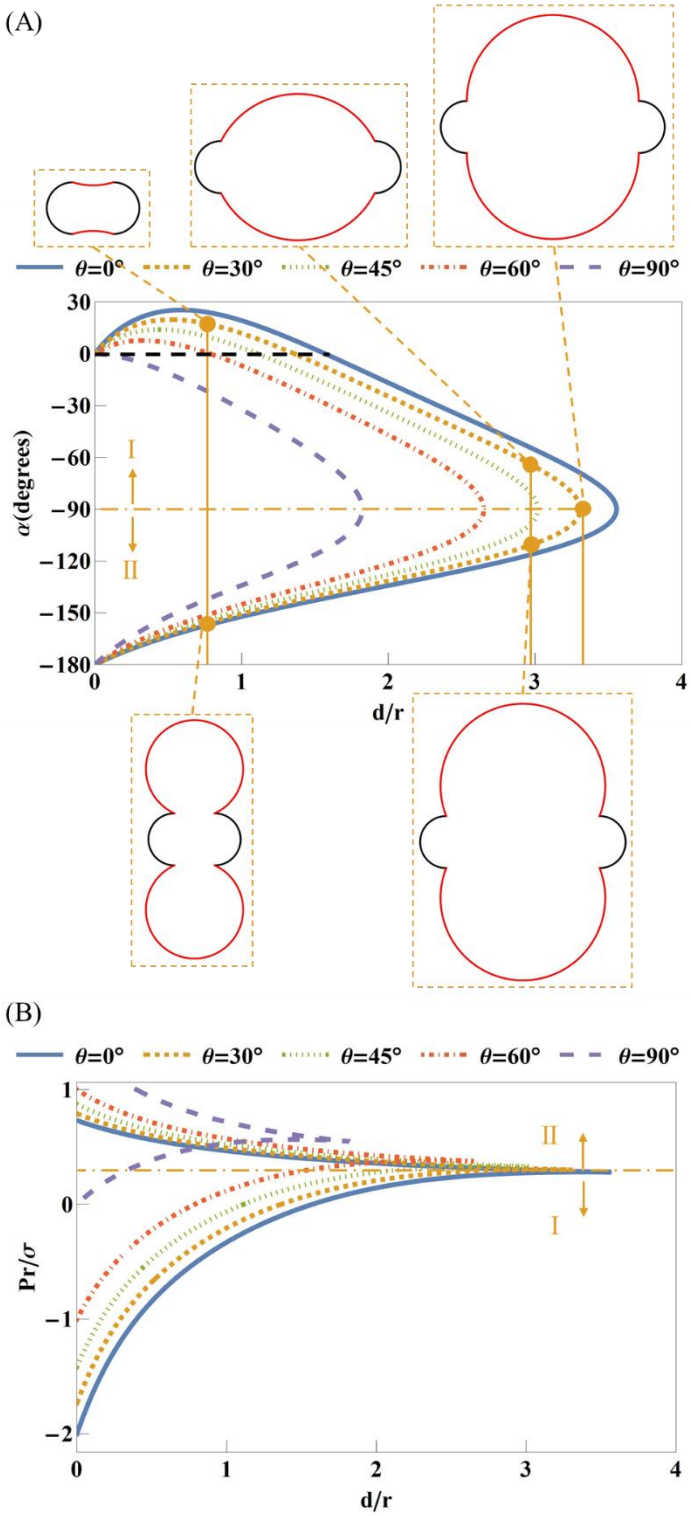

Figure 5.17. (A) The angle α as a function of the dimensionless separation distance d/r for both concave and convex menisci. (B) Dimensionless pressure inside the liquid column, Pr/σ , as a function of the dimensionless separation distance d/r for both concave and convex menisci.

5.3.5 The capillary force exerted on the galeae

Considering the force per unit length of the galea f (i.e., force density), we can evaluate it using the free-body diagram for both concave and convex scenarios in region I. An imaginary cut is made along the columnar bridge, the dashed line, Fig. 5.18(A). The obtained cross-section of this column along the tube axis is a curved rectangle: two sides of the rectangle are straight lines running parallel to the proboscis axis Z, the side that belongs to the frontal meniscus is curved, and the opposite side that ends somewhere near the base of the proboscis may be curved as well. We remove the left side of the column and introduce an equivalent system of forces to support the remaining part of the column in equilibrium. When the column is much longer than the diameter of the food canal, the contribution to the force balance of the two curved sides at the ends of this cut is negligibly small and we can neglect this contribution. Thus, the capillary force exerted by the columnar bridge on unit length of the galea consists of the two components: the surface tension component and pressure component:

$$f = 2\sigma - P \cdot \overline{AB}, \tag{5.13}$$

where the first term on the right side, $2\sigma \cdot 1$, is the tension on the two surfaces along the unit length of the A and B sides of the curved rectangle; the second term is the product of the cross-sectional area $\overline{AB} \cdot 1$ and pressure $P = \overline{+}\sigma/R$ in the saliva bridge for concave and convex columnar bridges in region I which are separated by $\alpha = 0°$, as marked by the black dashed line, Fig. 5.17(A).

Substituting into eq. (5.13) the relations $\overline{AB} = 2r \mp 2(R - R\cos\alpha)$, $d = \pm R\sin\alpha$, for concave and convex columnar bridges, respectively, we obtain:

$$f = 2\sigma \pm (\sigma/R)[2r \mp 2(R - R\cos\alpha)] = 2\sigma(\cos\alpha + \sin\alpha\,/(d/r)). \quad (5.14)$$

It is convenient to introduce a scale for the capillary force f as 2σ. We show the dependence of dimensionless force $f/2\sigma$ on the ratio d/r for different contact angles θ for both concave and convex cases which is separated by the red dash line (Fig. 5.18(B)). The force f is always positive for concave columnar bridges, which means it always pulls the two separated galeae together. Indeed, the surface tension acts to contract the air/liquid surface, tending to bring the galeae together. In addition, concave menisci generate a suction capillary pressure that adds to the surface tension pull of the galeae together. Convex columnar bridges also experience the surface tension pulling the galeae together. However, the capillary pressure of convex columnar bridges is greater than atmospheric pressure; hence, the pressure in these bridges always pushes the galeae to spread apart. Fig. 5.18(B) reveals a surprising effect: when the surface tension remains greater than the pressure acting over the galeal surfaces, some convex columnar bridges can be pulled together.

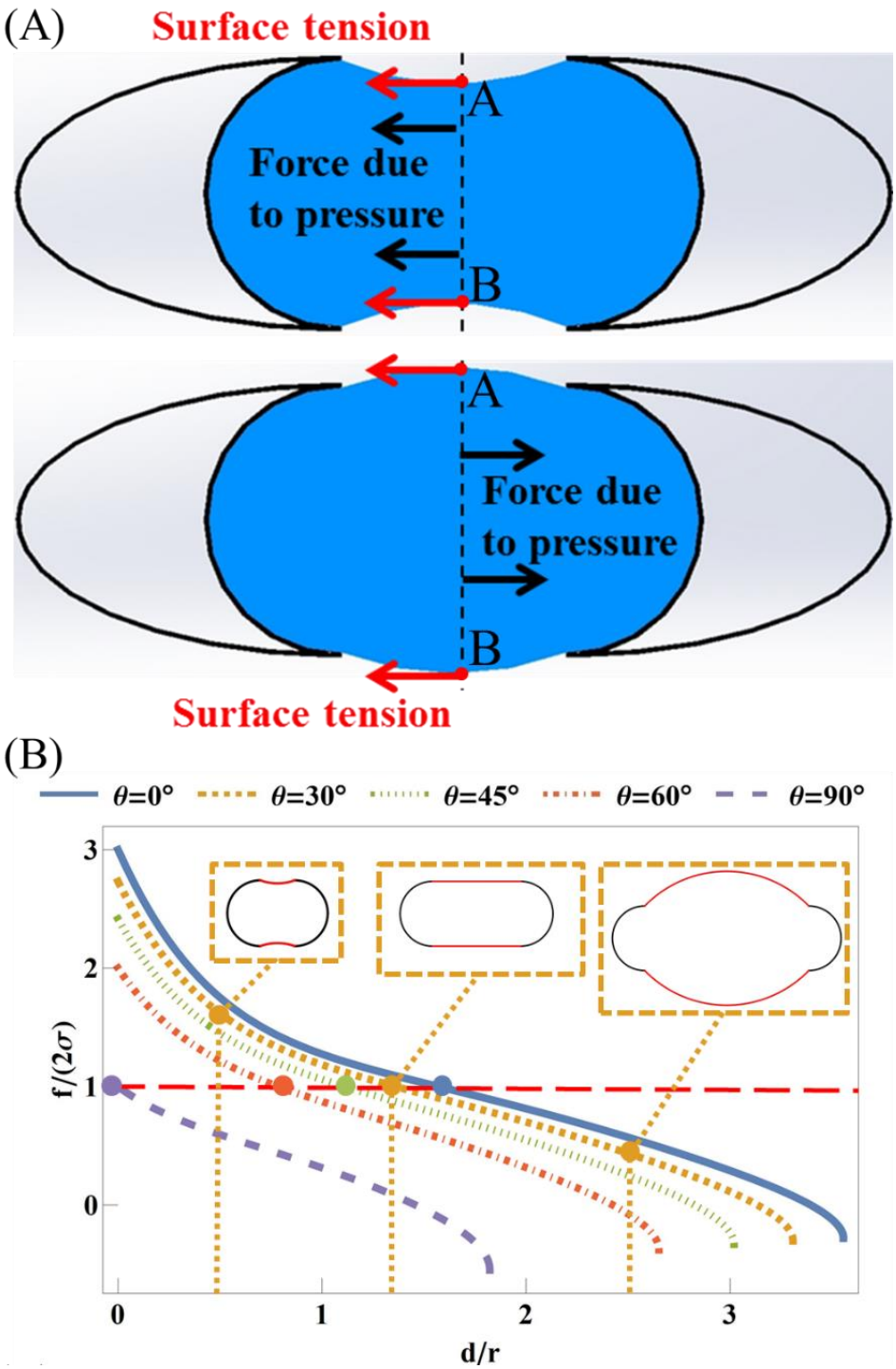

Figure 5.18. (A) Schematic illustrating the force analysis on concave and convex liquid bridges. (B) The normalized intergaleal force $f/2\sigma$ as a function of normalized intergaleal distance d/r at different contact angles $\theta = 0°, 30°, 45°, 60°, 90°$ for all scenarios. The red dashed line and the solid dots separate the concave (above) and the convex (below) columnar bridges. The meniscus profiles in the dashed boxes correspond to $\theta = 30°$ and different intergaleal distances.

5.3.5.1 Linear approximation of the capillary force acting on the galeae

Based on our experimental observations of monarch butterflies and painted lady butterflies [48], the columnar bridge breaks up to form the two separated saliva fingers when $d/r \approx 0.5$, and the contact angle between saliva and the food canal is close to 0°. Examination of the curves in Fig. 5.18(B) suggests that within this region, the force $f/2\sigma$ decreases almost linearly with d/r. Thus, approximation of the force in the form $f/2\sigma = a \cdot (d/r) + b$, is attractive due to its simplicity.

In Fig. 5.19(A), we show one example of the least-squares fit of the nonlinear force dependence with eq. (5.14), assuming that saliva makes contact angle $\theta = 0°$ with the wall of the food canal. What makes this approximation even more attractive is that the slope a and the intercept b both depend on $\cos\theta$ almost linearly (Fig. 5.19(B), (C)). The slope a and the intercept b weakly depend on the interval of approximation d/r: changing this interval from $d/r = 0.5$ to $d/r = 0.2$, the slope a changes by 17.2% and the intercept b changes by 1.6%. Thus, the linear approximation, eq. (5.14), can be used for a sufficiently wide range of experimental situations where the saliva column is present in the intergaleal gap with different openings ranging within the interval $d/r < 0.5$.

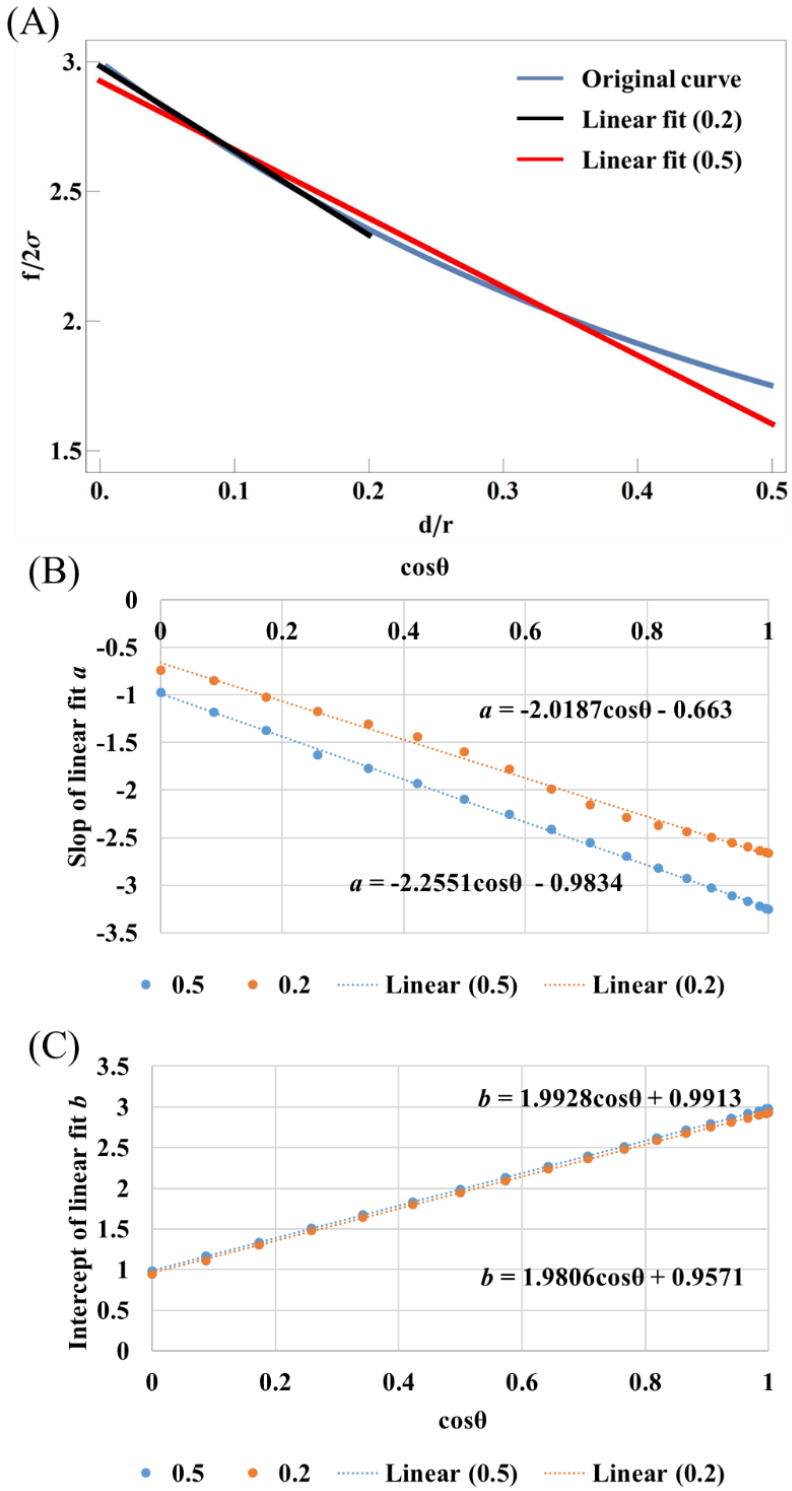

Figure 5.19. (A) Illustration of a linear approximation of the force density curve at contact angle $\theta = 0°$ for columnar saliva bridges spanning the intergaleal gap within the range $0 < d/r < 0.5$. (B) Dependence of the slope a on $\cos\theta$. (C) Dependence of the intercept b on $\cos\theta$.

5.3.5.2 Critical separation distances

For each contact angle θ, the maximum capillary force reaches at $d/r = 0$, as shown in Fig. 5.20(B). The limiting case as the intergaleal separation goes to zero, $d/r \rightarrow 0$, deserves special attention. This limit describes a united proboscis where the pressure in the liquid column is set up by the spherically capped frontal meniscus, which meets the wall of the food canal at the contact angle θ. Therefore, the pressure in the column becomes $P = -2\sigma \cos\theta / r$. The area of this rectangular cross-section of a column of unit length is $\overline{AB} = 2r \cdot 1$. Therefore, the force per unit length acting on the galea is $f_{max} = 2\sigma - P \cdot \overline{AB} = 2\sigma + 4\sigma \cos\theta$. This force is the upper limit for the capillary force exerted by the columnar bridge of saliva on the galeae. Taking $\theta = 0°$, we find, $f_{max} = 6\sigma$. Thus, in the limiting case as the galeae come together, the frontal meniscus significantly contributes to the force by increasing it threefold!

As the intergaleal distance increases, the capillary attraction between the galeae decreases. At the distance defined as $(d/r)_0$, the surface tension component and the pressure component balance each other which makes the $f/2\sigma = 0$. Since the surface tension component is always positive, the pressure component should be negative which corresponds to the convex meniscus, as shown in Fig. 5.18(B). We show $(d/r)_0$ as a function of θ in Fig. 5.20.

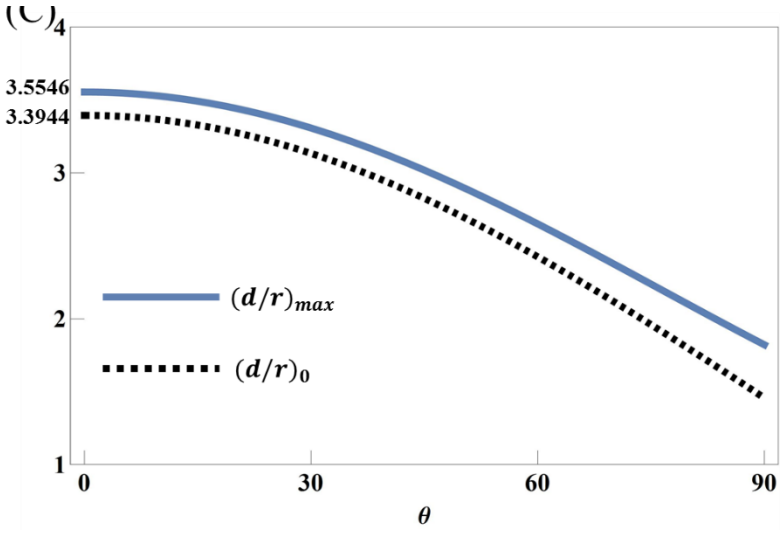

Figure 5.20. The maximum intergaleal distance $(d/r)_{max}$ below which a columnar bridge can exist and the intergaleal distance $(d/r)_0$ at which the intergaleal force goes to zero. They depend only on the contact angle.

Fig. 5.18(B) shows that stable menisci can be found at distances greater than $(d/r)_0$. The reason is that the developed model describes liquid columns formed between fixed galeae; the intergaeal distance in that case can be varied up to $(d/r)_{max} > (d/r)_0$ and the columnar bridge is expected to remain stable up to $(d/r)_{max}$. We show $(d/r)_{max}$ as a function of θ in Fig. 5.20 as well. In contrast, when the galeae are free to move, at point $(d/r)_0$ the total force flips from the attractive to repulsive pushing the galeae to spread apart; thus, the criterion for galea assembly by capillary action of a saliva column is $(d/r) < (d/r)_0$.

An order of magnitude estimate of the galea deflection due to the capillary force can be done using eq. (5.14): in the unloaded case, when the columnar bridge is absent, the force is zero. Therefore, the capillary force is expected to provide deflection on the order of $(d/r) \sim -b/a$. The experimental observations on monarch butterflies and painted lady

butterflies [48] support this order of magnitude estimate showing that the columnar bridge breaks up to form the two separated saliva fingers when $d/r \approx 0.5$ (i.e., the order of one).

As follows from this analysis, the longer the columnar bridge, the greater the force it exerts on the galeae. Thus, it is plausible that the galeae can be held in close contact, $d \ll r$, by the capillary force while the insect works to couple the legulae.

Figure 5.18(B) shows that the force remains attractive even if the meniscus becomes convex. Thus, the capillary attraction of galeae wetted by saliva is expected to show up not only in static cases when the pressure in the columnar bridge is below atmospheric, but also in some dynamic cases when the insect pumps saliva into the intergaleal gap, increasing the pressure above atmospheric pressure. To examine this possibility, we used an artificial proboscis.

5.3.6 Assembly of artificial proboscis

5.3.6.1 Columnar bridges with concave meniscus

To further demonstrate the effect of capillary force from the saliva column on the self-assembly of the Lepidopteran proboscis, the following physical model was constructed and studied experimentally. A 3M® Polyolefin (Poly(ethylene-co-vinyl acetate)) tube with a 2.2-mm outer diameter and 1.1-mm inner diameter was chosen to be about the same size as the hawk moth proboscis. The tube was partially cut along its axis. Young's modulus of these tubes, $E = 60$ MPa, measured on an Instron machine is greater or comparable to our measurements of Lepidopteran proboscises. The artificial proboscis consisted of a cylindrical tube with two half-tubes at one end. The tubular part was connected to a syringe filled with hexadecane forming zero contact angle with the tube. We chose hexadecane, a

completely wetting fluid, to remove any contact angle; it possibly mimics the effect of saliva, which presumably completely wets the food canal [7, 49]. Water provides the other limiting case by giving a contact angle of 90°. The syringe with the attached artificial proboscis was placed on a syringe pump (New Era Pump Systems, Inc., NE-300) (Fig. 5.21). During the experiment, hexadecane, which has a contact angle of 0° with the tube, was pumped through the tube, and the response of the separated half-tubes was recorded with the Redlake MotionPro X3 camera with microscopic lens (Meiji Techno® Short UNIMAC MacroZoom Lense MS-40) at a 30-fps frame rate. In this experiment, only capillary forces were expected to bring the separated half-tubes together; no other forces were involved. Thus, this setup models the effect of capillary action of saliva while excluding the effect of muscular action in the galeae and any behaviors of the butterfly.

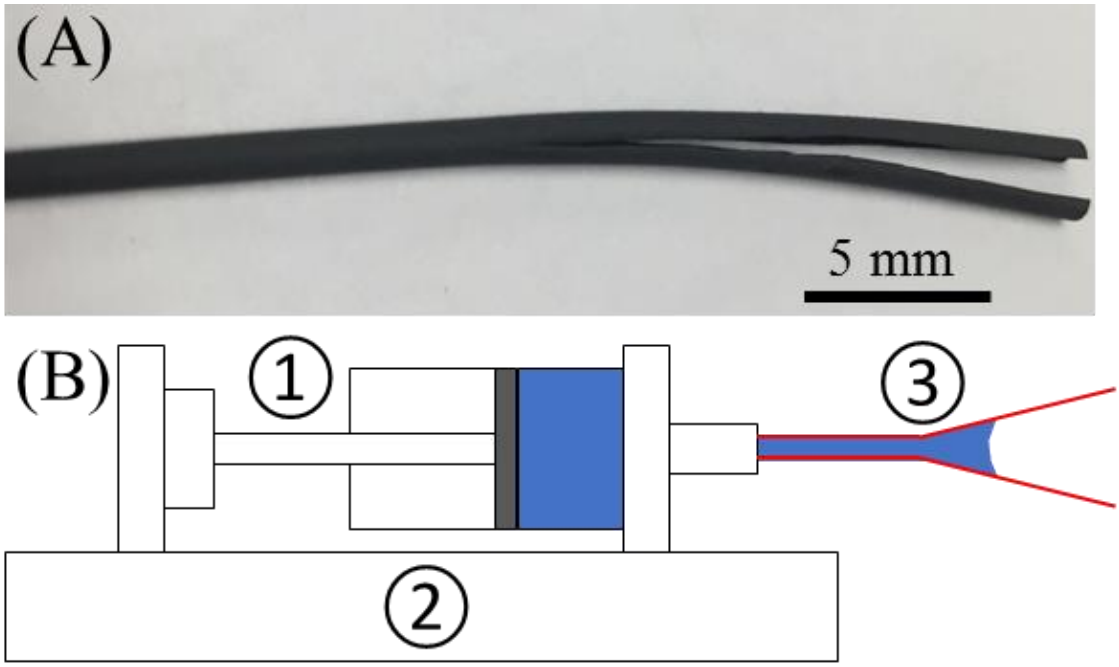

Figure 5.21. (A) Polyolefin tube partially cut along its axis. (B) Schematic of setup modelling the proboscis self-assembly. The partially cut tube (3) is connected to a syringe filled with (1) the wetting (blue) liquid and placed on (2) a syringe pump.

Two sets of experiments were conducted with this setup. In the first set, the liquid was pumped continuously through the tube at a constant rate of 0.1 ml/min. The response of the artificial galeae was recorded (Fig. 5.22). At the beginning of the experiment, the two halves were separated (Fig. 5.22(A)). In this example, the half-tubes remained almost parallel to one another with a small in-plane spontaneous curvature acquired by each half after cutting the whole tube.

When the meniscus reached the region of observation from the bottom (Fig. 5.22(B)), it brought the two halves closer: the gap between them decreased relative to that in Fig. 5.22(A). The two halves nearly connected behind the frontal meniscus while they remained separated ahead of it. We also observed this effect in live monarch butterflies.

As the pumping continued, the meniscus front, highlighted in the blue dashed box (Fig. 5.22(B), (C)) moved towards the top of these frames and then left the frame. The thickness of the air gap visibly decreased and finally disappeared (Fig. 5.22(D), (E)): the two halves came together to form a united artificial food canal. No other forces acted on the separated halves; thus, we can conclude that it was the capillary force from the hexadecane meniscus that brought the halves together.

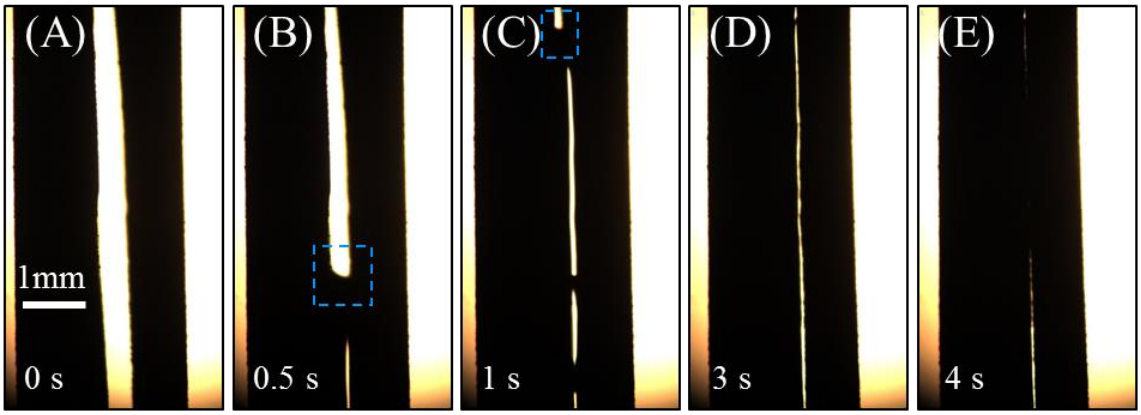

Figure 5.22. (A) The two dark half-tubes modeling the galeae are separated by an air gap; the tube base (bottom of image) and two halves are empty. (B), (C) When hexadecane is pumped through the tube base and fills the gap between the artificial galeae, the frontal meniscus boxed by the dashed lines moves forward (i.e., toward the top of the image) and the columnar bridge left behind this meniscus pulls the artificial galeae together. (D), (E) When the meniscus advances, the capillary force exerted by the columnar bridge gets stronger, bringing the artificial galeae in direct contact with one another.

In the second set of experiments, the meniscus was moved beyond the area of observation and then the pump was stopped (i.e., the piston in the pumping syringe was stopped). Thus, the hexadecane had no room to flow back to the syringe. The behavior of the separated half-tubes is illustrated with a sequence of frames in Fig. 5.23. In the reference (Fig. 5.23(A)), we show the shape of the two separated half-tubes in the region of observation before hexadecane pumping when they were completely empty. The red dashed lines mark the original position of each half, and are used to determine the displacement caused by the capillary forces. In this example, the right half-tube acquired a larger spontaneous radius of curvature after cutting the whole tube in half. Therefore, the right half is stiffer and difficult to deform. The left half has a small spontaneous curvature and, hence, is easier to deform.

During pumping, the meniscus moved from the bottom to the top of these frames, causing the left half-tube to move closer to the right stiffer half-tube. The left half moved

closer and closer to the right half-tube away from the reference marker while the right stiff half-tube remained almost nondeformed (Fig. 5.23(B)–(D)). When the pump was stopped, we observed the meniscus retracting. Fig. 5.23(E) depicts the equilibrium position of the meniscus after it has moved back. In the equilibrium state, the gap between the two half-tubes is larger compared to the case when these halves were bridged by the columnar menisci in Fig. 5.23(D), but the left half-tube remains deflected from the original configuration in Fig. 5.23(A). This deflection is caused by capillary forces acting along the remaining columnar liquid bridge.

The hexadecane had no room to flow back to the syringe; therefore, meniscus retraction was caused by two forces: the surface forces that tend to decrease the surface area of the columnar liquid bridge and the wetting forces that pull the columnar bridge forward, forcing the hexadecane to cover the surfaces of the half-tubes. The capillary force holding the two halves together decreased as the distance between the half-tubes increased (Fig. 5.18(B)). Therefore, when the pump stopped, some liquid moved to the liquid fingers present in the separated half-tubes. This flow resulted in meniscus retraction and simultaneous deflection of the left half-tube. The flow continued until the wetting and capillary forces of the columnar bridge were counterbalanced by the elastic force from the half-tubes. This phenomenon qualitatively mimics the observed self-assembly process of the Lepidopteran proboscis.

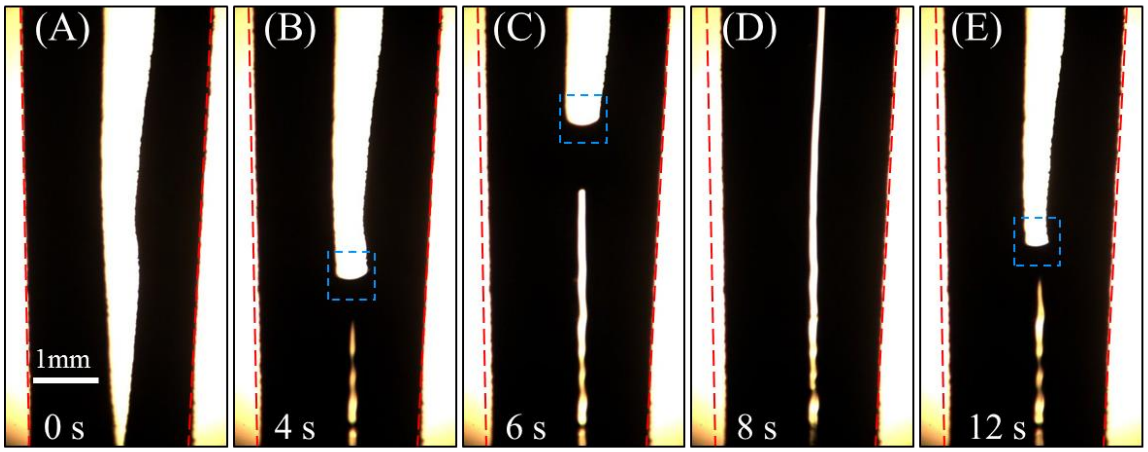

Figure 5.23. (A) Before hexadecane pumping, the two dark half-tubes modeling the galeae are separated by an air gap; the dashed borders are shown for reference to measure deflections of the half-tubes. (B)–(D) When hexadecane is pumped through the base tube and fills the artificial galeae, the frontal meniscus boxed by the dashed lines moves forward and the columnar bridge left behind this meniscus pulls the artificial galeae together. (E) The meniscus retracts after stopping the pump. This frame shows an equilibrium configuration of the half-tubes and the remaining columnar liquid bridge holding the half-tubes in close contact.

5.3.6.2 Columnar bridges with convex meniscus

The model predicts that the convex saliva meniscus can create an attractive force, given that muscular contraction and Lepidopteran behaviors are absent, at some range of separation d/r (Fig. 5.20). This result is counter-intuitive: the Laplace pressure in the columnar bridge is larger than atmospheric pressure; therefore, one would argue that the galeae should tend to separate. However, the surface tension of the columnar bridge always pulls the separated galeae together, counterbalancing the pressure within some range of intergaleal gaps.

To check this result experimentally, we used a nonwetting liquid. Our capillary rise experiments showed that water forms $\theta = 90°$ with the 3M® Polyolefin tubes. This contact angle guarantees formation of a columnar bridge with convex meniscus (Figs. 5.17, 5.18); moreover, at small intergaleal distances $d/r < 1$, this columnar bridge should exert

an attractive capillary force that pulls the artificial galeae together. Thus, water, which is similar to the nearly inviscid saliva, provides an opportunity to test our hypothesis that the columnar bridge with convex meniscus can create an attractive force.

We conducted the following experiments to test this hypothesis. First, water was pumped for 20 seconds through the artificial proboscis (Fig. 5.24(A)–(C)). When the water meniscus arrived at the bifurcation (Fig. 5.24(B)), the deflection of the two halves was negligible compared to their initial configurations. After 20 seconds of pumping when the water meniscus passed the observation area to form a long columnar bridge (Fig. 5.24(C)), a noticeable deflection of the left half was observed. This deflection remained almost unchanged after pumping for 10 more seconds, that is, when the water meniscus travelled about twice the distance to form the twice-longer columnar bridge. In contrast to the case of complete wetting of the artificial proboscis with hexadecane (Fig. 5.22), the free halves did not unite completely (Fig. 5.24(D)). This observation confirmed that the attractive capillary force is weaker compared with that of the wetting fluid, in full accord with theoretical predictions (Fig. 5.18(B)).

After pumping for 40 seconds, the pump was reversed to withdraw water from the artificial proboscis. Thus, the pressure in the columnar bridge decreased with respect to atmospheric pressure. An appreciable change in deflection of the left half-tube became apparent after 10 seconds of water withdrawal (i.e., at 55 seconds, Fig. 5.24(E))). After 15 more seconds, the two half-tubes united (Fig. 5.24(F)). When the water meniscus retracted to the observation area, the two half-tubes spread apart (Fig. 5.24(G)), and finally returned to the initial configuration when the water meniscus disappeared from the area of

observation (Fig. 5.24(H)). These two series of experiments confirmed the capillary attraction hypothesis for proboscis assembly.

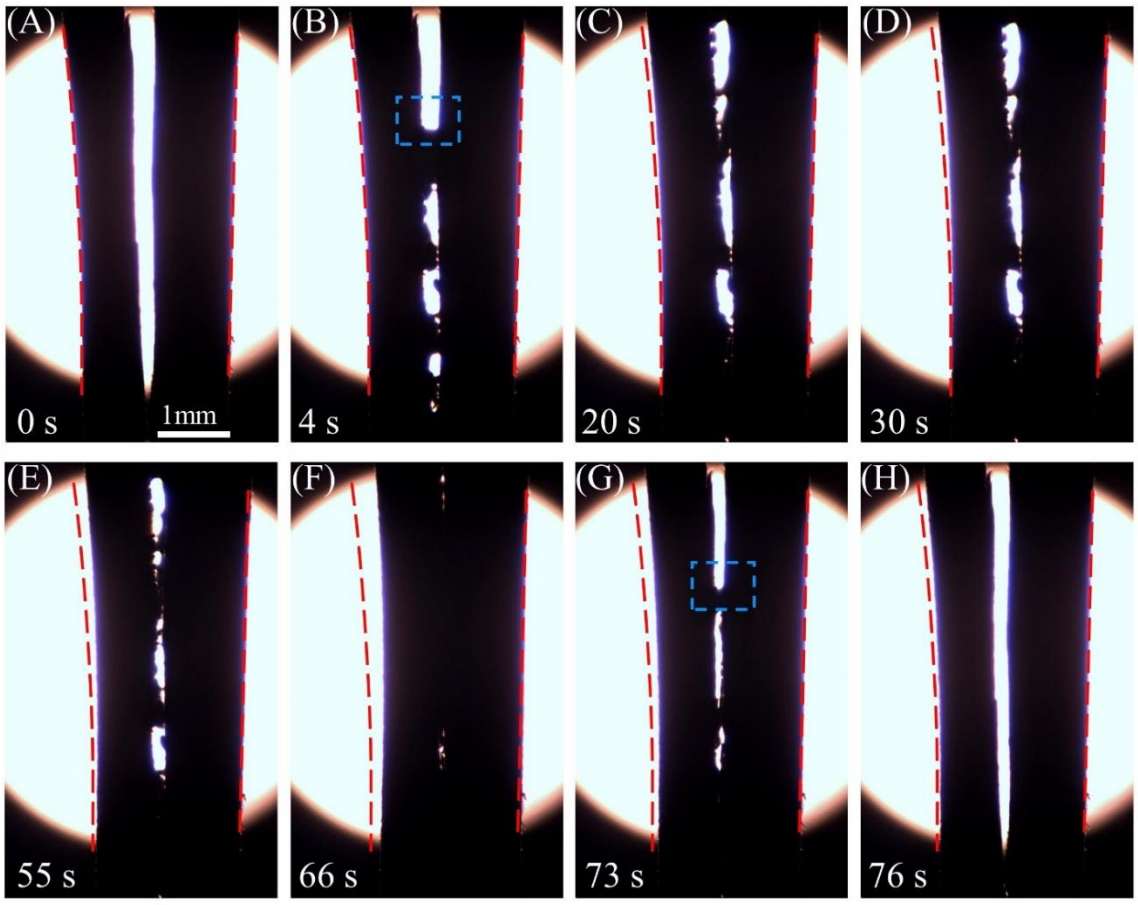

Figure 5.24. (A) Before water pumping, the two dark half-tubes modeling the galeae are separated by an air gap; the dashed borders are shown for reference to measure deflections of the half-tubes. (B)–(D) When water is pumped through the tube base and fills the artificial galeae, the frontal meniscus, boxed by the dashed lines, moves forward and the columnar bridge left behind this meniscus pulls the artificial galeae together. (E)–(H) The meniscus retracts after changing from pumping to withdrawing. (E), (F) The artificial galeae draw closer and closer after removing liquid from the meniscus by decreasing pressure in the column. (G), (H) The artificial galeae are further separated after shortening and complete removal of the columnar bridge.

5.3.7 Discussion

Proboscis self-assembly is an integrated behavioral and mechanical process involving galeal musculature, palp manipulations, legular coupling, and repeated coiling

and uncoiling of the proboscis [30]; we are addressing the role of these factors in ongoing experiments. Our focus here has been to isolate the passive forces involved in self-assembly. The routine discharge of saliva during proboscis assembly suggested our working hypothesis: Lepidoptera unite their galeae with the aid of capillary attraction by saliva. Our earlier analysis of saliva viscosity suggests that it lacks sliminess (i.e., viscoelasticity) and behaves like a simple, water-like Newtonian fluid [31].

X-ray computer tomography of freshly killed insects helped us identify the behavior of a wetting fluid inside partially separated galeae. We showed that when the intergaleal gap is small, a long columnar liquid bridge forms. The column terminates in two liquid fingers situated in the separated galeae. Consequently, we formulated a model based on our observations that saliva forms a column bridging the two galeae by capillary action. A theoretical investigation of the criteria for existence of these columns and the analysis of capillary forces exerted on the galeae revealed a set of plausible scenarios for passively holding the galeae together while the insect couples the ventral legulae to mechanically hold the galeae in place. We discovered that capillary attraction can be realized when capillary Laplace pressure of the wetting fluid is (1) lower than atmospheric pressure (i.e., the static case when the columnar bridge causes galeal attraction by suction effect) and (2) greater than atmospheric pressure (i.e., the dynamic case when surface tension pulls the galeae together but pressure pushes them apart, Fig. 5.18(A)). We confirmed our theoretical analysis with a series of illustrative experiments on artificial proboscises made of polyolefin tubes.

The often-copious production of saliva and its energy-conserving (passive) role in proboscis assembly suggest that a well-hydrated insect is critical to successful proboscis assembly. Small animals are highly susceptible to loss of body water as a function of their small size and the consequent high surface-to-volume ratio [50]. We periodically have observed Lepidopterans in our colonies, which have deformed wings and proboscises that remain uncoupled and distally withered, particularly under dry rearing conditions. We have shown that Lepidoptera can conserve fluids, including saliva, by bending and coiling the proboscis [33]. When saliva is alternately pumped into and retracted from the food canal, water could be lost to evaporation, especially in diurnal Lepidoptera. Bending and coiling the proboscis during assembly, however, facilitate fluid collection at the permeable dorsal and ventral legular bands [33]. Movement of fluid to the legular bands would promote not only capillary attraction but also re-entry of the fluid into the food canal, thus counteracting any tendency for fluid to remain on the larger evaporative surface of the outer galeal walls.

Because saliva serves as an attractive force for holding the galeae together, we suspect that the act of imbibing fluids not only benefits water balance and nutritional needs, but also facilitates galeal attraction. We suggest, therefore, that the act of fluid feeding would conserve saliva and help ensure that the galeae remain coupled despite mechanical stresses encountered during vigorous probing of a food source (e.g., floral corollas), bending and pressing the proboscis against a substrate (e.g., fig. 3 in [24]), and lateral sweeping of the proboscis over a substrate (e.g., decaying fruit [23]).

Lepidopteran saliva solubilizes encrusted sugars, other non-fluid nutriment, and highly viscous nectar [23, 24]. We have previously shown, however, that the viscosity of

Lepidopteran saliva does not differ significantly from the viscosity of nectar that butterflies typically imbibe. The role of saliva in rendering most nectars (i.e., up to 40% sugar solutions) used by Lepidoptera less viscous, therefore, would be minimal [29]. The principal functions of saliva for most adult Lepidoptera with a coilable proboscis would seem to be nutrient solubilization and galeal attraction during proboscis assembly. The unique pollen-gathering butterflies (e.g., certain *Heliconius* species) use saliva for processing the pollen for its constitutive nutrients [51]. Saliva in adult Lepidoptera also might serve as a medium for extra-oral delivery of enzymes, such as invertases [52], and in more restricted cases, proteases [53], a lubricant in antiparallel movements of the galeae after assembly, and a medium for dislodging debris and self-cleaning the proboscis.

The role of saliva in self-assembly allows testable predictions about the relative production of saliva and development of the salivary glands across the Lepidoptera. Moths with a proboscis too short to coil typically do not couple their galeae, or do so only weakly [24, 54]. Ancient Lepidopteran lineages, such as the Eriocraniidae, do not even couple the galeae during liquid uptake [55]. If proboscis assembly of these insects is minimal or absent, we would expect the role of saliva during assembly to be correspondingly minimal. Thus, these moths should have salivary glands less developed, *ceteris paribus*, than those of species with fully coilable proboscises that require assembly. The family Notodontidae offers an attractive opportunity for testing this hypothesis through behavioral studies of proboscis manipulation at eclosion from the pupa and comparative anatomical analyses of the salivary glands. The family includes representatives with short uncoilable organs and

long coilable proboscises, as well as intermediates with at least partially coilable organs mechanically coupled by ventral legulae [55, 56].

5.4 Conclusion

In this chapter, the effect of shape on several wetting phenomena of the Lepidopteran proboscis are explained based on the previous studies on wetting of complexly shaped fibers and channels.

In Section 5.1, the behavior of Lepidopteran feeding from a liquid pool is explained by the capillary rise of menisci on the proboscis. The menisci of two species of Lepidoptera show both unusual but different behaviors, which is caused by the difference in shape and surface wettability of their proboscises developed for different feeding habits. The monarch butterfly uses only the tip region for feeding, hence forming the cusped menisci to cover the most possible drinking area. The hawkmoth uses the entire length of its proboscis for feeding, hence the menisci rise up and cover a much larger length.

In Section 5.2, the evolution of the thin liquid film covering the entire proboscis, which is deposited after each dip of the proboscis into a flower or other food source, is discussed based on the study in Chapter III and IV. Because of the shape of the proboscis, the liquid film is collected at the dorsal and ventral legulae and form the liquid columns covering only the legular bands. This process can be facilitated by coiling and uncoiling the proboscis to create larger pressure differential. The coiling of proboscis can also break the film covering the wall of food canal and collect the liquid at the internal surface of the dorsal legular band to strengthen the linkage while allow them to slide over one another with little resistance.

In Section 5.3, the effect of capillary force of saliva meniscus on the self-assembly of proboscis is studied. The importance of saliva meniscus on the self-assembly process is proved by the observation on live monarch butterflies, and its features are characterized with the experiment on the dead hawkmoths through Micro-CT. A model of a pair of parallel C-shaped fibers is developed similarly to the model of ribbon rail in Section 2.4 based on the modified Prince theory. The equilibrium configuration of menisci at different separation distances is determined after considering all possible scenarios. Then the dependence of capillary force exerted on the galeae by the saliva meniscus on the separation distance is shown in Fig. 5.18, suggesting the saliva creates an attractive force for holding the galeae together to facilitate the galeae self-assembly. This effect is further proved with a series of experiments on artificial proboscis.

5.5 References

[1] Krenn, H.W., Zulka, K.P. & Gatschnegg, T. 2001 Proboscis morphology and food preferences in nymphalid butterflies (Lepidoptera: *Nymphalidae*). Journal of Zoology 254, 17-26. (doi: 10.1017/S0952836901000528).
[2] Kunte, K. 2007 Allometry and functional constraints on proboscis lengths in butterflies. Functional Ecology 21, 982-987. (doi:10.1111/j.1365-2435.2007.01299.x).
[3] Lehnert, M.S., Beard, C.E., Gerard, P.D., Kornev, K.G. & Adler, P.H. 2016 Structure of the lepidopteran proboscis in relation to feeding guild. Journal of Morphology 277, 167-182. (doi:10.1002/jmor.20487).
[4] Alimov, M.M. & Kornev, K.G. 2014 Meniscus on a shaped fibre: singularities and hodograph formulation. Proceedings of The Royal Society A 470, 20140113. (doi:10.1098/rspa.2014.0113).
[5] Lehnert, M.S., Monaenkova, D., Andrukh, T., Beard, C.E., Adler, P.H. & Kornev, K.G. 2013 Hydrophobic - hydrophilic dichotomy of the butterfly proboscis. Journal of the Royal Society Interface 10, 20130336. (doi: 10.1098/rsif.2013.0336).
[6] Lehnert, M.S., Monaenkova, D., Andrukh, T., Beard, C.E., Adler, P.H. & Kornev, K.G. 2013 Hydrophobic-hydrophilic dichotomy of the butterfly proboscis. Journal of The Royal Society Interface 10, 20130336. (doi:10.1098/rsif.2013.0336).
[7] Monaenkova, D., Lehnert, M.S., Andrukh, T., Beard, C.E., Rubin, B., Tokarev, A., Lee, W.K., Adler, P.H. & Kornev, K.G. 2012 Butterfly proboscis: combining a drinking straw

with a nanosponge facilitated diversification of feeding habits. Journal of The Royal Society Interface Interface 9, 720-726. (doi:10.1098/rsif.2011.0392).
[8] Capinera, J.L. 2008 Butterflies and moths. In *Encyclopedia of Entomology* (pp. 626–672). Springer.
[9] Krenn, H.W., Plant, J.D. & Szucsich, N.U. 2005 Mouthparts of flower-visiting insects. Arthropod Structure & Development 34, 1-40. (doi: 10.1016/j.asd.2004.10.002).
[10] Robert G. Foottit & Adler, P.H. 2009 Insect Biodiversity: Science and Society. England, Wiley-Blackwell Publishing.
[11] Bauder, J.A., Lieskonig, N.R. & Krenn, H.W. 2011 The extremely long-tongued neotropical butterfly *Eurybia lycisca* (Riodinidae): proboscis morphology and flower handling. Arthropod Structure & Development 40, 122-127. (doi: 10.1016/j.asd.2010.11.002).
[12] Krenn, H.W. 2010 Feeding mechanisms of adult Lepidoptera: structure, function, and evolution of the mouthparts. Annual Review of Entomology 55, 307-327. (doi:10.1146/annurev-ento-112408-085338).
[13] Schmitt, J.B. 1938 The feeding mechanism of adult Lepidoptera. Smithsonian Miscellaneous Collections 97, 1-28.
[14] Eastham, L.E.S. & Eassa, Y.E.E. 1955 The Feeding Mechanism of the Butterfly *Pieris-Brassicae* L. Philosophical Transitions of The Royal Society B 239, 1-43. (doi: 10.1098/rstb.1955.0005).
[15] Snodgrass, R.E. 1961 The caterpillar and the butterfly. Smithsonian Miscellaneous Collections 143, 1-51.
[16] Hepburn, H.R. 1971 Proboscis Extension and Recoil in Lepidoptera. J Insect Physiol 17, 637-656. (doi:Doi 10.1016/0022-1910(71)90114-4).
[17] Kwauk, K.J., Hasegawa, D.K., Lehnert, M.S., Beard, C.E., Gerard, P.D., Kornev, K.G. & Adler, P.H. 2014 Drinking with an unsealed tube: fluid uptake along the butterfly proboscis. Annals of the Entomological Society of America 107, 886-892. (doi:10.1603/An14027).
[18] Tsai, C.C., Monaenkova, D., Beard, C.E., Adler, P.H. & Kornev, K.G. 2014 Paradox of the drinking-straw model of the butterfly proboscis. Journal of Experimental Biology 217, 2130-2138. (doi:10.1242/jeb.097998).
[19] Karolyi, F., Szucsich, N.U., Colville, J.F. & Krenn, H.W. 2012 Adaptations for nectar-feeding in the mouthparts of long-proboscid flies (Nemestrinidae: *Prosoeca*). Biologcial Journal of the Linnean Society 107, 414-424. (doi:10.1111/j.1095-8312.2012.01945.x).
[20] Karolyi, F., Colville, J.F., Handschuh, S., Metscher, B.D. & Krenn, H.W. 2014 One proboscis, two tasks: adaptations to blood-feeding and nectar-extracting in long-proboscid horse flies (Tabanidae, *Philoliche*). Arthropod Structure & Development 43, 403-413. (doi: 10.1016/j.asd.2014.07.003).
[21] Kingsolver, J.G. & Daniel, T.L. 1995 Mechanics of food handling by fluid-feeding insects. In *Regulatory mechanisms in insect feeding* (eds. R.F. Chapman & G. de Boer), pp. 32-74. New York, Springer.
[22] Willmer, P.G. 1988 The role of insect water balance in pollination ecology: *Xylocopa* and *Calotropis*. Oecologia 76, 430-438. (doi:10.1007/BF00377039).

[23] Knopp, M.C.N. & Krenn, H.W. 2003 Efficiency of fruit juice feeding in Morpho peleides (*Nymphalidae*, Lepidoptera). Journal of Insect Behavior 16, 67-77. (doi: 10.1023/A:1022849312195).
[24] Adler, P.H. 1982 Soil- and puddle-visiting habits of moths. Journal of the Lepidopterists' Society 36, 161-173.
[25] Tsai, C.C., Mikes, P., Andrukh, T., White, E., Monaenkova, D., Burtovyy, O., Burtovyy, R., Rubin, B., Lukas, D., Luzinov, I., et al. 2011 Nanoporous artificial proboscis for probing minute amount of liquids. Nanoscale 3, 4685-4695. (doi:10.1039/c1nr10773a).
[26] Arditti, J., Elliott, J., Kitching, I.J. & Wasserthal, L.T. 2012 'Good Heavens what insect can suck it'- Charles Darwin, Angraecum sesquipedale and Xanthopan morganii praedicta. Botanical Journal of the Linnean Society 169, 403-432. (doi:10.1111/j.1095-8339.2012.01250.x).
[27] Norris, M.J. 1936 The feeding-habits of the adult Lepidoptera *Heteroneura*. Transactions of the Royal Entomological Society of London 85, 61-90.
[28] Wigglesworth, V.B. 1972 The Life of Insects. 3rd edition ed. New York, Weidenfeld and Nicolson.
[29] Krenn, H.W. 1997 Proboscis assembly in butterflies (Lepidoptera) - a once in a lifetime sequence of events. European Journal of Entomology 94, 495-501.
[30] Krenn, H.W. & Muhlberger, N. 2002 Groundplan anatomy of the proboscis of butterflies (Papilionoidea, lepidoptera). Zoologischer Anzeiger 241, 369-380. (doi:10.1078/0044-5231-00078).
[31] Tokarev, A., Kaufman, B., Gu, Y., Andrukh, T., Adler, P.H. & Kornev, K.G. 2013 Probing viscosity of nanoliter droplets of butterfly saliva by magnetic rotational spectroscopy. Applied Physics Letters 102, 033701. (doi:10.1063/1.4788927).
[32] Bico, J., Roman, B., Moulin, L. & Boudaoud, A. 2004 Elastocapillary coalescence in wet hair. Nature 432, 690-690. (doi:10.1038/432690a).
[33] Zhang, C., Beard, C.E., Adler, P.H. & Kornev, K.G. 2018 Effect of curvature on wetting and dewetting of proboscises of butterflies and moths. Royal Society Open Science 5, 171241. (doi:10.1098/rsos.171241).
[34] Pometto, S. 2014 Repair of the Proboscis of Brush-footed Butterflies (Lepidoptera: *Nymphalidae*) (Master's Thesis), Clemson University.
[35] Princen, H.M. 1970 Contact Angles from Capillary Rise Between Filaments in a V-Configuration. Textile Research Journal 40, 1069-1072. (doi:10.1177/004051757004001204).
[36] Soleimani, M., Hill, R.J. & van de Ven, T.G.M. 2015 Capillary Force between Flexible Filaments. Langmuir 31, 8328-8334. (doi: 10.1021/acs.langmuir.5b01351).
[37] Sauret, A., Boulogne, F., Somszor, K., Dressaire, E. & Stone, H.A. 2017 Drop morphologies on flexible fibers: influence of elastocapillary effects. Soft Matter 13, 134-140. (doi:10.1039/c6sm00921b).
[38] Princen, H.M. 1970 Capillary phenomena in assemblies of parallel cylinders: III. Liquid Columns between Horizontal Parallel Cylinders. Journal of Colloid and Interface Science 34, 171-184. (doi:10.1016/0021-9797(70)90167-0).

[39] Keis, K., Kornev, K.G., Kamath, Y.K. & Neimark, A.V. 2004 Towards Fiber-Based Micro- and Nanofluidics. In *Nanoengineered Nanofibrous Materials* (pp. 175-182). Kluwer Publishing.
[40] Duprat, C., Protière, S., Beebe, A.Y. & Stone, H.A. 2012 Wetting of flexible fibre arrays. Nature 482, 510-513. (doi:10.1038/nature10779).
[41] Liu, J.L. & Feng, X.Q. 2012 On elastocapillarity: A review. Acta Mechanica Sinica 28, 928-940. (doi:10.1007/s10409-012-0131-6).
[42] Boulogne, F., Sauret, A., Soh, B., Dressaire, E. & Stone, H.A. 2015 Mechanical Tuning of the Evaporation Rate of Liquid on Crossed Fibers. Langmuir 31, 3094-3100. (doi:10.1021/la5050361).
[43] Duprat, C. & Stone, H.A. 2016 Elastocapillarity. In *Fluid-Structure Interactions in Low-Reynolds-Number Flows* (pp. 193-246). Royal Society of Chemistry.
[44] Vogel, S. 2003 Comparative Biomechanics: Life's Physical World. Princeton, Princeton University Press.
[45] Alimov, M.M. & Kornev, K.G. 2014 Singularities of meniscus at the V-shaped edge. Mechanics Research Communications 62, 162-167. (doi: 10.1016/j.mechrescom.2014.10.003).
[46] Langbein, D.W. 2002 Capillary Surfaces: Shape — Stability — Dynamics, in Particular Under Weightlessness. New York, Springer.
[47] Roy, R.V. & Schwartz, L.W. 1999 On the stability of liquid ridges. Journal of Fluid Mechanics 391, 293-318. (doi:10.1017/s0022112099005352).
[48] Sande, L.M. 2017 Materials Properties of the Lepidopteran Proboscis and a Bio-Inspired Characterization Method of Capillary Adhesion (Master's Thesis). Clemson University.
[49] Liu, Y.-L., Guo, H., Huang, L.-Q., Pelosi, P. & Wang, C.-Z. 2014 Unique function of a chemosensory protein in the proboscis of two *Helicoverpa* species. The Journal of Experimental Biology 217, 1821.
[50] Hadley, N.F. 1994 Water Relations of Terrestrial Arthropods, San Diego, Academic Press.
[51] Hikl, A.L. & Krenn, H.W. 2011 Pollen processing behavior of Heliconius butterflies: a derived grooming behavior. Journal of Insect Science 11, 99. (doi:10.1673/031.011.9901).
[52] Burton, R.L. 1975 Carbohydrate digestion in the adult moth *Heliothis zea*. Journal Insect Physiology 21, 1855-1857. (doi:10.1016/0022-1910(75)90253-X).
[53] Eberhard, S.H., Hrassnigg, N., Crailsheim, K. & Krenn, H.W. 2007 Evidence of protease in the saliva of the butterfly *Heliconius melpomene* (L.) (Nymphalidae, Lepidoptera). Journal of Insect Physiology 53, 126-131. (doi: 10.1016/j.jinsphys.2006.11.001).
[54] Grant, J.I., Djani, D.M. & Lehnert, M.S. 2012 Functionality of a reduced proboscis: Fluid Uptake by *Phigalia Strigataria* (Minot) (Geometridae: Ennominae). Journal of the Lepidopterists' Society 66, 211-215. (doi:10.18473/lepi.v66i4.a4).
[55] Kristensen, N.P. & Nielsen, E.S. 1981 double-tube proboscis configuration in *Neopseustid* Moths (Lepidoptera, Neopseustidae). International Journal of Insect Morphology & Embryology 10, 483-486. (doi: 10.1016/0020-7322(81)90027-1).

[56] Kornev, K.G., Salamatin, A.A., Adler, P.H. & Beard, C.E. 2017 Structural and physical determinants of the proboscis-sucking pump complex in the evolution of fluid-feeding insects. Scientific Report 7, 6582. (doi:10.1038/s41598-017-06391-w).

CHAPTER VI

CONCLUSIONS

Inspired by the Lepidopteran proboscis, the wetting of complexly-shaped fibers and channels is studied in this Dissertation.

The study is started with the wetting of ribbon-like fibers. Several wetting phenomena including the droplet morphological transition and stability of coating film, the capillary rise of meniscus, and the analysis of liquid bridges in the ribbon rail are studied through different methods, which sets up fundamentals for the further study.

The study of capillary rise of meniscus on the ribbon-like fibers illustrates the effects of the shape and wettability of the fiber on the shape of meniscus. It is then applied to the study of capillary rise on the proboscis of different species of Lepidoptera to explain the mechanism of feeding from a liquid pool.

In the experimental study of droplet morphological transition on the ribbon-like fibers, the idea of two methods of forming droplet on the fibers, from direct disposition and from the breaking up of coating film, is set up. More advanced experimental setups are developed based on these two methods for the study of droplet morphology and coating film on elliptical fiber in Chapter III and Lepidopteran proboscis in Chapter V.

In the theoretical study of droplet morphological transition on the ribbon-like fibers, a core method for analyzing the force balance on the column morphology is developed by

modifying the Princen theory. This method takes into account both the cross-sectional shape of the column and the contact lines at the column ends, which is proved to be applicable for studying the equilibrium of liquid columns with different with cross-sectional shape. Therefore, it is widely used in the study of column morphology in the hollow elliptical fibers and the wetting/dewetting transition in V-shaped and C-shaped channels.

The method is further developed in the study of liquid bridges in the ribbon rail, which allows us to determine the liquid bridge morphology at different separation distances and calculate the resulting capillary force. This model builds solid fundamentals for thorough analysis of the role of saliva on the self-assembly of Lepidopteran proboscis.

The qualitative study of coating film stability on ribbon-like fibers emphasize the importance of curvature on the pressure distribution inside the liquid film based on the Laplace law of capillary. Furthermore, a model of an elliptical hollow fiber looped in a circular ring is proposed and the stability of the external and internal films is studied by analyzing the pressure distribution inside the liquid film. This model can be used to describe various fiber configurations by changing the fiber cross-sectional ellipticity and ring radius, and is applied to study the effect of coiling on the thin films deposited on the external surface and the wall of food canal of the Lepidopteran proboscis to explain the mechanism of feeding from the thin film covering the entire proboscis.

This Dissertation sets up the fundamentals for further study of wetting of complexly shaped fibers and channels, including directions, theoretical methodology, experimental protocols and design of experiment setups; it provides the physical principles for new

design of fiber-based fluidic devices and textiles with controlled wettability and transport properties.